VRIJE UNIVERSITEIT

Search for a drifting proton-to-electron mass ratio via optical and radio astronomy

ACADEMISCH PROEFSCHRIFT

ter verkrijging van de graad Doctor aan
de Vrije Universiteit Amsterdam,
op gezag van de rector magnificus
prof.dr. V. Subramaniam,
in het openbaar te verdedigen
ten overstaan van de promotiecommissie
van de Faculteit der Bètawetenschappen
op donderdag 20 november 2017 om 9.45 uur
in de aula van de universiteit,
De Boelelaan 1105

door

Mario Daprà

geboren te Turijn, Italië

promotor:	prof.dr. W. M. G. Ubachs
copromotor:	dr. H. L. Bethlem

This thesis was approved by the members of the reviewing committee:

prof.dr. M. P. Decowski	UvA Amsterdam
prof.dr. C. Dominik	UvA Amsterdam
prof.dr. L. Kaper	UvA Amsterdam
prof.dr. K. M. Menten	Max Planck Insitut für Radioastronomie Bonn
prof.dr. P. J. Mulders	Vrije Universiteit Amsterdam

Cover by Oliver Sitar.
ISBN
Printed in the Netherlands by Ipskamp Drukker.
A digital version of this thesis can be obtained at `www.ubvu.vu.nl`.

This work is part of the research programme of the 'Stichting voor Fundamenteel Onderzoek der Materie' (FOM), which is financially supported by the 'Nederlandse Organisatie voor Wetenschappelijk Onderzoek' (NWO). The research was performed at the LaserLab of the Vrije Universiteit Amsterdam.

a Sandra e Cecco

CONTENTS

1

INTRODUCTION AND SUMMARY

The laws of physics describing and explaining natural phenomena are based on a small set of parameters. Although these parameters cannot be derived from the theories in which they appear, their values were measured in a number of dedicated experiments. Since they represent the building blocks of any physical law, these parameters are referred to as 'fundamental' constants and they are considered to be invariable.

Dirac [1], in his *large number hypothesis*, was the first to suggest the idea that the fundamental constants should be considered as variables rather than pure mathematical numbers. This hypothesis was later implemented by Jordan [2], who developed a theory in which the gravitational constant, G, and the fine-structure constant, $\alpha = e^2/4\pi\epsilon_0\hbar c$, were treated as dynamicals. Today, given the substantial body of theoretical and experimental work produced over the last decades [for an extensive review see 3], the concept of 'varying constants' is not an oxymoron anymore. Rather, testing the invariance of fundamental constants means to test the laws of Nature as we understand them today. In particular, fundamental constants are deeply linked with the equivalence principle and general relativity. Indeed, the mass of any composite body includes the masses of the elementary particles as well as the binding energies associated with the different interactions. As a consequence, the mass of any composite body is a complex function of the fundamental constants. It follows that variations of the fundamental constants imply violations of the Einstein equivalence principle and deviations from general relativity. In other words, the detection of any variation of the fundamental constants implies the existence of new physical degrees of freedom in the current theories; that is 'new' physics.

Fierz [4] realised that, when the fine-structure constant varies, atomic spectra will become space-time dependent, allowing the varying-constant theories to be tested in dedicated experiments. Such experiments usually investigate the variation of *dimensionless* combinations of fundamental constants. The reason for this is that

there is no way to ascertain whether the variation happens in the dimensional fundamental constant or in the units system [5, 6].

The Standard Model of particle physics is built starting from 19 fundamental constants, plus up to 9 extra parameters describing massive neutrinos. As first pointed out by Born [7], only two of them, i.e. the fine-structure constant and the proton-to-electron mass ratio μ, are needed to describe the structure of atomic and molecular systems. While α sets the electrodynamic scale, μ is sensitive to the ratio of the chromodynamic to the electroweak scale [8].

The purpose of this thesis is to investigate the variation of the proton-to-electron mass ratio μ, the value of which was measured with a relative precision of 9.5×10^{-11} by Sturm *et al.* [9]:

$$\mu \equiv \frac{M_P}{m_e} = 1836.152\,673\,89(17). \tag{1.1}$$

It is worth noting that in many scenarios possible variations of α and μ are connected [8, 10–13] via the relation:

$$\frac{\Delta\mu}{\mu} = R\frac{\Delta\alpha}{\alpha}. \tag{1.2}$$

Although the proportionality factor R is strongly model dependent, its absolute value is large ($|R| \sim 20-40$) in many scenarios. As a consequence, a hypothetical variation in μ will be larger than that in α, making the proton-to-electron mass ratio an important target for detecting variations of fundamental constants.

1.1. THEORIES OF VARYING μ

Theories that allow fundamental constants to vary can be roughly divided into two main categories: the Kaluza-Klein theories, which introduce the variation of fundamental constants by means of extra dimensions, and the Bekenstein theories, in which the fundamental constants vary due to the coupling of an additional scalar field.

The Kaluza-Klein theories descend from the first unified field theory developed by Kaluza [14] and Klein [15], who postulated the existence of an extra dimension. While more modern string theories postulate the existence of up to eleven dimensions as for the M-theory [16–18], the underlying common idea is that fundamental constants are invariant over the whole multi-dimensional space. In our spacetime it is possible to perceive only their 3+1 dimensions projections, which are expected to vary with the cosmological evolution of our Universe, while the multi-dimensional fundamental constants stay invariant.

The second class of theories is based on the work of Bekenstein [19], who constructed a framework for α variability based on very general assumptions, such as covariance, gauge invariance, causality and time-reversal invariance of electromagnetism, by introducing a scalar field coupled to the matter density. This work was

later improved and generalised by Barrow *et al.* [20] and Sandvik *et al.* [21]. They related the variation of the fine structure constant to the coupling of a scalar field with matter energy density. Such variation is suppressed by the larger dark energy density.

Despite the fact that light scalar fields were widely investigated and are often invoked to explain the cosmic acceleration at low redshifts, $z < 1$ [22, 23], they were never detected in any of the tests of the equivalence principle. An explanation for the non detection was eventually provided by the so-called 'chameleon' scenario [24–26] which assumed that the light scalar fields acquire both effective potentials and masses because of the coupling to matter. In particular, the effective potential has a minimum whose value depends on the local matter density [24]. As a consequence, this coupling introduces a functional dependency of μ and α on the local matter density [27].

1.2. ASTROPHYSICAL CONSTRAINTS

As first suggested by Thompson [28], molecular lines provide a good testing ground to search for variations of μ. In the Born-Oppenheimer approximation, the energy level of the i-th molecular transition can be expanded as:

$$E_i = c_{\rm electr} + \frac{c_{\rm vibr}}{\sqrt{\mu}} + \frac{c_{\rm rot}}{\mu}, \tag{1.3}$$

where $c_{\rm electr}$, $c_{\rm vibr}$ and $c_{\rm rot}$ are related to the electronic, vibrational and rotational energies, respectively. Following Eq. 1.3, a variation of the proton-to-electron mass ratio will cause a variation of the rovibrational transition energies, which can be observed as a shift in the detected wavelengths, with respect to the expected, laboratory wavelengths. Varshalovich and Levshakov [29] proposed to parametrise the shift as:

$$\lambda_i^{\rm obs} = \lambda_i^{\rm em}(1+z_{\rm abs})(1+K_i\frac{\Delta\mu}{\mu}), \tag{1.4}$$

where $\lambda_i^{\rm obs}$, $\lambda_i^{\rm em}$ are respectively the observed and the emitted wavelengths of the i-th transition, i.e. in its rest-frame, $z_{\rm abs}$ is the redshift at which the transition originated and K_i is the sensitivity coefficient of the transition. The sensitivity coefficient, which defines the magnitude and sign of the wavelength shift, is defined as:

$$K_i = \frac{d\ln\lambda_i}{d\ln\mu} \tag{1.5}$$

and is specific for each transition.

The specificity of the sensitivity coefficients allows to break the degeneracy between the wavelength shift caused by the cosmological expansion of the Universe, which is common to all the transitions, and the shift due to a non-zero $\Delta\mu/\mu$, which is different per each transition and acts as a 'fingerprint' of the μ variation. Usually,

several spectral features related to multiple molecular and atomic species originate from the same astrophysical system. Since the atomic features are not sensitive to a varying μ, they can be used to unambiguously determine the redshift.

1.2.1. HIGH REDSHIFT CONSTRAINTS

Quasars are ideal targets to study the variation of fundamental constants over cosmological time-scales, since their spectra usually contain absorption features for a variety of molecular and atomic species. Such features originate in intervening absorbers which lie in the line of sight towards the background quasar.

Quasars are usually found at intermediate and high redshifts, $z_{\rm abs} > 1$ and therefore provide a powerful tool to investigate μ variations over time-scales of ≥ 10 Gyrs. Analyses of μ-variation at high redshifts are carried out targeting mostly molecular hydrogen, H_2, and deuterated molecular hydrogen, HD, absorption. Recently, an independent constraint on $\Delta\mu/\mu$ was derived from carbon monoxide, CO, absorption in quasar spectra [30, see Chapters 4-5].

Molecular hydrogen is the most abundant molecule in the Universe and it is sensitive to a varying μ. In spite of its abundance, H_2 absorption is found only in the spectra of a limited number of quasars. Zwaan and Prochaska [31] suggested that molecular hydrogen in damped Lyman-α systems, DLAs, is concentrated in few highly overdense regions with low covering factors ($\sim 1-6\%$), so that the detection of strong H_2 absorption, i.e. $\log[N_{\rm H\,2}/{\rm cm}^{-2}] > 21$, is relatively rare. In a more recent study, Jorgenson *et al.* [32] showed that the covering factor of strong H_2 systems in DLAs is $\sim 1\%$.

Molecular hydrogen absorption can be used to investigate μ variations only when certain additional conditions are met. The H_2 transitions that are typically detected in quasar spectra belong to rotational lines in the $B^1\Sigma_u^+ - X^1\Sigma_g^+$ Lyman and $C^1\Pi_u - X^1\Sigma_g^+$ Werner bands, the rest wavelengths of which are in the range 910-1410 Å. Such wavelengths can be observed using the large, ground-based telescopes only for absorption redshifts $z_{\rm abs} \geq 2$, when they are redshifted into the optical atmospheric window. Moreover, the H_2 transitions should be detectable yet not saturated, otherwise the determination of their centroids will have large uncertainties. This conditions translates into molecular hydrogen column densities in the range $14 \leq \log[N_{\rm H\,2}/{\rm cm}^{-2}] \leq 18$. Finally, since the H_2 transitions fall in the blue part of quasar spectra, which usually has a lower S/N, the background quasar should be bright enough to reach a good S/N in the Lyman-α forest within a reasonable observing time.

In μ-variation analyses the wavelengths of the molecular lines detected are compared to those measured in the laboratory. Therefore, it is crucial to know the rest wavelengths with the highest accuracy possible. More than 160 H_2 Lyman and Werner transitions, covering the range 900-1150 Å, were measured in the Amsterdam laboratory with relative accuracies $\Delta\lambda/\lambda \leq 8\times10^{-7}$, by direct XUV-laser and

two-step excitation processes [33–37]. These measurements probed only the vibrational ground state and the rotational states with $J = 0$-5, which are the transitions typically detected in quasar spectra. In a similar way, HD transitions were measured with relative accuracies $\Delta\lambda/\lambda \leq 4 \times 10^{-7}$ [38, 39]. These reference wavelengths are ~ 2 orders of magnitude more accurate than those observed in quasar spectra and are therefore usually considered exact for the purpose of μ-variation studies. The sensitivity coefficients were calculated within a semi-empirical framework, including effects beyond the Born-Oppenheimer approximation and are known with relative accuracies better than 5×10^{-4} [36]. Sensitivity coefficients for the Lyman and Werner band systems are in the range from -0.02 to $+0.06$. The low sensitivity of the H_2 molecule to a varying μ is compensated by the high redshifts at which it can be detected. Molecular hydrogen transitions relative to the Lyman and Werner band systems are detected at absorption redshifts $z_{\rm abs} > 2$, when they are redshifted into the optical band. The highest redshift at which H_2 is detected is $z_{\rm abs} = 4.22$ [40], which corresponds to a look-back time of ~ 12.5 Gyrs. Therefore, the temporal baseline to probe μ-variations provided by the H_2 molecule μ-variations is $\sim$ 9-10 orders of magnitude larger than that of pure laboratory investigations. A database including the molecular parameters needed to model the H_2 and HD absorption, namely laboratory wavelengths, sensitivity coefficients, oscillator strengths and radiative transfer damping parameters, was compiled and reported by Malec *et al.* [41].

Carbon monoxide is the second most abundant molecule in the Universe and its spectrum is one of the best studied in the laboratory. Despite its abundance, CO absorption is typically much weaker than H_2 absorption, therefore it is detected only in a few of DLA systems at redshifts $z_{\rm abs} > 1$. Carbon monoxide absorption at high redshifts is usually detected in the singlet-singlet $A^1\Pi - X^1\Sigma^+$ band system and the singlet-triplet $d^3\Delta - X^1\Sigma^+(5-0)$ perturbing band. All these bands have rest wavelengths in the range 1300-1540 Å, i.e. they fall at longer wavelengths than the Lyman α transition ($\lambda = 1215.67$ Å). Assuming that the difference between the emission redshift of the background quasar, $z_{\rm em}$, and that of the DLA system, $z_{\rm abs}$, is small, these CO bands fall in the red part of the quasar spectrum, i.e. outside the Lyman α forest. CO absorption in quasar spectra is detected also in other band systems, namely the singlet-singlet $B^1\Sigma^+ - X^1\Sigma^+$, $C^1\Sigma^+ - X^1\Sigma^+$ and $E^1\Pi - X^1\Sigma^+$ [30, see Chapter 4]. However, these band systems have rest wavelengths < 1215.67 Å, which implies that they fall in the Lyman α forest and they are likely to be overlapped by some intervening neutral hydrogen features.

As first proposed by the Amsterdam group [50], the CO $A^1\Pi - X^1\Sigma^+$ band system can be used to probe μ variation, since it has sensitivity coefficients showing a spread of $\Delta K_i = 0.068$, corresponding to that of the molecular hydrogen Lyman and Werner bands. Moreover, the $B^1\Sigma^+ - X^1\Sigma^+$, $C^1\Sigma^+ - X^1\Sigma^+$ and $E^1\Pi - X^1\Sigma^+$ band systems act like anchor bands as they have much smaller sensitivities to a varying μ, resulting in a more robust constraint on $\Delta\mu/\mu$. However, the individual rotational lines in the CO

TABLE 1.1: List of the 7 extragalactic CO absorption systems observed in the optical. The right ascension and declination values are listed in Columns 2-3, the column densities in Column 5 are given on a $\log_{10}$ scale.

Quasar	α (J2000)	δ (J2000)	$z_{\rm abs}$	$N_{\rm CO}$ [cm^{-2}]	References
J0000+0048	00:00:15.17	+00:48:33.29	2.52	15.0	Noterdaeme *et al.* [42], Daprà *et al.* [43]
J0857+1855	08:57:26.79	+18:55:24.4	1.72	13.5	Noterdaeme *et al.* [44]
J1047+2057	10:47:05.80	+20:57:34	1.77	14.7	Noterdaeme *et al.* [44]
J1237+0647	12:37:14.60	+06:47:59.5	2.69	14.2	Noterdaeme *et al.* [45], Daprà *et al.* [46]
J1439+1117	14:39:12.04	+11:17:40.5	2.42	13.9	Noterdaeme *et al.* [47], Srianand *et al.* [48]
J1604+2203	16:04:57.49	+22:03:00.7	1.64	14.6	Noterdaeme *et al.* [49]
J1705+3543	17:05:42.91	+35:43:40.3	2.04	14.1	Noterdaeme *et al.* [44]

bands are not resolved and there are typically fewer rotational transition than those found for H_2 absorption. This results in a slightly looser constraint on a varying μ. Another advantage of using CO absorption features in μ-variation analyses is that CO and H_2 probe the same molecular gas inside the absorbing system, hence they are observed under the same physical conditions. Therefore the two molecules provide independent constraints on $\Delta\mu/\mu$ at the same absorption redshift.

The constraints derived from H_2 and CO absorption at high redshift systems are presented in Fig. 1.1, their weighted average returns a constraint of $\Delta\mu/\mu = (3.2 \pm 1.6) \times 10^{-6}$, which is consistent with no variation over a look-back time of $\sim$ 10.5-12.5 Gyrs at a 3σ confidence level. In Chapter 4-5, the first two constraints on $\Delta\mu/\mu$ derived from electronic CO absorption are discussed. In particular, the results presented in Chapter 4 are derived from CO absorption in the same system analysed and discussed in Chapter 3 for molecular hydrogen.

1.2.2. INTERMEDIATE REDSHIFT CONSTRAINTS

The H_2 Lyman and Werner transitions have low sensitivities to a varying μ, as they are electronic transitions. Ubachs *et al.* [36] showed that the electronic H_2 transitions have sensitivity coefficients more than one order of magnitude smaller than pure rotational lines. More sensitive transitions, such as the ammonia, NH_3, inversion lines and methanol, CH_3OH, rotational lines can be targeted to search for a drift of μ. Ammonia is detected only in two extragalactic systems, B0218+357 Henkel *et al.* [51] at redshift $z_{\rm abs} = 0.7$ and PKS1830-211 [at redshift $z_{\rm abs} = 0.9$, 52], while methanol is detected only in PKS1830-211 [53].

The so-called ammonia method, i.e. the comparison of ammonia inversion transitions with rotational transitions of different molecules that were considered to be co-spatial with ammonia, led to stringent constraints on a varying μ at the level of $|\Delta\mu/\mu| < 3.6 \times 10^{-7}$ at a 3σ confidence level [54–56]. However, these constraints rely on the assumption of co-spatiality, which may introduce, due to chemical segregation, systematic effects affecting the $\Delta\mu/\mu$ value.

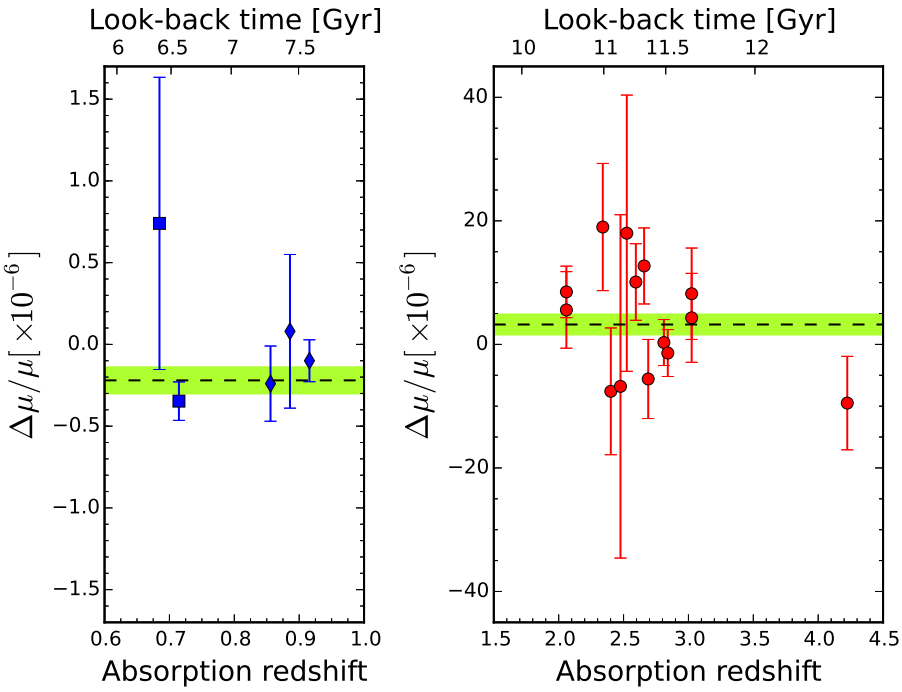

FIGURE 1.1: Left panel: measurements of $\Delta\mu/\mu$ at intermediate redshifts from methanol and ammonia absorption in B0218+357 at $z_{\rm abs}$ = 0.7 (blue squares) and PKS1830-211 at $z_{\rm abs}$ = 0.9 (blue diamonds). The weighted average of the constraints returns a value of $\Delta\mu/\mu = (-0.22 \pm 0.08) \times 10^{-6}$ which is indicated by the dashed line, while the shaded area shows its $\pm 1\sigma$ boundaries. **Right panel**: measurements of $\Delta\mu/\mu$ from H_2 and CO absorption at redshifts $z_{\rm abs} > 2$. The dashed line shows the weighted average of the high redshift $\Delta\mu/\mu$ values of $\Delta\mu/\mu = (3.1 \pm 1.6) \times 10^{-6}$, while the shaded area shows its $\pm 1\sigma$ boundaries. Artificial offsets of ± 0.03 were introduced on the x-axis to avoid overlaps among constraints derived in the same system.

Methanol is another molecule which is sensitive to variation of μ. In particular, some of its transitions have sensitivities one order of magnitude larger than that of ammonia inversion lines [57–59]. Despite being extensively observed in Galactic systems, extragalactic methanol transitions are detected only in the gravitational lens system in the line of sight towards quasar PKS1830 − 211 at the absorption redshift $z_{\rm abs} = 0.88582$ [53, 60], which corresponds to a look-back time of ∼ 7.5 Gyrs. The main advantages of using methanol to constrain μ variations are its enhanced sensitivity and the broad range of sensitivities of its transitions. In particular, the latter allows to extract $\Delta\mu/\mu$ constraints using only methanol transitions, thereby avoiding any assumptions on the co-spatiality of different molecules.

Early works on methanol absorption in PKS1830 − 211 delivered the first constraints on $\Delta\mu/\mu$ using only a single transition combined with ammonia inversion lines [53], and two methanol transitions [61]. The latter work constrained μ variations at the level of $|\Delta\mu/\mu| < 6.3 \times 10^{-7}$, at a confidence level of 3σ.

A later analysis target 10 methanol lines, at laboratory frequencies of 12-492 GHz, in the absorbing system towards PKS1830-211 using three telescopes: the Effelsberg 100m, the IRAM 30m and ALMA [62, 63]. Thanks to the spread in their sensitivities, $\Delta K_i = 31.8$, a constraint of $|\Delta\mu/\mu| \leq 3.9 \times 10^{-7}$ at 3σ significance is derived for a look-back time of ∼ 7.5 Gyrs. At the same time, the large data set allowed for a deep investigation of systematic effects like the chemical segregation between the E and A type methanol and the presence of inhomogeneities in the temperature distribution of the absorbing cloud. Moreover, the impact of the background quasar's time variability and frequency-dependent structure were inspected and included in an assessment of the systematics.

More recently, the higher sensitivity Very Large Array, VLA, was used to re-observe 4 methanol lines in PKS1830-211 [64]. This study targeted the extreme shifter $2_0 \rightarrow 3_{-1}$ E line, $\nu_{\rm lab} \simeq 12.18$ GHz, the $1_0 \rightarrow 0_0$ A^+ and E lines at $\nu_{\rm lab} \simeq 48.40$ GHz, and the $1_0 \rightarrow 2_{-1}$ E transition at $\nu_{\rm lab} \simeq 60.53$ GHz, indicating that the $2_0 \rightarrow 3_{-1}$ E line has a different velocity structure than the other methanol lines. The most likely cause is the frequency-dependent morphology of the background quasar due to the larger scatter-broadening at low frequencies [65]. The main consequence of this finding is that including the $2_0 \leftarrow 3_{-1}$ E line in μ-variation studies might introduce a systematic effect of unknown magnitude to the final value of $\Delta\mu/\mu$. Excluding this line from the sample yields a constraint of $|\Delta\mu/\mu| \leq 6 \times 10^{-7}$ at a 3σ confidence level for a look-back time of ∼ 7.5 Gyrs Kanekar *et al.* [64]. Even though this value is less stringent than that reported by Bagdonaite *et al.* [63], it is the most reliable of the present constraints on a temporal variation of μ based on methanol spectroscopy. The constraints derived from methanol and ammonia absorption in B0218+357 and PKS1830-211 are presented in Fig. 1.1. Their weighted average returns a constraint of $|\Delta\mu/\mu| < 2.4 \times 10^{-7}$ at a 3σ confidence level, which is consistent with no variation over a look-back time of ∼ 7.5 Gyrs.

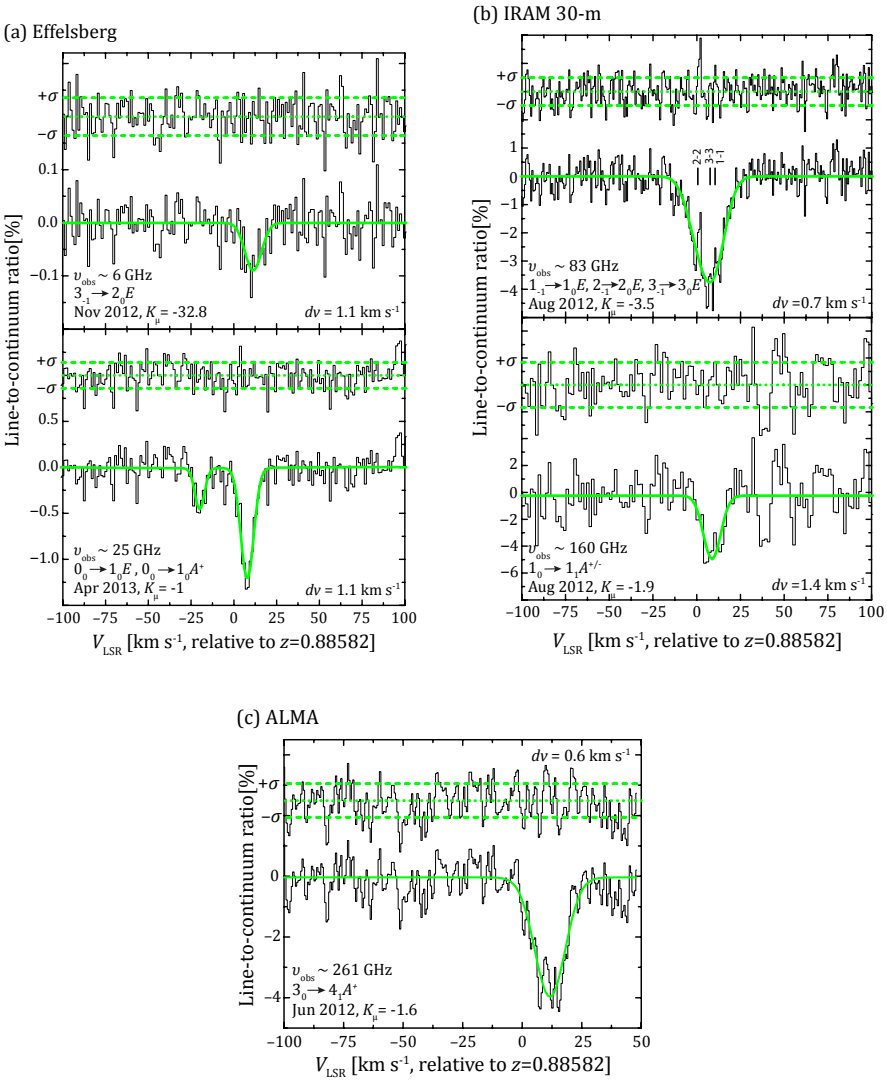

FIGURE 1.2: Observed methanol transitions towards PKS1830 – 211 with the Effelsberg 100m (Panel a), IRAM 30m (Panel b) and ALMA (Panel c) radio telescopes. The Gaussian profiles fitted to the spectra are presented by a (green) solid line, while the residuals and their $\pm 1\sigma$ boundaries are shown on top of each spectrum.

1.2.3. GALACTIC CONSTRAINTS

While extragalactic systems play a key role in probing μ variations over cosmological timescales, astrophysical systems in the Milky Way are ideal targets to investigate the dependence of μ on local environmental conditions. For example, Bagdonaite *et al.* [66] studied the dependence of μ on the gravitational field by observing molecular hydrogen absorption in white dwarf atmospheres. Another scenario which was investigated during the last decade is the so called chameleon scenario [24, 25], which predicts a variation of μ depending on the local matter density. This scenario can be investigated by targeting systems with much different densities than Earth ($n_{\rm Earth} \geq 10^{19}$ cm^{-3}). Dense cold cores of dark molecular clouds represent ideal targets to probe the chameleon scenario, as their densities ($n \sim 10^5$ cm^{-3}) are ≥ 14 orders of magnitude lower than on Earth. Moreover, their low kinetic temperatures, $T_{\rm kin} \sim 10$ K, and usually low degrees of turbulence result in narrow spectral features, with line widths down to ~ 100 m s^{-1}.

As in the case of extragalactic investigations at intermediate redshifts, observations of cold cores can target a variety of molecules with enhanced sensitivities to a varying μ. Levshakov *et al.* [67, 68] observed ammonia inversion transitions in 41 Galactic cores to constrain μ variation within the chameleon scenario. Their result was later improved by re-observing 9 cores and testing the results against potential instrumental errors, yielding to a constraint of $|\Delta\mu/\mu| \leq 2 \times 10^{-8}$ at a 3σ confidence level [69]. Since the ammonia inversion transitions have the same sensitivity to a varying μ, their observations were coupled with HC_3N lines, which have different sensitivity coefficients. Transitions of the two molecules were targeted together under the assumption that their emission regions are co-spatial. As a consequence, the presence of chemical segregation in the observed cores may introduce systematic effects affecting $\Delta\mu/\mu$.

As already mentioned, the methanol method involves the observation of methanol transitions which show enhanced sensitivities to a varying μ, thereby avoiding any assumption of co-spatiality between different molecules. Methanol emission is well documented in massive star-forming regions, although it is scarcely studied in cold cores [see e.g. 70, 71]. Recently, methanol emission lines were observed in the cold core L1498 and subsequently compared with their laboratory frequencies. The result was then tested against two major systematic error sources, the underlying methanol hyperfine structure and the Doppler tracking of the telescope, and their effects were included in the total error. This analysis returned a constraint of $|\Delta\mu/\mu| \leq 6 \times 10^{-8}$ at a 3σ confidence level, which represents the first Galactic constraint on a varying μ based on methanol only. This analysis is presented in Chapter 6.

1.3. OUTLINE OF THIS THESIS

In this thesis, possible variations of the proton-to-electron mass ratio are investigated by means of spectroscopic observations of molecular transitions in astrophysical environments. These observations target molecular hydrogen and carbon monoxide in high redshift absorbers and methanol in Galactic giant molecular clouds.

The content of this thesis can be divided in, roughly, three parts, each dedicated to the observations of one molecular species. All chapters included in this thesis are published as independent articles.

In Chapter 2, a constraint on $\Delta\mu/\mu$ is derived from the molecular hydrogen absorption system at absorption redshift $z_{\rm abs} = 2.34$ in the line of sight towards quasar Q1232+082. The absorption features related to molecular hydrogen, as well as to deuterated molecular hydrogen, are modelled with a comprehensive fitting method. The work presented in this chapter is based on archival data retrieved from the ESO data base. The magnitude of the systematics effects affecting the constraint on a varying μ is estimated and an attempt to correct for the predominant systematic error source, i.e. the long-range wavelength distortions, is made. This yields a value of $\Delta\mu/\mu = (19 \pm 9_{\rm stat} \pm 5_{\rm syst}) \times 10^{-6}$.

In Chapter 3, the molecular hydrogen absorption in the system at $z_{\rm abs} = 2.69$ in the line of sight towards quasar J1237+0647 is investigated in order to constrain a temporal variation of μ. This system exhibits a more complicated absorption profile, featuring three main absorption features per each molecular hydrogen transition, each composed of multiple, unresolved velocity components. The so-called supercalibration technique [72] is used to partially correct the quasar spectrum of J1237+0647 for the long-range wavelength distortions, while the other main contributors to the systematic uncertainty are analyzed and their contributions estimated. More than a hundred molecular absorption features are fitted simultaneously with a comprehensive fitting technique, yielding a value of $\Delta\mu/\mu = (-5.4 \pm 6.3_{\rm stat} \pm 4.0_{\rm syst}) \times 10^{-6}$.

Chapter 4 reports a follow-up investigation on the same system presented in the previous chapter. The carbon monoxide absorption in the absorption system towards J1237+0647 provides a unique opportunity to derive an independent constraint on $\Delta\mu/\mu$ using a different molecule under the same physical conditions that hold for H_2. The analysis of thirteen carbon monoxide absorption bands delivers a value of $\Delta\mu/\mu = (0.7 \pm 1.6_{\rm stat} \pm 0.5_{\rm syst}) \times 10^{-5}$, which represents the first constraint on the possible μ variation from this molecule.

In Chapter 5, the carbon monoxide absorption at $z_{\rm abs} = 2.52$ towards quasar J0000+0048 is investigated by applying the same method developed in Chapter 4. Nine vibrational carbon monoxide bands are detected and modeled, delivering a value of $\Delta\mu/\mu = (1.8 \pm 2.2_{\rm stat} \pm 0.4_{\rm syst}) \times 10^{-5}$.

In Chapter 6, the possible μ variation as result of the chameleon scenario is inves-

tigated via methanol emission in a Galactic molecular cloud. Six methanol lines were detected in the dense ($n \sim 10^5$ cm^{-3}) giant molecular cloud L1498. The comparison of their observed frequencies with the rest frame values delivered a constraint on μ variation of $|\Delta\mu/\mu| < 2 \times 10^{-8}$ at a 1σ confidence level.

2

CONSTRAINT ON A VARYING PROTON-TO-ELECTRON MASS RATIO FROM H_2 AND HD ABSORPTION AT $z_{ABS} \simeq 2.34$

Daprà, M., van der Laan, M., Murphy, M. T. & Ubachs, W.
Mont. Not. Roy. Astron. Soc. ***465****, 4057-4073 (2017)*

Molecular hydrogen absorption in the damped Lyman-α system at $z_{abs} = 2.34$ towards quasar Q 1232+082 is analyzed in order to derive a constraint on a possible temporal variation of the proton-to-electron mass ratio, μ, over cosmological timescales. Some 106 H_2 and HD transitions, covering the range 3290-3726 Å, are analyzed with a comprehensive fitting technique, allowing for the inclusion of overlapping lines associated with hydrogen molecules, the atomic hydrogen lines in the Lyman-α forest as well as metal lines. The absorption model, based on the most recent and accurate rest wavelength for H_2 and HD transitions, delivers a value of $\Delta\mu/\mu = (19 \pm 9_{stat} \pm 5_{syst}) \times 10^{-6}$. An attempt to correct the spectrum for possible long-range wavelength distortions is made and the uncertainty on the distortion correction is included in the total systematic uncertainty. The present result is an order of magnitude more stringent than a previous measurement from the analysis of this absorption system, based on a line-by-line comparison of only 12 prominent and isolated H_2 absorption lines. This is consistent with other measurements of $\Delta\mu/\mu$ from 11 other absorption systems in showing a null variation of the proton-to-electron mass ratio over a look-back time of 11 Gyrs.

2.1. INTRODUCTION

The search for possible variations in the values of fundamental constants over the course of cosmic history from spectroscopic observations of highly redshifted galaxies has become an established field of research in the past decade. In particular, drifts in dimensionless constants, such as the fine-structure constant $\alpha = e^2/(4\pi\epsilon_0\hbar c)$ and the proton-to-electron mass ratio $\mu = M_p/m_e$, can be probed by observing and calibrating atomic and molecular absorption lines from objects in the early Universe, and comparing their wavelengths with those measured in the laboratory [3, 73].

Temporal drifts of the proton-to-electron mass ratio, a dimensionless constant responsible of the structure of molecular matter, can be probed using transitions of a variety of molecules [74, 75]. Astronomical observations in the radio domain targeting ammonia [54, 56] and methanol [62–64] delivered tight constraints on $|\Delta\mu/\mu|$ at the level of 10^{-7}. However, ammonia is detected in only two extragalactic systems, B0218+357 [51] at $z_{\rm abs} \simeq 0.7$ and PKS1830-211 [52] at $z_{\rm abs} \simeq 0.9$, while methanol is detected only in the latter [53].

Thompson [28] first proposed to use molecular absorption in high redshift systems to probe the variation of μ. Molecular hydrogen, H_2, is found to have many transitions showing different sensitivities within its band systems [29, 36] and it is a good candidate to investigate a possible μ-variation. Being the most abundant molecule in the Universe, H_2 is found in a larger number of absorption systems, which display up to 100 H_2 absorption features. The Lyman and Werner band systems can be observed using the large, ground-based telescopes at $z_{\rm abs} > 2$, for which they are redshifted into the atmospheric transmission window ($\lambda > 3050$ Å). Nine H_2-bearing absorption systems in the range $z_{\rm abs} = 2.05 - 4.22$ were analyzed recently for μ-variation, delivering an average constraint of $|\Delta\mu/\mu| < 5 \times 10^{-6}$ at 3σ level [see 73, and references therein for the single absorbers].

The presence of molecular hydrogen in the damped Lyman-α (DLA) absorption system at $z_{\rm abs} \simeq 2.34$ in the line of sight towards quasar SDSS J123437.55+075843.3, hereafter Q1232+082, was first reported by Ge and Bechtold [76] from medium-resolution observations. Based on observations of Q1232+082 with the Ultraviolet and Visual Echelle Spectrograph (UVES) mounted on the 8.2 m Very Large Telescope (VLT), Srianand *et al.* [77] deduced a value for the cosmic microwave background temperature at the local redshift from the fine-structure lines of C I combined with H_2 lines. A measurement of a varying μ based on the analysis of 12 unsaturated and isolated H_2 absorption features was reported by Ivanchik *et al.* [78]. They derived two different values constraining $\Delta\mu/\mu$ at the level of $|\Delta\mu/\mu| < 2 \times 10^{-4}$ (3σ) using the H_2 laboratory wavelengths stemming from classical spectroscopic methods as reported by Morton and Dinerstein [79] and Abgrall *et al.* [80]. A later detailed analysis of the H_2 and HD absorption lines was reported by Ivanchik *et al.* [81], who found a ratio $N(\mathrm{HD})/N(H_2)$ significantly larger than that found in the interstellar clouds in the Galaxy. Moreover, they reported that the absorbing cloud does not cover entirely

the broad line region of the background quasar Q1232+082. Its partial coverage was further analysed by Balashev *et al.* [82].

The main goal of this work is to perform an improved re-analysis of the H_2 absorption system Q1232+082 in order to constrain a temporal variation of the proton-to-electron mass ratio. To achieve this, the powerful comprehensive fitting technique [41, 83] was applied to the quasar spectrum. This technique allows the treatment of partially overlapped absorption features, increasing the number of transitions included in the sample. This, along with an improved set of rest wavelengths, considered exact for the purpose of the comparison, led to a lower statistical uncertainty on the derived $\Delta\mu/\mu$ value. Finally, the absorption model includes H_2 and HD column densities that are corrected for the partial coverage of the absorbing cloud. The quasar observations used are presented in Section 2.2, the fitting method is described in Section 2.3, the results, including the measurement of $\Delta\mu/\mu$, are presented in Section 2.4, while the effect of systematics is discussed in Section 2.5.

2.2. DATA

The exposures used in this work were taken in five different observational programs obtained from the ESO data archive[1]. The programs, whose details are listed in Table 2.1, were carried out between 2000 and 2003 using UVES, for a total integration time on the target of 19.4 hrs. During all the observations, the blue arm of UVES was centred on 390 nm in order to cover the H_2 Lyman and Werner series window. Most of the exposures had a slit width of 1.0 arcsec and a CCD binning of 2×2 (spectral × spatial), with the only exception of program 70.A-0017(A), which had a slit width of 1.2 arcsec and a binning of 3×2.

The raw 2D exposures were reduced following the same procedure described by King *et al.* [84] and Bagdonaite *et al.* [85, 86]. The exposures were flat-fielded and bias-corrected using the Common Pipeline Language (CPL) version of the UVES pipeline. Subsequently, the CPL was used to optimally extract the quasar flux. Since none of the programs was carried out with attached ThAr calibration exposures, the single quasar exposures were wavelength calibrated using the standard ThAr exposures taken at the end of the night. After the standard reduction, the echelle orders were combined onto a common vacuum-heliocentric wavelength grid, with a dispersion of 2.5 km s^{-1} per pixel, in a single normalized spectrum using the custom software UVES_POPLER [87]. The flux density and variance was linearly redispersed from the original pixel scale to the new wavelength grid in the same way for all exposures, including the single 3×2-binned exposures. The flux arrays for all orders were scaled to optimally match each other where they overlapped in wavelength space and the final spectrum was formed using an inverse-variance weighted mean of the contributing exposures at each pixel. The combined 1D spectrum was manually in-

[1] http://archive.eso.org/eso/eso_archive_main.html

TABLE 2.1: Observational details of the Q1232+082 exposures with UVES/VLT obtained from the ESO archive and used in this work. The grating settings were 390 + 564 nm for each exposure.

Program ID	Date	Execution time (UT)	Integration time [s]	Slit width [arcsec]	CCD binning
65.P-0038(A)	06/04/2000	04:11:32	3600	1.0	2×2
	06/04/2000	05:15:52	3600		
	08/04/2000	05:26:42	3600		
68.A-0106(A)	08/01/2002	06:57:28	6000		2×2
	09/01/2002	06:56:17	6000		
	10/01/2002	06:59:36	6000		
69.A-0061(A)	02/06/2002	00:16:07	5400		2×2
	10/06/2002	00:46:31	5400		
70.A-0017(A)	04/01/2003	07:06:19	5200	1.2	3×2
71.B-0136(A)	02/04/2003	02:55:36	5400	1.0	2×2
	02/04/2003	04:29:52	5400		
	03/04/2003	03:37:30	3600		
	03/04/2003	04:39:58	3600		
	02/05/2003	03:00:06	3600		
	02/05/2003	04:02:07	3600		

spected and bad pixels and other spectral artifacts were removed. Subsequently, the quasar continuum was fitted with low-order polynomials.

The final spectrum of Q1232+082 (resolving power $R \sim 45000$) covers the wavelengths from 3290 to 6650 Å, with gaps between 4525-4620 Å and 5598-5672 Å due to the separation between the CCDs. The signal-to-noise ratio (S/N) is ∼ 20 per 2.5 km s^{-1} per pixel at ∼ 3500 Å, in the middle of the H_2 window in the quasar spectrum.

2.3. METHOD

The fitting technique used in this work is the comprehensive fitting method introduced by King *et al.* [83] and later refined by Malec *et al.* [41]. This method involves a simultaneous treatment of all the considered transitions. The main strength of this technique is that the fitting parameters used to describe the absorption features can be tied together. This results in a lower number of free parameters and allows the H_2 lines that are partially overlapped by or blended with intervening spectral features to be modelled.

The absorption model was created using VPFIT [88], a custom nonlinear least-squares Voigt profile fitting program developed specifically for quasar absorption. The absorption feature profiles were fitted using a Voigt profile, which consists in the

convolution of a Lorentzian profile reflecting the natural line profile, which is specific for each transition considered, a Gaussian profile describing the broadening due to the thermal and turbulent velocities of the absorbing cloud, and an instrumental profile assumed to be Gaussian. In VPFIT, each absorption feature is described by a set of 3 free parameters: the column density N, the redshift at which the absorption occurs $z_{\rm abs}$, and the Doppler line width b. The atomic and molecular properties of each transition included in the absorption model, namely the laboratory wavelength λ^0, the oscillator strength f, the damping parameter Γ, and the sensitivity coefficient K, are included in VPFIT as fixed values. The laboratory wavelengths for the H_2 transitions were measured with fractional accuracies of $\sim 5\times10^{-9}$ and $1-2\times10^{-8}$ for Lyman and Werner transitions respectively by Salumbides *et al.* [37], while HD transitions were measured by Hollenstein *et al.* [89] and Ivanov *et al.* [38] with a relative accuracy of $\sim 5\times10^{-8}$. The oscillator strengths and the damping parameters were calculated by Abgrall *et al.* [90] and by Abgrall *et al.* [91], respectively, for H_2 transitions and by Abgrall and Roueff [92] for HD transitions. The sensitivity coefficients were calculated via a semi-empirical analysis by Ubachs *et al.* [36] for H_2, while they were derived in ab initio calculations by Ivanov *et al.* [39] for HD transitions. The database used in this work was tabulated by Malec *et al.* [41].

The underlying assumption of this work is that absorption features detected at the same $z_{\rm abs}$ originate from the same absorbing cloud. In other words, they share the same physical conditions, like the turbulent motions and the temperature of the cloud. This is represented in VPFIT by tying the redshift and the Doppler width parameters among the different transitions. Moreover, it is assumed that transitions probing the same rotational states are sharing the same level population. As a consequence, their column densities N_J were tied together.

VPFIT works iteratively, starting from user-supplied initial values for each free parameter in the absorption model. During each iteration, the values of such parameters are changed in order to minimize the value of the control parameter χ^2. The program stops iterating once a stopping criterion, which is user-defined, is met, reporting convergence. Beside the chi-squared parameter, the Akaike Information Criterion [AICC 93] is used to control the goodness of the fit. In particular, this parameter is defined as:

$$AICC = \chi^2 + 2p + \frac{2p(p+1)}{n-p-1}, \tag{2.1}$$

where p is the number of free parameters, and n is the number of the data points included in the fit. In particular, a difference of $\Delta AICC > 5$ between two absorption models is considered to be strong evidence that the model with the lower $AICC$ value is statistically preferred.

2.4. ANALYSIS

The spectrum of quasar Q1232+082 ($z_{\rm em} = 2.57$) contains a DLA that features molecular hydrogen absorption, at $z_{\rm abs} = 2.33771$. The molecular hydrogen absorption in the system was investigated by Srianand *et al.* [77] and Varshalovich *et al.* [94], who reported the first deuterated molecular hydrogen (HD) detection in a DLA. A later, combined study of H_2 and HD absorption found evidence of partial coverage in the absorbing system [81].

The presence of partial coverage means that the angular radius of the absorbing cloud is smaller than that of the background source. As a consequence, even saturated absorption features originating in the cloud do not absorb all the quasar radiation, leaving a residual flux in the spectrum. The partial coverage is characterized by a covering factor $f = F_{abs}/F_{tot}$, which is defined as the ratio between the flux affected by the cloud absorption, F_{abs}, and the total flux of the background source, F_{tot}. If all the quasar radiation is covered by the cloud, then the covering factor is unity. This results in saturated lines going to the zero level in the spectrum. A covering factor $f < 1$ means that there is a residual flux from the background source which prevents saturated lines to go to the zero level, as shown in Fig. 1 of Ivanchik *et al.* [81]. It is worth noting that different elements/molecules' absorption features originate in different parts of the absorbing cloud, hence their covering factors are in principle different. The partial coverage phenomenon can be explained by invoking a number of different effects [e.g. 82], for example an effectively smaller radius of the absorbing cloud or the presence of multiple, unresolved background sources illuminating the absorber. However, to explain the causes of the partial coverage in this system is beyond the goal of this work. A detailed study of the partial coverage of the Q1232+082 broad line region, considering multiple elements, was reported by Balashev *et al.* [82].

Molecular hydrogen is detected in the spectrum in its two forms, H_2 and HD, with more than 100 lines detected for observed wavelengths shorter than 3726 Å. The dataset considered in this analysis was built considering only the transitions probing the rotational states with $J \leq 5$, and is presented in Table 2.2. The $J = 0 - 1$ transitions have a large column density and are heavily saturated. Therefore, they were included in the analysis only when no evidence of overlap with strong, intervening H I lines was found. Since the H_2 and HD transitions fall in the Lyman-α forest, overlaps with intervening neutral hydrogen and/or metal transitions are common. Within the comprehensive fitting method, partial overlaps can be handled, therefore such transitions were included in the dataset. However, molecular hydrogen transitions that are completely overlapped by saturated H I lines were excluded from the dataset, since they do not add relevant information to the signal. In total, 96 H_2 transitions, belonging to the Lyman and the Werner band systems, and 10 HD transitions were selected among 42 spectral regions in the range 3290-3726 Å.

Each absorption feature was modelled by assigning it a set of free parameters in

TABLE 2.2: List of the 106 molecular hydrogen transitions considered in this work.

J-level	Lyman transitions	Werner transitions	#
0	L0R(0), L1R(0), L2R(0), L4R(0),		4
1	L0P(1), L0R(1), L1P(1), L1R(1), L2P(1), L2R(1), L3P(1), L4P(1), L4R(1), L5P(1), L7P(1)		11
2	L0P(2), L0R(2), L1P(2), L1R(2), L2P(2), L2R(2), L3P(2), L3R(2), L4P(2), L4R(2), L5P(2), L5R(2), L6P(2), L7P(2), L7R(2), L8P(2), L9R(2), L9P(2)	W0P(2), W1P(2), W1Q(2)	21
3	L0P(3), L0R(3), L1P(3), L1R(3), L2P(3), L2R(3), L3P(3), L3R(3), L4P(3), L4R(3), L5P(3), L5R(3), L6P(3), L6R(3), L7P(3), L7R(3), L8R(3), L9P(3), L9R(3), L10P(3),	W0P(3), W1Q(3), W1R(3)	23
4	L1P(4), L1R(4), L2P(4), L2R(4), L3P(4), L3R(4), L4P(4), L4R(4), L5P(4), L5R(4), L6P(4), L6R(4), L8P(4), L9R(4), L10R(4)	W0P(4), W0Q(4), W0R(4), W1P(4)	20
5	L1P(5), L1R(5), L2P(5), L2R(5), L3P(5), L3R(5), L5P(5), L5R(5), L6P(5), L7P(5), L8P(5), L9P(5), L10P(5), L10R(5)	W0R(5), W1Q(5)	17
HD $J=0$	L1R(0), L2R(0), L3R(0), L4R(0), L5R(0), L6R(0), L7R(0), L8R(0)	W0R(0), W1R(0)	10

VPFIT. The absorption redshift $z_{\rm abs}$ and the width b were tied among all the H_2 transitions, while the column densities N_J were tied only among the transitions probing the same rotational state. All the HD absorption features were described by a different set of free parameters, with only the redshift tied to the H_2 value. In order to build a robust absorption model, the Lyman-α forest H I lines falling in the selected spectral regions were modelled by assigning to each of them a set of free parameters. Note that the parameters describing these lines were not tied to any value and were allowed to vary independently from each other. The initial value of each fitting parameter was user-provided.

To account for possible misplacements of the global quasar continuum, a continuum correction was introduced in each spectral region. This correction acts as a local continuum, limited to the spectral region considered. In VPFIT the local continua are fitted with a straight line to the spectrum, therefore diminishing the impact of a misplaced global quasar continuum on the absorption model. To account for the partial coverage, a zero-level correction was introduced in each spectral region. Working in a similar way than the continuum correction, this correction locally shifts the zero-level of the quasar spectrum. A covering factor of $f = 0.92 \pm 0.01$ was derived from the weighted average of the zero-level corrections of all the spectral regions considered. This value matches with that found by Ivanchik *et al.* [81] for the H_2 lines.

Even though molecular hydrogen absorption features were fitted using a single Voigt profile, it is common to find more complex velocity structures underlying the H_2 absorption features [e.g. 41, 46, 86]. Therefore the presence of extra velocity components (VCs) was investigated. A composite residual spectrum [CRS, 41] was built using single, isolated absorption features for both H_2 and HD. Combining the residuals of multiple transitions, the CRS exploits the presence/absence of VCs in the absorption model. The CRS relative to H_2 absorption features, presented in Fig. 2.1, suggests a possible extra VC at ~ 8.5 km s^{-1}, with respect to the absorption redshift $z_{\rm abs} = 2.33771$. To test the presence of an extra VC, multiple models were fitted, each including a second VC for each H_2 J-level. During the fitting process the second VC's column density and Doppler width values reached some user-defined limits, that were set to $\log[N/{\rm cm}^{-2}] < 8.0$ and $b < 0.05$ km s^{-1}, hence it was rejected by VPFIT. As a consequence, the single VC model was adopted. The same analysis was performed looking for extra VCs for the HD absorption features, but the CRS for HD, which is presented in Fig. 2.2, does not show evidence of extra VCs.

The parameters of the single VC model are presented in Table 2.3, while the complete absorption model is compared to the observed spectrum in Appendix 2.6. The values of the H_2 column densities are in good agreement with those reported by Ivanchik *et al.* [81], with only the rotational states with $J = 2$ and 3 having a larger N_J value, while the line width b presented here is smaller. The difference between the two b values may be explained by the fact that Ivanchik *et al.* [81] derived their value from the curve of growth of rotational states with $J = 2 - 5$, while the value

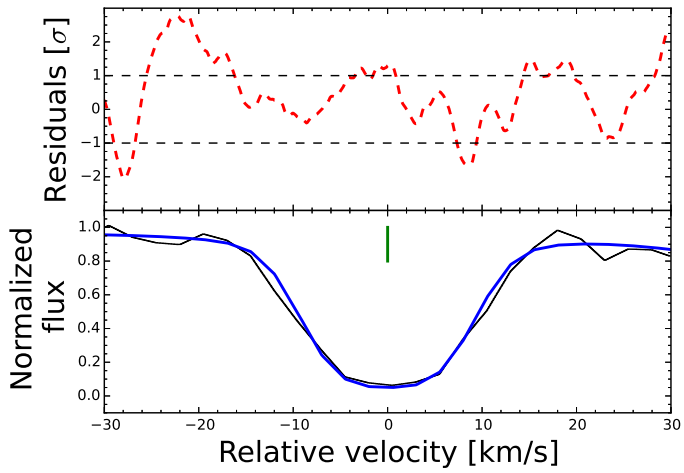

FIGURE 2.1: Top panel: normalised composite residual spectrum from 32 unblended and non-overlapping H_2 transitions. The dashed lines represent the $\pm 1\sigma$ boundaries. Bottom panel: the H_2 L3R(3) transition, with a rest wavelength of $\lambda^0 = 1067.5$ Å, is plotted as reference. The velocity scale is centred at the absorption redshift $z = 2.33771$. The solid (blue) line shows the absorption model, while the solid (green) tick shows the position of the VC.

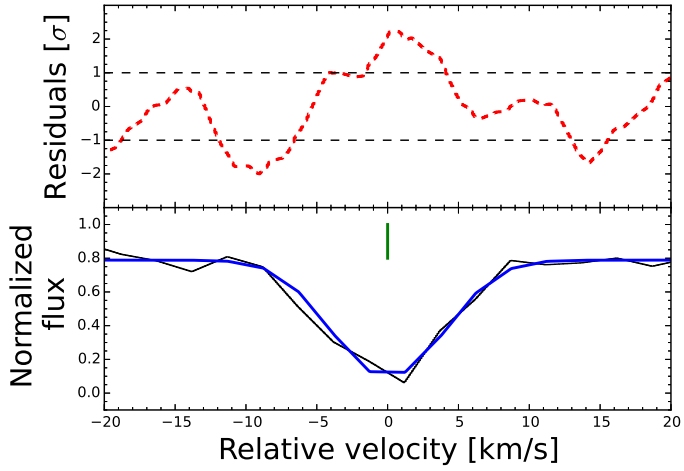

FIGURE 2.2: Top panel: normalised composite residual spectrum from 6 unblended and non-overlapping HD transitions. The dashed lines represent the $\pm 1\sigma$ boundaries. Bottom panel: the HD 7R(0) transition, with a rest wavelength of $\lambda^0 = 1021.5$ Å, is plotted as reference. The velocity scale is centred at the absorption redshift $z = 2.33771$. The solid (blue) line shows the absorption model, while the solid (green) tick shows the position of the VC.

TABLE 2.3: Column densities N_J and Doppler width b of the H_2 and HD transitions in the Q1232+082 spectrum.

Rotational level	$\log[N_J/\mathrm{cm}^{-2}]$	b [km s^{-1}]
$J=0$	19.41 ± 0.01	3.39 ± 0.06
$J=1$	19.26 ± 0.01	
$J=2$	17.47 ± 0.04	
$J=3$	17.16 ± 0.05	
$J=4$	14.76 ± 0.02	
$J=5$	14.23 ± 0.02	
HD $J=0$	15.74 ± 0.53	1.67 ± 0.27

presented in this work is derived considering the contribution from rotational states with $J < 5$. The Doppler width parameter of the H_2 lines was observed to vary with the J-level [e.g. in HE0027–1836, 95]. According to Balashev *et al.* [96], this can imply that the H_2 transitions with low J originate in the central part of the absorbing cloud, where the turbulence is minimal. On the other hand, high J transitions originate in the external part of the cloud, where larger turbulence may contribute more to the line broadening. As a consequence, the Doppler width derived only from the high-J states by Ivanchik *et al.* [81] is larger than that reported here, which includes the contribution from the states with $J = 0$ and 1. In Section 2.4.1 a test is performed to investigate the impact of the assumption of spatial homogeneity on the $\Delta\mu/\mu$ value derived in this work. The parameters describing the HD features are well in agreement with those reported by Ivanchik *et al.* [81].

2.4.1. CONSTRAINING $\Delta\mu/\mu$

As proposed by Thompson [28], the H_2 absorption detected in high-redshift systems can be used to detect a temporal variation of the proton-to-electron mass ratio μ. A variation of μ is reflected by a shift in the observed wavelength λ_i^z of the i-th transition according to:

$$\lambda_i^z = \lambda_i^0 (1 + z_{\rm abs})(1 + K_i \frac{\Delta\mu}{\mu}), \tag{2.2}$$

where λ_i^0 is the rest wavelength of the transition, $z_{\rm abs}$ is the absorption redshift, $\Delta\mu/\mu \equiv (\mu_z - \mu_0)/\mu_0$ is the relative difference between the proton-to-electron mass ratio in the absorption system and the value measured on Earth, and K_i is the sensitivity coefficient, defined as:

$$K_i \equiv \frac{\mathrm{d}\ln\lambda_i^0}{\mathrm{d}\ln\mu}. \tag{2.3}$$

The coefficient K_i determines the sign and magnitude of the sensitivity to a varying μ and is specific for the i-th transition. The K_i coefficients used in this work were

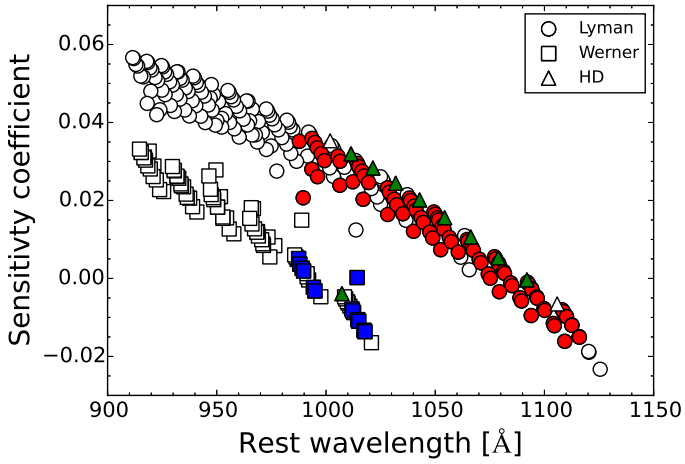

FIGURE 2.3: Sensitivity coefficients of Lyman and Werner transitions of H_2 and of HD transitions. The transitions considered in this analysis are marked with shaded markers.

calculated within a semi-empirical framework by Ubachs *et al.* [36], including the effects beyond the Born-Oppenheimer approximation and are presented in Fig 2.3.

The variation of μ is represented in VPFIT by an extra free parameter. It was added to the other parameters (N_J, $z_{\rm abs}$, b) of the H_2 and HD transitions only after having developed a robust absorption model. This fourth parameter was not added earlier in order to avoid that any flaw in the model itself would be compensated by an artificial variation of μ. The model returned a value of the variation of the proton-to-electron mass ratio of $\Delta\mu/\mu = (22 \pm 9_{\rm stat}) \times 10^{-6}$. It is worth noting that the statistical error was derived from the diagonal term of the final covariance matrix, representing thereby only the uncertainty arising from the S/N of the spectrum.

Ivanchik *et al.* [78] derived two values for $\Delta\mu/\mu$ using the H_2 absorption in the system towards Q1232+082. They analysed 12 isolated, unsaturated and unblended H_2 lines and used two independent sets of rest wavelengths λ^0 from Morton and Dinerstein [79] and Abgrall *et al.* [80] finding $\Delta\mu/\mu = (144 \pm 114) \times 10^{-6}$ and $\Delta\mu/\mu = (132 \pm 74) \times 10^{-6}$ respectively. The present analysis is based on ~ 10 times more lines, since the comprehensive fitting technique allows to fit partially overlapped and blended H_2 absorption features, and on more accurate rest wavelength measurements, which are considered exact for the purpose of comparison. This yielded a value of $\Delta\mu/\mu$ which is ~ 10 times more precise than that previously found for this system [78].

Following the same approach of Bagdonaite *et al.* [86], a number of tests were performed to investigate the statistical robustness of the $\Delta\mu/\mu$ value, hereafter the

fiducial value. In the following four sections, four different tests are presented along with their results, which are shown in Fig 2.4. Note that, in each test, the transitions that were not considered in the subset were included in the fit, but their K_i coefficients were set to zero, i.e. they contributed to the absorption profile but not directly to a constraint on the $\Delta\mu/\mu$ parameter.

ISOLATING LYMAN AND WERNER TRANSITIONS

Previous studies showed that, since the H_2 sensitivity coefficients are wavelength-dependent, the presence of a distortion in the UVES wavelength scale would be nearly degenerate with a variation in μ [36, 41, 97]. This degeneracy will, in principle, be broken to some extent by fitting together the Lyman and the Werner transitions, since they have different sensitivity coefficients at similar rest wavelengths. The effect of such wavelength-dependent distortions can be investigated by separating the two H_2 band systems.

The two values returned are $\Delta\mu/\mu = (21 \pm 10_{\rm stat}) \times 10^{-6}$ for the Lyman band systems and $\Delta\mu/\mu = (236 \pm 90_{\rm stat}) \times 10^{-6}$ for the Werner band systems. The fact that the two values do not match within 2σ is considered as a hint of the presence of systematic effects. The shift between the Lyman-only and the Werner-only $\Delta\mu/\mu$ values requires a distortion slope which is ~ 10 times larger than what commonly found in UVES, hence it cannot be ascribed only to long-range distortions. This is considered evidence of an extra, unknown systematic effect which is affecting the fiducial value of $\Delta\mu/\mu$. The larger uncertainty on the value of $\Delta\mu/\mu$ delivered by the Werner transitions is ascribed to three effects: (i) the Werner transitions fall in the bluest part of the spectrum, which has a low S/N (~ 10 per 2.5 km s^{-1} per pixel at 3320 Å); (ii) the Werner transitions represent $\sim 16\%$ of the total number of H_2 transitions considered; (iii) the spread in the sensitivity coefficients of the Werner transitions, $\Delta K_W = 0.02$, is lower than for Lyman transitions, $\Delta K_L = 0.05$.

ISOLATING LOW AND HIGH J TRANSITIONS

The impact of possible temperature inhomogeneities in the absorbing system on the constraint on $\Delta\mu/\mu$ was estimated by fitting the cold, low-J levels ($J < 2$) and the hot, high-J levels ($J = 2-5$) separately. This is possible because, due to the para-ortho distribution, the $J = 1$ rotational state is significantly populated even at low temperatures, as discussed by Ubachs *et al.* [36].

The two values derived from the cold and the warm transitions are $\Delta\mu/\mu = (-34 \pm 50_{\rm stat}) \times 10^{-6}$ and $\Delta\mu/\mu = (26 \pm 10_{\rm stat}) \times 10^{-6}$, respectively. The larger error on the measurement derived from the colder states can be explained from the fact that there are only 15 transitions with $J = 0-1$ in the sample and they are nearly saturated, resulting in larger uncertainties on the position of the centroids of such absorption features. The two values match within their uncertainties, showing that the temperature inhomogeneities in the absorbing system do not significantly affect the constraint.

UNTYING FREE PARAMETERS AMONG DIFFERENT J-LEVELS

As discussed in Section 2.3, the present analysis was performed under the assumption that all the H_2 transitions share the same value of z and b. However, this may not be true if there is a spatial inhomogeneity in the absorbing cloud. In this case, transitions with different J-levels will arise under different physical conditions, which would be reflected by different values of their Doppler width b.

To test the validity of this assumption, a fit was run with the free parameters z and b untied among the different J-levels. The test returned $\Delta\mu/\mu = (5 \pm 10_{\rm stat}) \times 10^{-6}$, which is in a good agreement with the fiducial value. As a consequence, the assumption of spatial homogeneity used in this analysis has almost no impact on the constraint on $\Delta\mu/\mu$.

EXCLUDING PROBLEMATIC REGIONS

Half of the selected spectral regions contain H_2 absorption features that show self-blending and overlap with intervening H I or narrow, unidentified absorption features that are likely to be metal absorption features. Such intervening lines were included in the fit, but they do not benefit from the strength of the comprehensive fitting method, since they cannot be tied in any way to other transitions. Hence, any flaw in modelling these lines will affect the fiducial value of $\Delta\mu/\mu$.

To test the impact of the unidentified intervening lines, a fit was performed considering only the 21 spectral regions that have a $\chi^2_\nu < 1$. The fit returned a value of $\Delta\mu/\mu = (-1 \pm 18) \times 10^{-6}$, which matches with the fiducial value within their uncertainties. It is concluded that the H_2 absorption model is robust enough not to be affected by flaws in the model of intervening neutral hydrogen and metal transitions.

SEPARATING EXPOSURES FROM DIFFERENT PERIODS

UVES is known to suffer from wavelength calibration distortions that are likely to originate in the internal settings of the instrument, as discussed in Section 2.5.1. Such distortions are likely to affect the fiducial value of $\Delta\mu/\mu$, hence quantifying this effect is crucial for any μ variation analysis. The attempt made to distortion-correct the spectrum is presented in Section 2.5.1, while here a test to estimate the consistency of the distortion slope across the observational programs is presented.

The final Q1232+082 spectrum was divided into 3 'subspectra' – combined spectra formed from subsets of exposures – each comprising observations taken only in 2000, 2002, and 2003. Any change in the magnitude of the wavelength distortions would be reflected in a significant variation of the $\Delta\mu/\mu$ values derived from the subspectra. A value for $\Delta\mu/\mu$ was derived from each subspectrum, returning $\Delta\mu/\mu = (15 \pm 24_{\rm stat}) \times 10^{-6}$ for exposures taken in 2000, $\Delta\mu/\mu = (30 \pm 18_{\rm stat}) \times 10^{-6}$ for 2002, and $\Delta\mu/\mu = (22 \pm 11_{\rm stat}) \times 10^{-6}$ for exposures taken in 2003. The differences in the errors among the values reflect the fact that the subsets do not have the same integration time, hence the S/N determining the statistical error changes among the subsets. The measurements agree well within their uncertainties, showing that the

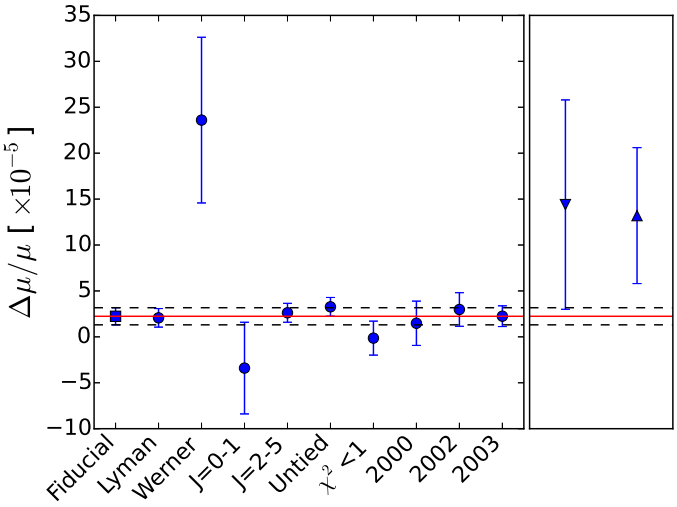

FIGURE 2.4: Left panel: Values of a varying μ obtained from the H_2 and HD absorption model, shown by a (blue) square, as well as from the consistency tests, shown by (blue) circles. The (red) solid line represents the fiducial $\Delta\mu/\mu$ value and the two dashed lines show its $\pm 1\sigma$ boundaries. Right panel: The (blue) upwards and downwards triangles represent the two measurements derived by Ivanchik *et al.* [78] using the laboratory wavelengths reported by Morton and Dinerstein [79] and Abgrall *et al.* [80], respectively.

relative differences in the telescope settings among the different exposures do not significantly affect the fiducial value of $\Delta\mu/\mu$.

2.5. SYSTEMATIC ERROR

Following from Eq. (2.2), the measurable effect of a non-zero $\Delta\mu/\mu$ is a shift between molecular absorption features. As a consequence, any effect that introduces a distortion of the wavelength scale is likely to introduce a systematic error on the measured $\Delta\mu/\mu$ value. Note that this holds only for wavelength-dependent distortions, since any constant velocity offset will not cause any relative shift between the absorption features. Such a systematic will affect the resulting value for the absorption redshift parameter. The role of wavelength calibration errors as well as the spectral redispersion on the fiducial value of $\Delta\mu/\mu$ was studied in previous works on different systems [41, 46, 84–86], while lack of attached ThAr calibrations was studied by Bagdonaite *et al.* [85, 86]. In the following, the contributions to the systematic error budget from four sources of systematics are discussed following the same approach that was used in the aforementioned works.

2.5.1. LONG-RANGE DISTORTIONS

The UVES spectrograph is known to suffer from wavelength calibration distortions. Long-range distortions were first detected by Rahmani *et al.* [98] and, more recently, analyzed in further detail by Whitmore and Murphy [72]. Such distortions are likely to be due to a difference in the path the light from the quasar and from the calibration lamp travels within the instrument.

The supercalibration technique [72] is a powerful method to correct the spectrum for the long-range distortions and was successfully applied to other systems [30, 46, 86]. It consists in a comparison of a spectrum taken with UVES with a reference spectrum from a Fourier Transform Spectrometer (FTS) solar spectrum, which has a more accurate frequency scale [99][2]. Typical supercalibration targets are asteroids and 'solar twin' stars. The former have the same spectrum as the Sun since they reflect the solar light, while the latter are objects that show a spectrum which is almost identical to the solar one [100, 101].

Since no supercalibration targets could be found in the ESO archive in a temporal window of ~ 2 weeks of the quasar exposures, the technique is not fully applicable to Q1232+082. However, the sparse sample reported by Whitmore and Murphy [72] suggests that the UVES wavelength distortions might be quasi-stable in the period 2004-2008, with a distortion slope of ~ 200 m s^{-1} per 1000 Å. Moreover, Whitmore and Murphy [72] found one supercalibration target in 2001 delivering a distortion slope of ~ 100 m s^{-1} per 1000 Å. Assuming that the distortions affecting UVES were stable in the period 2000-2003, the slope value of ~ 100 m s^{-1} per 1000 Å was used to distortion-correct the Q1232+082 spectrum, delivering an updated fiducial $\Delta\mu/\mu$ value of $\Delta\mu/\mu = (19 \pm 9_{\rm stat}) \times 10^{-6}$. An uncertainty on the distortion correction of ± 100 m s^{-1} per 1000 Å was estimated from the spread between the distortion slope values in 2001 and in the period 2004-2008. This translates into a systematic uncertainty on $\Delta\mu/\mu$ of $\sim 5 \times 10^{-6}$ (1σ) and it was added to the systematic error budget. The presence of the long-range distortions with a positive distortion slope is found to push the $\Delta\mu/\mu$ value towards a more positive value, as was found in other systems [40, 46, 86, 98].

2.5.2. INTRA-ORDER DISTORTIONS

At small scales, within single echelle orders, wavelength calibration distortions up to ~ 100 m s^{-1} are expected in the spectra taken with UVES [102, 103]. However, since the H_2 transitions are spread over multiple echelle orders, such distortions are not expected to be dominant in the systematic error budget.

To estimate the impact of such intra-order distortions on $\Delta\mu/\mu$, a sawtooth wavelength distortion with an amplitude of ± 100 m s^{-1} was introduced in each echelle order before combining them together into the final quasar spectrum. A fit of the artificially distorted spectrum returned a value of $\Delta\mu/\mu = (22 \pm 9) \times 10^{-6}$, which is well

[2] Available at `http://kurucz.harvard.edu/Sun/irradiance2005/irradthu.dat`

in agreement with the fiducial value before correcting for the long-range distortions. As a result, the intra-order distortions' contribution to the systematic uncertainty is $< 1 \times 10^{-6}$, which is of the same order of that found in previous, similar studies on different systems [41, 46, 84, 86, 104]. This effect, negligible compared to the uncertainty introduced by the long-range distortions, was included in the systematic error budget.

2.5.3. LACK OF ATTACHED THAR CALIBRATIONS

The Q1232+082 spectra available in the ESO archive were recorded without the use of the attached ThAr calibration lamp exposure, hence they were calibrated using the standard ThAr calibration taken at the end of the night. Previous studies on different systems reported that the lack of attached ThAr calibrations introduces an error on the final value of $\Delta\mu/\mu$ which is $< 1 \times 10^{-6}$ [46, 86], which was added to the systematic error budget.

2.5.4. SPECTRAL REDISPERSION

The final Q1232+082 spectrum is composed by adding several exposures together. This procedure implies a redispersion of all the individual exposures on a common wavelength grid. The rebinning can cause flux correlations between neighbouring pixels, while the choice of the grid can distort the line-profile shapes affecting the value of $\Delta\mu/\mu$.

The impact of the spectral redispersion on $\Delta\mu/\mu$ was investigated by deriving a value of $\Delta\mu/\mu$ from six Q1232+082 spectra constructed using six different velocity grids in the range $2.47 - 2.53$ km s^{-1} per pixel. The average deviation from the fiducial value is 1.4×10^{-6} and was included in the systematic uncertainty budget.

2.5.5. TOTAL SYSTEMATIC UNCERTAINTY

The total systematic uncertainty on the fiducial value was derived by adding in quadrature all the contributions to the systematic error budget. The returned systematic error is $\sim 5 \times 10^{-6}$, therefore the updated fiducial value becomes $\Delta\mu/\mu = (19 \pm 9_{\rm stat} \pm 5_{\rm syst}) \times 10^{-6}$.

2.6. CONCLUSIONS

A re-analysis of molecular hydrogen absorption at $z_{\rm abs} \simeq 2.34$ towards quasar Q1232+082 is presented, in order to constrain a possible temporal variation of μ over cosmological time scales. The absorption system shows 106 H_2 and HD transitions associated with the DLA feature and spread over a range of ~ 400 Å. The dataset contains strongly saturated absorption features as well as overlaps with intervening lines. The comprehensive fitting technique used is able to handle such overlaps, as well as the partial coverage of the absorption system, whose respective effects are

included in the absorption model. The H_2 and HD absorption was used to constrain a possible μ-variation.

Since no supercalibration exposures are available for the Q1232+082 spectrum, an attempt to correct the spectrum for the long-range distortions was made based on the very sparely-sampled information from Whitmore and Murphy [72]. An estimate of the uncertainty on the distortion correction was made, based on the same sample, and it was added to the systematic error budget. The contributions to the systematic error budget from four different sources were investigated and the total systematic uncertainty was found to be dominated by the long-range wavelength distortions. The fiducial $\Delta\mu/\mu$ value delivered by the analysis is $\Delta\mu/\mu = (19 \pm 9_{\rm stat} \pm 5_{\rm syst}) \times 10^{-6}$.

This value is ~ 10 times more precise than those reported by Ivanchik *et al.* [78]. This is due to several improvements: (i) the comprehensive fitting technique applied here allows to expand the transition sample by including partially overlapped absorption features, (ii) the spectrum of Q1232+082 was built including two observational programs from 2003, that contribute additional ~ 8 hrs of integration, (iii) Ivanchik *et al.* [78] used two sets of rest wavelengths with a low fractional accuracy, which is reflected in the uncertainty on the derived values of $\Delta\mu/\mu$. The updated fiducial value of $\Delta\mu/\mu$ presented in this work was derived using accurate rest wavelengths from laser spectroscopy [37, 38, 89]. Given the high accuracy of the studies, the rest wavelengths can be considered exact for the purpose of the comparison, (iv) the updated fiducial value of $\Delta\mu/\mu$ was derived after including a correction for the partial coverage in the H_2 absorption model.

The result presented here can be compared with other studies on different H_2 absorption systems, as shown in Fig. 2.5. The weighted mean of all the $\Delta\mu/\mu$ values considered results in a value of $\Delta\mu/\mu = (3.4 \pm 1.6) \times 10^{-6}$, which is consistent with no variation over a look-back time of $\sim$ 10.5-12.5 Gyrs at the 3σ level. It is noted that not all the measurements were corrected for the effect of wavelength distortions, which, for most cases, pushes the measured $\Delta\mu/\mu$ value towards more positive values by few parts per million. As a consequence, the averaged constraint should be considered as an upper limit to the temporal variation of μ over cosmological timescales.

A list of the known systems showing H_2 and/or CO absorption was compiled by Ubachs *et al.* [73]. The ten best absorbers for a μ variation analysis, because of their brightness, with a Bessel $R_{mag} \leq 18.4$, and H_2 column density, $\log N_{H_2} \geq 14.5$, are shown in Fig. 2.5. With the analysis presented here, we complete a set of the ten best absorbers for μ variation. Note that the set does not contain the system Q2100–0641 at $z_{\rm abs} = 3.09$, which has $R_{mag} = 17.52$ and $\log N_{H_2} = 18.76$ [107], and could represent a good target for future investigations.

The current constraint on $\Delta\mu/\mu$ is almost equally limited by statistical and systematic uncertainties. While the former can be improved by increasing the S/N, the latter is dominated by the long-range wavelength distortions. Such distortions affects not only UVES, but also the High Resolution Echelle Spectrograph, HIRES,

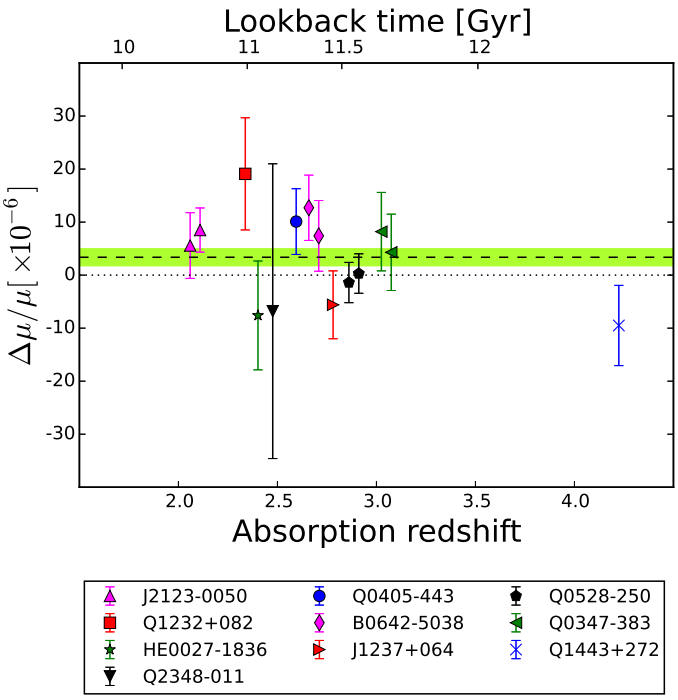

FIGURE 2.5: Measurements of $\Delta\mu/\mu$ derived from molecular hydrogen absorbing systems. The value presented here is shown with a (red) square. The other values of $\Delta\mu/\mu$ were derived from systems: J2123-0050 [41, 104], HE0027-1836 [98], Q2348-011 [85], Q0405-443 [83], B0642-5038 [86, 105], J1237+0647 [30, 46], Q0528-250 [83, 84], Q0347-383 [83, 106] and Q1443+272 [40]. Note that multiple $\Delta\mu/\mu$ measurements were derived from systems J2123-0050, B0642-5038, Q0528-250 and Q0347-383, and are presented with an offset of +0.05 on the x axis to avoid overlaps. The dashed line represents the weighted mean of all the values, the shaded area shows its $\pm 1\sigma$ boundaries, and the dotted line represents the zero level.

mounted on the Keck telescope, which is the other instrument used to investigate a temporal drift of μ. Whitmore and Murphy [72] expanded and refined the supercalibration technique to distortion-correct the quasar spectra, and they showed that the long-range distortions are ubiquitous across the entire UVES and HIRES history. The fact that most of the archival exposures do not have any attached supercalibration precludes a significant reduction in the systematic error on $\Delta\mu/\mu$ when using such data from these spectrographs.

The current constraint on a varying μ can be improved with the new generation of high resolution spectrographs, like the upcoming Echelle SPectrograph for Rocky Exoplanet and Stable Spectroscopic Observations [ESPRESSO, 108]. ESPRESSO, that has a resolution ~ 3 times higher than the one used in this work, and is able to resolve VCs with a Doppler broadening parameter as narrow as $\sim 1.0\,\mathrm{km\,s^{-1}}$. Moreover, being immune, in principle, to the long-range wavelength distortions, thanks to its fibre feed and frequency-comb wavelength calibration, it will deliver constraints on $\Delta\mu/\mu$ with smaller systematic uncertainties. However, ESPRESSO will not cover wavelengths shorter than ~ 3800 Å, which means it can only target H_2 absorption lines in systems at $z_{\rm abs} > 2.4$, and very few such systems are known towards bright quasars [73].

ACKNOWLEDGMENTS

The authors thank the Netherlands Foundation for Fundamental Research of Matter (FOM) for financial support. MTM thanks the Australian Research Council for *Discovery Project* grant DP110100866 which supported this work. The work is based on observations with the ESO Very Large Telescope at Paranal (Chile). WU thanks the European Research Council for an ERC-Advanced grant (No 670168).

APPENDIX

Figures 2.6-2.11 show the H_2 absorption model in the spectrum of the absorbing system at $z_{\rm abs} \simeq 2.34$ towards quasar Q1232+082.

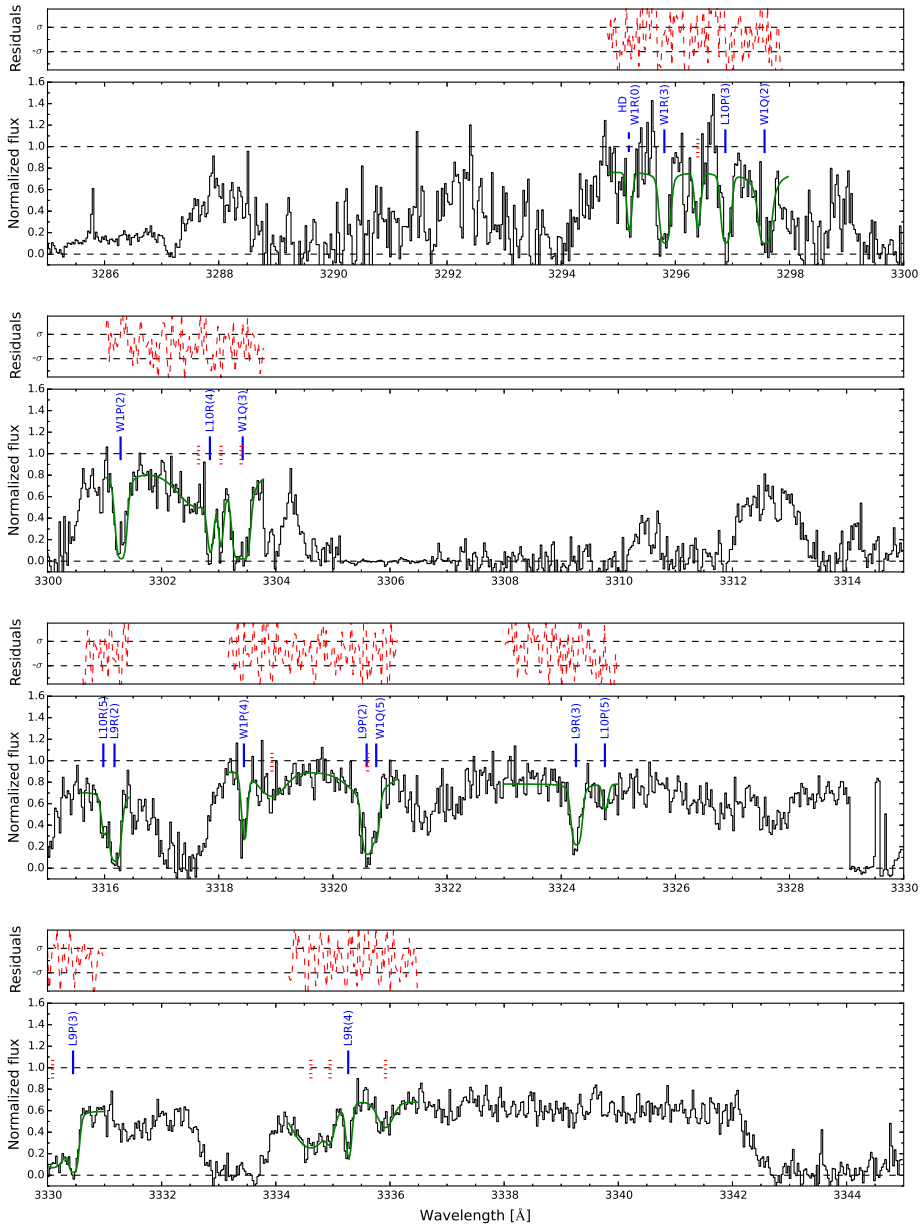

FIGURE 2.6: Spectrum of quasar Q1232+082 (part 1 of 8). The H_2 absorption model is represented with a (green) solid line. H_2 transitions are shown with (blue) solid ticks, HD transitions with (blue) dashed ticks, and the (red) dotted ticks show the position of the intervening H I and metal lines.

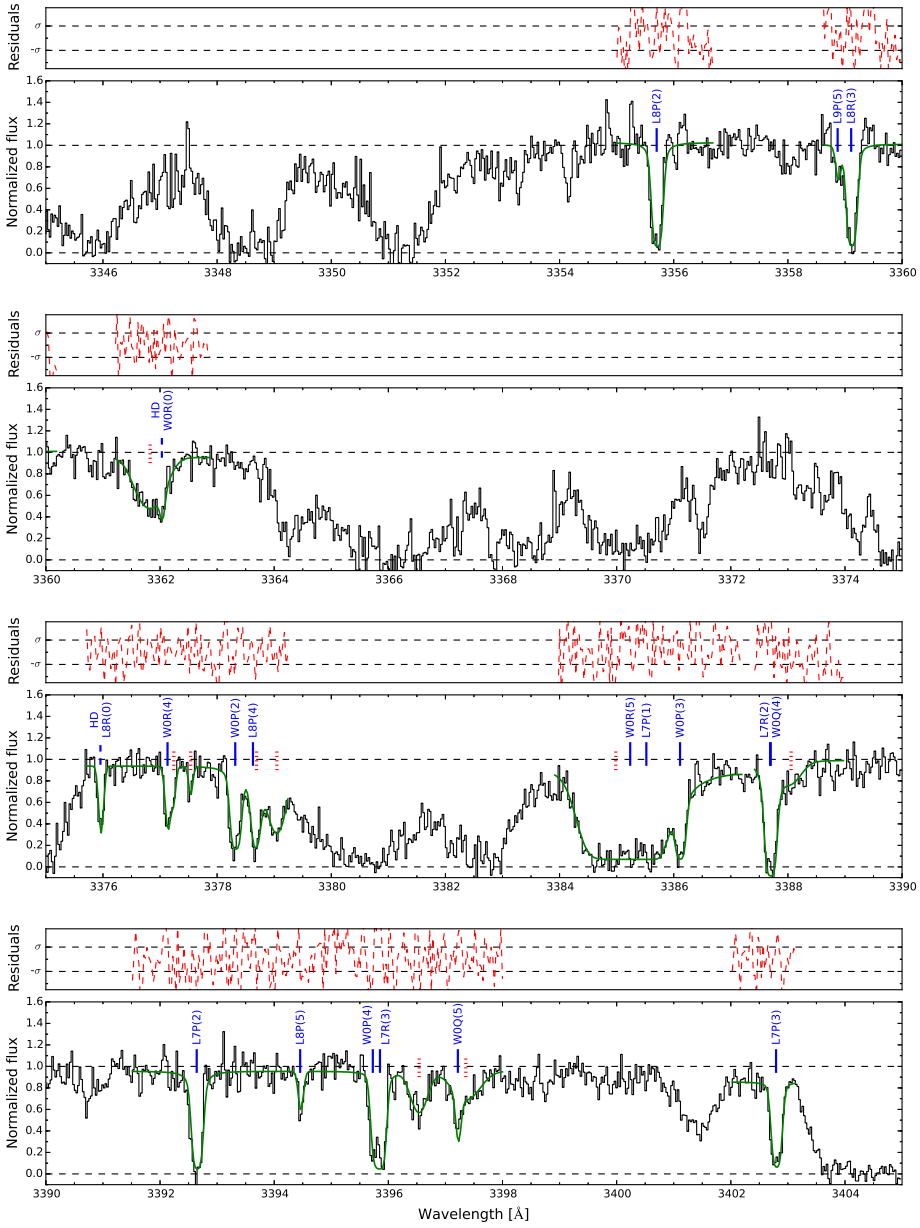

FIGURE 2.7: Spectrum of quasar Q1232+082 (part 2 of 8), continued.

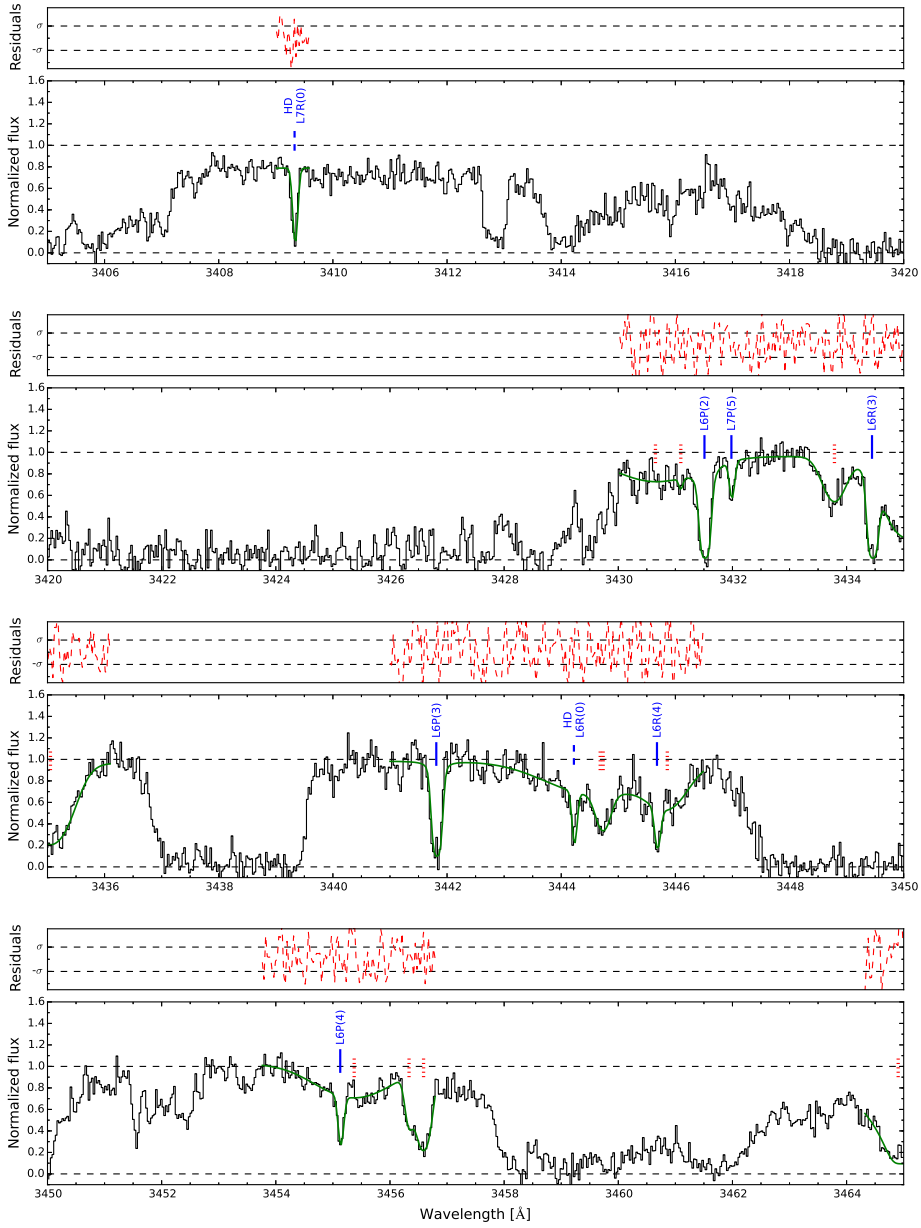

FIGURE 2.8: Spectrum of quasar Q1232+082 (part 3 of 8), continued.

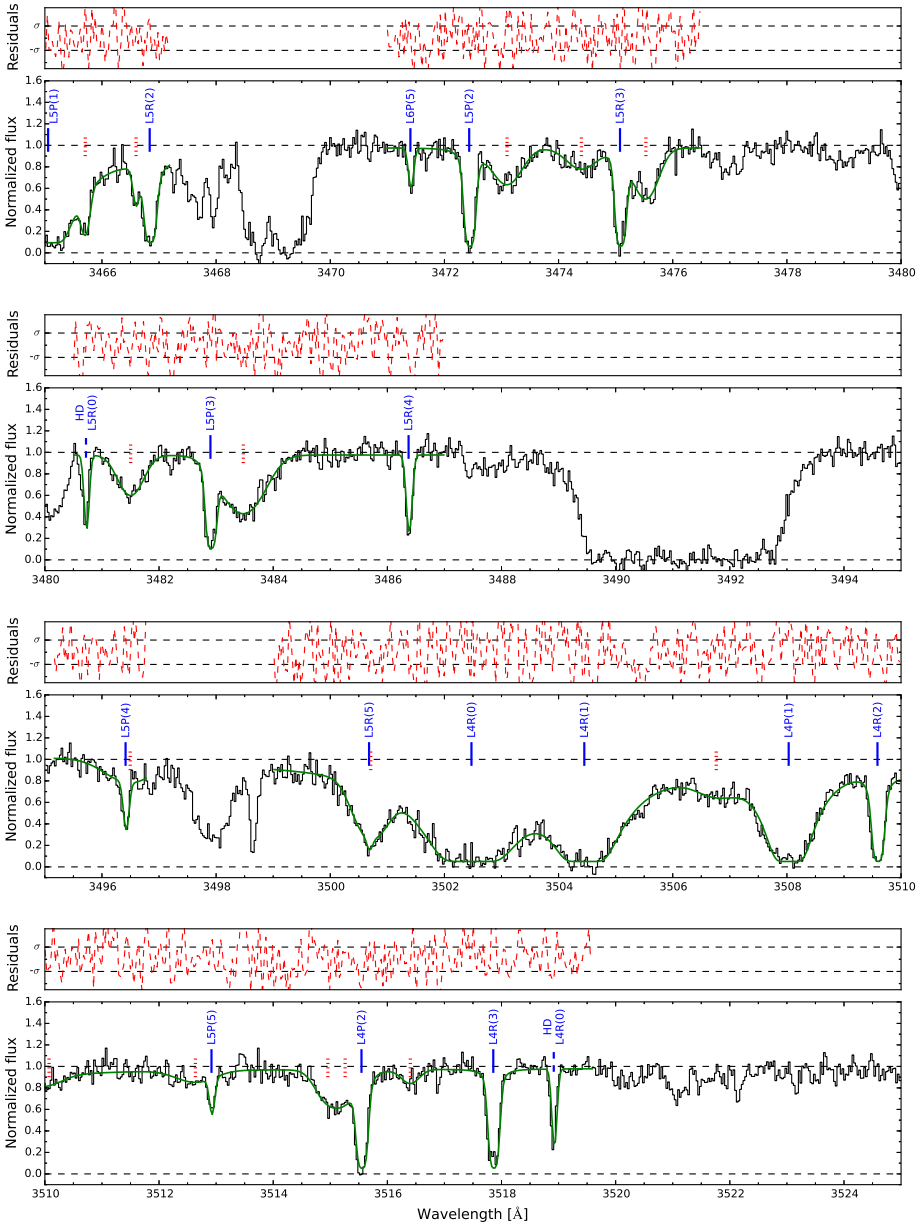

FIGURE 2.9: Spectrum of quasar Q1232+082 (part 4 of 8), continued.

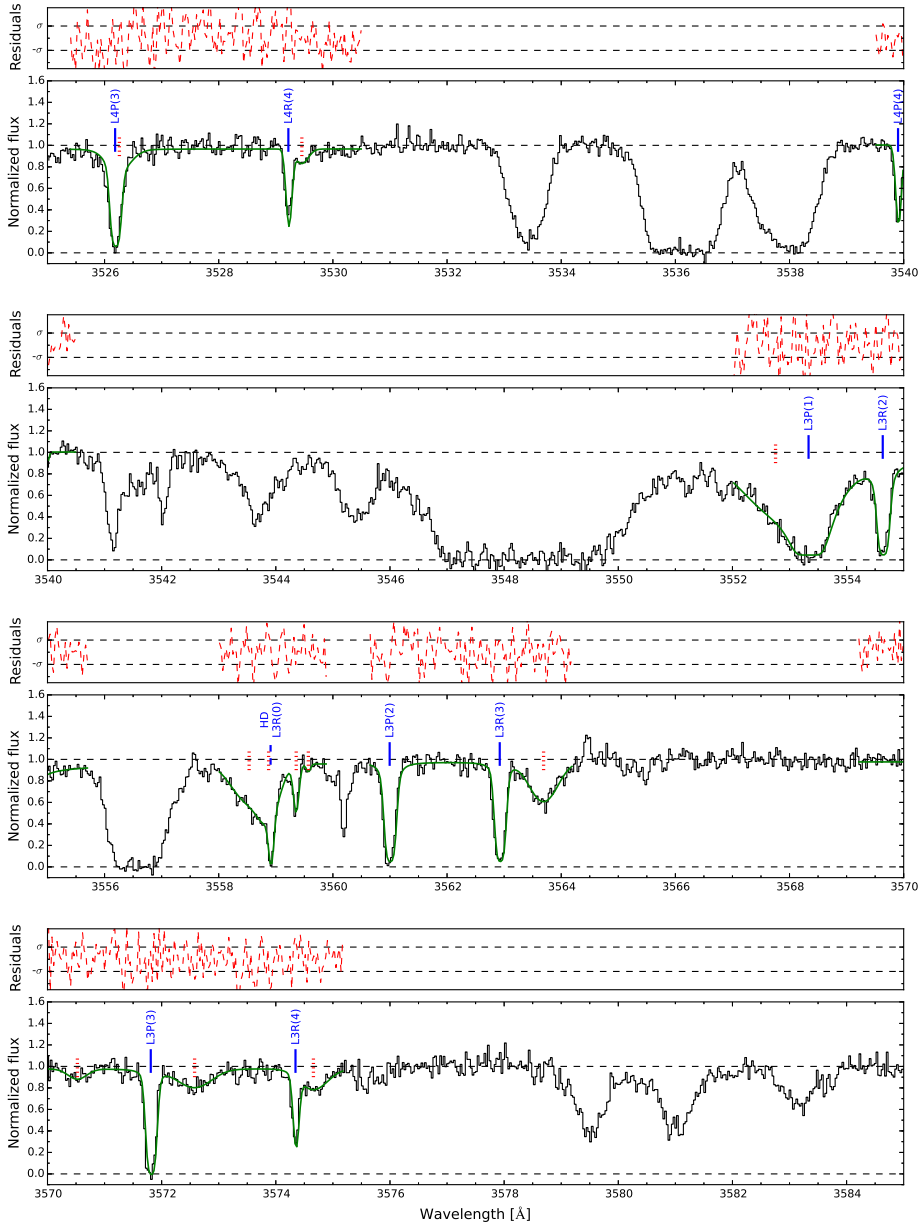

FIGURE 2.10: Spectrum of quasar Q1232+082 (part 5 of 8), continued.

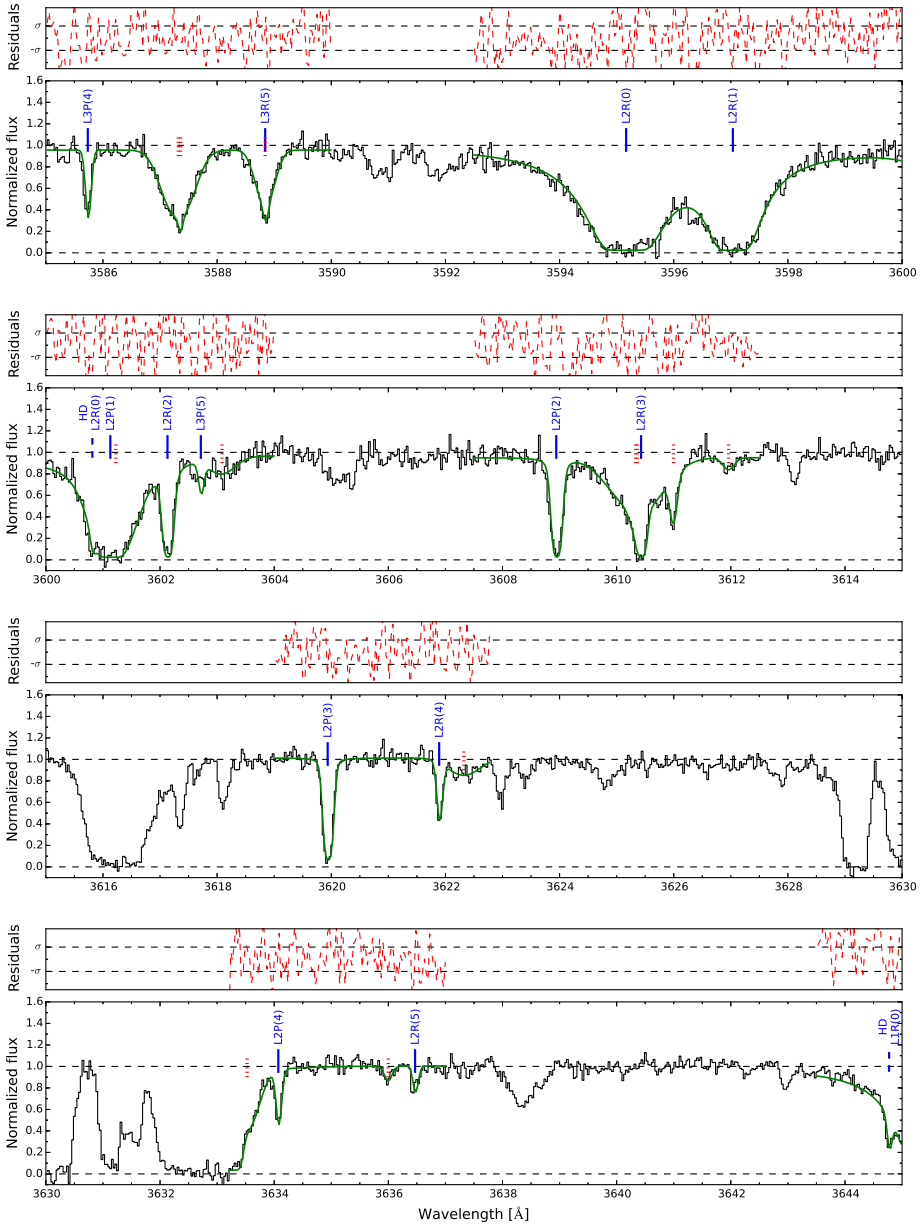

FIGURE 2.11: Spectrum of quasar Q1232+082 (part 6 of 8), continued.

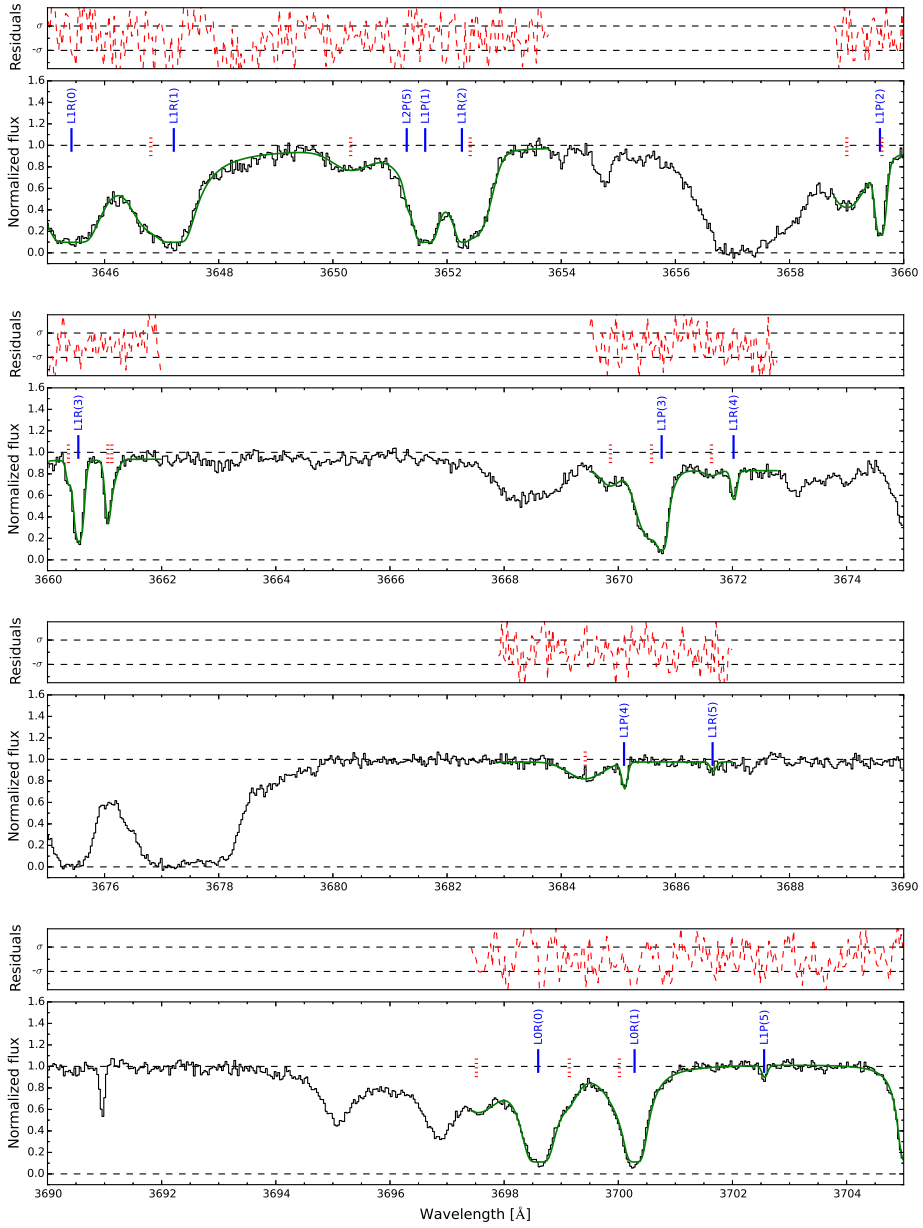

FIGURE 2.12: Spectrum of quasar Q1232+082 (part 7 of 8), continued.

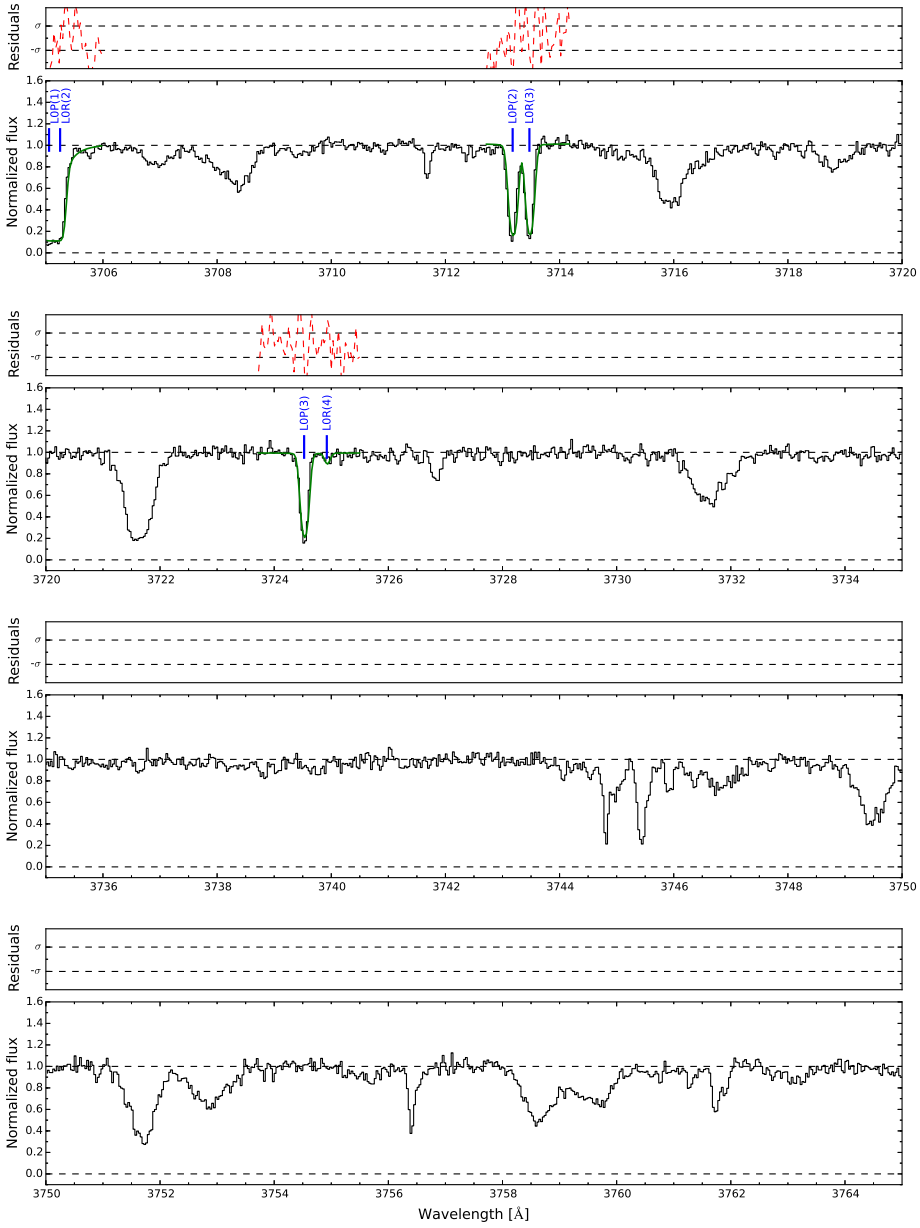

FIGURE 2.13: Spectrum of quasar Q1232+082 (part 8 of 8), continued.

3

CONSTRAINT ON A VARYING PROTON-TO-ELECTRON MASS RATIO FROM MOLECULAR HYDROGEN ABSORPTION TOWARD QUASAR SDSS J123714.60+064759.5

Daprà, M., Bagdonaite, J., Murphy, M. T. & Ubachs, W.
Mont. Not. Roy. Astron. Soc. ***454****, 489-506 (2015)*

Molecular hydrogen transitions in the sub-damped Lyman α absorber at redshift $z_{abs} \simeq 2.69$, toward the background quasar SDSS J123714.60+064759.5, were analyzed in order to search for a possible variation of the proton-to-electron mass ratio μ over a cosmological time-scale. The system is composed of three absorbing clouds where 137 H_2 and HD absorption features were detected. The observations were taken with the Very Large Telescope/Ultraviolet and Visual Echelle Spectrograph with a signal-to-noise ratio of 32 per 2.5 km s^{-1} pixel, covering the wavelengths from 356.6 to 409.5 nm. A comprehensive fitting method was used to fit all the absorption features at once. Systematic effects of distortions to the wavelength calibrations were analyzed in detail from measurements of asteroid and 'solar twin' spectra, and were corrected for. The final constraint on the relative variation in μ between the absorber and the current laboratory value is $\Delta\mu/\mu = (-5.4 \pm 6.3_{stat} \pm 4.0_{syst}) \times 10^{-6}$, consistent with no variation over a look-back time of 11.4 Gyrs.

3.1. INTRODUCTION

The investigation of highly redshifted absorption systems in the line-of-sight of quasars, by means of high-resolution spectroscopic observations, has become an established and powerful method to constrain a possible variation of the laws of physics over cosmological time. The variation of dimensionless fundamental constants, appearing as key building blocks in the laws of physics, is targeted in a comparison between astrophysical observation with laboratory measurement. For example, the fine-structure constant $\alpha = e^2/(4\pi\epsilon_0\hbar c)$ is probed via metal absorption searching for temporal [109] and spatial variations [110].

The other dimensionless constant of nature determining the structure of molecular matter, the proton-to-electron mass ratio $\mu \equiv m_p/m_e$, may be targeted by observing absorption lines of a wide variety of molecules [75]. While radio astronomical observations of ammonia [54, 56] and of methanol molecules [62–64] have proven to be very sensitive, constraining $|\Delta\mu/\mu|$ at the level of $\sim 10^{-7}$, there are are only two radio sources at extragalactic distances where these molecules are observed, and these lie at redshifts $z < 1$.

Molecular hydrogen (H_2) is a target to investigate a possible variation of μ at higher redshifts, where it is observed in larger numbers of absorption systems. H_2 has many spectral lines that are sensitive to a variation in μ [28, 29, 36]. Molecular hydrogen absorbing galaxies often display up to 100 H_2 spectral lines, which helps in improving the statistical basis of measurements made with this technique. Most importantly, H_2 absorbing systems can be observed, using ground-based telescopes, at redshifts $z > 2$, even extending to $z = 4.22$ [40], where the Lyman and Werner bands are redshifted into the optical band.

So far eight H_2 absorbing systems at $z > 2$ have been analyzed for μ-variation, most notably and most accurately the J2123–005 system at z=2.05 [41, 104], the HE0027–1836 [98] and the Q2348–011 system [85] both at z=2.42, the Q0405–443 system at z=2.59 [35, 83, 111], the Q0642–504 system at z=2.66 [86, 105], the Q0528–250 system at z=2.81 [35, 83, 84], the Q0347–383 system at z=3.02 [35, 83, 106, 111, 112], and the Q1443+272 system at z=4.22 [40]. A general conclusion from these studies is that the proton-to-electron mass ratio is constrained to $|\Delta\mu/\mu| < 10^{-5}$ for redshifts in the range z=2-4.2, corresponding to look-back times of up to 90 per cent of the age of the Universe. A review of the results of the analyses of H_2 absorbing systems has been given by Ubachs *et al.* [113] and by Wendt [114].

In the present study H_2 absorption at z=2.69 is investigated in the line of sight toward quasar SDSS J123714.60+064759.5, hereafter J1237+0647, for further constraining a variation of the proton-to-electron mass ratio. The importance of this system is that carbon monoxide (CO) absorption in the optical domain is observed alongside with H_2 [45]. This may be the basis for a simultaneous μ-variation analysis using H_2 and CO [50]. As a first step the H_2 absorption in this system is analyzed for constraining $\Delta\mu/\mu$, results of which are presented in this paper, and this will serve as the basis

for an analysis of the CO lines in a later paper.

3.2. DATA

The analysis presented in this work is based on observations made under four different observing programs, all carried out using the Ultraviolet and Visual Echelle Spectrograph (UVES) mounted on the 8.2m Very Large Telescope (VLT) at Paranal, Chile [115]. UVES is a cross-dispersed echelle spectrograph with two arms that are functionally identical: one covers the wavelengths in the range 300–500 nm (Blue) and the other covers the range 420–1100 nm (Red). Two dichroic beam splitters can be used to work in parallel with the two arms, centering them at different wavelengths. The details of the observational campaigns are presented in Table 3.1.

The raw 2D data were reduced following the procedure used by Bagdonaite *et al.* [86]. The Common Pipeline Language version of the UVES pipeline was used to bias correct and flat field the exposures and then to extract the flux. The ThAr lamp exposures were used for wavelength calibration; the ThAr flux was extracted by using the same object profile weights as in a corresponding quasar exposure. After the standard reduction, the custom software UVES_POPLER[1] was used to combine the extracted echelle orders into a single 1D spectrum which was then manually inspected and cleaned from bad pixels and other spectral artifacts, and the continuum was fitted with low-order polynomials.

The 'final spectrum', obtained by combining all the exposures together, covers the wavelengths from 329.0 to 960.0 nm with a signal-to-noise ratio (S/N) of 26 per 2.5 km s^{-1}per pixel at ~400 nm in the continuum.

3.2.1. DATA FROM 2013 AND 2014

The quasar J1237+0647 was observed in visitor mode in May 2013, program 091.A-0124(A), and in service mode in the period March-June 2014, program 093.A-0373(A). The total integration time amounted to 11.5 hrs. Each exposure was nominally 4800 s in duration and was expected to deliver a S/N of 13 per 2.5 km s^{-1}per pixel at 400 nm and a resolving power R of ~40 000, with a seeing of 0.8 arcsec, a slit of 1.0 arcsec, an airmass of 1.2 and 2×2 binning. Due to bad weather conditions, four exposures were shorter than scheduled and, therefore, the predicted S/N level could not be reached in those cases.

Each of the quasar exposures had an 'attached' standard ThAr calibration, which is a lamp exposure taken immediately after the science exposure leaving all the instrument parameters unchanged, and was immediately followed by a 'supercalibration' exposure without allowing any grating reset. The supercalibration is a method to quantify any long-range wavelength distortion and it involves observing objects with a solar-like spectrum, like asteroids or 'solar twin' stars (see Section 3.5).

[1] http://astronomy.swin.edu.au/~mmurphy/UVES_popler/

TABLE 3.1: Details of the J1237+0647 quasar observations with UVES/VLT included in the present analysis. The total integration time, summed over 17 exposures, is 19.9 hrs. Most of the listed exposures were followed by attached ThAr calibrations and additional 'supercalibrations' as indicated (see Section 3.5). The rest of the data were calibrated using the regular ThAr exposures taken at the end of the night. The CCD binning was 2×2 and the slit width was 1.0 arcsec for all frames. Data collected under programs 082.A-0544(A) and 083.A-0454(A) were retrieved from the ESO archive.

Program ID	Date	Integration time [s]	Central λ [nm]	ThAr	Supercalibration
082.A-0544(A)	27-03-2009	5400	390 + 564	Regular	No
	27-03-2009	5400		Regular	No
	29-03-2009	5400		Regular	No
	29-03-2009	5400		Regular	No
083.A-0454(A)	27-04-2009	4500	390 + 775	Regular	No
	27-04-2009	4500		Regular	No
091.A-0124(A)	15-05-2013	4800	390 + 580	Attached	Yes
	15-05-2013	1727		Attached	No
	15-05-2013	4800		Attached	Yes
	16-05-2013	4800		Attached	Yes
	16-05-2013	2025		Attached	No
093.A-0373(A)	23-03-2014	4800	390 + 580	Attached	Yes
	03-04-2014	4800		Attached	Yes
	28-05-2014	4800		Attached	Yes
	29-05-2014	826		Attached	No
	31-05-2014	4800		Attached	Yes
	02-06-2014	2800		Attached	No

3.2.2. DATA FROM 2009

Part of the total dataset used in this work was retrieved from the ESO data archive[2]. This was the case for observations from programs 082.A-0544(A) and 083.A-0454(A), which were carried out in March-April 2009 and were reported by Noterdaeme *et al.* [45]. The main difference with the most recent observations of J1237+0647 is that these exposures only had the regular 'non-attached' ThAr calibrations taken at the end of each night and dedicated observations of supercalibration targets were not carried out. These observations of J1237+0647 from 2009 added 8.5 hrs of integration on the target.

3.3. METHOD

3.3.1. THEORY

Thompson [28] originally proposed that a possible temporal variation of the proton-to-electron mass ratio $\mu = m_p/m_e$ can be detected using absorption spectra of molecular hydrogen observed at high redshift. The observed wavelength λ_i^z of the i-th transition will show a shift given by:

$$\lambda_i^z = \lambda_i^0(1+z_{\rm abs})(1+K_i\frac{\Delta\mu}{\mu}), \tag{3.1}$$

where λ_i^0 is the rest wavelength, $z_{\rm abs}$ is the redshift where the absorption occurs, $\Delta\mu \equiv \mu_z - \mu_0$ is the difference between the proton-to-electron mass ratio in the system observed and the value measured in the laboratory, and K_i is the sensitivity coefficient which, for a given transition, determines the shifting power and sign due to varying μ. These coefficients are defined as

$$K_i = \frac{{\rm d}\ln\lambda_i}{{\rm d}\ln\mu}. \tag{3.2}$$

The sensitivity coefficients for the H_2 molecule used in this analysis were calculated within a semi-empirical framework by Ubachs *et al.* [36], including effects beyond the Born-Oppenheimer approximation.

The H_2 laboratory wavelengths, λ_i^0, used as a reference in this analysis were measured by Salumbides *et al.* [37] with a fractional wavelength accuracy $\Delta\lambda/\lambda \sim 5\times10^{-8}$, and they can be considered exact in comparison with the uncertainties of the lines in the quasar spectrum. The complete list of laboratory data required for fitting the H_2 absorption lines observed in this work, including rest wavelengths λ_i^0, oscillator strengths f_i, damping coefficients Γ_i and the sensitivity coefficients K_i, was compiled by Malec *et al.* [41].

[2] http://archive.eso.org/eso/eso_archive_main.html

3.3.2. FITTING METHOD

A comprehensive fitting method [41, 84, 86], which involves a simultaneous treatment of all the lines, was used to model the H_2 spectrum. Furthermore this technique allows to tie part of the fitting parameters together, resulting in a smaller number of free parameters. Simultaneous fitting and parameter tying allows to include also those H_2 transitions that are overlapped by metal or H I lines from the Lyman α forest which can be modelled at the same time.

The program used is the non-linear least-squares Voigt profile fitting program VPFIT [88], developed specifically for quasar spectra analysis. A Voigt profile is obtained from the convolution of a Lorentzian profile, which describes the natural line broadening of the transitions and is specific for each molecular transition considered, and a Gaussian profile, which reflects the physical conditions within the absorbing clouds by describing the velocities, both thermal and turbulent, of the molecules. These two profiles are eventually convolved with a model for the instrumental profile, which is assumed to be Gaussian.

In VPFIT, the profile of each velocity component, of each transition, is described by three free parameters: the column density N, the redshift z at which the absorption occurs, and the Doppler width b. These parameters are used in addition to the molecular physics input for every i-th transition, like λ_i^0, f_i, whose product with N gives the optical depth of the absorption line, and Γ_i, which defines the lifetime broadening. Transitions probing the same rotational ground state share the same population, and as a consequence they are all described using the column density N_J. An important underlying assumption is that absorbing features at the same redshift originate from the same cloud, hence they share certain parameters related to the physical conditions of the cloud. In particular, they are assumed to share the redshift z and the width b, which reflects the turbulent motion and the kinetic temperature of the gas in the cloud. This is achieved by tying in VPFIT the z and b parameters of all the absorption lines associated with the gas in a single absorbing cloud.

The fitting program finds the best match between the data and the model iteratively by minimising the χ^2 parameter. The initial values of the free parameters are inserted by the user. Then, in each iteration, VPFIT changes the values of the free parameters of the model and checks the changes in relative χ^2, reporting convergence once a stopping criterion, which is user-defined, is met.

Since introducing too many free parameters may lead to an overfit of the spectrum, models with a different number of velocity components per H_2 transition were compared using the χ^2_ν and the Akaike Information Criterion [*AICC*, 93] parameter. In particular, the latter parameter is defined as

$$AICC = \chi^2 + 2p + \frac{2p(p+1)}{n-p-1} \tag{3.3}$$

where p is the number of free parameters and n is the number of spectral points included in the fit. $\Delta AICC > 5$ and $\Delta AICC > 10$ are considered to be a strong and a

very strong evidence respectively that the model with the lower *AICC* is statistically preferred.

Multiple fits, with a different number of velocity components each, were performed in order to develop a robust absorption model. Only after the results of the fitting process are stable, the possible variation of the proton-to-electron mass ratio expressed by the variable $\Delta\mu/\mu$ is invoked as an extra free parameter in the fit besides N_J, z and b. This fourth parameter is not introduced earlier during the fitting process to avoid that any over/underfitting can be compensated by an artificial variation of μ. The program derives the value of $\Delta\mu/\mu$ according to Eq. (3.1), therewith also using the sensitivity coefficients of Eq. (3.2). The consistency of the derived $\Delta\mu/\mu$ constraint is then tested for sensitivity to a number of assumptions made in the fitting process. The results will be discussed in detail in Section 3.4.2.

3.4. ANALYSIS

Quasar J1237+0647 is located at redshift z=2.78, thereby defining the extent of the Lyman α forest, which comprises multiple series of neutral hydrogen transitions arising from the intergalactic medium at all redshifts below the quasar redshift. Toward the quasar there is one major absorption system at redshift $z = 2.69$, which is a sub-damped Lyman α system (DLA) with a neutral hydrogen column density of $\log N = 20.0 \pm 0.15$ cm^{-2}, that features many absorption lines from atomic, ionized and molecular species [45].

Molecular hydrogen absorption lines associated with the DLA are spread in the range from 352.1 to 409.5 nm. H_2 is found in three absorption features at redshift z=2.688001, z=2.68868 and z=2.68955; their velocities relative to the redshift of the strongest feature at z=2.68955 are respectively v=−125 km s^{-1}, hereafter Z1, v=−72 km s^{-1}, hereafter Z2, and v=0 km s^{-1}, hereafter Z3. The presence of these three features close to each other results in the line profiles shown in Fig. 3.1. The presence of clearly separated velocity features is not uncommon and has been observed in various systems in the past. The number of such components can vary from one up to the seven distinct features observed in the absorbing system toward quasar Q2348–011 [85, 116].

Z3 has the highest column density for every J-level, resulting in heavily saturated absorption features for low J-levels with $J \leq 1$. Furthermore, Z3 shows also deuterated molecular hydrogen (HD) absorption, where only the J=0 level was detected [45]. The HD molecule is sensitive to a variation of μ [38, 39], and its detected transitions were included in the present μ-variation analysis.

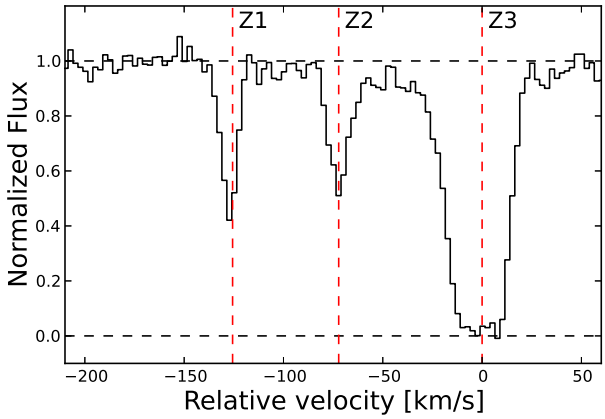

FIGURE 3.1: Typical line profile for the three absorption features toward J1237+0647. The transition plotted is L1P(3) at $\lambda_0 = 109.978$ nm. The vertical dashed lines (red) indicate the positions of the three H_2 spectral features fitted in this study. The velocity frame is centered on the strongest feature Z3.

3.4.1. CREATING AN ABSORPTION MODEL

SELECTING AND FITTING SPECTRAL REGIONS

Given the broad absorption profile, spanning ~ 150 km s^{-1}, overlaps between profiles of different molecular hydrogen transitions are common as well as overlaps with the H I transitions from the Lyman α forest. Within the comprehensive fitting method, all kinds of overlaps can be handled. However, no relevant information was gained in the case of a complete overlap with a saturated H I line, hence such absorption features were not included in this study. Less frequently, some H_2 features partially overlap with narrow metal transitions. However, these lines were not excluded from the dataset considered in this work. A large number of metal absorption features were identified by Noterdaeme *et al.* [45].

All the 137 potentially useful H_2 and HD transitions were contained in 66 spectral regions, in the range 351.0-413.5 nm, which were selected trying to avoid, whenever possible, H I transitions and too-heavily saturated low J-level H_2 absorption features in Z3. The useful H_2 transitions, probing six different rotational quantum states with J=0–5, are listed in Table 3.2. Absorption features originating at the same redshift had both the z and the b parameters tied together, while the column densities N_J were allowed to vary independently from each other. Z3 shows saturated H_2 lines, particularly in the low J-levels, but there is an apparent evidence of a partial coverage with a non-zero residual flux at the base of its absorption features. To take into account this effect, a zero-level correction was included as a free parameter in the fit for each

H_2 region.

In order to build a robust model, the neutral hydrogen absorption lines occurring in the Lyman α forest and included in the selected regions must be accounted for. The H I transitions were modelled by assigning to each of them a set of free parameters (N, z, b) in VPFIT. Initial guesses of the free parameters were user-provided for each H_2 HD and H I transition.

EXTRA VELOCITY COMPONENTS

The H_2 absorption spectrum toward J1237+0647 displays three clearly distinct features in velocity space. In order to fit the spectrum as accurately as possible, it is imperative to consider possible underlying substructures in velocity space. Physically this may relate to the existence of closely separated distinct clouds, or inhomogeneities in the clouds in the line-of-sight. To investigate such underlying velocity structure, the fitting residuals from the 66 selected regions were normalized, shifted to a common velocity scale and averaged together, creating a composite residual spectrum [CRS, 41]. Only the H_2 absorption features that were not overlapped by H I features were included in the CRS, in order to avoid that the residuals of the H I model could introduce any spurious effect. The CRS, by combining the residuals of many transitions, highlighted any over/underfitted structure in the absorption features.

Z1 could be described using only one velocity component (VC), while indications of underfitting were observed in the CRS for absorption features Z2 and Z3, hence they were modelled by adding extra VCs. They were added to the model until VPFIT started to reject them. Then the models with a different number of VCs were compared using the χ^2 and the *AICC* parameters, in order to decide which one better fitted the data. The CRS for the three absorption features Z1, Z2 and Z3 are shown in Figs. 3.2–3.4. Z2 could be modelled using two VCs, labelled as 'a' and 'b' in Fig. 3.3, and Z3 was modelled using three VCs, labelled as 'a', 'b' and 'c' in Fig. 3.4. Parameters for the model are summarized in Table 3.3 and the VCs are shown in Fig. 3.5. Previous studies found no strong evidences for a systematic shift in $\Delta\mu/\mu$ due to a segregation in different rotational levels [41, 84], hence it was assumed that the velocity structure is the same among all the J-levels in each absorption feature. The complete absorption model is shown in Section 3.6.

3.4.2. CONSTRAINING $\Delta\mu/\mu$

Once an optimal model was found, an extra free parameter, corresponding to $\Delta\mu/\mu$, was added to the H_2 transitions in VPFIT. All the transitions were included in the fit, without any distinction between their bands, their J-levels or absorbing clouds where they arose. The model returns $\Delta\mu/\mu = (-1.1 \pm 6.3_{\rm stat}) \times 10^{-6}$. The statistical error reported here was derived from the appropriate diagonal term of the final covariance matrix for the fit. Given the absorption model, it represents only the uncertainty in $\Delta\mu/\mu$ stemming from the photon statistics of the quasar spectrum, i.e.

TABLE 3.2: List of the molecular transitions used in this analysis.

J-level	Lyman transitions	Werner transitions	$n_{transitions}$
H_2 $J=0$	L0R(0), L2R(0), L3R(0), L4R(0), L6R(0), L7R(0), L8R(0), L10R(0)	W0R(0), W1R(0)	10
H_2 $J=1$	L0P(1), L0R(1), L1P(1), L1R(1), L2P(1), L2R(1), L3P(1), L7P(1), L9R(1), L10R(1), L12R(1)	W0R(1), W1R(1)	13
H_2 $J=2$	L0P(2), L0R(2), L1P(2), L1R(2), L2P(2), L2R(2), L3P(2), L4P(2), L4R(2), L5P(2), L6P(2), L7P(2), L7R(2), L8P(2), L9P(2), L10P(2), L10R(2), L11P(2), L11R(2), L13P(2), L13R(2)	W0P(2), W0Q(2), W1Q(2), W2P(2), W2Q(2), W2R(2)	27
H_2 $J=3$	L0P(3), L0R(3), L1P(3), L1R(3), L2R(3), L3P(3), L3R(3), L5P(3), L5R(3), L6P(3), L6R(3), L7P(3), L7R(3), L8P(3), L8R(3), L9R(3), L10P(3), L12R(3), L13P(3), L13R(3), L14P(3)	W0P(3), W0Q(3), W1R(3), W2P(3), W2Q(3), W2R(3), W3P(3)	28
H_2 $J=4$	L0P(4), L0R(4), L1P(4), L1R(4), L2R(4), L3P(4), L3R(4), L4P(4), L4R(4), L5R(4), L6P(4), L7P(4), L7R(4), L8P(4), L9P(4), L9R(4), L11P(4), L11R(4), L12R(4), L13P(4), L14P(4)	W0P(4), W0Q(4), W0R(4), W1P(4), W2Q(4), W2R(4), W3Q(4)	28
H_2 $J=5$	L0R(5), L1P(5), L2P(5), L2R(5), L3P(5), L3R(5), L4P(5), L5P(5), L5R(5), L7P(5), L8P(5), L9P(5), L10P(5), L11R(5), L12R(5), L13P(5), L14P(5), L15P(5)	W0P(5), W0R(5), W1Q(5), W2Q(5), W2R(5), W3P(5)	24
HD $J=0$	L3R0, L5R0, L8R0, L12R0, L15R0	W1R0, W3R0	7
Total number of lines			137

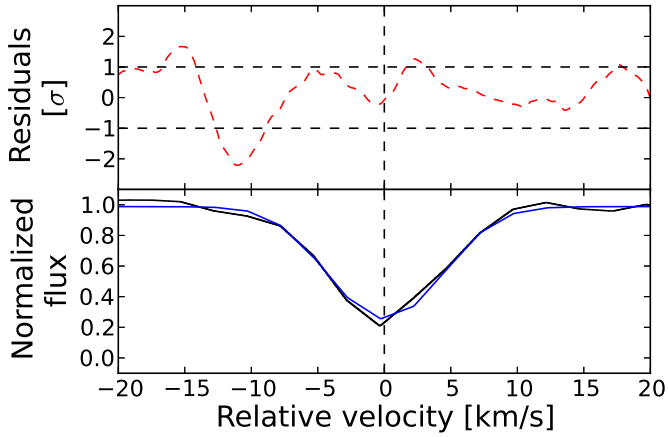

FIGURE 3.2: Top panel: normalized composite residual spectrum for Z1 formed from 30 H_2 absorption features. The dashed lines represent the $\pm 1\sigma$ boundaries. Bottom panel: an example transition shown on the same velocity scale. The velocity scale is centred at $z = 2.688009$. The vertical dashed line shows the position of the velocity component.

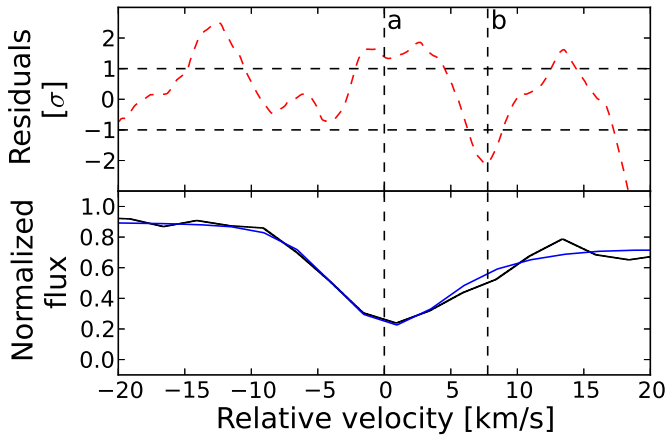

FIGURE 3.3: Top panel: normalized composite residual spectrum for Z2 formed from 33 H_2 absorption features obtained from the 2 VCs model. The dashed lines represent the $\pm 1\sigma$ boundaries. Bottom panel: an example transition shown on the same velocity scale. The velocity scale is centred at $z = 2.688664$, on the strongest velocity component. The vertical dashed lines show the positions of the two velocity components at $v = 0$ km s^{-1} (a) and +7 km s^{-1} (b).

TABLE 3.3: Column densities N_J, redshift z and Doppler parameters b of the H_2 transitions in the three clearly distinguishable absorption features and in their underlying velocity components a, b, c. Levels with $J = 4$ and 5 are too weak to be detected in Z1 and Z2. Levels with $J = 0$ and 1 are heavily saturated in Z3 and they have been discarded from the model.

	Z1	Z2		Z3		
J-levels	$\log N_J$ [cm^{-2}]	$\log N_J$ [cm^{-2}]		$\log N_J$ [cm^{-2}]		
		a	b	a	b	c
$J = 0$	15.74 ± 0.11	15.44 ± 0.11	13.78 ± 0.17		Discarded	
$J = 1$	16.29 ± 0.08	16.23 ± 0.11	14.56 ± 0.10		Discarded	
$J = 2$	15.35 ± 0.04	15.27 ± 0.07	13.90 ± 0.15	15.67 ± 0.10	17.64 ± 0.10	15.26 ± 0.16
$J = 3$	15.21 ± 0.02	14.88 ± 0.05	14.31 ± 0.08	15.66 ± 0.11	18.02 ± 0.06	14.64 ± 0.28
$J = 4$		–		14.79 ± 0.07	15.34 ± 0.04	13.93 ± 0.07
$J = 5$		–		14.50 ± 0.07	14.79 ± 0.04	13.33 ± 0.17
HD $J = 0$		–		–	14.36 ± 0.03	–
z	2.68801(06)	2.68866(09)	2.68872(82)	2.68950(96)	2.68955(14)	2.68972(52)
b [km s^{-1}]	2.94 ± 0.08	2.32 ± 0.13	6.99 ± 0.65	11.36 ± 0.48	5.78 ± 0.11	2.54 ± 0.48

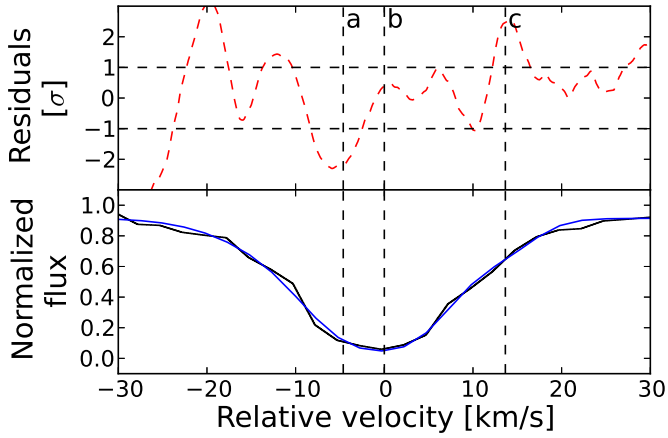

FIGURE 3.4: Top panel: normalized composite residual spectrum for Z3 formed from 33 H_2 absorption features obtained from the 3 VCs model. The dashed lines represent the $\pm 1\sigma$ boundaries. Bottom panel: an example transition shown on the same velocity scale. The velocity scale is centred at $z = 2.689555$, on the strongest velocity component. The vertical dashed lines show the positions of the three velocity components at $v = -4$ km s^{-1} (a), 0 km s^{-1} (b) and +13 km s^{-1} (c).

its signal-to-noise ratio. However, to evaluate the robustness of the result, hereafter the statistical value of $\Delta\mu/\mu$, a variety of consistency tests and sources of systematic error which contribute to the overall uncertainty budget were explored, results of which are shown in Fig. 3.6 and discussed below.

ISOLATING SINGLE ABSORBING FEATURES

Each of the absorbing features Z1, Z2 and Z3 can be investigated separately. The constraints on $\Delta\mu/\mu$ returned are $\Delta\mu/\mu|_{Z1} = (11.4 \pm 10.2_{\rm stat}) \times 10^{-6}$ for Z1, $\Delta\mu/\mu|_{Z2} = (-17.7 \pm 14.0_{\rm stat}) \times 10^{-6}$ for Z2 and $\Delta\mu/\mu|_{Z3} = (-6.1 \pm 14.8_{\rm stat}) \times 10^{-6}$ for Z3. The resulting constraints are in agreement with each other and with the statistical value for the entire dataset within 1σ boundaries.

ISOLATING LYMAN AND WERNER TRANSITIONS

All the H_2 transitions considered in this analysis belong either to the Lyman- or to the Werner band systems. Any long-range distortion of the wavelength scale will be nearly degenerate with a shift of the molecular hydrogen lines due to a non-zero value of $\Delta\mu/\mu$. This degeneracy is partly broken by fitting together H_2 transitions from both Lyman and Werner bands. The effect of such a distortion can be investigated by fitting separately transitions from the two band systems.

The values returned in this way are $\Delta\mu/\mu|_{\rm L} = (-0.6 \pm 6.4_{\rm stat}) \times 10^{-6}$ for Lyman

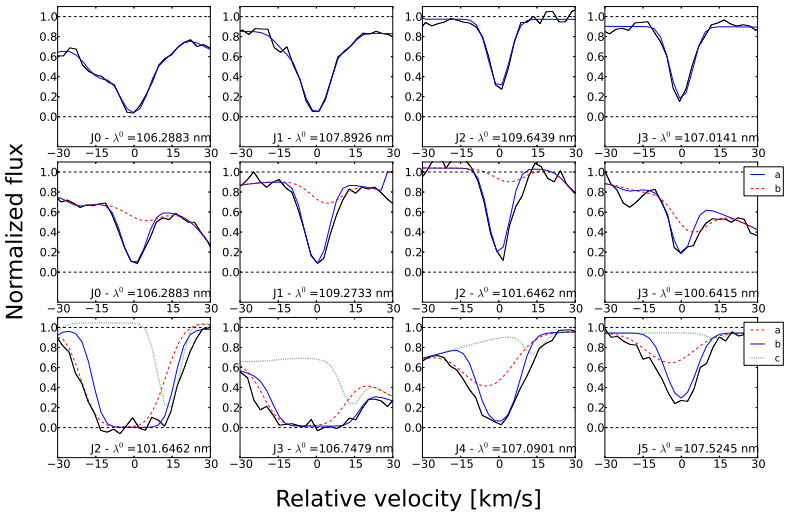

FIGURE 3.5: Example transitions for every J-level. Each velocity component is plotted against the fitted continuum. H I contributions to the line shapes are not highlighted. Top panel: J-levels 0-4 for Z1 (blue), the velocity scale is centred at z=2.688009. Middle panel: J-levels 0-4 for Z2. The velocity component at z=2.688664, Z2a, is depicted with the (blue) solid line and the one at z=2.688717, Z2b, with the (red) dashed line. The velocity scale is centred on Z2a. Bottom panel: J-levels 2-5 for Z3. The three velocity components at redshifts z=2.689498, Z3a, 2.689555, Z3b, and 2.689723, Z3c, are shown with the dashed (red), solid (blue) and dotted (green) line respectively. The velocity scale is centred on Z3b.

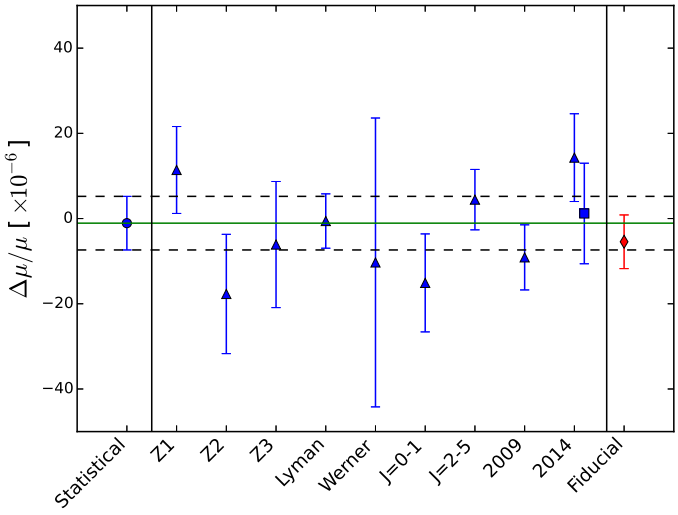

FIGURE 3.6: $\Delta\mu/\mu$ constraints obtained from various tests (triangles) compared with the statistical value from the entire dataset (circle). The solid (green) horizontal line indicates the value of the statistical constraint and the two dashed lines represent its 1σ statistical uncertainties. The square represents the $\Delta\mu/\mu$ value obtained only from the exposures taken in 2014 after applying to each of them a long-range distortion correction, as discussed in Section 3.5. The diamond (red) represents the fiducial value obtained for the entire dataset (2009+2013+2014) after applying the distortion corrections.

transitions and $\Delta\mu/\mu|_{\rm W} = (-10.3 \pm 33.9_{\rm stat}) \times 10^{-6}$ for Werner transitions. The larger error of the value returned by Werner transitions is due to three effects. Firstly, there are fewer Werner transitions than Lyman transitions in the spectrum, with a ratio between the former and the latter of ∼1:4. Then the spread of the sensitivity coefficients is larger for Lyman transitions, $\Delta K_{\rm L} = 0.092$, than the one of Werner transitions, $\Delta K_{\rm W} = 0.054$. Finally, the Werner transitions fall in the bluest part of the spectrum, where the S/N is much lower than in the region where Lyman transitions are. Such differences lead the statistical value of $\Delta\mu/\mu$ to be dominated by the Lyman transitions.

ISOLATING COLD AND WARM STATES

Using VPFIT it is possible to calculate a different value of $\Delta\mu/\mu$ for transitions originating in each J-level, in order to obtain the relative contributions of different levels to the statistical value. This is particularly useful to investigate the impact of possible temperature inhomogeneities in the absorbing clouds. Due to the para-ortho distribution, the J= 1 rotational state is significantly populated even at the lowest temperatures [36]. As a consequence, the H_2 transitions can be divided into two sets: rotational states with J=0,1 (cold) and with $J \geq 2$ (warm).

The constraints returned by the model are $\Delta\mu/\mu|_{\rm cold} = (-15.1 \pm 11.5_{\rm stat}) \times 10^{-6}$ for the cold states and $\Delta\mu/\mu|_{\rm warm} = (4.4 \pm 7.1_{\rm stat}) \times 10^{-6}$ for the warm states. The two values match within their uncertainties, which means that any temperature inhomogeneity in the absorbing clouds does not have a significant impact on the μ-variation.

Furthermore, the slightly larger error derived from the cold states reflects the fact that levels with $J \leq 3$ are saturated in Z3 and, in particular, cold states are heavily saturated. As a consequence of the saturation, there are fewer constraining pixels contributing to the fitting process and there are fewer transitions in the cold states dataset.

SEPARATING EXPOSURES FROM 2009

The dataset used in this work can be divided between the exposures taken in 2013 and 2014, which had an attached ThAr calibration and a supercalibration, and the exposures taken in 2009, retrieved from the ESO archive, which only had regular non-attached ThAr calibrations. In order to see how the absence of the individual calibrations affects the statistical value, two values for $\Delta\mu/\mu$ were derived from the two subsets.

The constraints obtained in this way are $\Delta\mu/\mu|_{2009} = (-9.1 \pm 7.6_{\rm stat}) \times 10^{-6}$ for the exposures taken in 2009 and $\Delta\mu/\mu|_{2014} = (14.3 \pm 10.3_{\rm stat}) \times 10^{-6}$ for the exposures taken in 2013 and 2014. The two values do not agree within their combined 1σ statistical uncertainties, although they do within 1.5σ. However, this comparison does not take into account the long-range distortion effect, which will be discussed in the next section.

3.5. SUPERCALIBRATIONS

In order to constrain a variation of μ, it is crucial to accurately wavelength calibrate the quasar observations. Attempts to perform advanced tests of the effective accuracy of UVES were performed by Molaro *et al.* [117] by comparing a UVES-recorded asteroid spectrum with a highly accurate solar reference spectrum. These measurements revealed zero offsets up to ≈ 50 m s^{-1}, likely due to a non-uniform slit illumination, but found no evidence for a wavelength-dependent velocity shift in the spectrum. Similar studies, that are now referred to as 'supercalibrations', showed that spectra taken with UVES and HIRES spectrographs suffer from intra-order calibration shifts on scales of single echelle orders but they did not uncover any evidence for a long-range distortion in the spectra on the scale of the spectrographs arms [102, 103]. Rahmani *et al.* [98] detected for the first time a long-range distortion in some UVES spectra up to ~ 400 m s^{-1} on a scale of ~ 600 Å. More recently, Whitmore and Murphy [72] found that significant wavelength calibration distortions, both intra-order and long-range, are ubiquitous across UVES and HIRES history, most likely due to a different light path of the astronomical object and the ThAr lamp within the instrument.

The presence of long-range distortions between the attached ThAr calibration and the main target spectrum velocity scales introduces a wavelength-dependent shift that mimics a non-zero $\Delta\mu/\mu$. This happens because the sensitivity coefficients K_i decrease with increasing wavelength (see Fig. 1 of Bagdonaite *et al.* [86]) and a long-range distortion of the wavelength scale would produce a strong systematic effect which will be nearly degenerate with the effect produced by a variation of μ. In principle, this degeneration can be broken by fitting Lyman and Werner transitions together; however, the paucity of Werner transitions and the low S/N in the spectral region where they fall prevent the degeneracy to be broken in this way, as illustrated by Malec *et al.* [41] and discussed in Section 3.4.2. Over most of UVES's history, the sign of measured long-range distortions was such that they spuriously pushed $\Delta\mu/\mu$ to more positive values [72].

3.5.1. METHOD

The first supercalibration performed with UVES consisted of a comparison between asteroid spectra and a Fourier Transform Spectrometer (FTS) solar atlas [117]. Rahmani *et al.* [98] cross-correlated asteroid spectra with a laboratory solar spectrum and, more recently, Whitmore and Murphy [72] improved the technique by forward modelling the FTS spectra to match observed asteroid spectra, thereby allowing information to be derived from much shorter spectral ranges, and by showing that the same technique can be applied on solar twin stars as well. Their method is used in this study to supercalibrate the quasar spectrum.

The supercalibration process consists in the comparison of a ThAr calibrated spectrum with a reference spectrum from a FTS, whose frequency scale is expected

to be much more accurate than the UVES one, hence it is considered 'absolutely calibrated' for the purpose of this study. The reference used is the FTS vacuum solar spectrum from Chance and Kurucz [99][3]. The targets for the supercalibrations were asteroids, which reflect the solar light and hence have the same spectrum as the Sun, and 'solar twin' stars, i.e. objects whose spectra are almost identical to the solar one [100, 101]. Since the supercalibration targets are astronomical objects, no changes are required in the focus or in the slit alignment.

The two spectra were divided into small regions of ≈ 500 km s^{-1} each, which corresponds to ≈ 8 Å. Their small size allows for sampling each echelle order with ≈ 10 regions, and for identifying any relative velocity distortion down to ~ 30 m s^{-1} [72]. The spectral regions of the two spectra were compared using a χ^2-minimization technique looking for any wavelength-dependent calibration distortions across each echelle order and across the wavelength range covered by all the echelle orders collectively. The overall velocity distortion was obtained by a linear fit of all the spectral regions and it was used to distortion-correct the corresponding quasar exposure.

3.5.2. SUPERCALIBRATION DATA

DATA FROM 2013 AND 2014

The exposures taken in 2013 and in 2014 were recorded with an attached ThAr wavelength calibration. Since the problems of long-range distortions and their effect on μ-variation analysis from H_2 spectra had been well identified and reported [86, 98], supercalibration exposures targeting asteroids and solar twins were purposely recorded immediately after the science exposures with their attached ThAr calibrations. In view of their accessibility during observations of J1237+0647, supercalibration spectra of the Eunomia asteroid, as well a solar twin stars HD 76440, HD 147513, HD 097356 and HD 117860, were used. Only some exposures, which had to be aborted due to bad weather conditions, were not supported by a supercalibration.

For each supercalibration spectrum, its long-range wavelength distortion was determined in terms of a slope parameter, which was found to range between 300 and 725 m s^{-1} per 1000 Å. In particular, during each observing run the values of the distortion slopes showed an apparent stability, with a spread in the slope values of, at most, ~200 m s^{-1} per 1000 Å in May 2014. These values, and in particular the positive sign, are commensurate with values found previously in such measurements [72, 98]. Results of the present analysis are plotted in Fig. 3.7 and numerical values listed in Table 3.4. Thereupon each individual J1237+0647 science exposure was corrected for its long-range distortion by introducing a counter-distortion based on these slopes, after which the exposures were rebinned and combined using UVES_POPLER. Exposures without a directly attached supercalibration were corrected using the average value of all the distortion slopes from the supercalibrations taken during the same

[3] Available at `http://kurucz.harvard.edu/sun/irradiance2005/irradthu.dat`

night, in view of the stability discussed above.

DATA FROM 2009

The data for J1237+0647 taken in 2009, retrieved from the ESO archive, were not supported by an attached ThAr calibration, and they were therefore wavelength calibrated against a regular ThAr calibration recorded at the end of the night. No supercalibration spectra were recorded with the J1237+0647 science exposures. In the ESO archive some suitable asteroid observations were found as three exposures of the Ceres asteroid, recorded in March and April 2009 within one week of the quasar exposures, under program 080.C-0881(B) (PI Dumas). These exposures did not share the same telescope settings as the J1237+0647 observations. In particular they had different grating settings, covering only half of the H_2 window, as shown in Fig. 3.7, and they did not have an attached ThAr calibration. Unlike the quasar observations, these exposures were not taken with the slit perpendicular to the horizon and hence an atmospheric dispersion corrector was used not to lose the blue part of the flux due to the atmospheric dispersion. Such differences can affect the light path of Ceres within the telescope, resulting in a different one from the quasar light path. Since the causes of the long-range distortions are unclear [72], it is not possible to estimate the impact of those differences on the supercalibration process.

Analysis of the Ceres exposures yields two distortion slopes of of ~ 150 m s^{-1}per 1000 Å, while a third one shows a negative distortion of ~ -500 m s^{-1}per 1000 Å. The presence of two values showing distortions with opposing signs for the same night is remarkable, in particular since these two Ceres spectra were calibrated using the same non-attached ThAr spectrum, and it prevents one to calculate a reliable average value of the distortion correction for these exposures. For these reasons, it was decided to not perform a counter-distortion analysis of the wavelength scale.

Nevertheless, a magnitude of the wavelength distortion can be estimated using the limiting values of the distortion slopes, given in Table 3.4. Both limiting values of opposing signs were considered as the largest distortions that could have affected the UVES exposures of J1237+0647 in 2009. Therefore the full sub-spectrum formed from 2009 exposures was first counter-distorted using the limit values of the distortion slope and then was combined with the distortion-corrected spectrum formed from exposures taken in 2013 and 2014 to derive the constraints on $\Delta\mu/\mu$. The two values derived were $\Delta\mu/\mu|_{\rm low} = (-4.6 \pm 6.1_{\rm stat}) \times 10^{-6}$ and $\Delta\mu/\mu|_{\rm up} = (0.1 \pm 6.1_{\rm stat}) \times 10^{-6}$ for the lower and for the upper limit respectively. The spread in resulting values for $\Delta\mu/\mu$ was interpreted in terms of a systematic uncertainty amounting to 2.4×10^{-6}.

OTHER SOURCES OF SYSTEMATICS

The supercalibrations allow to address the issues of both the intra-order and the long-range distortions that are known to affect UVES [72, 98, 102, 103, 117]. All the supercalibration targets used in this analysis are presented in Fig. 3.7. In each panel,

the correction that needs to be applied to the ThAr wavelength is shown; note that each echelle order is characterized by several (typically 4-9) measurements separated by ~8 Å. The vertical spread in each echelle order reflects the magnitude of the intra-order distortions, while the slopes, obtained by least-squares fits to the mean velocity shift correction from each echelle order as a function of wavelength [as in 72], represents the long-range distortions.

The impact of the intra-order distortions is, typically, not expected to be dominant in the systematic error budget on the fiducial value of $\Delta\mu/\mu$, because the H_2 and HD transitions are spread across multiple orders [41, 84, 86]. Nevertheless, the supercalibrations taken in 2014 show intra-order distortions that are ~ three times larger than the distortions in the exposures taken in 2009 and 2013. An estimation of the impact of the intra-order distortions on the systematic error on $\Delta\mu/\mu$ is made using $\delta(\Delta\mu/\mu) = [(\Delta v/c)/\sqrt{N}]/\Delta K_i$, where $\Delta v/c$ is the mean amplitude of the intra-order distortions, $N = 137$ is the number of H_2 and HD transitions detected and $\Delta K_i = 0.065$ is the spread in the sensitivity coefficients.

The supercalibration exposures return a mean velocity shift of $\sim 25\ \mathrm{m\,s^{-1}}$ for 2009 and 2013 and $\sim 60\ \mathrm{m\,s^{-1}}$ for 2014. The shifts translate into systematic uncertainties on $\Delta\mu/\mu$ of 1.2×10^{-6} and 3.2×10^{-6} respectively. The average value of $\delta(\Delta\mu/\mu) = 2.2\times10^{-6}$ is taken as the systematic uncertainty on the μ-variation due to the intra-order distortions. However, this estimation does not take into account various factors like the different sensitivity of the transitions, where they fall with respect to the order centre and the variation of the S/N across the H_2 window. As a consequence, this value should be considered as an upper limit [41].

Long-range and intra-order distortions are not the only contributors to the systematic error budget. In addition, other effects, like the spectral redispersion, the presence of exposures without any ThAr attached calibration and the calibration residuals, contribute to the total systematic error budget. Previous studies addressed these possible error sources, finding that the absence of attached ThAr calibrations introduces an error of $\sim 0.7\times10^{-6}$ [86], the calibration residuals have an effect of, at most, $\sim 2.0\times10^{-6}$ [86, 118], and the spectral redispersion can contribute up to $\sim 1.4\times10^{-6}$ for a pixel size of $\sim 2.5\ \mathrm{km\,s^{-1}}$ [84]. Adding in quadrature all these contributions to the systematic error budget yields a systematic error on the fiducial value of $\Delta\mu/\mu$ of $\sim 4.0\times10^{-6}$.

3.5.3. CONSTRAINING $\Delta\mu/\mu$ FROM THE DISTORTION-CORRECTED SPECTRUM

After having distortion-corrected the exposures taken in 2013 and 2014, an updated value of $\Delta\mu/\mu|_{2014} = (1.2 \pm 11.8_{\mathrm{stat}})\times10^{-6}$ was derived from the sub-spectrum formed from those exposures only. This value, which agrees within 1σ with the constraint derived only from exposures from 2009, is represented as a square in Fig. 3.6.

The 'final spectrum', obtained combining the distortion corrected exposures to-

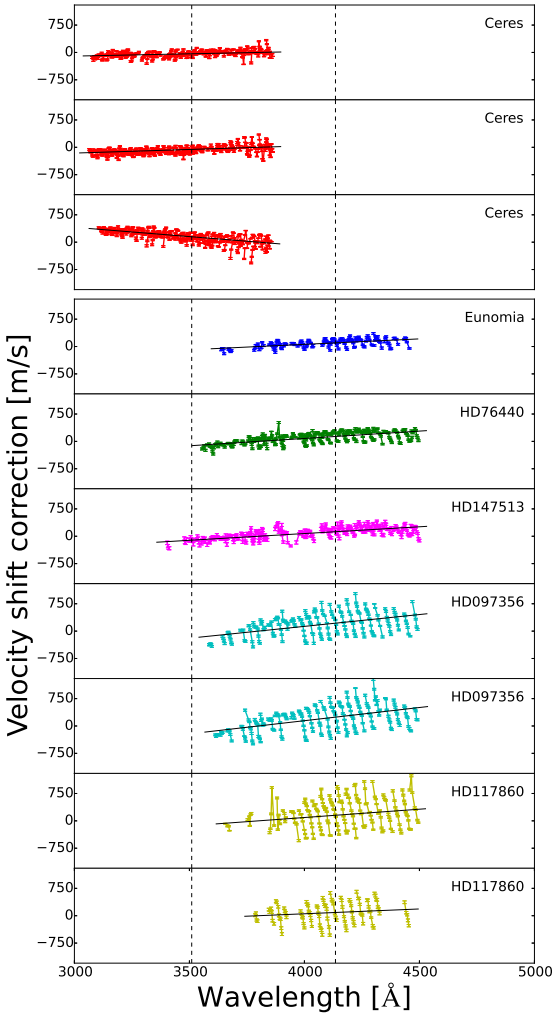

FIGURE 3.7: Distortion maps of the UVES wavelength scale derived from asteroid and solar twin targets used for the supercalibration of science exposures of J1237+0647. For each supercalibration exposure, the plot shows the velocity shift required to align the ThAr-calibrated wavelength scale with that derived from the FTS solar spectrum. One observes both intra-order and long-range distortions of the wavelength scale. Only the slopes of the latter, whose values are listed in Table 3.4 with a one-to-one correspondence, are the physically relevant parameters used in the distortion analysis. They were determined by least-squares fits to the mean velocity shift correction from each echelle order as a function of wavelength, as in Whitmore and Murphy [72]. The two dashed vertical lines show the window in which the H_2 absorption lines toward J1237+0647 fall. The radial velocities are unimportant for the analysis of the slopes and have been removed here; the distortion maps have all been shifted to zero velocity shift at 3800 Å. Top panel: three supercalibrations extracted from Ceres exposures taken in 2009 and retrieved from the ESO archive. Lower panel: seven supercalibrations extracted from asteroid and solar twin observations performed in 2013 and 2014. Eunomia, HD76440 and HD147513 were observed in visitor mode in May 2013 while the solar twins HD097356 and HD117860 were observed in service mode in 2014.

TABLE 3.4: Observations with VLT/UVES of the supercalibration targets used in this work. Data from program 080.C-0881(B) were retrieved from the ESO archive and have only the regular ThAr calibration taken at the end of the night. The slit width was 1.0 arcsec for all exposures. The uncertainty on the slopes is ~ 30 m s^{-1} per 1000 Å.

Target	Program ID	Date	Grating [nm]	Distortion slope [m s^{-1} per 1000 Å]
Ceres	080.C-0881(B)	23-03-2009	346	120
		01-04-2009	346	200
		01-04-2009	346	−510
Eunomia	091.A-0124(A)	15-05-2013	390+580	300
HD76440		15-05-2013	390+580	400
HD147513		16-05-2013	390+580	370
HD097356	093.A-0373(A)	23-03-2014	390+580	650
		03-04-2014	390+580	720
HD117860		28-05-2014	390+580	460
		31-05-2014	390+580	260

gether with the uncorrected exposures from 2009, delivers a fiducial constraint on the proton-to-electron mass ratio of $\Delta\mu/\mu = (-5.4 \pm 6.3_{\rm stat} \pm 4.0_{\rm syst}) \times 10^{-6}$, which is the final result of the present study.

3.6. CONCLUSION

In this work, the analysis of molecular hydrogen absorption in the system at redshift $z = 2.69$, in the line of sight toward quasar J1237+0647, is presented in order to constrain a possible variation of the proton-to-electron mass ratio μ. 137 H_2 and HD transitions, found in three distinct velocity features associated with the DLA, some even exhibiting further velocity fine-structure, were analyzed. The large number of absorption features considered in the dataset includes partially overlapped features, due to the complex velocity structure of the system, as well as strongly saturated lines. This was possible because of the comprehensive fitting method used in this analysis. Intra-order and long-range distortions, which are known to affect the UVES spectra, were taken into account by applying the supercalibration technique presented by Whitmore and Murphy [72] to the exposures taken in 2013 and 2014. For exposures taken in 2009, and retrieved from the ESO archive, the impact of such distortions was estimated using asteroid observations taken within one week of the quasar ones, and it was translated into a contribution to the systematic error budget. The resulting value of a constraint on a varying proton-to-electron mass ratio is $\Delta\mu/\mu = (-5.4 \pm 6.3_{\rm stat} \pm 4.0_{\rm syst}) \times 10^{-6}$.

This constraint can be improved using the upcoming new generation of high resolution spectrographs, like the Echelle SPectrograph for Rocky Exoplanet and Sta-

ble Spectroscopic Observations [ESPRESSO, 108]. The spectral resolution achieved in this work allows to resolve components with Doppler broadening parameters $b \sim 2.5$ km s^{-1}, while the high resolution of the new instruments, roughly three times higher than used here, will allow to resolve components with Doppler broadening parameters of the order of ~ 1.0 km s^{-1}. This may help further resolve finer structure within individual spectral features and hence result in a more precise $\Delta\mu/\mu$ constraint from J1237+0647. Moreover, the new instrument with fiber-fed and frequency-comb support should not suffer from the long-range wavelength distortions that are affecting UVES, and should lead to smaller systematic uncertainties in μ-variation analyses.

In Fig. 3.8 the result of the present work is compared with other constraints, taken from literature, on a varying μ obtained from previous investigations on other H_2 absorbers at medium-to-high redshifts. The weighted mean, obtained considering, where possible, both the statistical and the systematic errors, resulting from this larger set is $\Delta\mu/\mu = (2.9 \pm 1.7) \times 10^{-6}$. This is consistent with no variation of μ over a cosmological time-scale at a level of $\sim 10^{-5}$ for a look-back time of ~10.5–12.5 Gyrs.

ACKNOWLEDGMENTS

The authors thank the Netherlands Foundation for Fundamental Research of Matter (FOM) for financial support. MTM thanks the Australian Research Council for *Discovery Project* grant DP110100866 which supported this work. The work is based on observations with the ESO Very Large Telescope at Paranal (Chile).

APPENDIX

Figures 3.9-3.15 show the H_2 window in the spectrum of the absorbing system at $z \approx 2.69$ toward quasar J1237+0647 along with the absorption model.

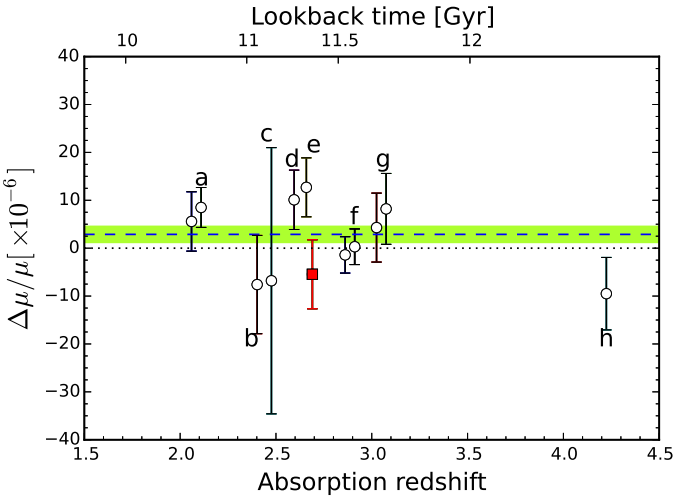

FIGURE 3.8: Overview of results from investigations on a varying proton-to-electron mass ratio using molecular hydrogen absorbing systems. The result on J1237+0647 presented in this work is indicated with a (red) square. The circles show results from previous analyses on systems: a) J2123–0050 [41, 104], b) HE0027–1836 [98], c) Q2348–011 [85], d) Q0405–443 [83], e) B0642–5038 [86], f) Q0528–250 [83, 84], g) Q0347–383 [83, 106] and h) Q1443+272 [40]. Note that multiple values for the constraint on $\Delta\mu/\mu$ were derived from systems J2123–0050 (labelled as 'a'), Q0528–250 (labelled as 'f') and Q0347–383 (labelled as 'g'). To avoid overlaps between observations of the same system, their points are presented with an offset of +0.05 on the z-scale. The dotted line represents the zero level, while the dashed line shows the weighted mean of all the $\Delta\mu/\mu$ values and the shaded area shows its 1σ boundaries.

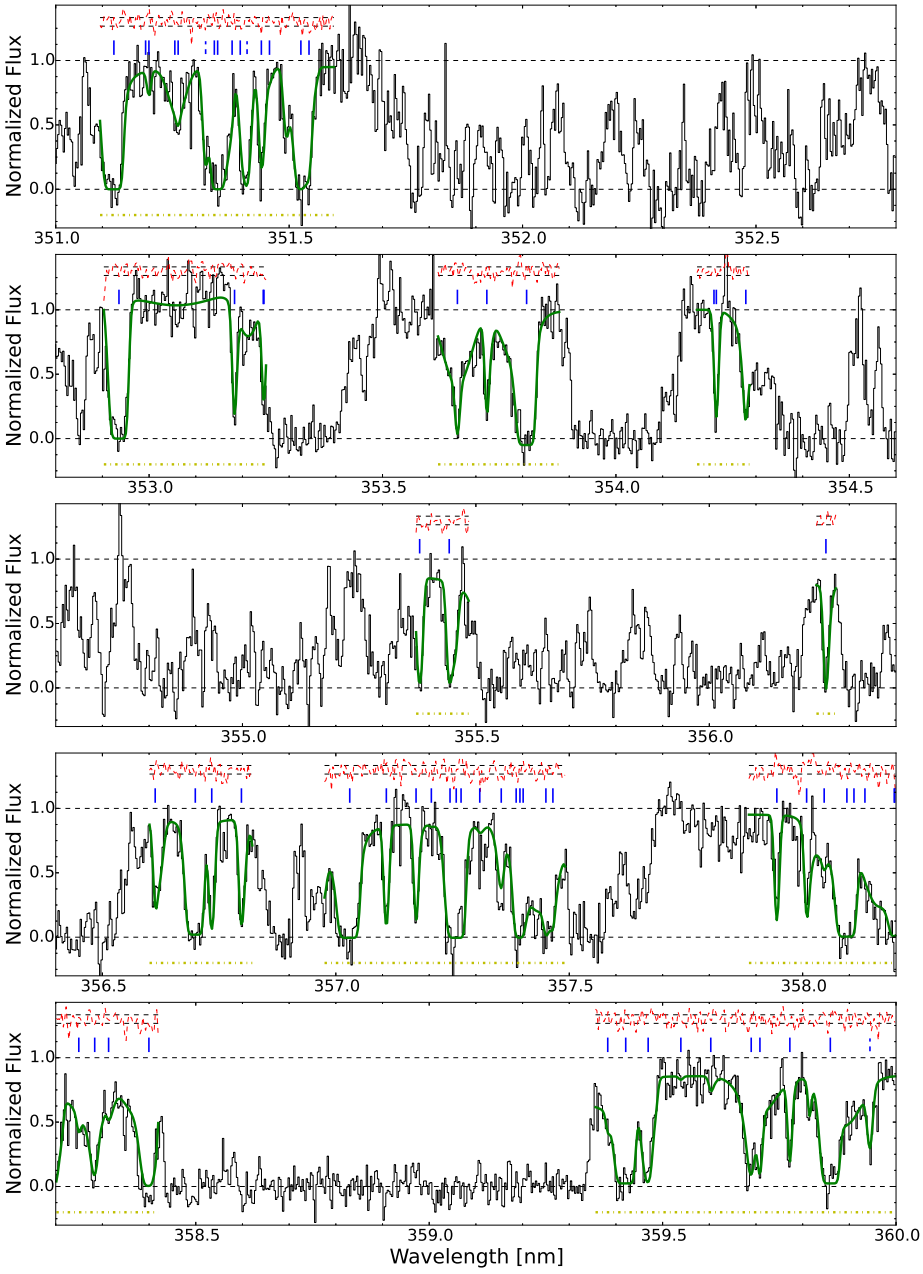

FIGURE 3.9: Spectrum of quasar J1237+0647 (part 1 of 7). Regions containing the H_2 transitions used in this analysis are indicated by a green line of the fitted model. H_2 transitions are marked with a vertical solid line, HD transitions are marked with a dashed line and metal transitions are marked with a dotted line.

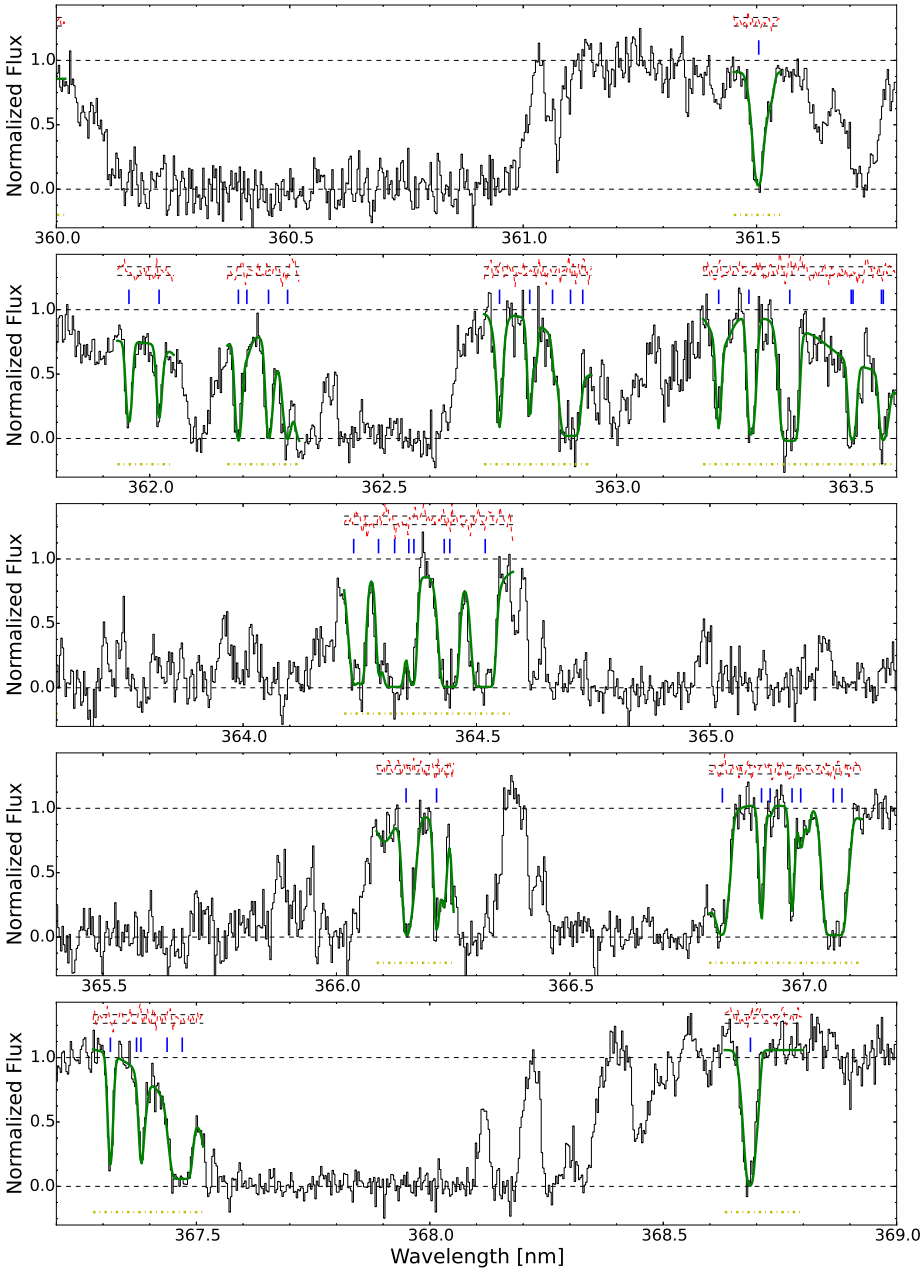

FIGURE 3.10: Spectrum of quasar J1237+0647 (part 2 of 7), continued.

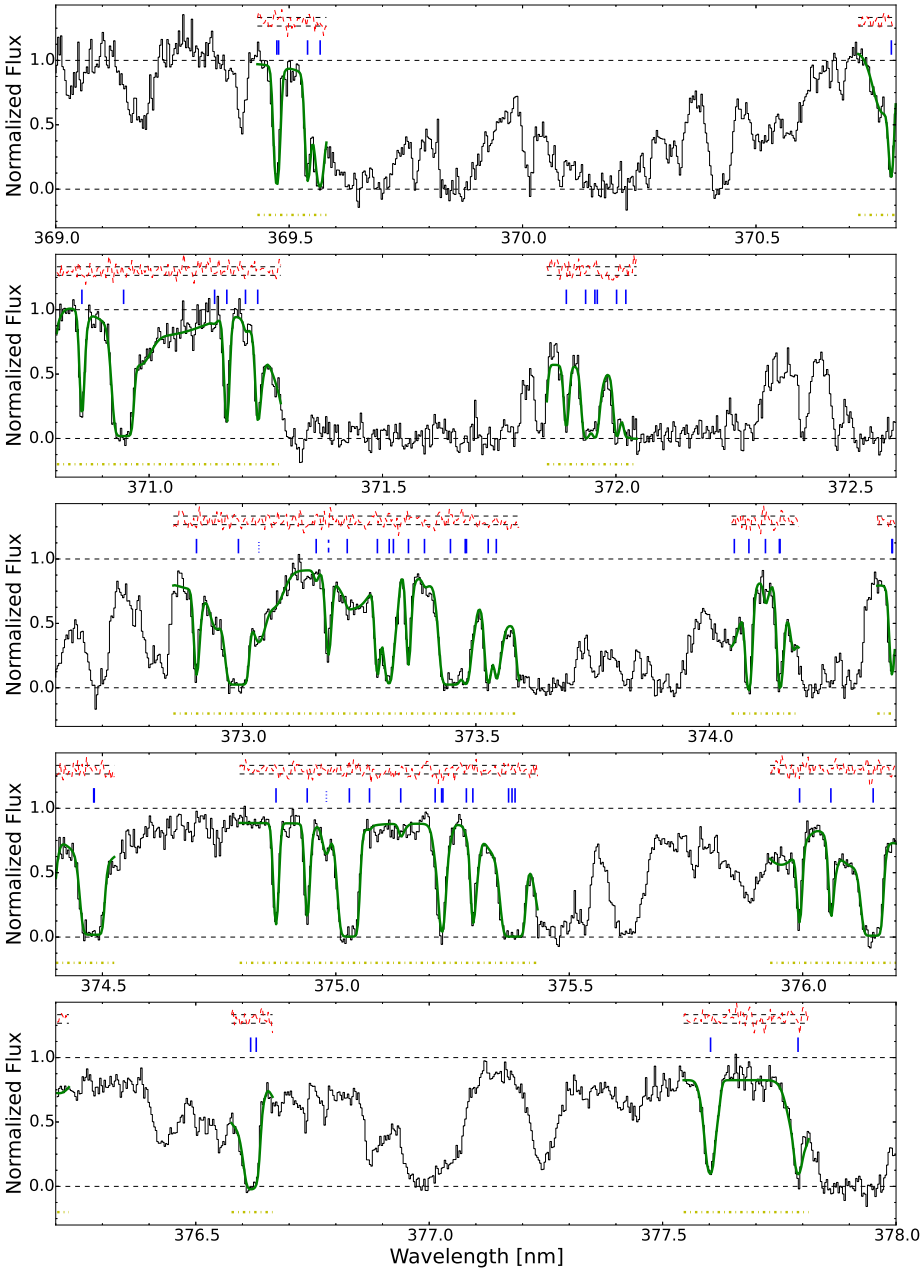

FIGURE 3.11: Spectrum of quasar J1237+0647 (part 3 of 7), continued.

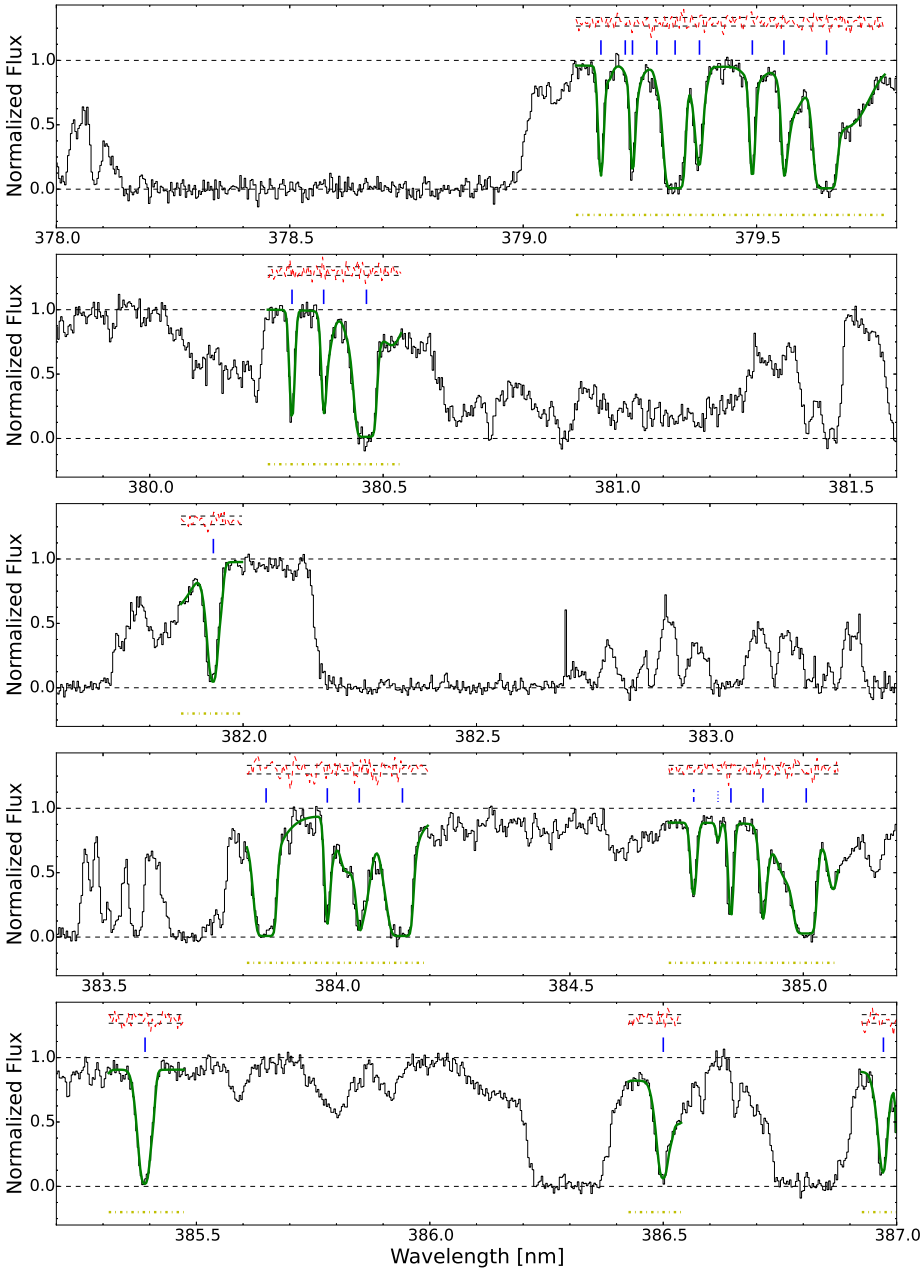

FIGURE 3.12: Spectrum of quasar J1237+0647 (part 4 of 7), continued.

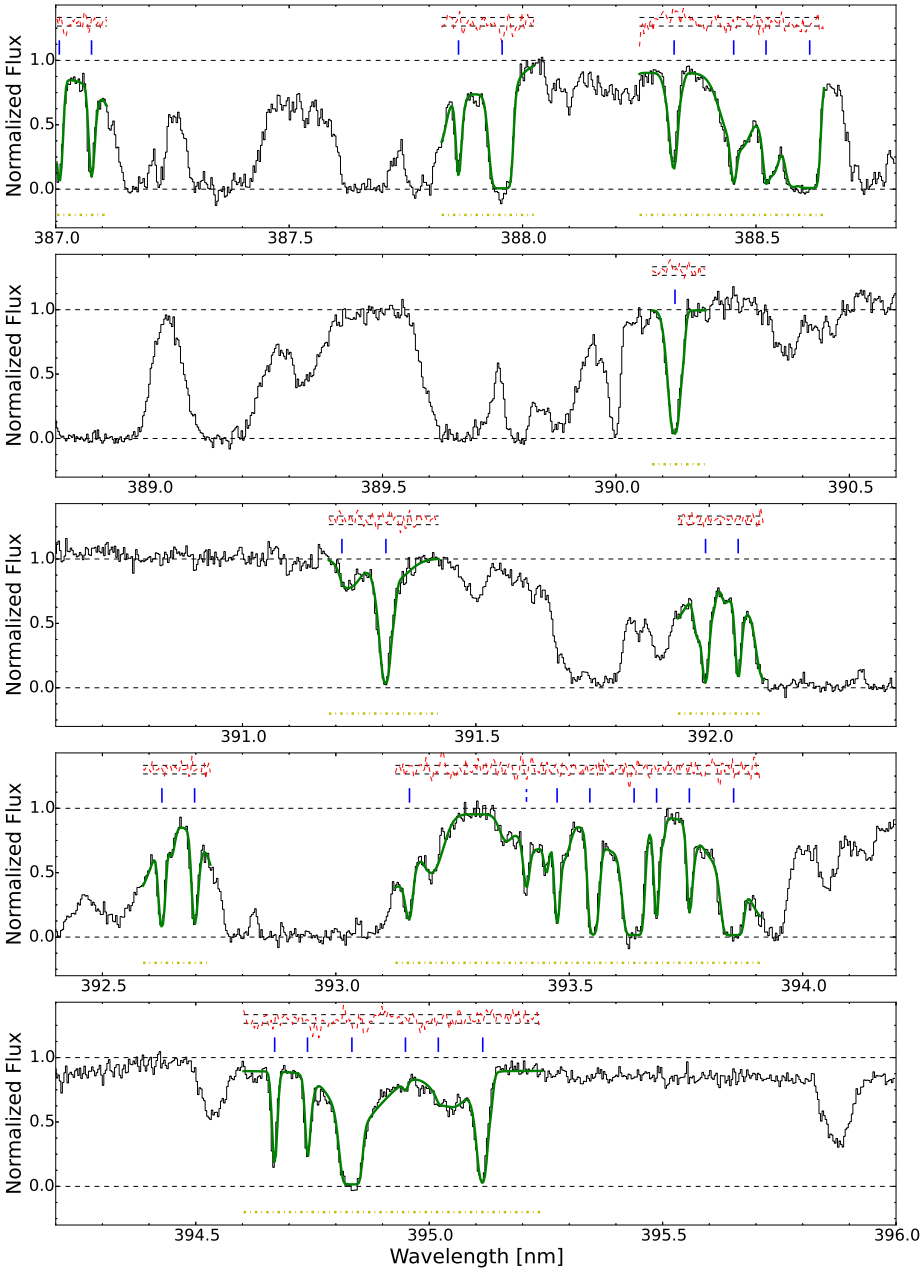

FIGURE 3.13: Spectrum of quasar J1237+0647 (part 5 of 7), continued.

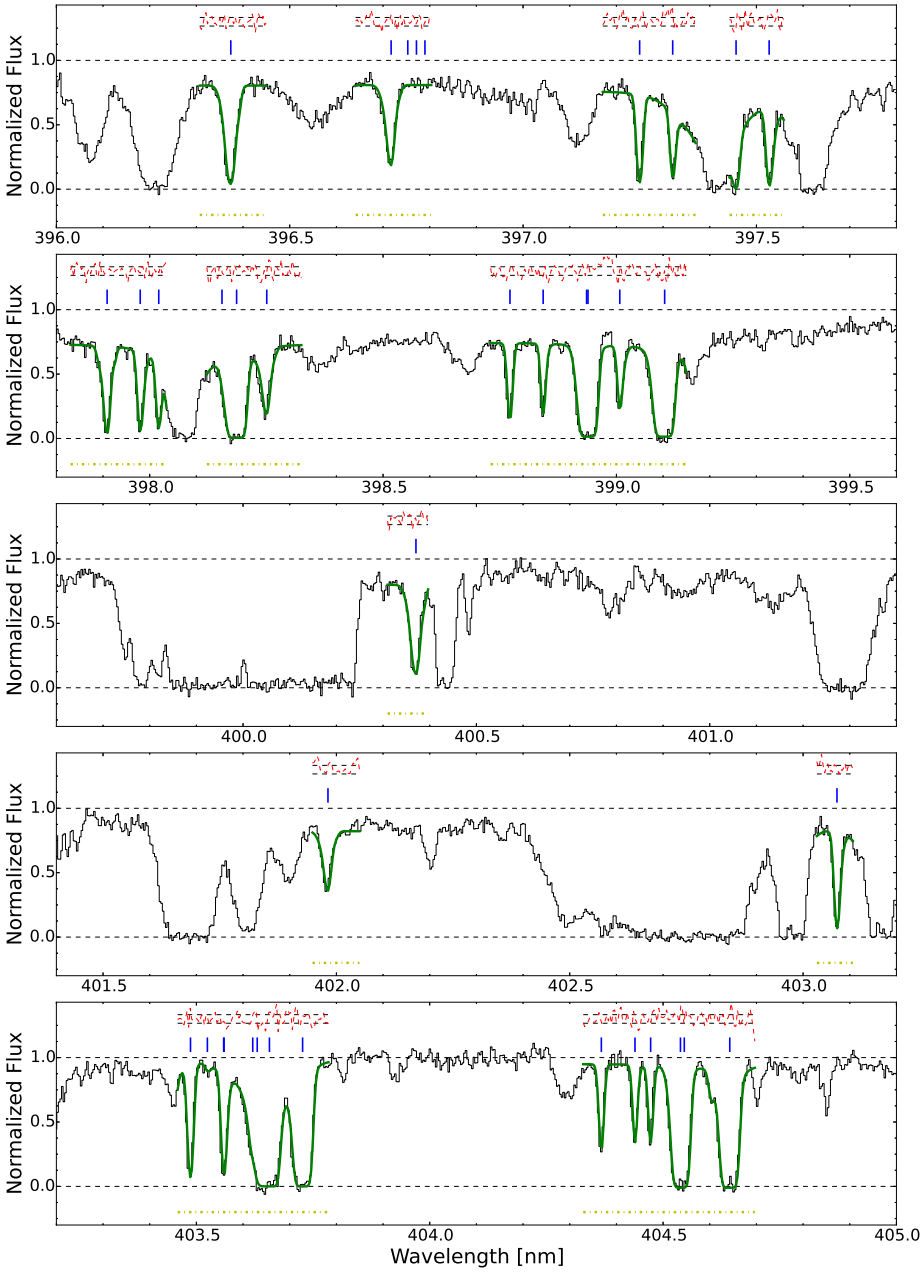

FIGURE 3.14: Spectrum of quasar J1237+0647 (part 6 of 7), continued.

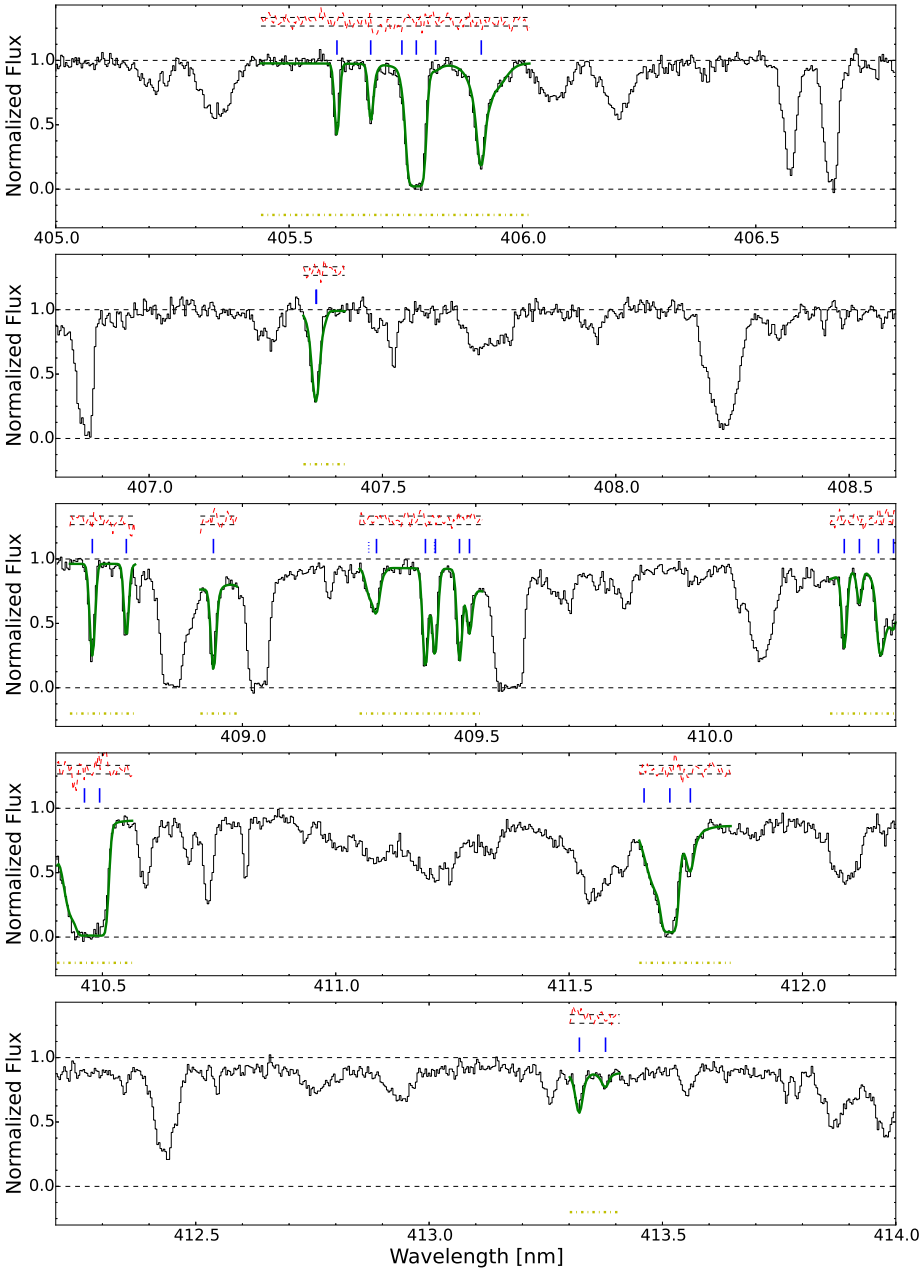

FIGURE 3.15: Spectrum of quasar J1237+0647 (part 7 of 7), continued.

4

CONSTRAINT ON A COSMOLOGICAL VARIATION IN THE PROTON-TO-ELECTRON MASS RATIO FROM ELECTRONIC CO ABSORPTION

Daprà, M., Niu, M. L., Salumbides, E. J., Murphy, M. T. & Ubachs, W.
Astrophys. J. ***826****, 192-210 (2016)*

Carbon monoxide (CO) absorption in the sub-damped Lyman-α absorber at redshift $z_{abs} \simeq 2.69$*, toward the background quasar SDSS J123714.60+064759.5 (J1237+0647), was investigated for the first time in order to search for a possible variation of the proton-to-electron mass ratio,* μ*, over a cosmological time-scale. The observations were performed with the Very Large Telescope/Ultraviolet and Visual Echelle Spectrograph with a signal-to-noise ratio of 40 per 2.5 km* s^{-1} *per pixel at* ~ 5000 *Å. Thirteen CO vibrational bands in this absorber are detected: the* $A^1\Pi$ - $X^1\Sigma^+$ *(*v'*,0) for* $v' = 0-8$*,* $B^1\Sigma^+$ - $X^1\Sigma^+$ *(0,0),* $C^1\Sigma^+$ - $X^1\Sigma^+$ *(0,0), and* $E^1\Pi$ - $X^1\Sigma^+$ *(0,0) singlet-singlet bands and the* $d^3\Delta$ - $X^1\Sigma^+$ *(5,0) singlet-triplet band. An updated database including the most precise molecular inputs needed for a* μ*-variation analysis is presented for rotational levels* $J = 0-5$*, consisting of transition wavelengths, oscillator strengths, natural lifetime damping parameters, and sensitivity coefficients to a variation of the proton-to-electron mass ratio. A comprehensive fitting method was used to fit all the CO bands at once and an independent constraint of* $\Delta\mu/\mu = (0.7 \pm 1.6_{stat} \pm 0.5_{syst}) \times 10^{-5}$ *was derived from CO only. A combined analysis using both molecular hydrogen and CO in the same J1237+0647 absorber returned a final constraint on the relative variation of* $\Delta\mu/\mu = (-5.6 \pm 5.6_{stat} \pm 3.1_{syst}) \times 10^{-6}$*, which is consistent with no variation over a look-back time of* ~ 11.4 *Gyrs.*

4.1. INTRODUCTION

The Standard Model of particle physics depends on a number of parameters that cannot be explained from the model itself. These parameters, including for example the fine-structure constant $\alpha = e^2/(4\pi\epsilon_0\hbar c)$, and the proton-to-electron mass ratio $\mu \equiv M_P/m_e$, are referred to as fundamental constants and are assumed to be space-time invariant. Whether they are really constant or whether they undergo variations over time is a question that became subject of observation when Savedoff [119] established the alkali-doublet method to compare galaxy values of physical constants with local values. Subsequently, Thompson [28] suggested that a cosmological variation of μ could be probed using molecular hydrogen (H_2) absorption in quasar spectra. A number of theories predicting a variation of constants have been proposed [an extensive review has been given by 3], often associated with forces beyond the four known in the Standard Model or with extra dimensions beyond the 3+1 presently assumed. It is noted that a variation of the fundamental constants implies a violation of Einstein's equivalence principle, which is a basic assumption of General Relativity.

A sensitive search for a cosmological variation of dimensionless fundamental constants α and μ is possible via the measurement of atomic and molecular absorption lines detected at high redshifts in the line-of-sight towards quasars, using high resolution spectroscopic observations in the optical and in the radio domain. The fine-structure constant α was investigated by recording spectroscopic lines of atoms [120], looking for variations in the temporal [109] and spatial domains [110]. The cosmological variation of proton-to-electron mass ratio μ, which is sensitive to the ratio of the chromodynamic to the electroweak scale [8], can be probed using molecular absorption [57, 58, 75]. Various searches for μ-variation via observation of ammonia [NH_3, 54, 56, 121] and methanol [CH_3OH, 62–64] spectral lines at intermediate redshifts $z < 1$, yielded a constraint on $\Delta\mu/\mu$ on the order of $\sim 10^{-7}$ at the 1σ level.

Molecular hydrogen, the most abundant molecule in the Universe, is used to investigate μ-variation in absorbing systems at redshifts $z_{\rm abs} > 2$, for which the Lyman and Werner bands fall into the optical band. The analysis of H_2 absorption was performed in nine systems detected in the range $z = 2.05 - 4.22$ [35, 40, 41, 46, 83–86, 98, 104–106, 111, 112], delivering an averaged constraint (at the 3σ level) of $|\Delta\mu/\mu|$ of $< 5 \times 10^{-6}$ [73]. The analysis procedure used in the H_2 method relies on the calculation of sensitivity coefficients for the hydrogen molecule, i.e. how much each transition shifts in wavelength for a given change in μ [29, 36]. In addition, some molecules exhibit sensitivities to both fundamental constants α and μ. Tzanavaris *et al.* [122] combined H I 21-cm lines with UV metal absorption lines to estimate the time variation of the combination $\alpha^2 g_p \mu$, with g_p the dimensionless proton g-factor. Kanekar *et al.* [123] observed OH microwave lines and searched for a combined variation of both constants α and μ.

Carbon monoxide (CO) is the second most abundant molecule in the Universe and it is one of the best studied molecules in spectroscopy. Being sensi-

tive to μ-variation, Salumbides *et al.* [50] proposed to use its electronic $A^1\Pi$ - $X^1\Sigma^+$ system as a suitable target to constrain a cosmological variation of μ. So far, optical absorption bands of CO are detected in six absorption systems at redshifts $z_{\rm abs} > 1$: SDSS J160457.50+220300.5 [49], SDSS J085726+185524, SDSS J104705.75+205734.5, SDSS J170542+354340 [44], SDSS J143912.04+111740.5 [47, 48], and SDSS J123714.60+064759.5 [45]. The absorbing system at $z_{\rm abs} \simeq 2.69$ towards quasar SDSS J123714.60+064759.5, hereafter J1237+0647, is an exemplary absorbing system that contains high quality spectra of both H_2 and CO, providing a case for a combined analysis of μ-variation using the two molecules.

In the present study, the electronic CO absorption in this absorber is investigated in order to obtain a constraint on a temporal μ-variation over cosmological timescales. The molecular database containing the parameters used to build the absorption model of CO is presented in Section 4.2, while the observations used in this work are described in Section 4.3. The model, as well as the comparison with a previous constraint derived from the analysis of H_2 absorption in the same system [46] is presented in Section 4.4, and the analysis of the systematic uncertainty is given in Section **??**. The results are summarised in Section 4.7.

4.2. CO MOLECULAR DATA

In this section the existing molecular data of the electronic absorption systems of carbon monoxide relevant for quasar absorption studies are reviewed and collected. An extensive data compilation of the CO electronic transitions had been published by Morton and Noreau [124] some two decades ago, but in the mean time improved spectroscopic data have been produced, in particular through the accurate wavelength calibrations by laser-based methods and VUV synchrotron absorption studies [50, 125–127]. Based on these studies, an updated perturbation analysis was performed for excited states of singlet and triplet character. These perturbations also cause an intensity borrowing phenomenon and affect the rotational line strengths. For this reason also some aspects of rotational line strengths, as discussed by Larsson [128] and Morton and Noreau [124], are re-evaluated for the calculation of line strengths of perturbed lines.

Noterdaeme *et al.* [45] reported CO absorption from ten bands in the absorbing system towards J1237+0647. The detected bands belong to three different systems: the $A^1\Pi$ - $X^1\Sigma^+$ (v',0) for $v' = 0-7$, $C^1\Sigma^+$ - $X^1\Sigma^+$ (0,0), and $d^3\Delta$ - $X^1\Sigma^+$ (5,0) bands. In the present re-analysis of J1237+0647 data, additional absorption features associated with the $A^1\Pi$ - $X^1\Sigma^+$ (8,0), $B^1\Sigma^+$ - $X^1\Sigma^+$ (0,0), and $E^1\Pi$ - $X^1\Sigma^+$ (0,0) bands are identified as well. The review of molecular data focuses primarily on all these detected band systems.

Spectroscopic information is collected for transitions restricted to the lowest rotational quantum states $J = 0-5$, which are typically populated in the cold environments investigated in quasar absorption studies [$T \sim 10$ K at $z \sim 2.5$; 45, 48]. The

CO rotational transitions in the band systems mentioned are described using four molecular parameters: the rest wavelength λ_i, the rotational line oscillator strength $f^i_{J'J''}$, the natural damping constant γ_i, and the sensitivity coefficient K_i to a variation of the proton-to-electron mass ratio. These parameters, specific for each transition, are derived directly from laboratory measurements or via calculational methods. In the following section, methods to derive these molecular parameters are first outlined, and then the values for each electronic band system of CO are presented in subsequent subsections. Molecular parameters relative to the detected bands, including the undetected A-X(9 – 0) band (see Section 4.4.2), are listed in order to provide a complete database for future uses in studies of quasar spectra. To avoid any ambiguity, in the following sections the adopted notation and relationships are presented explicitly.

4.2.1. OSCILLATOR STRENGTHS

In SI units, the absorption oscillator strength of a single rotational transition in a vibronic molecular band is defined as:

$$f_{J'J''} = 4\pi\epsilon_0 \frac{m_e c}{\pi e^2} \frac{B^{abs}_{J'J''}}{4\pi} \frac{hc}{\lambda_{J'J''}}, \tag{4.1}$$

where $\lambda_{J'J''}$ is the transition wavelength, J' refers to the upper level of the transition, J'' to the lower level, and the other constants have their traditional meaning. $B^{abs}_{J'J''}$ is the Einstein absorption coefficient defined as:

$$B^{abs}_{J'J''} = \frac{\lambda^3_{J'J''} A_{J'J''} (2J'+1)}{2hc(2J''+1)}, \tag{4.2}$$

which is connected to the $A_{J'J''}$ Einstein coefficient for spontaneous emission:

$$A_{J'J''} = \frac{1}{4\pi\epsilon_0} \frac{64\pi^4}{3h} \frac{1}{\lambda^3_{J'J''}} \frac{S_{J'J''}}{(2J'+1)}. \tag{4.3}$$

$S_{J'J''}$ is a line strength factor connected to the squared transition dipole matrix element:

$$S_{J'J''} \equiv \sum_{M'} \sum_{M''} |\langle \psi_{J',M'} | \overline{\mu} | \psi_{J'',M''} \rangle|^2 \tag{4.4}$$

summed over all magnetic substates M of each J level, and the operator $\overline{\mu}$ is the electronic transition dipole moment. Using Eq. (4.2) and Eq. (4.3), the line oscillator strength can be rewritten as:

$$f_{J'J''} = \frac{8\pi^2 m_e c}{3he^2} \frac{S_{J'J''}}{\lambda_{J'J''}(2J''+1)}. \tag{4.5}$$

In the Born-Oppenheimer approximation, the wavefunction of the molecule can be rewritten in terms of a product of its electronic and nuclear, i.e. vibrational and rotational, components resulting in the relation:

$$S_{J'J''} = q_{v'v''}|R_e(r_{v'v''})|^2 s_{J'J''}, \tag{4.6}$$

in which $q_{v'v''} = |\langle\psi_{v'}|\psi_{v''}\rangle|^2$ is the Franck-Condon factor, $R_e(r_{v'v''})$ is the electric dipole moment function, $r_{v'v''}$ is the vibrationally averaged internuclear distance, and $s_{J'J''}$ is the Hönl-London factor for spin-allowed transitions. Inserting Eq. (4.6) in Eq. (4.5) gives the final expression for the oscillator strength of a rotational line in a rovibronic molecular band:

$$f_{J'J''} = \frac{8\pi^2 m_e c}{3he^2} q_{v'v''}|R_e(r_{v'v''})|^2 \frac{s_{J'J''}}{\lambda_{J'J''}(2J''+1)}. \tag{4.7}$$

In experimental spectroscopy, it is not always possible to separately resolve individual rotational transitions for each J ground state level. Often an entire set of transitions associated with vibrational levels v' and v'', hereafter referred to as a vibrational band, is addressed. It is possible to define an oscillator strength for a vibrational band, in analogy to Eq. (4.7):

$$f_{v'v''} = \frac{8\pi^2 m_e c}{3he^2} q_{v'v''}|R_e(r_{v'v''})|^2 \frac{1}{\lambda_{v'v''}} \delta_{\Sigma,\Pi}, \tag{4.8}$$

where $\lambda_{v'v''}$ is the wavelength of the band origin, and $\delta_{\Sigma,\Pi} = \{1,2\}$ for Σ and Π excited states respectively. This band oscillator strength is equivalent to a sum over all single line oscillator strengths $f_{J'J''}$. Hence there is a relation between the band oscillator strength and the line oscillator strength:

$$f_{J'J''} = f_{v'v''} \frac{\lambda_{v'v''}}{\lambda_{J'J''}} \frac{s_{J'J''}}{(2J+1)} \frac{1}{\delta_{\Sigma,\Pi}}. \tag{4.9}$$

Note that the ratio between the wavelengths of the vibrational band origin $\lambda_{v'v''}$ and the individual rotational lines $\lambda_{J'J''}$ is $\simeq 1$, because the spread in the wavelengths of each vibrational band is limited and the band origin wavelength can be considered as the average wavelength of the band.

The above analysis and Eq. (4.9) is valid if no perturbations occur in the electronic structure. In case of a perturbation, a transition to a perturber state, which could be forbidden, 'borrows' intensity from an allowed electronic transition. Hence the effective band oscillator strength will be divided between the allowed and forbidden transitions. The actual wavefunction Ψ_i is mixture of the zero-order wavefunctions Ψ_i^0's, the latter describing the system in the absence of the non-diagonal terms in the interaction Hamiltonian. Ψ_i can be expressed as a linear superposition

$$\Psi_i = \alpha_i \Psi_i^0 + \sum_j \alpha_j \Psi_j^0, \tag{4.10}$$

where α are the mixing coefficients obtained in a deperturbation analysis [e.g. 125], that are normalized at $|\alpha_i|^2 + \sum |\alpha_j|^2 = 1$. Note that the i-th state is normally assigned to the state with the greatest α, i.e. the dominant electronic wavefunction character, and that the summation holds for the case where multiple perturbing states are involved. As will be discussed below for d-X transitions, dipole-forbidden transitions can be observed if an interaction exists with levels that have dipole-allowed transitions, e.g. the A($v = 1$) and d($v = 5$) levels. In this case, the oscillator strengths $f_{\rm d5}$ can be expressed as:

$$f_{\rm d5} = f^0_{\rm A1} |\alpha_{\rm d5}|^2, \tag{4.11}$$

in terms of the dipole-allowed deperturbed oscillator strengths $f^0_{\rm A1}$ of the A-X transitions, for levels with d(v=5) character given by the mixing coefficient $|\alpha_{\rm d5}|^2$. This is a general effect that occurs in the presence of perturbations, where the *intensity borrowing* phenomenon transfers a fraction of the allowed transition oscillator strength to those of forbidden lines.

4.2.2. DAMPING CONSTANTS

The natural damping parameter $\gamma_{v'}$ can directly be obtained from experiments through measurement of the excited lifetime $\tau_{v'}$ which, in absence of collisions, predissociation and autoionization, can be expressed in terms of the sum of the Einstein coefficients for spontaneous emission to all the ground state vibrational and rotational levels:

$$\gamma_{v'J'} = \frac{1}{\tau_{v'J'}} = \sum_{v'',J''} A_{v'J'v''J''}, \tag{4.12}$$

which, considering the Born-Oppenheimer approximation and substituting Eq. (4.3) and Eq. (4.6), becomes:

$$\gamma_{v'J'} = \frac{1}{4\pi\epsilon_0} \frac{64\pi^2}{3h} \delta_{\Sigma,\Pi} \sum_{v'',J''} \frac{1}{\lambda^3_{J'J''}} q_{v'v''} |R_e(r_{v'v''})|^2 \frac{s_{J'J''}}{(2J'+1)}. \tag{4.13}$$

In case of perturbations, the lifetime is no longer a constant across the J levels because of the local interactions between the short-lived perturbed state and the usually long-lived perturbing states. In this case, the damping parameter is given by:

$$\gamma_{v'J',i} = |\alpha_i|^2 \gamma^0_{v'J',i} + \sum_j |\alpha_j|^2 \gamma^0_{v'J',j}, \tag{4.14}$$

in which α_i and α_j are the mixing coefficients as in Eq. (4.10), while $\gamma^0_{v'J',i}$ and $\gamma^0_{v'J',j}$ are the damping parameters of each pure state. Note that the state with the largest $|\alpha|^2$ is indicated with the subscript i and it is referred to as the 'perturbed state', while the other j states are referred to as the 'perturbing states'.

In cases where the decay is not purely radiative, but includes rates associated with predissociation, the damping rates are associated with the natural lifetimes according to:

$$\gamma_{v'J'} = \frac{1}{\tau_{v'J'}} = A^{rad}_{v'J'} + A^{pred}_{v'J'}. \tag{4.15}$$

4.2.3. SENSITIVITY COEFFICIENTS

One ingredient in a search for a varying proton-to-electron mass ratio based on spectral lines in molecules is an assessment of the sensitivity coefficients K_i, which are defined as [36]:

$$K_i = \frac{\mathrm{d}\ln\lambda_i}{\mathrm{d}\ln\mu}. \tag{4.16}$$

Salumbides *et al.* [50] calculated the sensitivity coefficients for the CO A-X bands up to $v' = 10$, starting from a Dunham expansion of the rovibrational level energies. The calculation of the sensitivity coefficients exploits the known mass-dependence of the Dunham parameters, which are obtained in the semi-empirical modelling of the rovibrational level energies. While this procedure is straightforward for unperturbed states, the presence of local interactions introduces a difficulty, since a state is in fact a mixture of two or more states, which in general have energies with different mass-dependencies. To account for the effects of local interactions, μ-sensitivity coefficients K^0 are first calculated in the *idealized* case when the interaction between bands is zero, i.e. using the diagonal terms in the interaction matrix obtained in a deperturbation analysis. Subsequently, the *true* K-coefficients that include the effect of perturbations are recovered, to first-order, by adopting the wavefunction admixture coefficients as weights in a relation similar to that of Eq. (4.10):

$$K_i = |\alpha_i|^2 K^0_i + \sum_j |\alpha_j|^2 K^0_j, \tag{4.17}$$

where α and K^0 values are obtained using results from the deperturbation analysis.

4.2.4. THE A-X SYSTEM

The excited electronic structure of the CO molecule is a textbook example of perturbations involving a large number of states of singlet and triplet character. Many of the details of these perturbations had been unravelled by Field *et al.* [129] and Le Floch *et al.* [130]. For the case of quasar absorption analysis of CO in particular the perturbation between the A-X$(1-0)$ and d-X$(5-0)$ vibrational bands is of relevance, because the interaction is strongest at the low J levels that are populated in cold clouds. This specific case has been re-analyzed by Niu *et al.* [125].

Accurate rest wavelengths are compiled from Salumbides *et al.* [50] and Niu *et al.* [125, 126], who measured CO transitions in five bands, detecting ~ 200 lines per each

band up to the rotational level with $J = 50$. These laboratory wavelengths were determined using two independent studies: a vacuum ultraviolet Fourier-transform (VUV-FT) and a two-photon Doppler-free laser-based excitation experiment. Starting from these measurements, Niu *et al.* [125] developed a semi-empirical model, including all the perturbing states relative to the five observed A-X($v' - 0$) bands for $v' = 0 - 4$. These studies delivered CO transitions wavelengths, including A-X($v' - 0$) bands for $v' = 5 - 9$, with an accuracy better than $\Delta\lambda/\lambda = 3 \times 10^{-7}$ and can be considered exact for comparisons with the observed CO bands in quasar spectra. Laboratory wavelengths for the A-X system for $J = 0 - 5$ ground state levels are listed in Table 4.1.

Band oscillator strength $f_{J'J''}$ values for the A-X system were measured using a variety of different techniques. Eidelsberg *et al.* [131] used optical absorption, while Chan *et al.* [132] and Zhong *et al.* [133] determined the band oscillator strengths using electron scattering. An additional set of $f_{v'v''}$ values was calculated via Eq. (4.8), using the Franck-Condon factors reported by Eidelsberg *et al.* [131], while the dipole moment was calculated starting from the lifetime measurements of Field *et al.* [134]. The linear dipole-moment function $R_e(r_{v'v''}) = 7.48(34)[1 - 0.683(7)r_{v'v''}]$ [the dipole moment is in Debyes and $r_{v'v''}$ is in Å, 134] was adopted, rather than the extended parabolic one presented by DeLeon [135], because the latter does not represent well the low v levels considered in this work. This results in four sets of band oscillator strength values, with an accuracy of ~ 10% or better, which agree with each other within their combined error. While Morton and Noreau [124] relied entirely on values derived by Chan *et al.* [132], presently the four sets are averaged together to obtain a value for the band oscillator strength which was used to calculate the $f_{J'J''}$ values for each transition based on Eq. (4.9). For the single case of the A-X($1 - 0$) band, which is perturbed by the d-X($5 - 0$) band, the state mixing analysis of Eq. (4.11) was invoked to determine the $f_{J'J''}$ values. The mixing coefficients were obtained from the revised perturbation analysis performed by Niu *et al.* [125]. The line oscillator strengths for the A-X system are reported in Table 4.2, and the sensitivity coefficients from Salumbides *et al.* [50] are listed in Table 4.3.

Field *et al.* [134] measured the lifetimes for the levels $v' = 0 - 7$ with an accuracy of ~ 1%, and these values were used to estimate lifetimes for states $v' = 8 - 9$. The damping parameters relative to the A-X system were calculated using Eq. (4.12) and Eq. (4.14). Note that the value of $\gamma_{v'}$ for the level $A^1\Pi$, $v' = 1$ includes the effect of the perturbation by the longer lived $d^3\Delta$, $v' = 5$. The other $A^1\Pi$, v' states are mainly perturbed at high rotational states, hence they were considered unperturbed for the relevant low-J levels during this work. The damping parameters $\gamma_{v'}$ of the A-X bands are presented in Table 4.4.

TABLE 4.1: Laboratory wavelengths for A-X($v' - 0$) bands of CO.

J''	Wavelength [Å]			Wavelength [Å]		
	R	Q	P	R	Q	P
		(0-0)[a]			**(1-0)**[a]	
0	1544.44965(5)*	-	-	1509.74781(5)*	-	-
1	1544.38952(5)*	1544.54133(5)*	-	1509.69595(5)*	1509.83545(5)*	-
2	1544.34528(5)*	1544.57263(5)*	1544.72485(5)*	1509.66147(5)*	1509.87124(5)*	1510.01077(5)*
3	1544.31734(24)†	1544.61950(5)*	1544.84819(5)*	1509.64364(5)*	1509.92437(5)*	1510.13424(5)*
4	1544.30586(24)†	1544.68226(5)*	1544.98742(5)*	1509.64196(23)†	1509.99415(5)*	1510.27510(5)*
5	1544.31235(24)†	1544.76096(5)*	1545.14298(24)†	1509.65592(23)†	1510.08008(5)*	1510.43261(5)*
		(2-0)[b]			**(3-0)**[b]	
0	1477.56549(4)*	-	-	1447.35311(4)*	-	-
1	1477.51338(4)*	1477.64944(4)*	-	1447.30514(4)*	1447.43368(4)*	-
2	1477.47721(4)*	1477.68137(4)*	1477.81737(4)*	1447.27343(4)*	1447.46624(4)*	1447.59479(4)*
3	1477.45705(4)*	1477.72920(4)*	1477.93318(4)*	1447.25798(4)*	1447.51507(4)*	1447.70795(4)*
4	1477.45279(4)*	1477.79304(4)*	1478.06494(4)*	1447.25885(4)*	1447.58021(4)*	1447.83737(4)*
5	1477.46449(4)*	1477.87294(4)*	1478.21273(4)*	1447.27595(4)*	1447.66165(4)*	1447.98308(4)*
		(4-0)[b]			**(5-0)**[c]	
0	1419.04491(4)*	-	-	1392.52551(20)†	-	-
1	1419.00170(4)*	1419.12198(4)*	-	1392.48517(20)†	1392.60017(20)†	-
2	1418.97534(4)*	1419.15561(4)*	1419.27723(4)*	1392.46133(20)†	1392.63391(20)†	1392.74951(20)†
3	1418.96575(4)*	1419.20618(4)*	1419.38890(4)*	1392.45435(20)†	1392.68473(20)†	1392.85776(20)†
4	1418.97285(20)†	1419.27367(4)*	1419.51744(4)*	1392.46365(20)†	1392.75203(20)†	1392.98290(20)†
5	1418.99625(20)†	1419.35858(20)†	1419.66277(4)*	1392.49041(20)†	1392.83642(20)†	1393.12476(20)†
		(6-0)[c]			**(7-0)**[c]	
0	1367.62386(20)†	-	-	1344.18593(20)†	-	-

Continued on next page

TABLE 4.1: Laboratory wavelengths for A-X($v' - 0$) bands of CO.

J''	Wavelength [Å]			Wavelength [Å]		
	R	Q	P	R	Q	P
1	1367.58645(20)†	1367.69587(20)†	-	1344.15142(20)†	1344.25550(20)†	-
2	1367.56681(20)†	1367.73029(20)†	1367.83936(20)†	1344.13426(20)†	1344.29056(20)†	1344.39411(20)†
3	1367.56494(20)†	1367.78248(20)†	1367.94620(20)†	1344.13480(20)†	1344.34278(20)†	1344.49877(20)†
4	1367.58065(20)†	1367.85264(20)†	1368.07047(20)†	1344.15233(20)†	1344.41273(20)†	1344.62098(20)†
5	1367.61544(20)†	1367.94040(20)†	1368.21216(20)†	1344.18756(20)†	1344.49985(20)†	1344.76003(20)†
		(8-0)^{c}			**(9-0)**^{c}	
0	1322.15058(20)†	-	-	1301.40162(35)†	-	-
1	1322.11912(20)†	1322.21754(20)†	-	1301.37300(35)†	1301.46598(35)†	-
2	1322.10531(20)†	1322.25355(20)†	1322.35252(20)†	1301.36148(35)†	1301.50274(35)†	1301.59659(35)†
3	1322.10898(20)†	1322.30671(20)†	1322.45534(20)†	1301.36894(35)†	1301.55746(35)†	1301.69740(35)†
4	1322.13118(20)†	1322.37822(20)†	1322.57585(20)†	1301.39349(35)†	1301.62946(35)†	1301.81873(35)†
5	1322.17069(20)†	1322.46724(20)†	1322.71423(20)†	1301.43702(35)†	1301.71892(35)†	1301.95399(35)†

[a] From Niu *et al.* [125].
[b] From Niu *et al.* [126].
[c] From Salumbides *et al.* [50].
* Derived from the laser study.
† Derived from the VUV-FTS study.

4.2.5. THE D-X SYSTEM

The laboratory wavelengths of the d-X(5 – 0) band up to levels with $J = 10$ were partially listed by Niu *et al.* [125]. Wavelengths for the transitions that were not directly measured in the VUV-FT or in the laser studies, were calculated using the semi-empirical model developed by Niu *et al.* [125], since it is more accurate and consistent than the other laboratory measurements of the d-X band present in literature.

The d-X band is a spin-forbidden transition which borrows its intensity from the interaction between the $A^1\Pi$ and $d^3\Delta$ states. Values for the line oscillator strengths $f_{J'J''}$ are obtained via state mixing as governed by Eq. (4.11), where the mixing coefficients are obtained from the perturbation analysis of Niu *et al.* [125].

A similar procedure was used to derive the sensitivity coefficients of this band, which were calculated according to Eq. (4.17), using as K_i^0 the sensitivity coefficients of the unperturbed d-X transitions and as K_j^0 the unperturbed coefficients of the A-X(1 – 0) band transitions. In other words, the sensitivity coefficients for the d-X transitions were calculated considering the A-X(1 – 0) band as the perturber of the d-X(5 – 0) band.

Lifetimes for $d^3\Delta$ state with $v' = 1 - 16$ were measured by van Sprang *et al.* [136] and they found lifetimes depending on vibrational level between 7.3 and 2.9 μs increasing with vibrational quantum number. These measured lifetimes are averages of the lifetimes of rotational levels in a vibrational manifold. As a consequence of the state mixing, a J dependent damping parameter was obtained for each rotational state in $d^3\Delta$, $v' = 5$ following Eq.(4.14) and the mixing coefficients from the perturbation model by Niu *et al.* [126].

TABLE 4.2: Line oscillator strengths for A-X($v'-0$) bands of CO. Uncertainties on the oscillator strengths are better than ~ 10%.

J''	$f_{J'J''}$			$f_{J'J''}$		
	R	Q	P	R	Q	P
		(0-0)			**(1-0)**	
0	1.582E-02	-	-	2.835E-02	-	-
1	7.893E-03	7.908E-03	-	1.439E-02	1.417E-02	-
2	6.294E-03	7.893E-03	1.582E-03	1.174E-02	1.439E-02	2.835E-03
3	5.590E-03	7.868E-03	2.255E-03	1.072E-02	1.468E-02	4.111E-03
4	5.168E-03	7.826E-03	2.623E-03	1.023E-02	1.501E-02	4.893E-03
5	4.847E-03	7.753E-03	2.846E-03	9.969E-03	1.535E-02	5.458E-03
		(2-0)			**(3-0)**	
0	4.151E-02	-	-	3.651E-02	-	-
1	2.075E-02	2.075E-02	-	1.825E-02	1.825E-02	-
2	1.660E-02	2.075E-02	4.151E-03	1.460E-02	1.825E-02	3.651E-03
3	1.482E-02	2.075E-02	5.930E-03	1.304E-02	1.825E-02	5.216E-03
4	1.384E-02	2.075E-02	6.918E-03	1.217E-02	1.826E-02	6.085E-03
5	1.321E-02	2.075E-02	7.547E-03	1.162E-02	1.826E-02	6.639E-03
		(4-0)			**(5-0)**	
0	2.448E-02	-	-	1.582E-02	-	-
1	1.229E-02	1.224E-02	-	7.912E-03	7.912E-03	-
2	9.888E-03	1.229E-02	2.448E-03	6.330E-03	7.912E-03	1.582E-03
3	8.876E-03	1.236E-02	3.513E-03	5.652E-03	7.912E-03	2.261E-03
4	8.448E-03	1.243E-02	4.120E-03	5.275E-03	7.912E-03	2.637E-03
5	7.977E-03	1.249E-02	4.519E-03	5.035E-03	7.912E-03	2.877E-03
		(6-0)			**(7-0)**	
0	9.501E-03	-	-	5.354E-03	-	-
1	4.746E-03	4.750E-03	-	2.677E-03	2.677E-03	-
2	3.789E-03	4.746E-03	9.501E-04	2.142E-03	2.677E-03	5.354E-04
3	3.371E-03	4.736E-03	1.356E-03	1.912E-03	2.677E-03	7.649E-04
4	3.121E-03	4.720E-03	1.579E-03	1.785E-03	2.677E-03	8.923E-04
5	2.902E-03	4.682E-03	1.716E-03	1.704E-03	2.677E-03	9.735E-04
		(8-0)			**(9-0)**	
0	2.636E-03	-	-	1.294E-03	-	-
1	1.318E-03	1.318E-03	-	6.470E-04	6.470E-04	-
2	1.054E-03	1.318E-03	2.636E-04	5.176E-04	6.470E-04	1.294E-04
3	9.414E-04	1.318E-03	3.766E-04	4.621E-04	6.470E-04	1.849E-04
4	8.787E-04	1.318E-03	4.393E-04	4.313E-04	6.470E-04	2.157E-04
5	8.387E-04	1.318E-03	4.793E-04	4.117E-04	6.470E-04	2.353E-04

TABLE 4.3: Sensitivity coefficients for A-X($v' - 0$) bands of CO. Uncertainties on the sensitivity coefficients are better than ~ 1%.

J''		K_i			K_i	
	R	Q	P	R	Q	P
		(0-0)			**(1-0)**	
0	-0.00232	-	-	0.01312	-	-
1	-0.00227	-0.00237	-	0.01280	0.01306	-
2	-0.00223	-0.00238	-0.00249	0.01235	0.01269	0.01294
3	-0.00219	-0.00239	-0.00257	0.01183	0.01218	0.01251
4	-0.00216	-0.00240	-0.00264	0.01129	0.01160	0.01195
5	-0.00212	-0.00239	-0.00273	0.01077	0.01100	0.01132
		(2-0)			**(3-0)**	
0	0.01850	-	-	0.02756	-	-
1	0.01853	0.01844	-	0.02759	0.02750	-
2	0.01855	0.01842	0.01833	0.02761	0.02748	0.02740
3	0.01856	0.01838	0.01825	0.02761	0.02744	0.02732
4	0.01856	0.01834	0.01816	0.02761	0.02739	0.02723
5	0.01854	0.01828	0.01806	0.02759	0.02734	0.02712
		(4-0)			**(5-0)**	
0	0.03784	-	-	0.04329	-	-
1	0.03783	0.03697	-	0.04331	0.04324	-
2	0.03771	0.03680	0.03695	0.04332	0.04321	0.04314
3	0.03749	0.03659	0.03685	0.04332	0.04317	0.04306
4	0.03720	0.03636	0.03667	0.04331	0.04312	0.04297
5	0.03690	0.03614	0.03643	0.04328	0.04305	0.04286
		(6-0)			**(7-0)**	
0	0.05039	-	-	0.05612	-	-
1	0.05044	0.05034	-	0.05614	0.05607	-
2	0.05051	0.05034	0.05024	0.05615	0.05605	0.05598
3	0.05061	0.05034	0.05019	0.05614	0.05600	0.05590
4	0.05066	0.05037	0.05016	0.05611	0.05594	0.05581
5	0.05124	0.05048	0.05016	0.05607	0.05587	0.05570
		(8-0)			**(9-0)**	
0	0.06162	-	-	0.06646	-	-
1	0.06163	0.06157	-	0.06647	0.06641	-
2	0.06169	0.06154	0.06147	0.06647	0.06638	0.06632
3	0.06162	0.06149	0.06139	0.06646	0.06633	0.06624
4	0.06159	0.06143	0.06136	0.06642	0.06627	0.06615
5	0.06154	0.06135	0.06119	0.06638	0.06619	0.06604

TABLE 4.4: Natural damping constants for A-X($v'-0$) bands of CO.

v'	$\gamma_{v'}$ [a] $[\times 10^8\ \mathrm{s}^{-1}]$
0	1.00
1	0.96[b]
2	1.03
3	1.04
4	1.06
5	1.09
6	1.10
7	1.12
8	1.12[c]
9	1.12[c]

[a] From Field *et al.* [134].
[b] Including the effect of perturbation.
[c] Values estimated.

TABLE 4.5: Molecular parameters for the d-X(5 – 0) band. Uncertainties in sensitivity coefficients estimated to be better than ~ 1%.

J''	Wavelength [Å]			$f_{J'J''}$			K_i			$\gamma_{v'}{}^d$ [$\times 10^8$ s^{-1}]
	R	Q	P	R	Q	P	R	Q	P	
0	1510.34131(20)[b]	-	-	5.70E-03	-	-	0.031298	-	-	0.18
1	1510.30590(5)[c]	1510.42893(5)[c]	-	2.64E-03	2.85E-03	-	0.031660	0.031298	-	0.16
2	1510.29756(5)[c]	1510.48138(5)[a]	1510.60448(20)[b]	1.88E-03	2.64E-03	5.70E-04	0.032123	0.031634	0.031271	0.14
3	1510.31694(5)[c]	1510.56071(5)[a]	1510.74454(5)[c]	1.45E-03	2.35E-03	7.53E-04	0.032628	0.032072	0.031581	0.13
4	1510.36485(5)[a]	1510.66783(5)[a]	1510.91169(5)[c]	1.13E-03	2.02E-03	7.84E-04	0.033123	0.032553	0.031994	0.10
5	1510.44207(5)[a]	1510.80354(5)[c]	1511.10612(20)[b]	8.76E-04	1.69E-03	7.36E-04	0.033562	0.033027	0.032453	0.09

[a] Derived from a Doppler-free laser excitation study [125].
[b] Derived from a VUV-FT study [125].
[c] Derived from the semi-empirical model developed by Niu *et al.* [125].
[d] Derived from lifetimes measured by van Sprang *et al.* [136].

4.2.6. THE B-X SYSTEM

Drabbels *et al.* [137] determined the rest wavelengths of the B-X$(0-0)$ band with an accuracy of 0.003 cm^{-1}. The band oscillator strength $f_{v'v''}$ used to calculate the oscillator strength values according to Eq. (4.9) were obtained by averaging the values of Chan *et al.* [132] and Zhong *et al.* [133], both measured via electron scattering, and Federman *et al.* [138] and Stark *et al.* [139], who measured the $f_{v'v''}$ values using optical absorption experiments. The sensitivity coefficients were calculated according to Eq. (4.16), and the excited state lifetime $\tau = 29.3 \pm 1.6$ ns, used to calculate the damping parameter using Eq. (4.12), was measured by Drabbels *et al.* [140]. This value was found to be in good agreement with data from Krishnakumar and Srivastava [141]. The molecular parameters for the B-X$(0-0)$ band are listed in Table 4.6.

TABLE 4.6: Molecular parameters for the B-X(0 – 0) band. The uncertainties on the sensitivity coefficients are estimated to be better than ~ 1%.

J''	Wavelength [Å]		$f_{J'J''}$		K_i		$\gamma_{v'}{}^a$ [s^{-1}]
	R	P	R	P	R	P	
0	1150.48254(13)	-	6.62E-03	-	−0.00012	-	0.34×10^8
1	1150.43039(3)	1150.58513(3)	4.41E-03	2.21E-03	−0.00008	−0.00021	
2	1150.37746(3)	1150.63531(13)	3.97E-03	2.65E-03	−0.00003	−0.00026	
3	1150.32399(3)	1150.68482(3)	3.78E-03	2.84E-03	0.00001	−0.00030	
4	1150.26961(3)	1150.73368(3)	3.68E-03	2.94E-03	0.00006	−0.00034	
5	1150.21457(3)	1150.78202(3)	3.61E-03	3.01E-03	0.00011	−0.00038	

[a] Derived from lifetimes measured by Drabbels *et al.* [140].

4.2.7. THE C-X SYSTEM

The C-X$(0-0)$ band rest wavelengths adopted in this analysis were measured by Drabbels *et al.* [137] with an overall accuracy of 0.003 cm^{-1}. The band oscillator strengths $f_{v'v''}$ were measured by Federman *et al.* [138] and Stark *et al.* [139], using optical absorption, and by Chan *et al.* [132] and Zhong *et al.* [133], using electron scattering. The weighted average value from these studies was adopted in this work to calculate the $f_{J'J''}$ values. The sensitivity coefficients were calculated according to Eq. (4.16). Cacciani *et al.* [142] used the time domain pump-probe technique to investigate the excited state lifetime of the $C^1\Sigma^+$, $v' = 0$ level and showed that it is not predissociated. They measured a value of $\tau = 1.78 \pm 0.10$ ns for the C-X$(0-0)$ band, which was converted into a value for the damping parameter $\gamma_{v'J'}$. The molecular parameters for the C-X$(0-0)$ band are listed in Table 4.7.

TABLE 4.7: Molecular parameters for the C-X(0 – 0) band. The uncertainties on the sensitivity coefficients are estimated to be better than ~ 1%.

J''	Wavelength [Å]		$f_{J'J''}$		K_i		$\gamma_{v'}{}^a$ [s^{-1}]
	R	P	R	P			
0	1087.86761(4)	-	1.14E-01	-	0.000055	-	5.6×10^8
1	1087.82110(4)	1087.95910(4)	7.61E-02	3.80E-02	0.000097	−0.000029	
2	1087.77413(4)	1088.00408(4)	6.85E-02	4.57E-02	0.000140	−0.000070	
3	1087.72668(4)	1088.04871(4)	6.52E-02	4.89E-02	0.000184	−0.000111	
4	1087.67876(4)	1088.09263(4)	6.34E-02	5.07E-02	0.000228	−0.000152	
5	1087.63014(10)	1088.13620(10)	6.23E-02	5.19E-02	0.000272	−0.000192	

[a] Derived from lifetimes measured by Cacciani *et al.* [142].

4.2.8. THE E-X SYSTEM

The rest wavelengths for the E-X (0,0) band, as listed by Morton and Noreau [124], were in part adopted in this work for the R and P-branches. Much more accurate values for wavelengths of Q-branch lines were later measured by Cacciani and Ubachs [143]. The oscillator strengths were calculated starting from the weighted average of the $f_{v'v''}$ values reported by Chan *et al.* [132], Zhong *et al.* [133], Federman *et al.* [138], and Stark *et al.* [139], while the sensitivity coefficients were calculated using Eq. (4.16). As for the natural lifetime damping coefficients it should be considered that the $E^1\Pi$, $v = 0$ state is predissociated [144, 145], and that both radiative and predissociative decay contribute to the natural lifetime broadening, resulting in a value of $\tau = 0.91 \pm 0.06$ ns for the excited state lifetime. This value was converted into a value for $\gamma_{v'J'}$ using Eq.(4.12). The molecular parameters for the E-X$(0-0)$ band are listed in Table 4.8.

TABLE 4.8: Molecular parameters for the E-X(0 − 0) band. The uncertainties on the oscillator strengths are estimated to be better than ~ 10%, and the sensitivity coefficients are estimated to be better than ~ 1%.

J''	Wavelength [Å]			$f_{J'J''}$			K_i			$\gamma_{v'}{}^a$ [s^{-1}]
	R	Q	P	R	Q	P	R	Q	P	
0	1076.03361(12)	-	-	6.44E-02	-	-	−0.00010	-	-	10.96×10^8
1	1075.98718(12)	1076.07891(3)	-	3.22E-02	3.22E-02	-	−0.00006	−0.00014	-	
2	1075.93960(12)	1076.07751(3)	1076.16713(12)	2.58E-02	3.220E-02	6.44E-03	−0.00001	−0.00014	−0.00022	
3	1075.89133(12)	1076.07540(3)	1076.20975(12)	2.30E-02	3.220E-02	9.20E-03	0.00003	−0.00014	−0.00026	
4	1075.84202(12)	1076.07261(3)	1076.25133(12)	2.15E-02	3.220E-02	1.07E-02	0.00008	−0.00013	−0.00030	
5	1075.79167(12)	1076.06913(3)	1076.29199(12)	2.05E-02	3.220E-02	1.17E-02	0.00012	−0.00013	−0.00034	

[a] Derived from lifetimes measured by Cacciani *et al.* [145].

4.3. OBSERVATIONS

The dataset used in this work is gathered from four different observing programs carried out between 2009 and 2014 using the Ultraviolet and Visual Echelle Spectrograph (UVES) mounted on the 8.2m Very Large Telescope (VLT) at Paranal, Chile [115]. Three programs were performed in service mode; two in March-April 2009 (082.A-0544(A) and 083.A-0454(A), PI Ledoux), of which an analysis was reported by Noterdaeme *et al.* [45] and which were retrieved from the ESO archive[1] for the present re-analysis, and one between March and June 2014 (093.A-0373(A), PI Ubachs). The program 091.A-0124(A), PI Ubachs, was run in visitor mode in May 2013.

Exposures taken in 2009 have only the standard ThAr calibration taken at the end of the night, while exposures taken under programs 091.A-0124(A) and 093.A-0373(A) were followed by an attached ThAr calibration exposure and a 'supercalibration' exposure of an asteroid or a solar twin taken immediately after the quasar exposure, without allowing for any change in the instrument parameters [46, 72]. The raw data were bias corrected, flat fielded and their flux was extracted using the Common Pipeline Language version of the UVES pipeline. The wavelength calibration was performed using ThAr lamp exposures. The custom software UVES_POPLER [87] was used after the standard reduction procedure to combine the echelle orders into the 1D final spectrum and to remove bad pixels and spectral artifacts as well as to fit the continuum using low-order polynomials [46, 86]. The four observational programs return a total of 20 hrs of integration on the target, with a slit width of 1.0 arcsec, a typical seeing of ~ 0.9 arcsec, a binning of 2×2, yielding a resolving power of $\lambda/\Delta\lambda \sim 40000$. The spectrum of J2137+0647 covers the wavelengths from 3290 to 9600 Å, with a signal-to-noise ratio (S/N) of ~ 13 per 2.5 km s^{-1} per pixel at ~ 4000 Å, in the blue arm of UVES, and ~ 40 per 2.5 km s^{-1} per pixel at ~ 5000 Å, in its red arm.

Quasar exposures taken between 2013 and 2014 were recorded with a supercalibration exposure and were processed following the supercalibration method used by Daprà *et al.* [46] in order to correct for wavelength calibration distortions (see Section **??**). Some Ceres exposures were taken in 2009 (program 080.C-0881(B), PI Dumas), in a time separation of one week maximum from the quasar observations using only the blue arm of UVES. These exposures were used to supercalibrate the J1237+0647 spectrum at wavelengths shorter than the Lyman-α emission feature of the quasar.

4.4. QUASAR ABSORPTION MODEL

Quasar J1237+0647 is located at the emission redshift $z_{\rm em} = 2.78$ and in its line-of-sight is located a sub-damped Lyman-α system, $\log[N_{\rm H\,I}/{\rm cm}^{-2}] = 20.00 \pm 0.15$, featuring atomic and molecular absorption features at an absorption redshift of

[1] http://archive.eso.org/eso/eso_archive_main.html

$z_{\rm abs} = 2.69$ [45]. Molecular hydrogen and deuterated molecular hydrogen (HD) absorption features were investigated by Daprà *et al.* [46], who used H_2 and HD to derive a constraint on variation in μ. Here is presented the analysis of the CO absorption in the spectrum of J1237+0647 and the constraint on μ that it delivers.

4.4.1. THE FITTING METHOD

The absorption model was created using the non-linear least-squares Voigt profile fitting program VPFIT [88]. Within the program, a Voigt profile is described by a set of three free parameters, which are used together with the molecular parameters: the column density N, the redshift at which the absorption occurs z, and the Doppler line width b. A comprehensive fit was performed, involving a simultaneous treatment of all the lines [41, 46, 84, 86]. The main strength of this method is that each free parameter can be shared by different transitions, thus minimizing the number of free parameters needed to perform the fit. This allows one to fit even the molecular absorption features that show partial overlaps with intervening lines from metals and H I as well as to deal with the blending of the P, Q and R branches of the CO features that the weak transitions involving high rotational levels, up to $J = 5$.

Since the CO transitions originate in the same absorber and they are assumed to share the same physical conditions of the absorbing cloud, the redshift z and the width b parameters were tied together. The rotational state-dependent column densities N_J were linked together assuming thermodynamic equilibrium yielding a Boltzmann distribution at a temperature T:

$$N_J = N_{col} P_J(T) = N_{col} \frac{(2J+1)e^{-E_{rot}/kT}}{\sum (2J+1)}, \tag{4.18}$$

where $N_{col} = \sum N_J$ is the total column density for CO, and $P_J(T)$ is the partition function giving the relative population of the single rotational J-states. The gas temperature $T_{\rm CO}$ was used to calculate the partition function, but was not treated as a free parameter in VPFIT. Models corresponding to different CO temperatures were fitted to the spectrum in multiple runs, under the assumption that CO is in thermodynamic equilibrium, resulting in the best-fit temperature $T_{\rm CO} = 11.2 \pm 0.1$ K, as shown in Fig. 4.1. This temperature is close to the expected temperature due to the excitation of the cosmic microwave background (CMB) $T_{\rm CMB}(z_{\rm abs} = 2.69) = 10.05$ K and verifies the assumption of equilibrium for the population distribution [45]. The procedure results in a model which consists of only three free parameters describing the CO transitions: the redshift z, the line width b, and the total column density of the gas N_{col}. Effectively, a shared vibrational band contour of overlapping CO lines is fitted, rather than multiple, individual rovibronic line profiles.

It is noted here that while CO and H_2 are the main molecular constituents of interstellar clouds in galactic media, their behaviour and thermodynamic properties are usually very different. The CO gas, as observed in the high-redshift absorbing

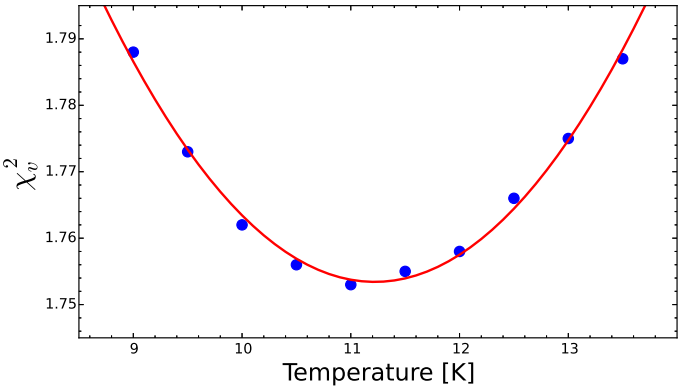

FIGURE 4.1: Reduced χ^2 from fitted CO models with different temperatures. The values of the χ^2_ν are indicated with (blue) dots and the best fit is presented with a (red) solid line.

systems, is found to exhibit thermalized population distributions at the local cosmic microwave background temperature [45]. In contrast, the population distribution of H_2 molecules is non-thermal with higher rotational states populated superthermal. For the lowest levels a temperature-like distribution is found with $T_{01} \sim 50-100$ K for the lowest two rotational levels [146]. Also the observed widths of the absorption lines in all high-redshift extra-galactic objects exceeds the kinetic temperatures that would correlate with the Boltzmann temperatures. These widths, treated with a Doppler parameter b in studies probing varying constants, are ascribed to turbulent motions in the observed clouds. For this reason the physical parameters b do not represent a temperature, nor can be they be equated for the different species observed.

4

4.4.2. CO BANDS

The CO bands pertaining to the A-X system fall in the red part of the spectrum, at redshifted wavelengths $\lambda > 4877$ Å, and their absorption profiles do not show significant overlaps with any other spectral feature. Nine spectral regions were selected in the range $\lambda = 4877-5702$ Å covering the A-X bands. The region containing the A-X$(1-0)$ band also includes the perturbing d-X$(5-0)$ band, which however is not overlapping the A-X$(1-0)$ band. Some metal absorption features, namely Si IV at $z_{\rm abs} \simeq 2.69, 2.62$ and C IV at $z_{\rm abs} \simeq 2.59$, fall near the CO bands, in which cases the atomic lines were included in the fit in order to obtain a better constraint on the continuum level close to the CO features. From the Franck-Condon factor analysis, the A-X$(9-0)$ band is strong enough to be detected, but it is almost completely overlapped by strong metal features at $\lambda \sim 4802$ Å and it was not included in the model.

The other CO absorption bands in the spectrum of J1237+0647, C-X, B-X, and E-

X, are detected in the blue arm of UVES at redshifted wavelengths shorter than the Lyman-α emission feature of the quasar. This region is referred to as the Lyman-α forest and shows multiple H I absorption features arising from the intergalactic medium at redshifts $z < z_{\rm em}$. It is common that such neutral hydrogen lines overlap absorption features falling in the Lyman-α forest. In such cases, the overlapping H I features occurring in the selected CO regions were included in the model by assigning to each of them a set of free parameters in VPFIT.

The B-X electronic system falls in the Lyman-α forest at redshifted wavelengths $\lambda < 4246$ Å. Of its three known vibrational levels, only the B-X$(0-0)$ is strong enough to be detected in this absorber in the region $\lambda = 4242-4246$ Å. Its R branch is partially overlapped by an intervening saturated H I line at $\lambda \sim 4243.7$ Å, and an additional narrow, unidentified feature at $\lambda \sim 4243.1$ Å.

Of the four known vibrational levels of the C-X electronic system, only the C-X$(0-0)$ band was detected in the region $4243-4246$ Å. It is partially overlapped, mainly in its R branch, by a saturated H I line occurring at $\lambda \sim 4013$ Å. The C-X$(1-0)$ band has an oscillator strength which is of the same order as the B-X$(0-0)$ band; however, the former falls in a heavily saturated region, thus is not detected.The C-X$(2-0)$ and $(3-0)$ bands have an oscillator strength $\sim 10^4$ times weaker than the C-X$(0-0)$ band [124], hence are not detected.

The E-X electronic system is detected in the J1237+0647 spectrum at wavelengths $\lambda < 3972$ Å. Compared to E-X$(0-0)$, the E-X$(1-0)$ band is one order of magnitude weaker, while the E-X$(2-0)$ band is two orders of magnitude weaker [124], hence these bands are too weak to be detected. The transitions of the Q branch of the E-X$(0-0)$ band are overlapped, resulting in a clear feature at ~ 3970.3 Å, while an intervening H I line partially overlaps the P branch at $\lambda \simeq 3971$ Å.

CO has two more electronic systems, V-X at a rest wavelength $\lambda \sim 1011$ Å, and F-X at $\lambda \sim 1003$ Å. While the V-X$(0-0)$ band is too weak to be detected, the F-X$(0-0)$ band is stronger [~ 2 times stronger than the B-X$(0-0)$ band, 124]. However, the F-X$(0-0)$ is completely overlapped by strong H I lines and cannot be identified in this absorber. CO has many more absorption systems lying at $\lambda < 1000$ Å that are generally weaker and not included in the present discussion [147, 148].

For CO absorption, a total column density of $\log[N/{\rm cm}^{-2}] = 14.29 \pm 0.02$, an absorption redshift of $z_{\rm abs} = 2.689566(1)$ and a width of $b = 0.73 \pm 0.03$ km s^{-1} are obtained from the fit. These values agree with those of Noterdaeme *et al.* [45] within 1.5σ significance. Moreover, the normalized residuals are distributed in the range $\pm 1\sigma$ in each fitted spectral region, validating the assumption that there is no overlap with other undetected spectral features. The absorption model for the CO bands is presented in Fig. 4.2 for the A-X system, and in Fig. 4.3 for the B-X$(0-0)$, C-X$(0-0)$, and E-X$(0-0)$ bands.

The reduced chi-squared parameter returned by the model is $\chi^2_\nu = 1.5$ with $\nu = 7391$ degrees of freedom. The main contributors to the final χ^2_ν value being some-

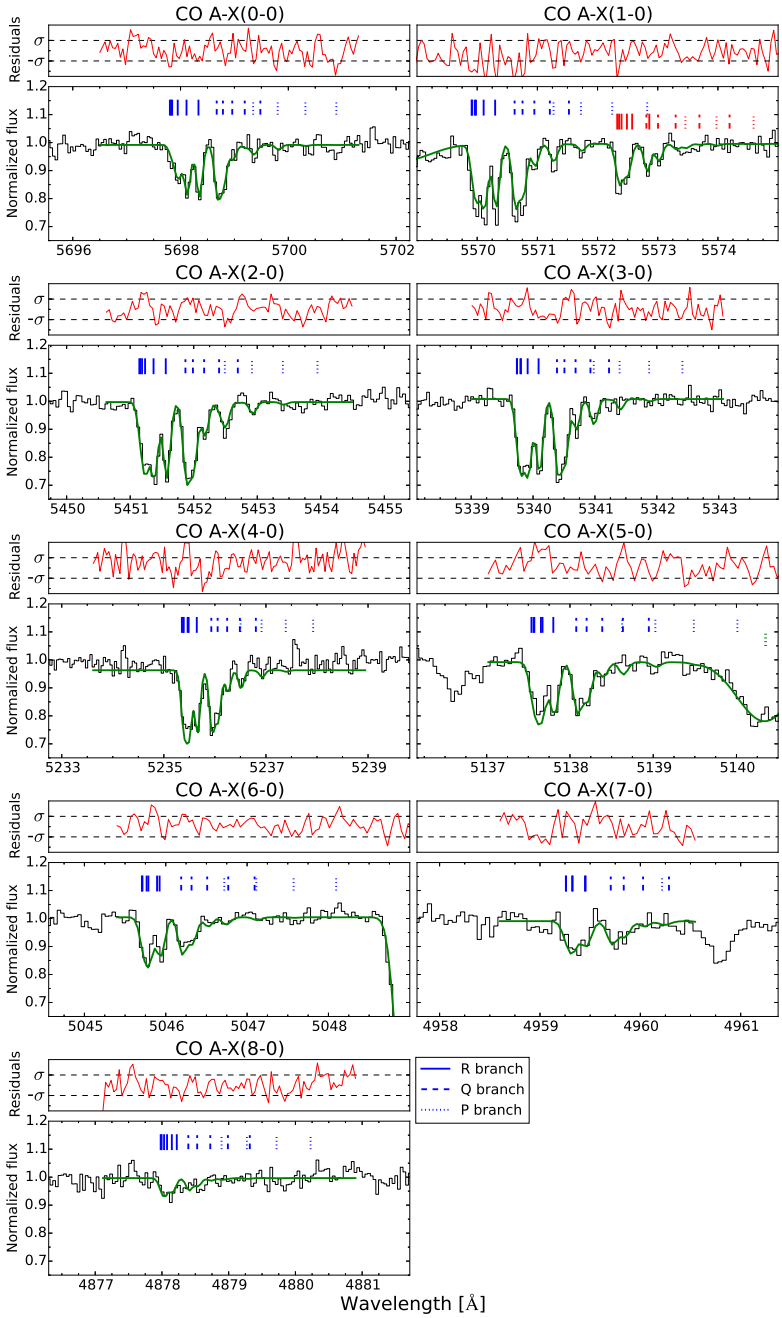

FIGURE 4.2: Absorption model for the CO bands from A-X(0−0) to A-X(8−0). The (green) solid line represents the fitted model while the (blue) ticks show the wavelengths of the rotational lines for ground states $J = 0-5$ and their different branches. Band A-X(1−0) is perturbed by the inter-system band d-X(5−0), whose rotational levels are shown by the (red) ticks. Band A-X(5−0) falls close to a Si IV absorption feature at $\lambda \sim 5140.5$ Å, which is indicated by the (green) dotted tick. The (red) solid lines represent the residuals of the fits with their $\pm 1\sigma$ boundaries.

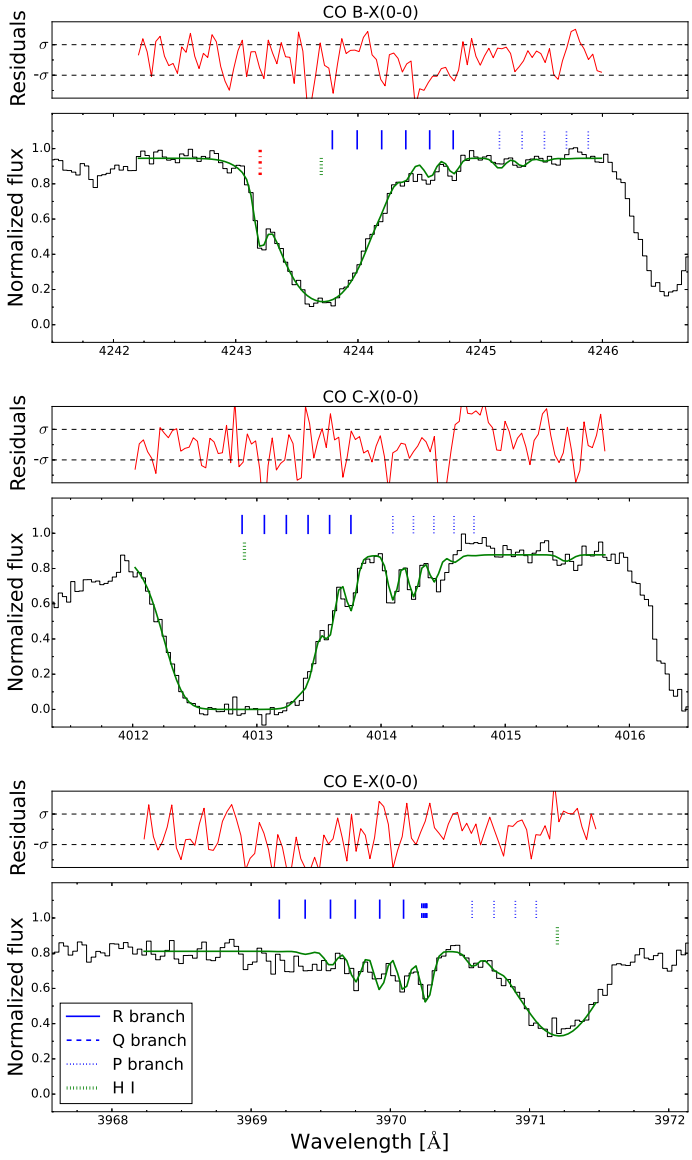

FIGURE 4.3: Top panel: absorption model for the B-X(0 – 0) band. Middle panel: absorption model for the C-X(0 – 0) band. Bottom panel: absorption model for the E-X(0 – 0) band. The (green) solid line represents the fitted model while the (blue) ticks show the wavelengths of the rotational lines for ground states $J = 0 - 5$ and their different branches. The (red) solid lines represent the residuals of the fits with their $\pm 1\sigma$ boundaries. The (green) dashed ticks show the positions of the intervening H I lines. The (red) dashed tick at $\lambda \sim 4243.1$ shows the position of an unidentified narrow absorption feature.

what larger than unity are the CO bands in the blue arm; indeed the fit of only the A-X bands returns a $\chi^2_\nu = 1.22$. This is due to the fact that the B-X$(0-0)$, C-X$(0-0)$, and E-X$(0-0)$ bands show overlaps with intervening, saturated H I lines at $\lambda \sim 4243.5$ and 4013 Å. Another contributor is the region that includes the A-X$(1-0)$ and the d-X$(5-0)$ bands. Both these bands appear slightly stronger in the spectrum compared to the absorption model, while the other A-X$(v'-0)$ bands appear slightly weaker than predicted by the model. This may be related to possible, small errors in the values of their band oscillator strengths included in the CO molecular database. Excluding the spectral regions containing these CO bands from the absorption model delivers a reduced chi-squared of $\chi^2_\nu = 1.2$.

Another reason for a $\chi^2_\nu > 1$ may be the possible presence of extra velocity components that were not included in the model. To investigate this, a composite residual spectrum [CRS, 41] was created by combining the residual structure between the spectrum and the model for all the CO bands. The CRS, as shown in Fig. 4.4, does not show evidence for missing velocity components in the CO absorption model. Moreover, multiple trial models with two CO velocity components were fitted to the spectrum, but the second, weaker velocity component was rejected by VPFIT. As a consequence, the presence of an extra CO velocity component was excluded.

Finally, small shifts in individual transitions are likely to cause discrepancies between the recorded spectrum and the absorption model, and will be another reason for a final $\chi^2_\nu > 1$. Such shifts are caused by wavelength calibration distortions on scales of single echelle orders. The effect of these intra-order distortions is discussed in Section 4.5.1 and is included in the systematic error budget. The uncertainties on the CO fitting parameters $\log N$, z, and b were scaled by the square root of the final χ^2_ν value, in order to take into account the discrepancies between the model and the spectrum. The aforementioned phenomena originate as well the larger χ^2_ν value of the fit to determine the CO population temperature (see Fig. 4.1).

4.4.3. CONSTRAINING $\Delta\mu/\mu$

A variation of the proton-to-electron mass ratio can be probed using the absorption spectra of rovibronic molecular transitions. A change in the value of μ will be reflected in a shift of the observed wavelengths. This shift, which is assumed to be linear, is given by:

$$\lambda_i^{obs} = \lambda_i^{rest}(1+z_{\rm abs})(1+K_i\frac{\Delta\mu}{\mu}), \tag{4.19}$$

where λ_i^{obs} is the observed wavelength of the i-th transition, λ_i^{rest} is its rest wavelength, and $z_{\rm abs}$ is the redshift at which the absorption occurs. $\Delta\mu/\mu = (\mu_z - \mu_{lab})/\mu_{lab}$ is the relative difference between the value of the proton-to-electron mass ratio in the absorption system, μ_z, and the one measured on Earth, μ_{lab}, and K_i is the sensitivity coefficient specific for each transition i.

It follows from Eq. (4.19) that, if the sensitivity coefficients are wavelength-

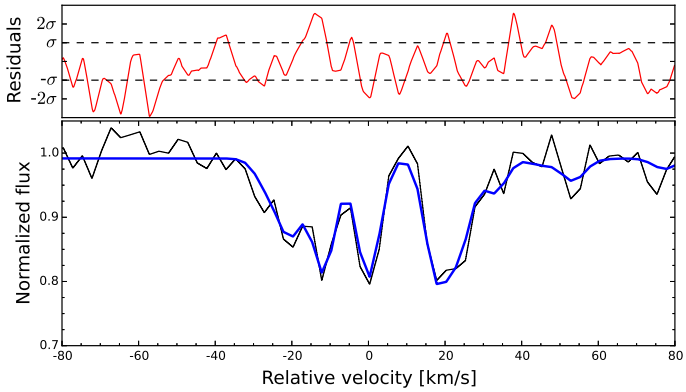

FIGURE 4.4: Top panel: normalized composite residual spectrum from the 13 CO bands detected. Bottom panel: the absorption model for the CO A-X(1−0) band is plotted as a reference. The (blue) solid line represents the fitted model. The velocity scale is centred on the R(0) transition for both the panels.

dependent, the presence of a wavelength distortion could mimic a shift in μ [36, 41, 97]. The CO bands, whose K_i coefficients are shown in Fig. 4.5, show a wavelength dependence only in the A-X electronic system, while the B-X(0−0), C-X(0−0), and E-X(0−0) bands all have sensitivity coefficients ~ 0 at rest wavelengths of $\lambda \sim 1075-1151$ Å and were used as anchor transitions in this analysis. The degeneracy can be further broken by including in the model the d-X(5−0) band, since it has very different coefficients than the A-X(1−0) band at similar wavelength.

After having developed a robust absorption model, an extra free parameter was introduced, beside the set of parameters describing the CO absorption, in a final fitting run in VPFIT in order to constrain the μ-variation. The extra parameter $\Delta\mu/\mu$ was not introduced earlier to avoid that a wrong estimate of the absorption redshift was compensated by an artificial μ variation caused by the degeneracy between the redshift and a non-zero $\Delta\mu/\mu$. The model returned a constraint on the variation of the proton-to-electron mass ratio of $\Delta\mu/\mu = (0.7 \pm 1.6_{\rm stat}) \times 10^{-5}$, hereafter referred to as the fiducial value of $\Delta\mu/\mu$. The statistical error is derived from the diagonal term of the final covariance matrix for the fit, and it represents only the uncertainty in $\Delta\mu/\mu$ derived from the S/N of the quasar spectrum. The statistical error derived from CO is larger than the error obtained from the previous analysis of H_2 absorption in the same system by a factor of ~ 3 [46].

4.5. SYSTEMATIC UNCERTAINTY

An estimation of the systematic error affecting the constraint on $\Delta\mu/\mu$ derived from CO absorption only was made considering the contributions to the error budget

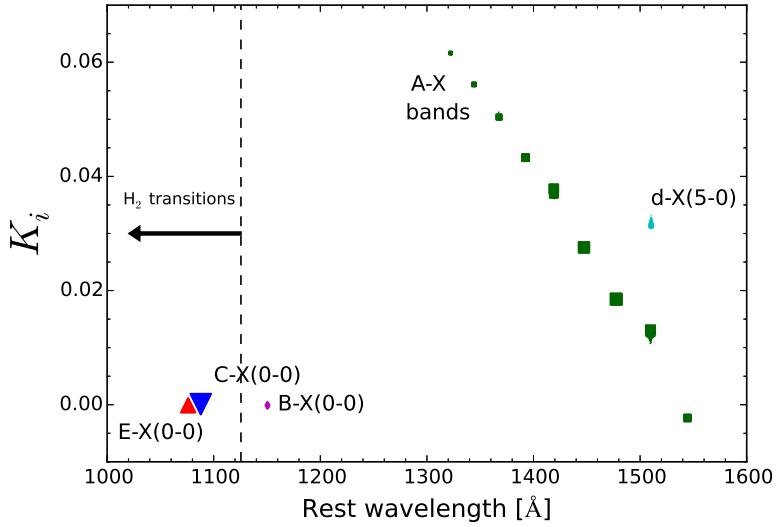

FIGURE 4.5: Sensitivity coefficients of the CO bands detected in the blue arm (left panel) and in the red arm of UVES (right panel). A-X bands are shown with (green) squares, the d-X(5 – 0) band with (cyan) circles, the B-X(0 – 0) with (magenta) diamonds, the C-X(0 – 0) with (blue) downward-pointing triangles, and the E-X(0 – 0) with (red) upward-pointing triangles. The size of each marker is proportional to the line intensity. Note that the 'tear drop' shape of the d-X(5 – 0) and some A-X bands inserts is a consequence of contributions by a number of rotational lines in the bands, some of which undergo perturbations. The H_2 and HD transitions fall in the area shown by the (black) arrow, delimited by the dashed line.

from the five most dominant sources and discussed extensively below.

4.5.1. WAVELENGTH SCALE DISTORTIONS

In recent years the UVES spectrograph was found to suffer from wavelength calibration distortions both on scales of single echelle orders [72, 102, 103] and longer scales [72, 98]. These distortions are most likely due to different light paths between the object observed during the science exposures and the ThAr lamp located on the VLT platform [117]. The long-range distortions in particular would introduce a wavelength-dependent velocity shift which is nearly degenerate with a non-zero $\Delta\mu/\mu$, as discussed in Section 4.4.3. In principle such degeneracy can be broken by fitting together CO bands that have different sensitivity coefficients at similar wavelengths, as in the case of the A-X$(1-0)$ and the d-X$(5-0)$ bands, or bands whose K_i are not wavelength dependent, like the B-X$(0-0)$, C-X$(0-0)$, and E-X$(0-0)$ bands. Excluding the d-X$(5-0)$ and the three anchor bands from the fit results in a constraint of $\Delta\mu/\mu = (-0.4 \pm 2.1_{\rm stat}) \times 10^{-5}$, whose uncertainty is $\sim 35\%$ larger than the fiducial value, indicating some effectiveness in breaking this degeneracy. However, the three anchor bands are overlapped by intervening H I lines, reducing the effectiveness of this approach in breaking the degeneracy.

LONG-RANGE DISTORTIONS

To account for the calibration distortions, the technique now referred to as 'supercalibration' was first demonstrated by Molaro *et al.* [117] and later improved by Rahmani *et al.* [98] and, more recently, Whitmore and Murphy [72], whose method was used to supercalibrate the spectrum of J1237+0647. The 'supercalibration' technique consists in the comparison of a ThAr-calibrated UVES spectrum to a reference Fourier-transform absorption spectrum with a much more accurate frequency scale [99][2]. Targets for supercalibrations are asteroids, which reflect the solar light and hence show the same spectrum of the Sun, and 'solar twin' stars, which are objects with a spectrum that is almost identical to the solar one [100, 101]. The spectrum of J1237+0647 was partially corrected for long-range distortions following the same supercalibration procedure used by Daprà *et al.* [46].

Exposures taken in 2013 and 2014, for ~ 11.5 hrs of integration, have dedicated supercalibrations for both the blue and the red arm of UVES. The supercalibrations for the spectrum of J1237+0647 in the red arm are presented in Fig. 4.6, while the blue arm was calibrated as in Daprà *et al.* [46]. The impact of the long-range distortions affecting the exposures taken in 2009, covering ~ 8.5 hrs of integration, was estimated using observations of the Ceres asteroid performed within one week of the quasar exposures (program 080.C-0881(B), PI Dumas). The Ceres exposures were taken using only the blue arm of UVES and yielded two distortion slopes of ~ 150 m s^{-1} per 1000 Å and one of ~ -500 m s^{-1} per 1000 Å. The positive slope value was used to correct

[2] Available at `http://kurucz.harvard.edu/sun/irradiance2005/irradthu.dat`

for the distortions in the exposures taken in 2009 in the blue arm, while the negative value was translated into a systematic uncertainty on $\Delta\mu/\mu$ of $\sim 2.4\times10^{-6}$, as in Daprà *et al.* [46]. On average, the long-range distortions in the red arm of UVES have a slightly larger magnitude than what is measured in the blue arm. A comparison between the red and the blue arm returns, for the supercalibrations exposures taken in 2013 and 2014, returns an average ratio of ~ 1.2, with only the 'solar twin' HD117860 delivering a larger ratio of ~ 2.5. The average ratio was used to estimate the magnitude of the long-range distortions in the red arm for the exposures taken in 2009. Another constraint of $\Delta\mu/\mu = (0.5\pm1.6_{\rm stat})\times10^{-5}$ was derived using the larger ratio from HD117860, and a spread in $\Delta\mu/\mu$ of $\sim 2\times10^{-6}$ between the two constraints was added to the systematic error budget.

The 'solar twins' HD097356 and HD117860 were observed in 2014 two times in a time window of 10 and 3 days respectively. These target show a variation of their distortions slopes of +5% and −5% respectively. The distortion corrections of each J1237+0647 exposure were first enhanced and subsequently decreased by 5% to simulate the effect of a temporal variation of ~ 1 week. Two different constraints of $\Delta\mu/\mu = (0.6\pm1.6_{\rm stat})\times10^{-5}$ and $\Delta\mu/\mu = (0.7\pm1.6_{\rm stat})\times10^{-5}$ were derived from the positive and from the negative variation respectively. These constraints show that the temporal difference between the quasar exposures and the Ceres supercalibration exposures introduces an error of, at most, 1×10^{-6} on the fiducial value of the constraint.

INTRA-ORDER DISTORTIONS

The presence of intra-order wavelength distortions introduces in each exposure a velocity shift which translates into a $\Delta\mu/\mu$ uncertainty given by $\delta(\Delta\mu/\mu) = [(\Delta v/c)/\sqrt{N}]/\Delta K_i$. Here, Δv is the mean amplitude of the intra-order distortions, $\Delta K_i = 0.06$ is the spread in the CO sensitivity coefficients, and N is the number of CO transitions considered in the analysis. The mean amplitude of the intra-order distortions in the red arm is $\Delta v = 520$ m s^{-1} for exposures taken in 2013 and 2014. This amplitude is very similar to what was measured in the blue arm for all the exposures used in the analysis. Therefore, it was taken as the mean amplitude of the intra-order distortions for all exposures, including the ones taken in 2009.

Since the CO bands have mostly blended R and Q branches, while the P branches are weak, a band contour, including the higher J levels was effectively fitted. The number of transitions containing valuable signal is reflected by the enhancement of the statistical precision on $\Delta\mu/\mu$ after combining the constraint obtained from CO only with the constraint from 137 H_2 and HD transitions $\Delta\mu/\mu(H_2) = (-5.4\pm6.3_{\rm stat}\pm4.0_{\rm syst})\times10^{-6}$. A combined constraint (see Section 4.6) results in a statistical uncertainty on $\Delta\mu/\mu$ which is ~ 10% smaller, since the statistical error scales with $\sqrt{N}$, a value of $N = 36$ of CO transitions that are effectively contributing to the signal was adopted, resulting in an uncertainty on $\Delta\mu/\mu$ of $\sim 4.5\times10^{-6}$.

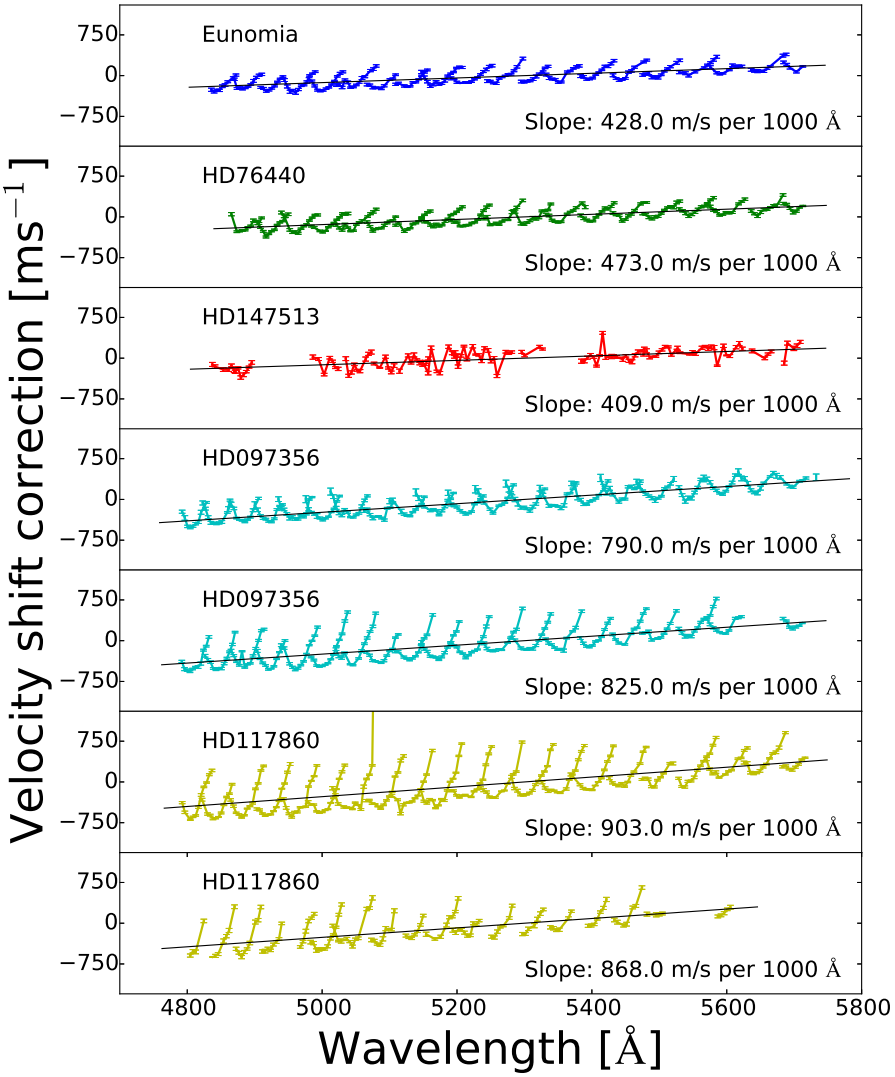

FIGURE 4.6: Distortions in exposures of one asteroid (Eunomia) and six 'solar twin' stars, of the UVES wavelength scale used to supercalibrate the exposures of quasar J1237+0647 taken in 2013 and 2014. For each exposure, the velocity shift measurements are made on ~ 10 echelle orders. The slopes of the fitted lines show the velocity shift needed to counter the effect of the long-range distortions. The values of the slopes are indicated for each supercalibration. The 'solar twin' stars HD097356 and HD117860 were observed in service mode throughout the period March - May 2014, while the other targets were observed in visitor mode in May 2013. In all cases the supercalibrations exposures were taken immediately after the J1237+0647 science exposures. Since only the slopes are the physically relevant parameters for the supercalibration process, the distortions were shifted to a zero velocity shift at $\lambda = 5300$ Å.

4.5.2. UNCERTAINTY FROM USING DIFFERENT UVES ARMS

Another potential cause of error is the presence of an offset between the wavelength scales of the blue arm of UVES where the B-X$(0-0)$, C-X$(0-0)$, and E-X$(0-0)$ bands are covered, and the lower red arm where the A-X bands fall. To quantify this effect, metal absorption features detected both in the blue and in the red arms, were investigated. Since the considered transitions belong to the same atom, the redshift $z_{\rm abs}$ at which they originate is expected to be the same for features detected in the two arms of UVES. Any non-zero offset $\Delta z_{\rm abs} = z_{\rm abs}^{\rm blue} - z_{\rm abs}^{\rm red}$ is evidence that there is a shift between the wavelength scales of the two arms, and such shift would introduce an effect mimicking $\Delta\mu/\mu \neq 0$.

Fe II is found in the absorbing system at $z \simeq 2.69$, the same that contains CO, and it has a velocity profile composed by 13 velocity components (VC) spanning ~ 400 km s^{-1}, as presented in Fig. 4.7. Si II absorption occurs at the same redshift. Three transitions are detected in the red part of the spectrum, in the range $\lambda = 4647 - 5644$ Å, and two in the blue part in the range $\lambda = 4389 - 4409$ Å. In Fig. 4.8, the broad profile of ~ 600 km s^{-1}, featuring ~ 20 VCs, is plotted. Almost all the Si II lines, particularly those detected in the blue arm, between -200 and $+130$ km s^{-1} are heavily saturated forming a broad absorption feature that is excluded in this analysis, since it results in poorly fitted redshifts. Therefore only the 6 VCs detected between $+130$ and $+400$ km s^{-1} were considered for Si II. The transitions considered are listed in Table 4.9. For each element, each VC was modelled using a set of free parameters (N, z, b) in VPFIT, that were tied together among transitions detected in the same arm of UVES. This results in two outputs, one relative to the blue arm and one to the red. The fitted redshift values relative to each UVES arm were translated into relative velocities and compared exploiting any velocity shift between the two arms of UVES $\Delta v = v_{\rm blue} - v_{\rm red} = [\Delta z_{\rm abs}/(1+z_{\rm abs})]c$. Here $\Delta z_{\rm abs}$ is the difference between the fitted redshift value in the blue and in the red arm, and $z_{\rm abs}$ is the redshift at which the absorption of the considered element occurs. The results of this comparison are presented in Fig. 4.9. Fe II absorption returns an average value for the offset of $\Delta v({\rm Fe\,II}) = -0.04 \pm 0.19$ km s^{-1} and Si II returns $\Delta v({\rm Si\,II}) = 0.11 \pm 0.37$ km s^{-1}, while the weighted average of these two offsets is $\Delta v = -0.01 \pm 0.17$ km s^{-1}. The main contributors to this value are the unblended Fe II VCs, which have smaller errors on their z parameters and are better described by the absorption model than the blended Fe II VCs at ~ 60 - 150 km s^{-1}. Note that the Fe II and Si II transitions reported by Murphy and Berengut [149] have laboratory wavelength uncertainties in velocity space of $\delta v = 14.5$ and 3.2 m s^{-1} respectively, while the transitions reported by Morton [150] have uncertainties $\delta v \sim 300$ m s^{-1}. These errors were added in quadrature to the statistical redshift errors returned from the fit. In conclusion, this analysis shows that there is no evidence of any spurious effect on $\Delta\mu/\mu$ introduced by a combined analysis of CO absorption features detected using different arms in UVES for the J1237+0647 spectrum considered.

TABLE 4.9: Metal transitions.

Ion	Rest wavelength [Å]	Reference
Fe II	1144.9379(1)	Morton [150]
Fe II	1608.450852(78)	Murphy and Berengut [149]
Si II	1190.4158(1)	Morton [150]
Si II	1193.2897(1)	Morton [150]
Si II	1260.4221(1)	Morton [150]
Si II	1304.3702(1)	Morton [150]
Si II	1526.706980(16)	Murphy and Berengut [149]

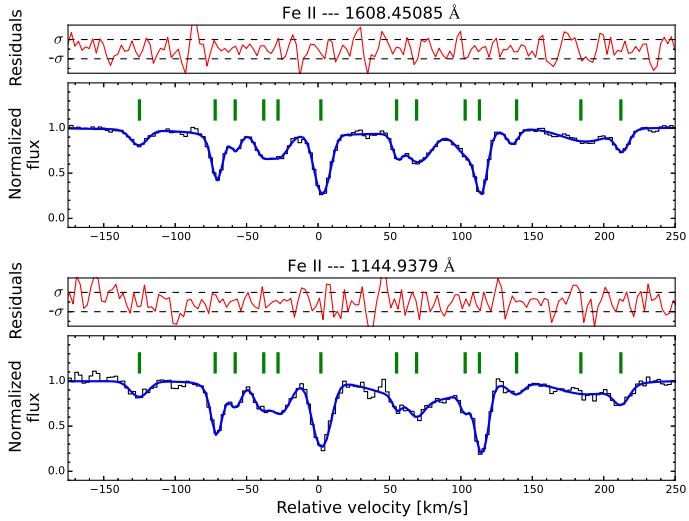

FIGURE 4.7: Velocity profiles of two transitions of Fe II in the red part (top panel) and in the blue part of the spectrum (bottom panel). The solid blue line shows the absorption models, and the green ticks show the position of the VCs. On top of each spectrum, residuals are shown with a red dashed line, and the two horizontal dashed lines show their $\pm 1\sigma$ boundaries. The velocity scale is centred at redshift $z = 2.689570$.

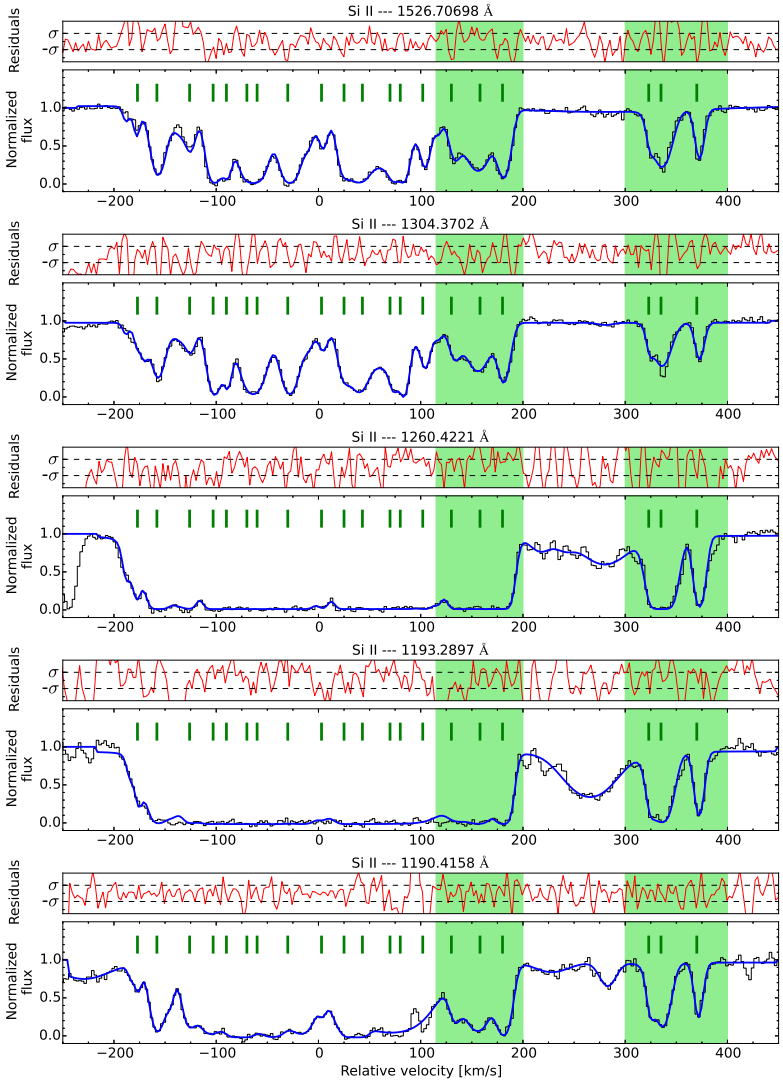

FIGURE 4.8: Velocity profiles of five transitions of Si II in the red part (three top panels) and in the blue part of the spectrum (two bottom panels). The solid blue line shows the absorption models, the solid green ticks show the position of the VCs, and the green shaded area shows the absorption features considered for the analysis. On top of the spectrum, residuals are shown with a (red) dashed line, and the two horizontal dashed lines show their $\pm 1\sigma$ boundaries. The velocity scale is centred at redshift $z = 2.689959$.

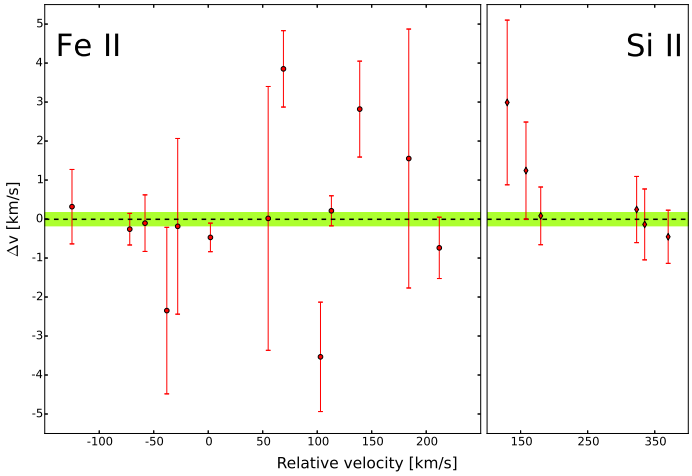

FIGURE 4.9: Calculated velocity offset $\Delta v = v_{\rm blue} - v_{\rm red}$ between the blue and the red arm in UVES for two atomic species. Left panel: offsets between 13 VCs of Fe II at $z_{\rm abs} = 2.689570$. Right panel: offsets between 6 VCs of Si II at $z_{\rm abs} = 2.689959$. The velocity scales are relative to these absorption redshifts. The dashed line shows the weighted average offset between the two arms and the (light green) shaded area represents its 1σ boundaries.

4.5.3. LACK OF ATTACHED THAR CALIBRATIONS

The lack of attached ThAr calibrations on some exposures can introduce an error on $\Delta\mu/\mu$ of up to 0.7×10^{-6} [86], however no evidence for a shift of μ was found in a previous analysis of the H_2 absorption in J1237+0647 [46].

Only half of the dataset used in this work, that from 2009, has attached ThAr calibrations, while the other half was calibrated using the standard ThAr exposure taken at the end of the night. The impact of the lack of dedicated attached ThAr calibrations on the final value of $\Delta\mu/\mu$ was evaluated by dividing the dataset in two subsets, one containing only the exposures taken in 2009 and the other containing the exposure taken in 2013 and 2014. From these subsets, two different constraints were retrieved: $\Delta\mu/\mu = (0.1 \pm 2.5_{\rm stat}) \times 10^{-5}$ for 2009 and $\Delta\mu/\mu = (1.9 \pm 2.3_{\rm stat}) \times 10^{-5}$ for 2013 and 2014. The two values agree within their uncertainties, showing that the lack of dedicated attached ThAr calibrations does not have any significant impact on the final value of $\Delta\mu/\mu$ derived from CO absorption only presented here.

4.5.4. SPECTRAL REDISPERSION

Another potential source of systematic uncertainties is spectral redispersion, caused by the co-addition of the single exposures. This implies a rebinning of the spectra on a common wavelength scale and it can distort the line-profile shapes, possibly causing a shift in μ. King *et al.* [84] investigated the magnitude of this effect on a

similar absorbing system, and they estimated the error on $\Delta\mu/\mu$ from 83 H_2 and HD absorption features as $\sim 1.4\times10^{-6}$. Scaling this value to the 36 CO transitions that are effectively contributing to the signal returns an error on $\Delta\mu/\mu$ of $\sim 2.0\times10^{-6}$.

4.5.5. TOTAL SYSTEMATIC UNCERTAINTY

The total systematic uncertainty on the fiducial value of the combined constraint on μ was calculated by adding all the contributions from the aforementioned sources in quadrature. This returns a systematic error of $\sim 5.5\times10^{-6}$. The fiducial constraint on $\Delta\mu/\mu$ derived from CO absorption only therefore becomes $\Delta\mu/\mu = (0.7\pm1.6_{\rm stat}\pm0.5_{\rm syst})\times10^{-5}$. This value is delivered by the analysis of CO absorption features, divided among 13 bands, from the spectrum of quasar J1237+0647 obtained by combining distortion-corrected exposures taken in 2013 and 2014 and uncorrected exposures taken in 2009.

4.6. COMBINED ANALYSIS WITH H_2 AND CO

Daprà *et al.* [46] performed an independent analysis of the J1237+0647 absorption system using molecular hydrogen to constrain μ variation. Analyzing only the H_2 absorption, they found a constraint of $\Delta\mu/\mu = (-5.4\pm6.3_{\rm stat}\pm4.0_{\rm syst})\times10^{-6}$, which is in agreement with the constraint obtained from CO absorption only. The CO absorption is associated with the strongest velocity component of the H_2 absorption feature at $z_{\rm abs}$=2.689551(1). The difference in redshift between this H_2 component and the CO absorption features translates into a velocity shift of ~ 1.2 km s^{-1} between the two absorbing clouds where the molecular absorption originates. Since there is no evidence for a systematic velocity offset between the arm of UVES in the spectrum of J1237+0647, the shift between H_2 and CO is not considered an artifact. Moreover, it is comparable to what was found by Noterdaeme *et al.* [45] and this was considered as evidence that the absorbing system is composed of several small and dense molecular clouds.

A combined analysis using H_2, HD, and CO absorption features was performed by adding the CO fitted regions to the dataset analyzed by Daprà *et al.* [46]. Only the free parameter corresponding to $\Delta\mu/\mu$ was tied among the three molecules, while the other fitting parameters were not tied. The combined analysis delivered a constraint on the μ-variation of $\Delta\mu/\mu = (-5.6\pm5.6_{\rm stat})\times10^{-6}$, whose statistical uncertainty is $\sim 10\%$ smaller than what returned from the H_2 and HD absorption only. A weighted average of the statistical uncertainties, using the inverse of the variances as weights, delivered an error of 5.9×10^{-6}, which is close to what obtained from the combined analysis. Assuming that the quoted systematic uncertainties between the two measurements are not correlated, the systematic error on the combined constraint was estimated using the same procedure, which delivered an error of 3.1×10^{-6}. The final value of the combined constraint on a varying μ derived from H_2, HD and CO absorption is $\Delta\mu/\mu = (-5.6\pm5.6_{\rm stat}\pm3.1_{\rm syst})\times10^{-6}$.

4.7. CONCLUSION

An analysis of CO absorption at high redshift in order to constrain a variation of the proton-to-electron mass ratio is performed for the first time. The absorption system at $z_{\rm abs} = 2.69$ towards quasar J1237+0647 was investigated in detail for CO and H_2 molecular absorption, while metal absorption of Fe II and Si II was used to analyze systematic effects. CO was found in 13 bands spread in the range 3968 – 5702 Å, falling both bluewards and redwards of the Lyman-α emission peak in the quasar absorption spectrum. An absorption model describing the CO features was created starting from four molecular parameters, namely the rest wavelengths λ, the oscillator strengths $f_{J'J''}$, the sensitivity coefficients K, and the damping constants $\gamma_{v'J'}$, which were included in an updated molecular database. The model was then fitted against the quasar spectrum using the comprehensive fitting technique, that allowed to fit simultaneously all the vibrational bands using only 4 free parameters: the total CO column density N_{col}, the redshift z, the Doppler width b, and $\Delta\mu/\mu$.

The constraint on a varying proton-to-electron mass ratio from the CO spectrum, $\Delta\mu/\mu = (0.7 \pm 1.6_{\rm stat} \pm 0.5_{\rm syst}) \times 10^{-5}$, is less stringent than that obtained from the H_2 spectrum in this absorption system. This may in part be due to the overlap of the B-X(0 – 0), C-X(0 – 0), and E-X(0 – 0) bands by broad H I features, which may be absent in other absorption systems than that towards J1237+0647 analyzed here. The present paper lists the database covering the relevant molecular properties of CO electronic absorption lines that may be used in future studies searching for μ-variation based on optical absorption of carbon monoxide in the line-of-sight of high redshift quasars. Thus far CO electronic absorption has been detected in six different systems towards quasars [44, 45, 47–49], as well as in some Gamma-Ray-Burst observations [151], where the same methods can potentially be applied to detect μ-variation.

The CO absorption was included in a combined analysis involving the previously investigated H_2 [46], leading to a more stringent constraint on a varying μ of $\Delta\mu/\mu = (-5.6 \pm 5.6_{\rm stat} \pm 3.1_{\rm syst}) \times 10^{-6}$. Various potential sources of systematics were investigated, including the long-range distortions that are known to affect the UVES spectra. The J1237+0647 spectrum was partially corrected for such distortions using the supercalibration technique presented by Whitmore and Murphy [72]. This result is the first independent constraint on a varying μ obtained from the analysis of optical absorption for two different molecules detected in the same absorbing system, thus observed under the same physical conditions. The constraint agrees with previous results derived from 10 different systems in the range $z_{\rm abs} = 2.05 - 4.22$, which correspond to a time interval of 10 – 12.5 Gyrs. They return an averaged constraint that shows a null μ-variation at a level of $\sim 5 \times 10^{-6}$ (3-σ) [73].

ACKNOWLEDGMENTS

The authors thank the Netherlands Foundation for Fundamental Research of Matter (FOM) for financial support. The work is based on observations with the ESO Very Large Telescope at Paranal (Chile). WU acknowledges funding from the European Research Council (ERC) under the European Union's Horizon 2020 research and innovation programme (grant agreement No 670168). MTM thanks the Australian Research Council for *Discovery Project* grant DP110100866 which supported this work.

5

ANALYSIS OF CARBON MONOXIDE ABSORPTION AT $z_{\rm ABS} \simeq 2.5$ TO CONSTRAIN THE VARIATION OF THE PROTON-TO-ELECTRON MASS RATIO

Daprà, M., Noterdaeme, P., Vonk, M., Murphy, M. T. & Ubachs, W.
Mont. Not. Roy. Astron. Soc. ***467****, 3848-3855 (2017)*

Absorption by carbon monoxide in the spectrum of quasar SDSS J000015.16+004833.2 is investigated in order to derive a constraint on the temporal variation of the proton-to-electron mass ratio, μ. The spectrum was recorded using Very Large Telescope/Ultraviolet and Visual Echelle Spectrograph, and it was partially corrected for long-range wavelength scale distortions using the supercalibration technique. Eight vibrational CO singlet-singlet bands belonging to the $A^1\Pi - X^1\Sigma^+$ electronic absorption system, and the perturbing $d^3\Delta - X^1\Sigma^+(5,0)$ singlet–triplet band are detected in the damped Lyman α system at $z_{abs} \simeq 2.52$. The spectra are modeled using a comprehensive fitting technique, resulting in a final value of $\Delta\mu/\mu = (1.8 \pm 2.2_{stat} \pm 0.4_{syst}) \times 10^{-5}$, which is consistent with no variation over a look-back time of ~ 11.2 *Gyr.*

5.1. INTRODUCTION

The search for a temporal variation proton-to-electron mass ratio, $\mu \equiv M_P/m_e$, is performed by investigating molecular absorption in high-redshift systems. Thompson [28] first suggested to probe a possible variation of μ using the absorption of molecular hydrogen, H_2, and carbon monoxide, CO, in quasar spectra. More recently, a wide variety of molecules was found to be sensitive to a variation of μ [57, 58, 75]. Observations of ammonia [54, 56] and methanol [62–64] molecules in the radio domain returned a constraint $|\Delta\mu/\mu| < 10^{-7}$ (1σ) from two absorption systems at $z_{\rm abs} < 1$. Molecular hydrogen is a target for constraining a μ-variation in absorbing systems at redshifts $z_{\rm abs} > 2$. The analysis of H_2 absorption in the 10 best absorbers, in terms of brightness (Bessel $R_{\rm mag} \leq 18.4$) and H_2 column density ($\log[N/{\rm cm}^{-2}] \geq 14.5$), delivered the constraint of $|\Delta\mu/\mu| < 5 \times 10^{-6}$ (3σ) covering a window of look-back times of $\sim 10.5 - 12.5$ Gyr [73].

Carbon monoxide, the second most abundant molecule in the Universe, is another target for a μ-variation analysis. In particular, its $A^1\Pi - X^1\Sigma^+$ band system was detected in eight absorbers at absorption redshifts $z_{\rm abs} > 1$: SDSS J160457.50+220300.5 [49], SDSS J085726.78+185524.3, SDSS J104705.75+205734.5, SDSS J170542.91+354340.2 [44], SDSS J143912.04+111740.5 [48], SDSS J121143.42+083349.7 [152], SDSS J123714.60+064759.5 [45], and SDSS J000015.16+004833.2, hereafter J0000+0048, [42]. Salumbides *et al.* [50] reported high-accuracy laboratory wavelength measurements, with an accuracy of $\Delta\lambda/\lambda = 3 \times 10^{-7}$, for this band system, yielding to a constrain varying μ at a level of $\sim 10^{-5}$. Daprà *et al.* [30] reported the first measurement of $\Delta\mu/\mu = (0.7 \pm 1.6_{\rm stat} \pm 0.5_{\rm syst}) \times 10^{-5}$ from electronic CO absorption only in the system SDSS J123714.60+064759.5, which was then combined with the $\Delta\mu/\mu$ value derived from H_2 absorption.

Noterdaeme *et al.* [42] presented a detailed study of the absorption system towards J0000+0048, including CO, H_2, deuterated molecular hydrogen, HD, as well as atomic species and dust, in order to understand the chemical and physical properties of the absorbing gas. Here, a new analysis of the CO lines in this system is presented, specifically focused on deriving a constraint on the temporal variation of $\Delta\mu/\mu$ over cosmological time-scales. The observations used in this work are presented in Section 5.2, the absorption model and the derived value of $\Delta\mu/\mu$ are presented in Section 5.3, and the discussion of the systematic uncertainty is given in Section 5.4.

5.2. DATA

Quasar J0000+0048 was observed using the Ultraviolet and Visual Echelle Spectrograph [UVES, 115] mounted on the 8.2 m Very Large Telescope (VLT) in two programmes: 093.A-0126(A) in 2014 (PI Paris), and 096.A-0354(A) in 2015 (PI Noter-

daeme). The former programme was carried out using the 390+564 dichroic setting and a slit width of 0.9 arcsec (resolving power $R \sim 50\,000$), while the latter used the same settings but a narrower slit width of 0.7 arcsec ($R \sim 65\,000$) in the red arm of UVES. The work presented here is based on the same set of UVES exposures presented by Noterdaeme *et al.* [42]. A summary of the exposures considered in this analysis is presented in Table 5.1.

TABLE 5.1: Observational details of the J0000+0048 exposures with UVES/VLT used in this work.

Programme ID	Date	Exposure time [s]	Grating [nm]	Slit width [arcsec] Blue arm	Red arm	Dedicated supercalibration
093.A-0126(A)	02-08-2014	4800	390+564	0.9	0.9	No
093.A-0126(A)	03-08-2014	4800	390+564	0.9	0.9	No
093.A-0126(A)	04-08-2014	1934	390+564	0.9	0.9	No
093.A-0126(A)	05-08-2014	4800	390+564	0.9	0.9	No
093.A-0126(A)	20-08-2014	4800	390+564	0.9	0.9	No
093.A-0126(A)	21-08-2014	4800	390+564	0.9	0.9	No
096.A-0354(A)	11-10-2015	4200	390+564	0.9	0.7	Yes
096.A-0354(A)	03-11-2015	4200	390+564	0.9	0.7	Yes
096.A-0354(A)	09-11-2015	4200	390+564	0.9	0.7	Yes
096.A-0354(A)	12-11-2015	4200	390+564	0.9	0.7	Yes
096.A-0354(A)	13-11-2015	4200	390+564	0.9	0.7	Yes
096.A-0354(A)	13-11-2015	4200	390+564	0.9	0.7	Yes
096.A-0354(A)	01-12-2015	4200	390+564	0.9	0.7	Yes
096.A-0354(A)	09-11-2015	4800	437+760	0.9	0.9	No
096.A-0354(A)	09-11-2015	4800	437+760	0.9	0.9	No

The raw 2D exposures were reduced following the same procedure of Bagdonaite *et al.* [86]. The Common Pipeline Language (CPL) version of the UVES pipeline was used first to flat-field and bias-correct the exposures, and then to optimally extract the quasar flux. Each quasar exposure was wavelength calibrated using the standard 'attached' ThAr exposure taken immediately after the science exposure. In addition to the standard wavelength calibration, exposures recorded in 2015 were followed by a 'supercalibration' exposure of the solar twin star HD001835 taken with the same grating settings as the quasar one (see Section 5.4.3). After the standard reduction, the custom software UVES_POPLER [87] was used to combine the echelle orders on to a common vacuum-heliocentric wavelength grid. The spectral resolution is ~ 6 and ~ 4.5 km s^{-1} for exposures taken in 2014 and 2015, respectively. In order not to undersample the latter exposures, a dispersion of 2.0 km s^{-1} per pixel was used for wavelength grid. This software was also used to identify and remove 'bad' pixels and other spectral artefacts and to fit a continuum using low-order polynomials.

The final J0000+0048 spectrum, after the reduction, covers the wavelengths from 3284.2 to 9465.8 Å, with gaps between 5615.6 – 5671.1 and 7525.7 – 7655.7 Å due to the CCDs' separations. The signal-to-noise ratio (S/N) is $\sim$ 19 per 2.5 km s^{-1} per pixel at $\sim$ 5000 Å, in the middle of the CO window in the spectrum.

5.3. CARBON MONOXIDE ABSORPTION

CO absorption in the spectrum of J0000+0048 was first reported by Noterdaeme *et al.* [42], who detected nine CO bands belonging to the $A^1\Pi(\nu' = 0-8) - X^1\Sigma^+(\nu'' = 0)$ band system and one to the $d^3\Delta(\nu' = 5) - X^1\Sigma^+(\nu'' = 0)$ inter-band system. They found that the A–X(5 – 0) band is completely blended with Si IV absorption at $z_{\rm abs} = 2.52$, while the A-X(2-0) band is overlapped in its R and Q branches by C IV absorption at $z_{\rm abs} = 2.36$. Similarly, the A-X($\nu' = 6$, 7–0) bands have their P branches overlapped by intervening H I lines from the Lyman-α forest.

5.3.1. FITTING METHOD

The same approach used by Daprà *et al.* [30] was used to model the CO absorption in the quasar spectrum. They created a shared vibrational contour for the CO bands and they fitted it to the spectrum using the comprehensive fitting technique. This technique, introduced by King *et al.* [83] and later refined by Malec *et al.* [41], involves a simultaneous treatment of all the transitions, achieved by tying some of the fitting parameters together, which results in a lower number of free parameters in the fit. Moreover, the comprehensive fitting technique allows to handle the overlaps of CO absorption features with intervening spectral features, like the H I lines from the Lyman α forest and narrow metal lines, as well as the blending of the different branches of the CO bands.

To create the absorption model, the non-linear least-squares Voigt profile fitting program VPFIT [88] was used. In VPFIT a Voigt profile is described by a set of free pa-

rameters describing the properties of the absorbing system, and a set of fixed values describing the atomic and molecular properties. The free parameters are the column density N, the absorption redshift $z_{\rm abs}$, and the Doppler linewidth b. The shared vibrational contour for the CO bands was created by tying together the free parameters relative to each CO transition. The fixed values are the laboratory wavelength λ^0, the oscillator strength f, the damping parameter Γ, and the sensitivity coefficient K. For the CO molecule, such parameters are summarized in the data base reported by Daprà *et al.* [30].

5.3.2. TEMPERATURE DETERMINATION

Following the same approach used by Daprà *et al.* [30], a shared vibrational band contour of overlapping CO lines was constructed and fitted against the quasar spectrum. The band contour was created by tying together the absorption redshift and line-width parameters of each transition. Moreover, assuming thermodynamic equilibrium, the column densities N_J were linked using a temperature-dependent partition function given by:

$$N_J = N_{\rm CO} P_J(T) = N_{\rm CO} \frac{(2J+1) e^{-E_{rot}/kT_{\rm CO}}}{\sum (2J+1)}, \tag{5.1}$$

where $N_{\rm CO}$ is the total CO column density, and $P_J(T)$ is the partition function determining the population distribution over the rotational levels.

Since VPFIT does not include the temperature as a fitting parameter, it was determined by fitting multiple absorption models, corresponding to different $T_{\rm CO}$ values. At this stage of the analysis, only the non-overlapping CO bands were considered. This was done to exclude from the absorption model any non-CO feature, in order to avoid that the $T_{\rm CO}$ value was affected by uncertainties in the modelling of such features.

The χ^2_ν values as a function of the temperature yielded, as shown in Fig. 5.1, a statistically preferred value of $T_{\rm CO} = 11.4 \pm 0.1$ K, which represents an excitation temperature averaged over $J = 0-5$ levels. This is not the same temperature as what is measured by Noterdaeme *et al.* [42], who do not assume thermodynamic equilibrium and used the excitation of the lower rotational levels, i.e. $J = 0-3$, to derive the CMB temperature, after correction for collisional excitation. Indeed, they also showed that higher-J levels, which have much larger energy difference, appear to slightly deviate from thermodynamical equilibrium. Here, no attempt has been made to extract a similar physical meaning for $T_{\rm CO}$ were done, but rather the temperature was used to model the CO band contours with the aim of accurate wavelength measurement. The effect of the assumed population partition function on the derived $\Delta\mu/\mu$ is discussed in Section 5.4.1.

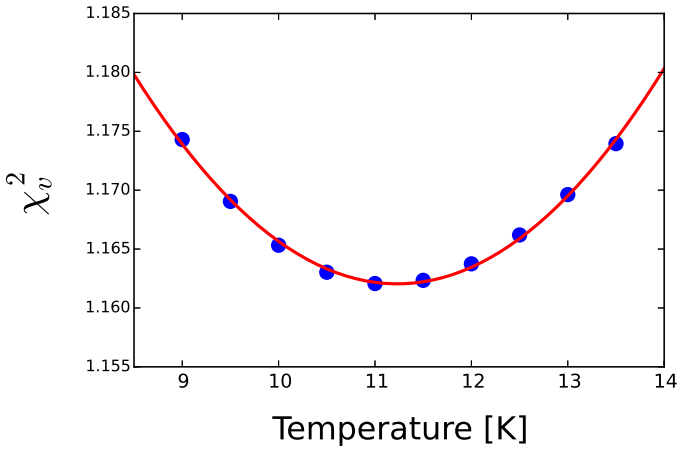

FIGURE 5.1: Reduced χ^2 values returned by the CO models with different temperatures. The (blue) dots show the χ^2_ν values and the (red) solid line indicates the best fit.

5.3.3. ABSORPTION MODEL

After a value of $T_{\rm CO}$ was determined, the population distribution was fixed via Eq. 5.1. This means that thermodynamic equilibrium is imposed in this analysis for fitting the absorption model against the quasar spectrum. Since the comprehensive fitting technique can handle overlaps among absorption features, the CO bands that are partially overlapped by intervening lines were included in the model. This does not hold for the A–X$(5-0)$ band, which is completely overlapped by metal absorption. Since no relevant information is gained in such a case of complete overlap, this CO band was not considered in this work.

The intervening H I lines that are partially overlapping the A–X$(v'=6,7-0)$ bands were included in the absorption model. A set of free parameters, N, $z_{\rm abs}$, and b, was assigned to each line in VPFIT. Since no assumptions were done about the origin of such absorption features, their corresponding parameters were left untied and free to vary independently from each other. The A–X$(2-0)$ band is partially overlapped by the shorter wavelength component of the C IV doublet. To handle the overlap and properly model the C IV, the longer wavelength component of the doublet was included in the absorption model. C IV shows a complex absorption profile, featuring multiple velocity components (VCs) that were modelled by assigning to each of them a set of free parameters. Each VC originates at a slightly different $z_{\rm abs}$ and, in principle, is observed under different physical conditions. To reflect this, the fitting parameters of different VCs were not tied together.

To account for possible quasar continuum misplacements, a continuum correction was included in each spectral region considered. Such correction locally applies

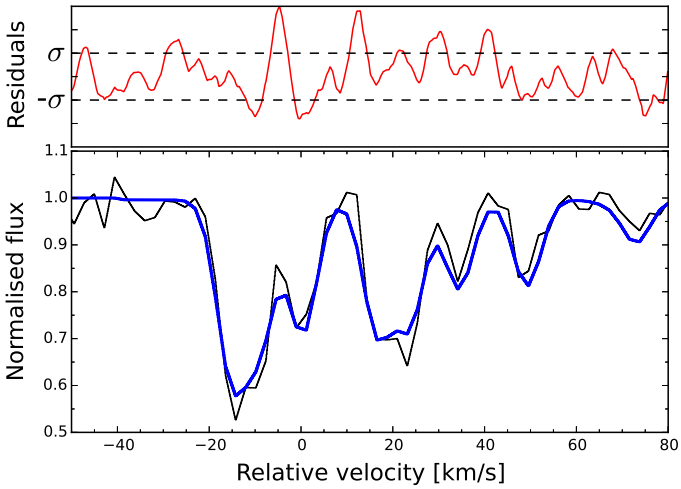

FIGURE 5.2: Top panel: normalized CRS from 6 non-overlapping CO bands. The dashed lines represent the $\pm 1\sigma$ boundaries. Bottom panel: the CO A-X(4-0) band is plotted as reference. The velocity scale is centre at the absorption redshift $z_{\rm abs} = 2.525464$.

a constant rescaling of the global continuum, therefore minimising the impact of any global misplacement. Since the CO A-X$(4-0)$ band falls on top of the quasar N V emission line, its continuum correction included an extra linear term beside the constant rescaling term.

The χ^2_ν parameter returned by the best-fit model is $\chi^2_\nu = 1.1$, which is slightly larger than unity. This may be due to the presence of extra, unresolved CO VCs that were not included in the model. The presence of such VCs was investigated using a composite residual spectrum [CRS, 41] built by combining the residuals of the 6 non-overlapping CO bands. The CRS, which is presented in Fig. 5.2, shows possible evidence for extra VCs in the CO absorption profile (specifically, the $> 1.5\sigma$ deviations at velocities ~ -5 and ~ 15 km s^{-1}). Multiple 2 VCs models were fitted, resulting either in the rejection of the extra VC in VPFIT or in significantly higher χ^2_ν parameters. Thus, the presence of a second VC was excluded from the absorption model.

The best-fit model, shown in Fig. 5.3, returned a total CO column density of $\log[N_{\rm CO}/{\rm cm}^{-2}] = 15.00 \pm 0.04$, an absorption redshift of $z_{\rm abs} = 2.525464(3)$, and a line width $b = 0.84 \pm 0.04$ km s^{-1}. The total column density is in good agreement with that reported by Noterdaeme *et al.* [42], while the Doppler width is $\sim 18\%$ larger than the value reported by Noterdaeme *et al.* [42]. This difference is due to the deviation from thermodynamic equilibrium of the high-J rotational levels, which are not corrected for collisional excitation. As for $T_{\rm CO}$, the Doppler parameter b is ascribed to the turbulent motions in the absorber rather than representing a temperature.

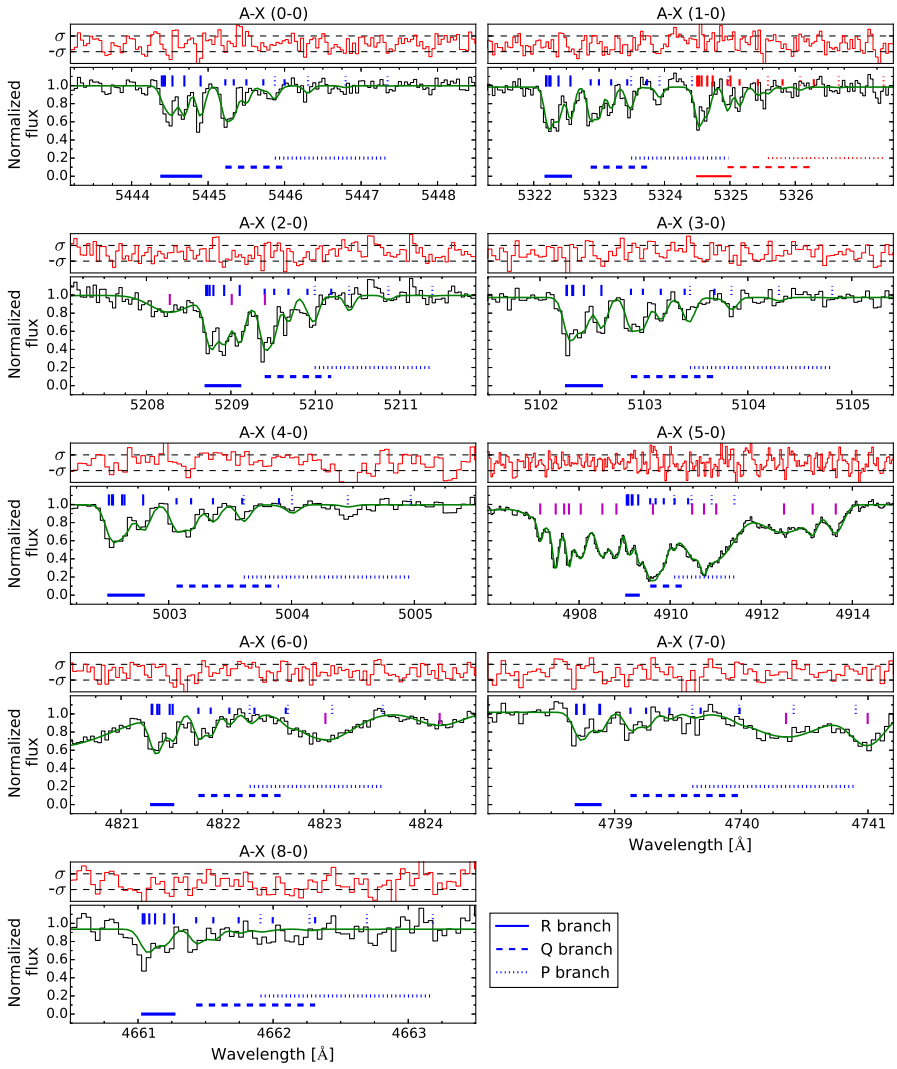

FIGURE 5.3: Absorption model for the CO bands considered in this work. The (green) solid line shows the fitted model, while the (blue) ticks indicate the wavelengths of the rotational lines for ground states $J = 0-5$ and their different branches. The residuals, as well as their $\pm 1\sigma$ boundaries, are shown by the (red) solid line plotted above each panel. Band A-X(1-0) is perturbed by the inter-system band d-X(5-0), indicated by the (red) ticks. The extent of the R, Q and P branches is shown by the horizontal solid, dashed, and dotted lines respectively. The intervening absorption features that are overlapping the CO bands are indicated by solid (magenta) ticks. The band A-X$(2-0)$ is overlapped by C IV absorption features at $z_{\rm abs} \simeq 2.36$, band A-X$(5-0)$ is overlapped by Si IV absorption features ($z_{\rm abs} \simeq 2.52$), and bands with $v' = 6$ and 7 are overlapped by H I lines from the Lyman-α forest.

5.3.4. CONSTRAINING $\Delta\mu/\mu$

The rotational states of the detected CO bands are sensitive to a variation of μ, which will cause a shift of the wavelengths at which such lines are detected. This shift, which is assumed to have a linear dependence on a varying μ, is given by:

$$\lambda_i^{obs} = \lambda_i^{lab}(1+z_{\rm abs})(1+K_i\frac{\Delta\mu}{\mu}), \tag{5.2}$$

where λ_i^{obs} is the observed wavelength of the i-th transition, λ_i^{lab} its rest wavelength, $z_{\rm abs}$ is the redshift at which absorption occurs, $\Delta\mu/\mu \equiv (\mu_z - \mu_{lab})/\mu_{lab}$ is the relative difference between the proton-to-electron mass ratio measured in the absorbing system, μ_z, and in the laboratory, μ_{lab}, and K_i is the sensitivity coefficient of the i-th transition. The sensitivity coefficients express the sign and magnitude of the sensitivity to a varying μ and are specific for each transition.

The $\Delta\mu/\mu$ value was calculated in VPFIT by adding an extra free parameter to the set describing the CO absorption. This fourth free parameter was added only after a robust absorption model was developed in order to avoid that an artificial μ-variation compensated any flaw in the model itself. The model returned a value of $\Delta\mu/\mu = (2.2 \pm 2.2_{\rm stat}) \times 10^{-5}$, hereafter referred to as the fiducial value. The statistical error is derived only from the diagonal terms of the final covariance matrix for the fit, and it represents the statistical uncertainty in $\Delta\mu/\mu$ derived from the S/N of the quasar spectrum.

5.4. SYSTEMATIC UNCERTAINTY

5.4.1. TEMPERATURE CHOICE

The fiducial value presented here was derived assuming a Boltzmann level population determined by a CO temperature $T_{\rm CO} = 11.2$ K. The uncertainty on the fiducial value of $\Delta\mu/\mu$ introduced by the temperature choice was tested by imposing $T_{\rm CO} = 9.9$ K, as reported by Noterdaeme *et al.* [42]. The $\Delta\mu/\mu$ value returned by the model built starting from this CO temperature is $\Delta\mu/\mu = (2.3 \pm 2.2_{\rm stat}) \times 10^{-5}$. The difference of $\sim 0.1 \times 10^{-5}$ between this value and the fiducial one was interpreted as the contribution to the total systematic uncertainty due to the temperature determination, and was added to the systematic error budget.

5.4.2. VELOCITY SHIFT BETWEEN UVES ARMS

The CO bands used in this work fall in the red arm in all the exposures taken with the gratings 309+564 nm, while they are partially covered by the blue arm in the two exposures taken with the 437+760 nm. The presence of a velocity offset between the blue and the red arm of UVES will, in principle, introduce a systematic error on the fiducial value of $\Delta\mu/\mu$ when combining the exposures.

To estimate the impact of such shift, a sub-spectrum was built using only the 564 nm exposures: the same procedures described in Section 5.2 for combining the

exposures were followed, but the 437+760 nm exposures were then removed and the spectrum recombined. A value of $\Delta\mu/\mu = (2.4 \pm 2.2_{\rm stat}) \times 10^{-5}$ was extracted from the sub-spectrum and its deviation from the fiducial value was interpreted as the effect of a velocity shift between the arms of UVES. Therefore, an uncertainty on $\Delta\mu/\mu$ of $\sim 0.2 \times 10^{-5}$ was added to the systematic error budget.

5.4.3. WAVELENGTH SCALE DISTORTIONS

An accurate wavelength calibration of the quasar exposures is crucial in order to constrain a variation of μ. It is noted that any wavelength-dependent distortion is likely to introduce a systematic error on the fiducial value of $\Delta\mu/\mu$. This is because such distortion will produce a relative shift between the CO absorption features which mimics the effect of a non-zero $\Delta\mu/\mu$ in Equation 5.2. This phenomenon can, in principle, be limited by fitting bands that have different K_i values at similar wavelengths, like the A-X(1−0) and the d-X(5−0) bands. However, the presence of a single CO band limits its effectiveness in breaking the degeneracy.

In the recent years, UVES has been found to suffer from 'intra-order distortions' – wavelength-dependent velocity shifts whose pattern repeats across echelle orders, i.e. at scales of ∼ 50-100 Å [72, 103]. Rahmani *et al.* [98] also found that UVES suffers from wavelength calibration distortions on longer scales. A detailed investigation showed that UVES such long-range wavelength distortions, on scales of ∼ 1000-3000 Å, are ubiquitous across the entire history of UVES [72]. It is commonly accepted that such distortions are due to different paths in the light-beam from the quasar and from the ThAr calibration lamp (though the evidence for this remains unclear at present).

LONG-RANGE WAVELENGTH DISTORTIONS

Molaro *et al.* [117] first proposed the technique, now often referred to as 'supercalibration', to correct the spectrum for such distortions. The technique, which was later improved and refined by Whitmore and Murphy [72], consists in a comparison between a UVES spectrum and a reference one with a much more accurate frequency scale. The reference spectrum used in this work is the solar spectrum[1] taken with a Fourier Transform Spectrometer (FTS) and reported by Chance and Kurucz [99]. Typical targets for the supercalibration technique are asteroids and 'solar-twin' stars (STs), since the former reflect the spectrum of the Sun and the latter show a spectrum which is almost identical to the solar one [100, 101].

The J0000+0048 exposures taken in 2015 were distortion-corrected using dedicated solar twin supercalibrations taken immediately after the quasar exposure and its attached ThAr calibration exposure. Each quasar exposure was distortion-corrected using its dedicated supercalibrations, following the same procedure as

[1] `http://kurucz.harvard.edu/sun/irradiance2005/irradthu.dat`

TABLE 5.2: Details of the solar twin HD001835 supercalibration exposures taken in 2015. Each exposure was taken with the same settings of the relative science quasar exposure. The uncertainty on the slopes is ~ 30 m s^{-1} per 1000 Å. Note that the CO bands are detected only in the red arm of UVES, the distortions slopes for the blue arm are included for completeness.

Date	Distortion slope [m s^{-1} per 1000 Å]	
	Blue arm	Red arm
11-10-2015	350	280
03-11-2015	420	300
09-11-2015	380	240
12-11-2015	570	370
13-11-2015	440	330
13-11-2015	510	340
01-12-2015	590	280

Bagdonaite *et al.* [86] and Daprà *et al.* [30, 46]: briefly, the long-range velocity distortions are characterized by a single slope as a function of wavelength in each of the blue and red arms of UVES. The supercalibration velocity measurements are shown in Fig. 5.4 and the measured values of the distortion slopes are listed in Table 5.2.

Since exposures from 2014 were not recorded with dedicated supercalibrations, an attempt to distortion correct them was made following the same approach as Bagdonaite *et al.* [86] and Daprà *et al.* [153]. The ESO archive was inspected looking for asteroids and STs exposures taken within ~ 1 week of the quasar exposures. More than 300 observations of the ST star HD217014 were recorded in August 2014 under the program 093.C-0929(D) (PI Martins). However, such exposures were taken using only the red arm of UVES, with the lower red CCD centred at 580 nm, a slit width of 0.3 arcsec and a 1×1 CCD binning. The narrower slit width used may, in principle, alter the path of the light from the ST with respect to the quasar. As a consequence, the wavelength distortion corrections derived from the supercalibration exposures may not be the same as the distortions affecting the quasar exposures. Because of this, the supercalibration technique cannot be applied. Nevertheless, it is possible to use the ST exposures to estimate the magnitude of the long-range distortions in August 2014, assuming than the distortions are the same in the 564 and in the 580 nm settings. The comparison between the HD217014 spectrum and the reference solar spectrum returned distortion slope values in the range 90-130 m s^{-1} per 1000 Å, with an average distortion slope of ~ 100 m s^{-1} per 1000 Å. The spectrum created by counter-distorting the exposures taken in 2014 with the average distortion slope values returned an updated fiducial value of $\Delta\mu/\mu = (1.8 \pm 2.2_{\rm stat}) \times 10^{-5}$. The difference between the minimum and the maximum value for the distortion slope was interpreted as the uncertainty on the adopted value of the slope. This translates into a systematic uncertainty on $\Delta\mu/\mu$ of $\sim 0.2 \times 10^{-5}$, which was added to the systematic

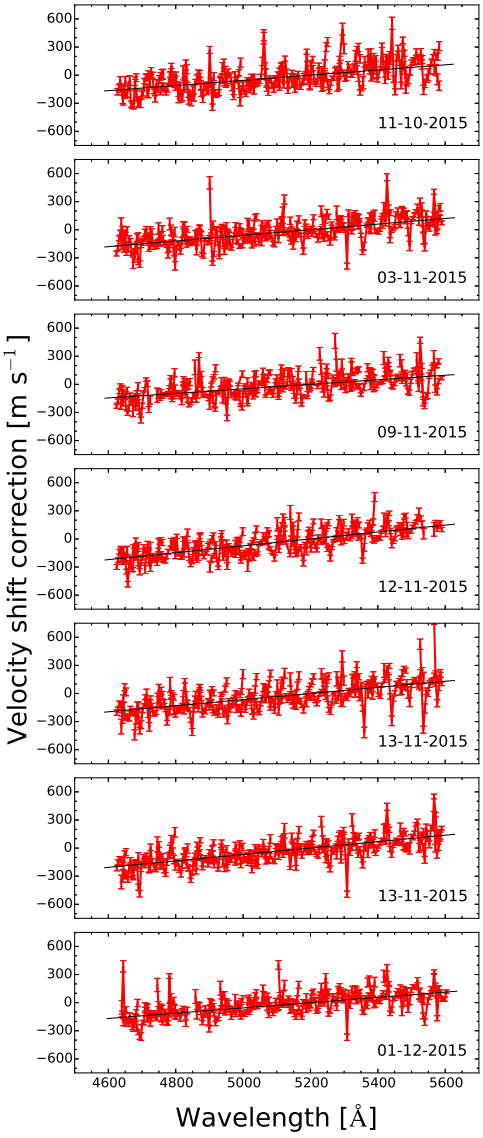

FIGURE 5.4: Map of the UVES long-range wavelength scale distortions in the solar twin HD001835 exposures taken in 2015, with a one-to-one correspondence with the values listed in Table 5.2, i.e. the top panel corresponds to the first row of the table. All the exposures were recorded immediately after their corresponding J0000+0048 science exposures. In each panel, the long-range distortions relative to a single quasar exposure are shown for the lower CCD in the red arm of UVES. The velocity shifts were measured on ~ 10 echelle orders in each exposure. The fitted slopes show the velocity shift needed to counter the long-range distortions. Since any constant velocity offset is not relevant for the long-range distortions analysis, the map was shifted to a zero velocity at $\lambda = 5300$ Å.

error budget.

INTRA-ORDER DISTORTIONS

Whitmore *et al.* [103] found that the wavelength scale of the ThAr calibration suffers from velocity shifts within each echelle order. These shifts have a magnitude of several hundreds of m s^{-1} and may affect the fiducial value of $\Delta\mu/\mu$ by introducing a relative shift among the CO transitions. However, since the position of the CO transitions along their respective echelle orders is independent of the repeated pattern of intra-order distortions across the orders, the velocity shift imparted to a given CO transition can be considered as randomly distributed. The intra-order distortions introduce in each exposure a velocity shift which is translated into a systematic error on $\Delta\mu/\mu$ by:

$$\delta(\frac{\Delta\mu}{\mu}) = \frac{(\Delta v/c)}{\sqrt{N}\Delta K_i}, \tag{5.3}$$

where Δv is the mean magnitude of the intra-order distortions, $\Delta K_i = 0.06$ is the spread in the sensitivity coefficients, and N is the number of the CO transitions. Because of the self-blending of the CO branches, the number of CO transitions that are effectively contributing to the signal is lower than the total number of CO transitions considered to build the band contour. By analyzing CO absorption from the same band systems in a different absorber, Daprà *et al.* [30] found that only $\sim 20\%$ of the total number of CO lines effectively contribute to the signal. As a consequence, a value of $N = 25$ was adopted for the number of transitions effectively contributing to the signal. The dedicated supercalibration exposures taken in 2015 returned a mean amplitude of the intra-order distortions of $\Delta v = 67.1$ m s^{-1}, while the ST exposures from 2014 delivered a mean amplitude of $\Delta v = 52.4$ m s^{-1}. These values translate into $\Delta\mu/\mu$ uncertainties of $\delta_{2015} = 0.34 \times 10^{-5}$ and $\delta_{2014} = 0.27 \times 10^{-5}$. The systematic uncertainty due to the intra-order distortions was derived by combining these two values using a weighted average, using the S/N of the two sub-spectra as weights. This procedure delivered an uncertainty on $\Delta\mu/\mu$ of $\sim 0.3 \times 10^{-5}$, which was included in the systematic uncertainty.

5

5.4.4. SPECTRAL REDISPERSION

A potential source of systematic uncertainties is the spectral redispersion. While building the final 1D spectrum, the different exposures were redispersed onto a common wavelength grid. This procedure implies a rebinning of the spectra, which can cause flux correlations between adjacent pixels, and the (arbitrary) choice of the grid can slightly distort the line profiles, affecting the value of $\Delta\mu/\mu$.

To estimate the impact of the spectral redispersion on the fiducial value presented in this work, the exposures were recombined using ten different wavelength grids in the range 1.9-2.1 km s^{-1} per pixel. Subsequently, a value for $\Delta\mu/\mu$ was returned by each spectrum and was compared with the fiducial value. The average

deviation from the fiducial valued was 0.1×10^{-5}, which was added to the systematic error budget.

5.4.5. TOTAL SYSTEMATIC UNCERTAINTY

The total systematic uncertainty on the fiducial value of $\Delta\mu/\mu$ was calculated by adding in quadrature all the contributions to the systematic error. The updated fiducial $\Delta\mu/\mu$ value therefore becomes $\Delta\mu/\mu = (1.8 \pm 2.2_{\rm stat} \pm 0.4_{\rm syst}) \times 10^{-5}$. This value is delivered by the analysis of 9 CO bands in the spectrum of J0000+0048, which was partially corrected for the long-range distortions. The impact of such distortions in the exposures taken without dedicated supercalibrations was estimated and it is included in the systematic error budget.

5.5. CONCLUSION

In this work, the analysis of CO absorption in the system at $z_{\rm abs} = 2.52$ in the line-of-sight towards quasar J0000+0048 was presented, in order to constrain the temporal variation of the proton-to-electron mass ratio. CO was found in 10 different bands, although one is completely overlapped by intervening metal absorption, covering the wavelengths 4660-5448 Å. A CO temperature of $T_{\rm CO} = 11.2$ K was derived and, starting from the updated molecular database reported by Daprà *et al.* [30], an effective band contour was created and it was fitted using the comprehensive fitting technique against the quasar spectrum. This approach allowed the simultaneous fitting of all the CO vibrational bands using four free parameters only, namely the total column density $N_{\rm CO}$, the absorption redshift $z_{\rm abs}$, the Doppler width $b_{\rm CO}$, and the relative variation of the proton-to-electron mass ratio $\Delta\mu/\mu$. The absorption model returned $\Delta\mu/\mu = (1.8 \pm 2.2_{\rm stat} \pm 0.4_{\rm syst}) \times 10^{-5}$. This value agrees well with the value of $\Delta\mu/\mu = (0.7 \pm 1.6_{\rm stat} \pm 0.5_{\rm syst}) \times 10^{-5}$ derived by Daprà *et al.* [30] from the spectrum of SDSS J123714.60+064759.5 in showing no variation of μ over a look-back time of ~ 11.2 Gyrs.

A way to improve this $\Delta\mu/\mu$ value is to include the CO absorption in a combined analysis with different molecules, which are sensitive to a varying-μ. Molecular hydrogen is the main candidate for such a combined analysis, since it is assumed to be cospatial with CO and it is often observed in > 50 transitions at $z_{\rm abs} > 2$. Daprà *et al.* [30] reported the first combined analysis of CO and H_2 in the absorbing system towards quasar SDSS J123714.60+064759.5. They found that the constraint on $\Delta\mu/\mu$ returned by the combined analysis of CO and H_2 is ~ 38% more stringent than that derived from CO absorption only. Molecular hydrogen absorption in J0000+0048 was reported by Noterdaeme *et al.* [42], who detected it using an XShooter spectrum with a higher S/N and a lower resolution than the UVES one. However, the faintness of the background quasar results in a very low S/N < 2 at the H_2 absorption wavelengths in the UVES spectrum (~ 3600 Å). Moreover, molecular hydrogen has a high column density [$N(H_2) \sim 10^{20.43}$cm^{-2}, 42], which results in strongly saturated tran-

sitions. Because of these two effects, H_2 absorption is unlikely to add any valuable signal to the analysis of $\Delta\mu/\mu$ in this system. Another way to improve the $\Delta\mu/\mu$ value presented here is to increase the S/N in the spectral regions containing the CO absorption features by further observing the quasar.

ACKNOWLEDGMENTS

The authors thank the Netherlands Foundation for Fundamental Research of Matter (FOM) for financial support. MTM thanks the Australian Research Council for *Discovery Project* grant DP110100866 which supported this work. PN gratefully acknowledges support from the Indo-French Centre for the Promotion of Advanced research under grant 5504-2. WU thanks the European Research Council for an ERC-Advanced grant (No 670168). The work is based on observations with the ESO Very Large Telescope at Paranal (Chile).

6

TESTING THE VARIABILITY OF THE PROTON-TO-ELECTRON MASS RATIO FROM OBSERVATIONS OF METHANOL IN THE DARK CLOUD CORE L1498

Daprà, M., Henkel, C., Levshakov, S. A., Menten, K. M., Muller, S., Bethlem, H., Leurini, S., Lapinov, A. V., Ubachs, W.
Mont. Not. Roy. Astron. Soc. ***472****, 4434-4443 (2017)*

The dependence of the proton-to-electron mass ratio, μ, on the local matter density was investigated using methanol emission in the dense dark cloud core L1498. Towards two different positions in L1498, five methanol transitions were detected and an extra line was tentatively detected at a lower confidence level in one of the positions. The observed centroid frequencies were then compared with their rest frame frequencies derived from least-squares fitting to a large data set. Systematic effects, as the underlying methanol hyperfine structure and the Doppler tracking of the telescope, were investigated and their effects were included in the total error budget. The comparison between the observations and the rest frame frequencies constrains potential μ variation at the level of $\Delta\mu/\mu < 6 \times 10^{-8}$, at a 3σ confidence level. For the dark cloud we determine a total CH_3OH (A+E) beam averaged column density of $\sim 3-4 \times 10^{12}$ cm^{-2} (within roughly a factor of two), an E- to A-type methanol column density ratio of $N(A\text{-}CH_3OH)/N(E\text{-}CH_3OH) \sim 1.00 \pm 0.15$, a density of $n(H_2) = 3 \times 10^5$ cm^{-3} (again within a factor of two), and a kinetic temperature of $T_{kin} = 6 \pm 1$ K. In a kinetic model including the observed line intensities, the $n(H_2)$ density is higher and the temperature is lower than that derived in previous studies based on different molecular species; the intensity of the $1_0 \rightarrow 1_{-1}$ E line strength is not well reproduced.

6.1. INTRODUCTION

Theories postulating the space-time dependence of fundamental constants, all implying some form of a violation of the Einstein equivalence principle [3], typically invoke additional quantum fields, beyond those of the Standard Model of particle physics, which then couple to the matter or energy density [e. g., 19–21]. Such theoretical frameworks may be subdivided into two classes, one connecting to the cosmological scenario of a growing dark energy density, the other connecting to local environmental effects.

A similar division holds for the observational perspective as well. Variation of fundamental constants, such as the fine structure constant, $\alpha = e^2/4\pi\epsilon_0\hbar c$, and the proton-to-electron mass ratio, $\mu = M_P/m_e$, on a cosmological time scale is probed by spectroscopy in the early Universe, either via measurements of metal ions [109, 119, 120, 154, 155], molecular hydrogen [28, 29, 73], ammonia molecules [54–56, 121], or methanol molecules [62–64]. On the other hand, the so-called chameleon scenario [24, 25] assumes the existence of light scalar fields that acquire effective potential and mass because of their coupling to matter. This phenomenon depends on the local matter density and therefore can be probed through comparisons of different local environments [156]. As an example, the dependency of the fundamental constants on the gravitational field was investigated via atomic [157] and molecular spectra [66] in the photosphere of white dwarfs. Another example is the coupling of light scalar fields to the local matter density [27]. Such dependency can be investigated by comparing the measurements of physical properties in the high-density terrestrial environment, $n_{\rm Earth} \geq 10^{19}$ cm^{-3} and in the comparatively very low-density interstellar clouds, where densities are ≥ 14 orders of magnitude lower than on Earth.

As in most studies targeting variation of fundamental constants, molecules and their spectra are ideal test grounds. Levshakov *et al.* [67, 68] used the ammonia method, i.e. they compared ammonia, NH_3, inversion transitions with rotational transitions of molecules that were considered to be co-spatial with ammonia, to investigate the relative difference between the observed proton-to-electron mass ratio, $\mu_{\rm obs}$, and the reference laboratory value $\mu_{\rm lab}$:

$$\frac{\Delta\mu}{\mu} = \frac{\mu_{\rm obs} - \mu_{\rm lab}}{\mu_{\rm lab}}. \tag{6.1}$$

They derived an upper limit of $|\Delta\mu/\mu| \leq 3 \times 10^{-8}$ at a level of confidence of 3σ by observing 41 cold cores in the Galaxy [67]. More recently, Levshakov *et al.* [69] tested this upper limit against potential instrumental errors by employing spectrometers with different spectral resolution. By re-observing 9 cores with the Medicina 32m and the Effelsberg 100m telescopes, they derived a constraint of $|\Delta\mu/\mu| < 2 \times 10^{-8}$ at a 3σ confidence level.

As already mentioned, the ammonia method relies on the assumption that the emission regions of the considered molecules are co-spatial. This may introduce

systematic effects affecting the $\Delta\mu/\mu$ value due to chemical segregation. This particularly holds when - as it is commonly being done - NH_3 line frequencies are coupled to HC_3N line frequencies. HC_3N is a molecule representing young, early time chemistry of a molecular cloud, while NH_3 stands for late time chemistry [158]. The relevant time scales range from several 10^5 to $\sim 10^6$ yrs.

Methanol, CH_3OH, is another molecule sensitive to a variation in μ and it is abundantly present in the Universe, with more than 1000 lines detected in our Galaxy [159]. It represents a better target than ammonia for a μ variation analysis for two main reasons: i) it has several transitions showing higher sensitivities to a varying μ [57–59, 75], and ii) methanol transitions have different intrinsic sensitivities, therefore it is possible to derive a value for $\Delta\mu/\mu$ based only on its transitions, avoiding the assumption of co-spatiality between different molecules as for the ammonia method.

L1498 is a dense core in the Taurus-Auriga complex and represents an example of the simplest environment in which stars form. Its dense gas content was first studied by Myers *et al.* [160] and it is considered a starless core, since it is not associated with IRAS [161] or 1.2 mm point sources [162]. L1498 was identified as a chemically differentiated system by Kuiper *et al.* [163] [for extra details about its chemical structure see also 164, 165]. Tafalla *et al.* [162] presented line and continuum observations, finding a systematic pattern of chemical differentiation. In a later study, Tafalla *et al.* [166] characterised its physical structure and chemical composition, finding that the density distribution of L1498 traced by the 1.2 mm dust continuum emission is very close to that of an isothermal sphere, with a central density of $n \sim 10^5$ cm^{-3}. They also reported that the gas temperature distribution in the core is consistent with a constant value of $T_{\rm kin} = 10 \pm 1$ K and that lines have a constant, non-thermal full width at half maximum, *FWHM*, of $\Delta V \sim 0.125$ km s^{-1} in the inner core. More recently, Tafalla *et al.* [71] investigated the molecular emission of 13 species, including methanol, in L1498. They found that the abundance profiles of most species suffer from a significant drop towards the core centre [see Fig. 1 of 71], resulting in a ring-like distribution around the central dust peak indicating depletion of these molecules onto icy dust grain mantles ('freeze out'). They showed that methanol emission forms a ring with two discrete peaks, one to the SE (hereafter L1498-1) and one to the NW (hereafter L1498-2) of the dust peak. It is noted that the NW methanol peak is dimmer, with a peak intensity of $\sim 80\%$ of the SE peak intensity.

In view of its low $T_{\rm kin}$ and low degree of turbulence [non-thermal *FWHM* $\simeq 0.12$ km s^{-1}, 166], L1498 shows narrow emission lines and therefore it is an ideal target for measuring a μ-variation. This dense core was already included in the sample studied by Levshakov *et al.* [67, 68, 69]. In the following, the detection of 5 methanol lines in L1498-1 and L1498-2 using the Institut de Radio Astronomie Millimétrique, IRAM, 30m telescope[1] is presented and it is used to derive a value for $\Delta\mu/\mu$ to test

[1] Based on observations carried out under project number 014-14 with the IRAM 30m Telescope. IRAM is

the chameleon scenario and to constrain physical parameters of the cloud. The observations are described in Section 6.2, and their results in Section 6.3. The physical parameters of L1498 are derived in Section 6.4, while the laboratory rest frequencies used in this work are discussed in Section 6.5. Finally, the measurement of $\Delta\mu/\mu$ is presented in Section 6.6, and the results obtained are summarised in Section 6.7.

6.2. OBSERVATIONS

The IRAM 30m observations of L1498 were carried out on July 20th and 21st 2014 using the Eight MIxer Receiver [EMIR, 167]. Two EMIR setups were used throughout the observations to target the methanol transitions. The 3 mm E090 band was used to measure methanol lines in the range 96.7-109 GHz, while lines in the range 145-157.3 GHz were observed using the 2 mm E150 band. For both setups, the EMIR lower and upper inner sidebands, LI and UI respectively, were used in dual-polarisation mode. The data were recorded using the VErsatile SPectrometer Array (VESPA) with its 3 kHz channel width, corresponding to velocity channels of ~ 10 and 7 m s^{-1} for the E090 and E150 bands, respectively.

The observations were performed using the position switching mode with offsets of $\pm$600, $\pm$900, or $\pm$1800 arcsec in azimuth. Alternating between western and eastern offsets helped to provide flat spectral baselines. Comparing data with different offset positions did not reveal any significant differences, thus ensuring that emission from the offset positions did not affect the resulting spectra. A single scan's duration was ~ 6 min, divided into two parts. The first half involved integration in the off-source position and the second half was devoted to the on-source integration. Sky frequencies were updated at the beginning of each scan (see Section 6.6.2). Pointing was checked frequently and was found to be stable within 3 arcsec. Calibration was obtained every 12 minutes using standard hot/cold-load absorber measurements. The data reduction was performed using the GILDAS software's CLASS package[2]. Only linear baselines were subtracted from the individual spectra. The raw frequencies were Doppler shifted in order to correct for Earth motion relative to L1498 during the observations [v_{LSR} = 7.8 km s^{-1}, 166]. The same value of v_{LSR} was used for the two observed positions.

The IRAM 30m telescope adopts the optical definition of radial velocity, while the radio definition is implemented in CLASS. The optical radial velocity is defined as:

$$\frac{v_{LSR}^{opt}}{c} = \frac{\nu_{rest}}{\nu_{obs}} - 1, \tag{6.2}$$

where ν_{obs} is the observed frequency and ν_{rest} is the reference frequency in the rest

supported by INSU/CNRS (France), MPG (Germany) and IGN (Spain).
[2] http://www.iram.fr/IRAMFR/GILDAS/

frame. In contrast, the radio definition of the radial velocity is given by:

$$\frac{v_{LSR}^{rad}}{c} = 1 - \frac{\nu_{obs}}{\nu_{rest}}, \tag{6.3}$$

using the same symbols as in Eq. (6.2). As a consequence, the radial velocities returned by the two definitions are different, $v_{opt} \neq v_{rad}$. For L1498, which has $v_{LSR} = 7.8$ km s^{-1}, the discrepancy between the two definitions is of the order of $\sim 10^{-8}$ km s^{-1} and hence is considered negligible.

The observation time was divided unevenly between the two peaks, resulting in ~ 14 hrs of integration on L1498-1 and ~ 4 hrs on L1498-2. This was done in order to reach a good signal-to-noise ratio, S/N, for the source with the brighter emission [the SE peak L1498-1, see 71].

6.3. RESULTS

Several methanol transitions were detected at a $> 10\sigma$ confidence level in L1498-1 and L1498-2, respectively. All the detected lines are well described by a single Gaussian profile, as shown in Fig. 6.1, which has three fitting parameters: the line intensity, expressed in terms of the main beam brightness temperature T_{mb}, the line width *FWHM*, and the transition frequency ν_{obs}, which is corrected for the shift introduced by the radial velocity of L1498 [$v_{LSR} \sim 7.8$ km s^{-1}, 71]. The line parameters related to each detected transition in L1498-1 and L1498-2 are listed in Table 6.1. All the detected methanol transitions turn out to be optically thin.

The weak transition $2_0 \rightarrow 1_0$ E (at a rest-frame frequency of $\nu_{rest} \simeq 96.744545$ GHz) was detected at a confidence level of 5σ in the brighter position L1498-1 only. Although weak, it is well described by a single Gaussian profile, as shown in Fig. 6.1, whose parameters are included in Table 6.1. An extra line, the $2_0 \rightarrow 2_{-1}$ E transition ($\nu_{rest} \simeq 157.276023$ GHz), may have also been detected with a confidence level of 3σ in L1498-1. However, the detection is tentative. The line may be broadened by the noise and is hence not considered further in this work.

6.4. CLOUD PROPERTIES

As already briefly mentioned in Section 6.1, Tafalla *et al.* [166] determined physical and chemical characteristics of the dark cloud L1498, based on measurements of NH_3, N_2H^+, CS, $C^{34}S$, $C^{18}O$ and $C^{17}O$. Our CH_3OH line data can be used to complement their results. To simulate the measured line parameters we applied the RADEX non-LTE code model [168, 169], which is based on collision rates with H_2 reported by Rabli and Flower [170], using kinetic temperature, density, and E- or A-type methanol column density as variables. The code calculates line intensities for a uniform sphere, which is justified because of the overall shape of the cloud and

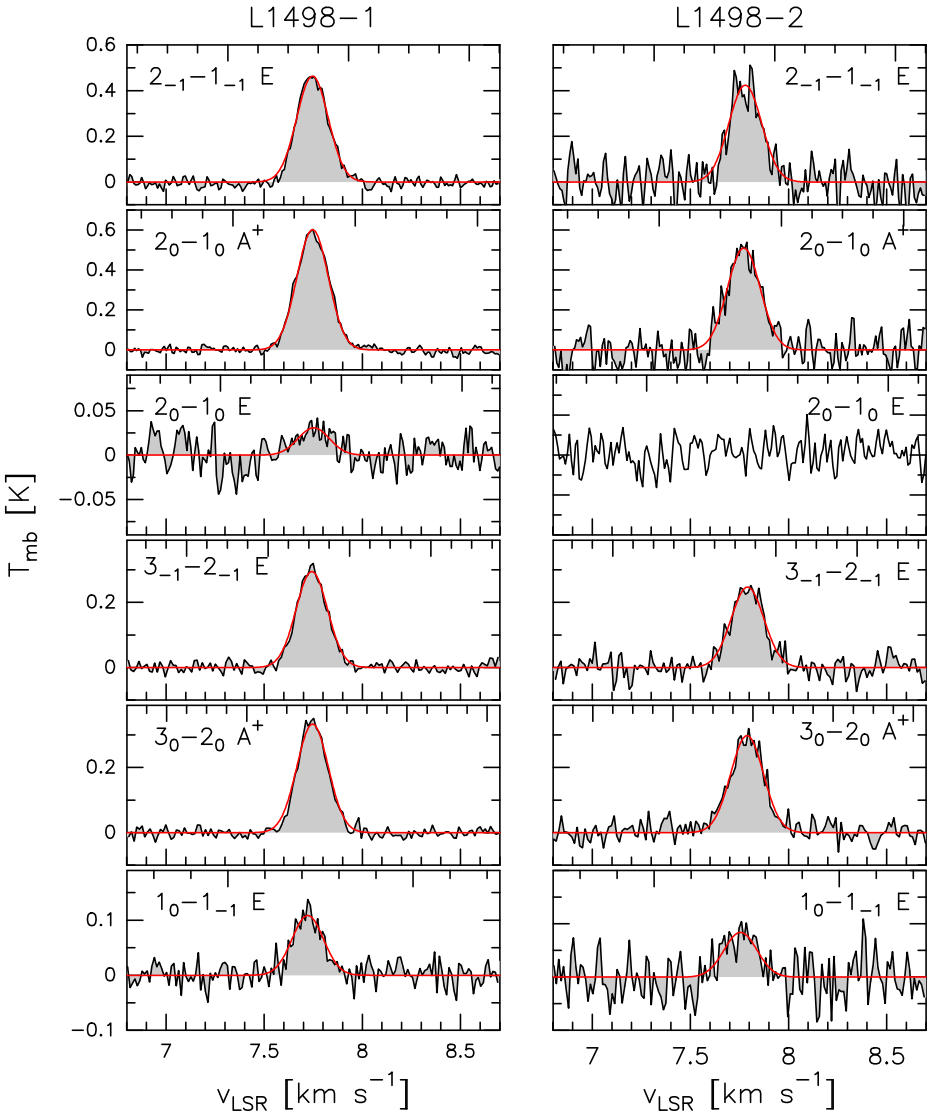

FIGURE 6.1: Spectra of the detected methanol transitions in L1498-1 (left panels; $\alpha_{J2000} = 04^h\ 10^m\ 56.6^s$, $\delta_{J2000} = +25°\ 09'\ 08''$) and L1498-2 (right panels; $\alpha_{J2000} = 04^h\ 10^m\ 47.0^s$, $\delta_{J2000} = +25°\ 10'\ 18''$). The (red) solid lines show the Gaussian fits. The transition $3_{-1} \rightarrow 2_{-1}$ E fell near the edge of the sideband, hence the background is not provided beyond radial velocities of ~ 8.8 km s^{-1}. The $2_0 - 1_0$ E transition was not detected towards the L1498-2 position.

the radial profile derived from ammonia for the kinetic temperature [166], which resulted in a constant value. For the background temperature we adopted 2.73 K and for the line width, being relevant for the methanol column density, an average value derived from Table 6.1 ($\Delta V = 0.165$ km s^{-1}; note that this is slightly larger than the value taken from the literature and given in Section 6.1). Since the line width is known to a far higher accuracy than the column density (the latter is only known to a factor of roughly two), the specific choice of ΔV is not critical. With this model most line intensities are well reproduced. This also includes our non-detection of the $2_0 \rightarrow 2_{-1}$ E transition, with the model mostly indicating absorption at line intensities below our sensitivity limit. Nevertheless, none of the fits is perfect, because we do not obtain good simulations of the $1_0 \rightarrow 1_{-1}$ E transition. For this transition the modelled intensities are too low by factors of $\sim 2-3$.

To find the best solution(s), we used RADEX to create a grid in $T_{\rm kin}$ and $n(H_2)$, optimising for each ($T_{\rm kin}$, $n(H_2)$) pair the column density by calculating reduced χ^2 values. With six (L1498-1) and five (L1498-2) transitions and three free parameters (kinetic temperature, density, and column density), there are three and two degrees of freedom, respectively. Because of the above mentioned $1_0 \rightarrow 1_{-1}$ E line, reduced χ^2 values, i.e the sum of the squared differences between observed and modelled line intensities, divided by the square of the uncertainty in the measured parameter (10% of the line temperature and standard deviation of the Gaussian amplitude, added in quadrature) never get close to unity. Nevertheless, Fig. 6.2 provides resulting values for L1498-1 and L1498-2 in the two dimensional ($T_{\rm kin}$, $n(H_2)$) space with background shading and contours reflecting the reduced χ^2 values. For L1498-1, the source with best determined line intensities, the best solution yields a column density of order N(E+A methanol) $\sim 3 \times 10^{12}$ cm^{-2}, $T_{\rm kin} \sim 6$ K, and $n(H_2) \sim 3 \times 10^5$ cm^{-3}. For position L1498-2, the optimal solution returns a similar density, a lower value for $T_{\rm kin}$ of ~ 5 K and a methanol column density of N(E+A methanol) $\sim 4 \times 10^{12}$ cm^{-2}. In other words, the gas traced by methanol appears to be cooler and denser than that analysed by Tafalla *et al.* [166], but the temperatures are close to the value of 7.1 ± 0.5 K reported by Levshakov *et al.* [68]. The results returned by the RADEX code are presented in Column 6 of Table 6.1.

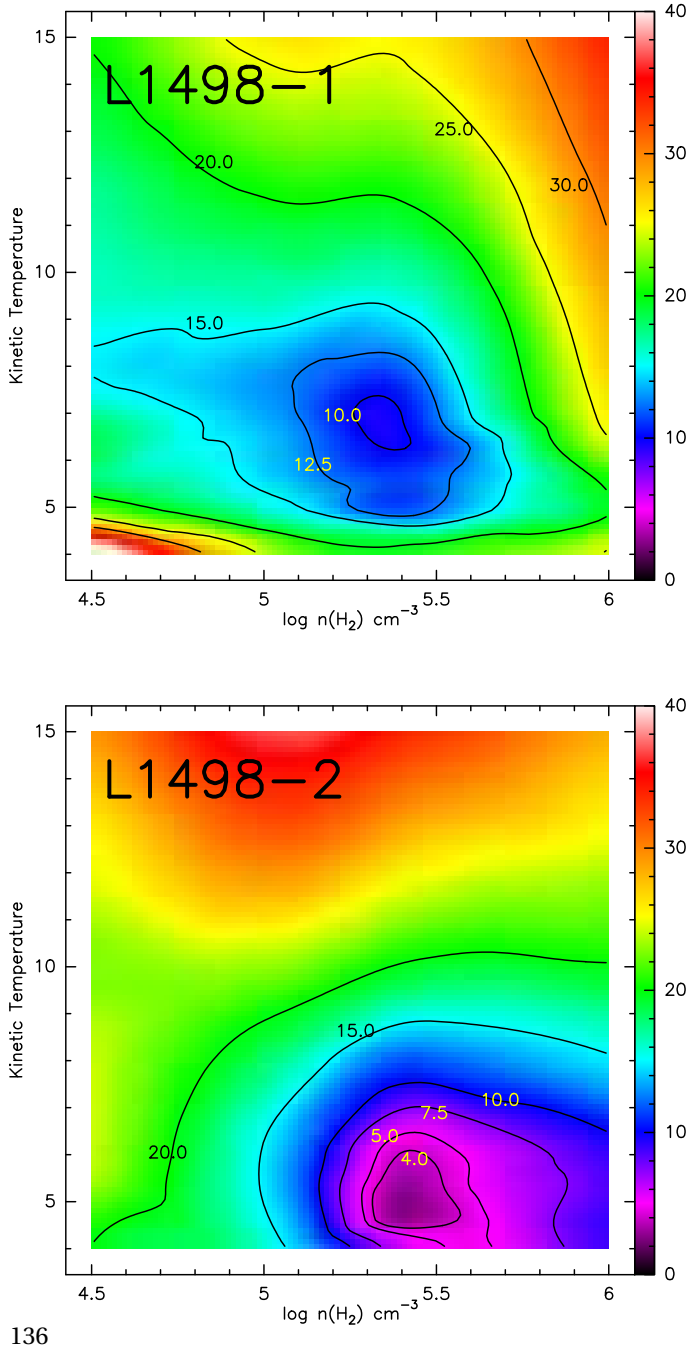

FIGURE 6.2: Map of the reduced χ^2 value as function of density and kinetic temperature values used to simulate the E- and A-type main beam brightness temperatures in L1498-1 (upper panel) and L1498-2 (lower panel).

TABLE 6.1: Details of the methanol transitions observed in L1498. Columns 3-4 show the measured frequencies and line widths. Columns 5-6 present the measured and modeled (main beam) brightness temperatures, the latter for the solution with the lowest reduced χ^2 value. The optical depths τ_v, calculated with the LVG code, are listed in column 7. Columns 8-9 present the energies of the upper and lower states above the ground state. Column 10 shows the sensitivities of the transitions to a varying proton-to-electron mass ratio and column 11 presents the EMIR band in which the transitions were observed. The LVG simulations were performed assuming a molecular hydrogen density of $n(H_2) = 3 \times 10^5$ cm^{-3}, a kinetic temperature of $T_{kin} = 6$ K, and an E- and A-type methanol column density of $N_E = N_A = 3.3 \times 10^{12}$ cm^{-2} for L1498-1. For simulating the methanol transitions in L1498-2, a molecular hydrogen density of $n(H_2) = 3 \times 10^5$ cm^{-3}, a kinetic temperature of $T_{kin} = 5$ K, and an E- and A-type methanol column density of $N_E = N_A = 4.3 \times 10^{12}$ cm^{-2} were assumed.

Source	Transition	Observed frequencies[a] [MHz]	FWHM [MHz]	T_{mb} [mK]	T_{RADEX} [mK]	τ_v	E_{up} [K]	E_{low} [K]	Sensitivity coefficients	Band
L1498-1	$2_{-1} \rightarrow 1_{-1}$ E	96739.376 ± 0.001	0.046 ± 0.003	556 ± 15	524	0.23	12.2	7.7	-1.0	E090
α = 04:10:56.6	$2_0 \rightarrow 1_0$ A$^+$	96741.388 ± 0.001	0.049 ± 0.003	716 ± 15	620	0.27	6.8	2.3	-1.0	
δ = +25:09:08.0	$2_0 \rightarrow 1_0$ E	96744.560 ± 0.007	0.055 ± 0.003	32 ± 17	60	0.03	19.5	15.0	-1.0	
	$3_{-1} \rightarrow 2_{-1}$ E	145097.464 ± 0.001	0.085 ± 0.001	374 ± 14	412	0.23	19.0	12.2	-1.0	E150
	$3_0 \rightarrow 2_0$ A$^+$	145103.212 ± 0.001	0.077 ± 0.001	426 ± 12	423	0.23	13.6	6.8	-1.0	
	$1_0 \rightarrow 1_{-1}$ E	157270.877 ± 0.003	0.079 ± 0.005	137 ± 19	94	0.44	15.0	7.7	-3.5	
	$2_0 \rightarrow 2_{-1}$ E	Not detected			52	0.32	19.5	12.2	-3.5	
L1498-2	$2_{-1} \rightarrow 1_{-1}$ E	96739.365 ± 0.002	0.048 ± 0.003	508 ± 75	545	0.37	12.2	7.7	-1.0	E090
α = 04:10:47.0	$2_0 \rightarrow 1_0$ A$^+$	96741.380 ± 0.001	0.054 ± 0.003	608 ± 69	619	0.42	6.8	2.3	-1.0	
δ = +25:10:18.0	$2_0 \rightarrow 1_0$ E	Not detected			60	0.04	19.5	15.0	-1.0	
	$3_{-1} \rightarrow 2_{-1}$ E	145097.440 ± 0.001	0.097 ± 0.005	325 ± 29	360	0.36	19.0	12.2	-1.0	E150
	$3_0 \rightarrow 2_0$ A$^+$	145103.191 ± 0.002	0.091 ± 0.003	372 ± 26	357	0.30	13.6	6.8	-1.0	
	$1_0 \rightarrow 1_{-1}$ E	157270.858 ± 0.010	0.100 ± 0.013	115 ± 38	88	0.66	15.0	7.7	-3.5	
	$2_0 \rightarrow 2_{-1}$ E	Not detected			41	0.41	19.5	12.2	-3.5	

[a] corrected for the radial velocity of L1498

This kinetic temperature is lower than the lower limit reported by Goldsmith and Langer [171], who claimed that there is no equilibrium solution for $T_{\rm kin} < 8$ K in their model of thermal balance in dark clouds. Assuming that cosmic rays are the only heating source of the dark cloud, their model returns gas temperatures in the range 8-12 K. A similar result was obtained by Goldsmith [172], who used an LVG model for radiative transfer including the effect of the gas-dust coupling at different depletions of the major molecular coolants.

While a reduced χ^2 value of order 10, mainly due to the $1_0 \rightarrow 1_{-1}$ E line, in L1498-1 and of order 3 in L1498-2 may raise doubts about the above mentioned results, it is nevertheless a result worth to be presented and to be confirmed (or rejected) by other methanol transitions as well as by lines from other molecular species. A possible explanation for the high values of the reduced χ^2 may lie in the uncertainties in the collisional rates used in RADEX and in our limited knowledge on cloud geometry and 3-dimensional velocity field. However, testing this is beyond the goal of this work. Another remarkable result is that N(E-CH_3OH) $\sim N$(A-CH_3OH), with an accuracy of $\sim 15\%$. Here we should consider that the lowest E-state, the 1_{-1} E level, is 7.9 K above the lowest (0_0) A-state. Following Friberg *et al.* [70], the E/A abundance ratio for a thermalisation temperature of 10 K becomes 0.69, which is as far from unity as our calculations may (barely) permit. For a thermalisation at 6 K, our determined E/A abundance ratios would then clearly be too large. Perhaps, the bulk of the methanol has been formed prior to the occurrence of highly obscured deeply shielded regions with kinetic temperatures below 10 K.

6.5. REST FREQUENCIES

The methanol lines detected in L1498 are very narrow, with a width of less than ~ 0.2 km s^{-1} corresponding to ~ 50 kHz for the lines observed at 96 GHz and ~ 80 kHz for the lines observed near 150 GHz (see Table 6.1). In order to derive a tight constraint on a varying proton-to-electron mass ratio, the astrophysical data need to be compared with the most accurate values for the rest frequencies. In the following, a concise review on the laboratory frequencies is provided.

The main body of laboratory frequencies for methanol lines stems from the study of Lees and Baker [173] and the subsequently published database [174]. The lines presently observed in L1498 are all contained in that list and are reproduced in Table 6.2. The estimated uncertainty for these laboratory measurements is about 50 kHz for all transitions. Later, transition frequencies at a much higher accuracy were measured for a limited number of lines by beam-maser spectroscopy [175–177] and by microwave Fourier-transform spectroscopy [178]. None of these measurements refer to the transitions considered in this work.

Hougen *et al.* [182] developed the BELGI code, which is a program to calculate and fit transitions of molecules containing an internally hindered rotation. This program was employed by Xu and Lovas [183] to produce a fit of 6655 molecular lines

TABLE 6.2: List of rest-frame frequencies derived from laboratory data and numerical calculations.

Transition	Measured frequency [MHz]		Calculated frequency [MHz]
$2_{-1} \rightarrow 1_{-1}$ E	96739.390(50)[a]	96739.362(5)[b]	96739.358(2)[d]
$2_0 \rightarrow 1_0$ A$^+$	96741.420(50)[a]	96741.375(5)[b]	96741.371(2)[d]
$2_0 \rightarrow 1_0$ E	96744.580(50)[a]	96744.550(5)[b]	96744.545(2)[d]
$3_{-1} \rightarrow 2_{-1}$ E	145097.470(50)[a]	145097.370(10)[c]	145097.435(3)[d]
$3_0 \rightarrow 2_0$ A$^+$	145103.230(50)[a]	145103.152(10)[c]	145103.185(3)[d]
$1_0 \rightarrow 1_{-1}$ E	157270.700(50)[a]	157270.851(10)[c]	157270.832(12)[d]

[a] from Lees and Baker [173]
[b] from Müller *et al.* [179]
[c] from Tsunekawa *et al.* [180]
[d] from Xu *et al.* [181]

delivering the values of 64 molecular constants describing the rotational structure of methanol. Based on these molecular parameters the transition frequencies can be recalculated with a higher accuracy, assuming that the fitting procedure averages out the statistical uncertainties in the experimental data.

In 2004, Müller *et al.* [179] published a study focusing on the laboratory measurements of methanol lines that can be observed either in masers or in dark clouds. In their studies, they used the Cologne spectrometer, in the range 60-119 GHz, and the Kiel spectrometer, in the range 8-26 GHz. The three lines at 96 GHz, presently observed in L1498, were measured with an estimated accuracy of 5 kHz. Müller *et al.* [179] also listed transition frequencies for four lines at 145 and 157 GHz, that were previously measured with a claimed accuracy of 10 kHz by Tsunekawa *et al.* [180]. These most accurate experimental values for the presently observed lines are also listed in Table 6.2.

More recently, Xu *et al.* [181] improved the theoretical analysis based on an extended version of the BELGI program, with the inclusion of a large number of torsion-rotation interaction terms to the Hamiltonian, and by fitting a huge data set including ~ 5600 frequency measurements in the microwave, sub-millimetre wave and Terahertz regime, as well as a set of 19 000 Fourier transform far infrared wavenumber measurements to 119 molecular parameters. By replacing some older measurements, which exhibit larger residuals, with more accurate frequency measurements obtained since 1968, they derived an improved set of rest frequencies[3] that is included in the last column of Table 6.2.

Inspection of Table 6.2 shows that a unique and consistent data set of rest frame

[3] `https://spec.jpl.nasa.gov/ftp/pub/catalog/catdir.html`

frequencies does not exists for the six lines of relevance to our observations. Moreover it is clear that the observations in the cold L1498 core are more accurate than most experimental data from the laboratory, and for most lines are also more accurate than the results from the least-squares fitting treatment based on the BELGI model. For the three lines at 96 GHz the laboratory measurements performed with the Köln spectrometer [179], with an estimated uncertainty of 5 kHz, agree very well with the data resulting from the extended BELGI analysis that have an estimated uncertainty of 2 kHz [181]. The deviations between the data sets are ≤ 5 kHz. The frequencies of these lines are some 40-50 kHz lower than in the old measurements of Lees and Baker [173], but in that study the accuracy was estimated at 50 kHz, so that the older data agree with the more recent and more accurate data within 1σ. From this we conclude that for the 96 GHz lines we have a consistent set of rest frame frequencies to an accuracy well below our already rather narrow channel spacing of 10 kHz. Therefore, the most accurate set represented by the values from the extended BELGI analysis of Xu *et al.* [181] was chosen as reference.

For the two higher frequency transitions at 145 GHz the situation is less clear. Experimental laboratory data stem from the Toyama atlas [180] for which a measurement uncertainty of 10 kHz was claimed. These data deviate with 65 kHz and 33 kHz from the extended BELGI analysis. In a 2008 updated least-squares analysis an uncertainty of 3 kHz is specified. In comparison to the older measurements of Lees and Baker [173] the calculated values [181] are at the limit of 1σ deviation while the deviation from the Toyama data amounts to 2σ.

For the line at 157 GHz the Toyama value agrees well within combined error margins with the calculated value. However both values for this line deviate by 3σ from the older value measured by Lees and Baker [173]. In view of the fact that for the other five lines the theoretical value is expected to be most accurate, for consistency we will also include the extended BELGI analysis of Xu *et al.* [181] for the 157 GHz line in the rest frame set.

From the above evaluation and the graphical comparison of data sets presented in Fig. 6.3 we decide that the results from the comprehensive least-squares fitting treatment [181] provides the best and most consistent set of rest frequencies, in agreement with the accurate data from Müller *et al.* [179], the 157 GHz line measured by Tsunekawa *et al.* [180], and with the older measurements reported by Lees and Baker [173]. Future improved laboratory measurements may decide on the validity of this choice.

The weighted average of the deviations between the observed and the BELGI frequencies returns values of $\Delta\nu_1 = \nu_{\rm obs} - \nu_{\rm lab} = 22 \pm 9$ and $\Delta\nu_2 = 7 \pm 6$ kHz for L1498-1 and L1498-2, respectively. These deviations were translated into radial velocities using the radio definition, as in Eq. (6.3), delivering $v_{\rm LSR1} = 7.745 \pm 0.010$ and $v_{\rm LSR2} = 7.784 \pm 0.012$ km s^{-1} for position L1498-1 and L1498-2 respectively, as shown in Fig. 6.4. We deduce from this that the two positions L1498-1 and L1498-2 have

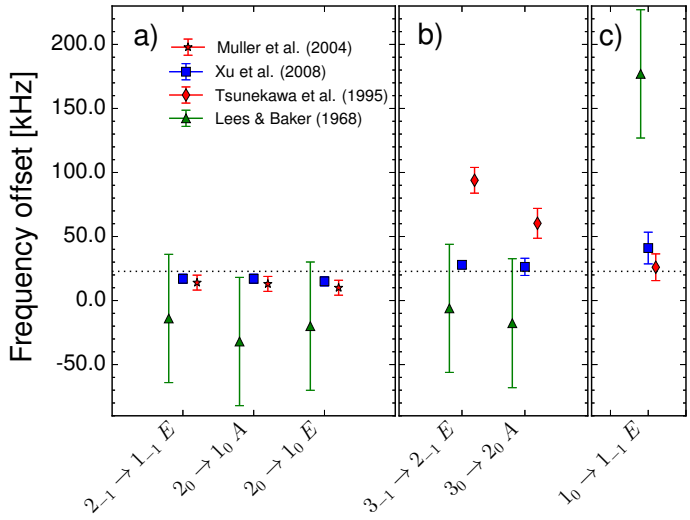

FIGURE 6.3: Frequency offsets between the observed, velocity corrected (see Section 6.5) frequencies and the rest frame frequencies for the methanol transitions detected in L1498-1 at ~ 96 GHz (Panel a), ~ 145 GHz (Panel b) and ~ 157 GHz (Panel c). The (blue) squares show the comparison with the frequencies reported by Xu *et al.* [181], the (green) triangles the frequencies measured by Lees and Baker [173], the (red) stars and the (red) diamonds the frequencies reported by Müller *et al.* [179] and Tsunekawa *et al.* [180], respectively. The dotted line at ~ 22 kHz shows the average deviation of the preferred rest frequency data from the observations.

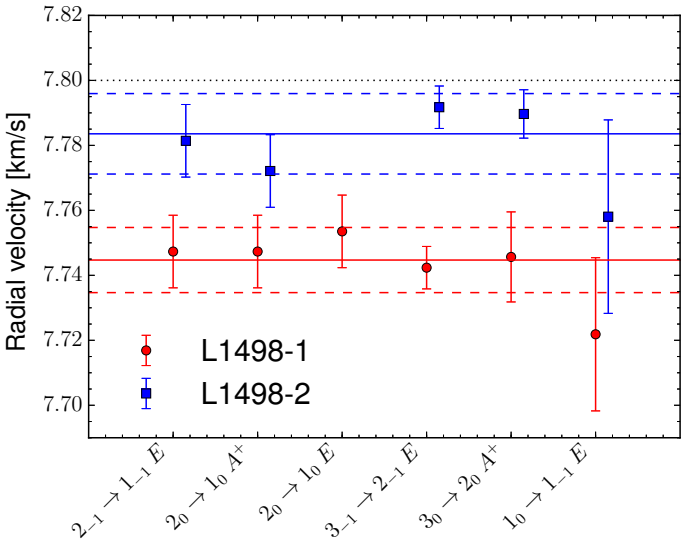

FIGURE 6.4: Radial LSR velocities for positions L1498-1 (red circles) and L1498-2 (blue squares) derived by the comparison of the observed frequencies with those calculated using the extended version of the BELGI program [181]. The solid line represent the radial velocity of the two positions, while the dashed lines show their $\pm 1\sigma$ boundaries. The (black) dotted line shows the v_{LSR} reported by Tafalla *et al.* [166].

different radial velocities.

As will be discussed in the next section, the analysis of the presently observed highly accurate astronomical data, exhibiting an accuracy of 5 kHz or better (see Table 6.1), will provide a consistency check on the choice of the preferable, most accurate rest frame data set.

6.6. CONSTRAINING $\Delta\mu/\mu$

The variation of the proton-to-electron mass ratio was investigated using the methanol transitions that were detected in the two emission peaks of the dark cloud L1498. The observed frequencies of the selected transitions were compared with the rest frame frequencies reported by Xu *et al.* [181], as discussed in Section 6.5, and were subsequently interrelated via:

$$\frac{\Delta\nu_i}{\nu} = K_i \frac{\Delta\mu}{\mu}, \tag{6.4}$$

where $\Delta\nu_i/\nu = (\nu_{obs} - \nu_{lab})/\nu_{lab}$ is the relative difference between the observed and the calculated frequency, of the i-th transition, K_i its sensitivity coefficient, and $\Delta\mu/\mu$

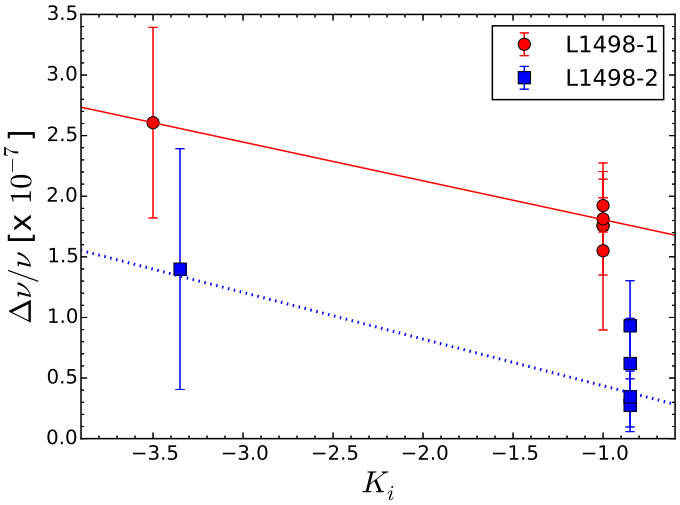

FIGURE 6.5: The relative shifts between the observed, after applying the velocity correction (see Section 6.5), and the calculated frequencies from Xu *et al.* [181] of the methanol transitions observed in L1498-1 (red circles) and in L1498-2 (blue squares) are plotted against their sensitivity coefficients. The solid (red) and the dotted (blue) lines show the linear fit to the data set of L1498-1 and L1498-2, respectively, and their slopes represent the two values of $\Delta\mu/\mu$ delivered. For clarity, a constant offset of +0.15 was applied to the measurements relative to L1498-2 on the x-axis.

is the relative difference between the proton-to-electron mass ratio in the dark cloud and on Earth.

The velocity corrected frequencies of the detected methanol transitions were subsequently compared to the rest-frame frequencies via Eq. (6.4). The comparison with the preferred rest frame frequencies as obtained from the BELGI fit [181] returned values of $\Delta\mu/\mu_1 = (-3.2 \pm 2.0_{\text{stat}}) \times 10^{-8}$ and $\Delta\mu/\mu_2 = (-3.8 \pm 6.6_{\text{stat}}) \times 10^{-8}$, for positions L1498-1 and L1498-2, respectively, as shown in Fig. 6.5. The larger uncertainty in the $\Delta\mu/\mu$ value derived from L1498-2 reflects the spread in the observed frequencies of the lines with $K_i = -1$, which includes the shorter integration time spent on that position. Assuming that the physical conditions of the core are the same in L1498-1 and L1498-2 (see Section 6.4), the weighted average of these two values yields to $\Delta\mu/\mu = (-3.3 \pm 1.9_{\text{stat}}) \times 10^{-8}$, hereafter the fiducial value of $\Delta\mu/\mu$.

The comparison with the measured laboratory frequencies [179, 180] delivered the values of $\Delta\mu/\mu_1 = (3.6 \pm 14.5_{\text{stat}}) \times 10^{-8}$ and $\Delta\mu/\mu_2 = (5.6 \pm 21.4_{\text{stat}}) \times 10^{-8}$, for positions L1498-1 and L1498-2, respectively. The large statistical uncertainties on these values are due to the spread in the frequencies of the lines with $K_i = -1$, i.e. the 96 and the 145 GHz lines, which reflects the inconsistencies between the experimental

data sets.

6.6.1. HYPERFINE STRUCTURE

In the past two years the hyperfine structure in the microwave spectrum of methanol has attracted much attention [184–186], for a part connected to the importance of methanol as the most sensitive probe for varying constants. The underlying hyperfine structure of microwave transitions will cause an asymmetrical line shape, depending on the spread of the hyperfine components within the Doppler profile. However, the presently observed lines in L1498 do not display any asymmetry (see Fig. 6.1) and they can be very well reproduced by a single Gaussian shaped profile.

In addition, unresolved hyperfine structure may cause a shift of the centre-of-gravity determined by the hyperfine-less rotational Hamiltonian. The hyperfine coupling involves three contributions: the magnetic dipole interactions between nuclei with spin $I > 0$, the coupling between the nuclear spins and the rotation, and the coupling between the nuclear spins and the torsion. While the spin-torsion interaction is represented by a vector, hence an irreducible tensor of rank 1, the contributions by the magnetic dipole interactions are described by rank 2 tensors. The dipole-dipole interaction is represented by a traceless irreducible tensor of rank 2 that retains the centre of gravity of the line, i.e. when weighting the intensity contributions of all hyperfine components. The spin-rotation coupling comprises also an irreducible tensor of rank 2, but in addition a scalar contribution (tensor of rank 0) giving rise to a trace that may shift the centre-of-gravity. This effect is quantified here based on the hyperfine calculations by Lankhaar *et al.* [186].

The calculated intensities for the individual hyperfine components of a transition [186] were convoluted using Gaussian profiles with *FWHM*= 35-80 kHz, as shown in Fig. 6.6 for the $2_0 \rightarrow 1_0$ A$^+$ transition, thus creating a line shape profile for each transition. This profile was subsequently compared and fitted to a Gaussian function and its computed line centre was compared with the position of the hyperfine-less zero-point. This procedure was followed for all transitions listed in Table 6.2, resulting in small (< 1 kHz) frequency shifts of the rotational lines. It is noted that this shift comes in addition to the rotational structure and is not contained in the Hamiltonian underlying the BELGI model, although some of the effects of hyperfine shift may, in principle, be covered by adapting the molecular parameters in the fitting procedure.

However, since the shift introduced by the underlying hyperfine structure is below the kHz level, it is not expected to affect significantly the fiducial $\Delta\mu/\mu$ values presented in this analysis. To estimate its impact on a varying μ and to account for possible moderate but not quantifiable deviations from the local thermodynamical equilibrium, an artificial shift of ± 1 kHz, which is a conservative estimate, was introduced in the rest-frame frequency sets and new values for $\Delta\mu/\mu$ were calculated using Eq. (6.4). The difference with the fiducial values was $\delta_{\rm HFS}^{\Delta\mu/\mu} = 0.1 \times 10^{-8}$ at most, and this was added to the systematic error budget.

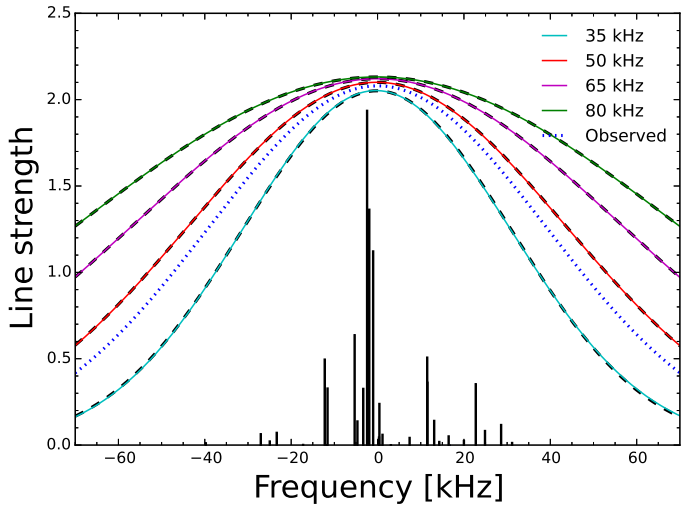

FIGURE 6.6: Comparison of the line shape derived from the hyperfine structure and calculated by BELGI for the $2_0 \rightarrow 1_0$ A$^+$ transition at $\nu_{\rm rest} = 96.741$ GHz. The solid lines represent the convolution of the Gaussian profiles relative to the hyperfine components, while the dashed line represents the fit to the observed line profile centred on the calculated transition frequency. The dotted (blue) line corresponds to the fit to the observed line profile in L1498-1. The vertical bars indicate the individual hyperfine transitions with a length proportional to their intensity in the optically thin case under conditions of local thermodynamical equilibrium.

6.6.2. DOPPLER TRACKING

The motion of the Earth around the Sun and Earth's rotation axis introduces Doppler shifts in the observed frequencies. The IRAM 30m telescope automatically corrects the observed frequencies, i.e. the band centre, for the velocity of the observatory with respect to the solar system barycentre. It is noted that correcting the band centre, introduces small frequency shifts to the positions of lines observed simultaneously at different frequencies, which are automatically corrected for in CLASS (see Section 6.2).

The sky frequencies were adjusted at the beginning of each scan, with a Doppler correction defined as:

$$D = \frac{1}{1 + \frac{\mathrm{v}^{\mathrm{tel}}}{c}}, \tag{6.5}$$

where $\mathrm{v}^{\mathrm{tel}}$ is the Doppler velocity of the telescope relative to the LSR, which is calculated using Eq. (6.2). As already outlined in Section 6.2, each scan consisted of an integration time of 3 min off-source followed by 3 min of integration on L1498. Thus, the methanol lines were measured starting ~ 3 min after the Doppler adjustment. It is noted that, while relative velocity shifts among the spectral lines introduce an effect that mimics a non-zero $\Delta\mu/\mu$, a constant velocity shift does not have any impact on the fiducial value of $\Delta\mu/\mu$, although it affects the $\mathrm{v}_{\mathrm{LSR}}$ value.

L1498 was observed on two consecutive days in July 2014, when its latitude in the ecliptic system was ~ 4 deg. This implies that the Earth was approaching the cloud with a very small acceleration, with respect to its orbit and hence with its almost maximal angular speed of $\sim 10^{-5}$ deg s^{-1}. The motion of the Earth around the Sun causes, in a time interval of $\Delta t = 3$ min, a change in the velocity of the telescope relative to the LSR of $\Delta\mathrm{v}^{\mathrm{tel}} \sim 1$ m s^{-1} corresponding to a frequency shift of, at most, 0.6 kHz. The variation of $\mathrm{v}^{\mathrm{tel}}$ during the off-source integration was not considered in the systematic error budget, as it affects all the methanol lines in the same way, while the $\Delta\mathrm{v}^{\mathrm{tel}}$ introduced during the integration on L1498 causes differential shifts of the methanol lines. Since the observations were performed at the same time in two consecutive days, these shifts were assumed to be in common for all scans. To quantify the impact of the Doppler tracking on the fiducial values, the observed frequencies were shifted by ±0.6 kHz and new $\Delta\mu/\mu$ values were derived and compared with the fiducial ones. The largest offset from the fiducial values returned by this comparison is $\delta^{\Delta\mu/\mu}_{\mathrm{orbit}} \leq 0.1 \times 10^{-8}$, which was added to the systematic error budget.

The Earth's rotation, the velocity of which is $\sim 4.2 \times 10^{-3}$ deg s^{-1}, was estimated in a similar way. Throughout the observing run, the elevation of L1498 changed from a minimal value of 30 deg to a maximal value of 78 deg. The changes in the target's elevation result in velocity shifts in the range from 1.3 to 2.5 m s^{-1} for scans taken at the minimal and the maximal elevation value, respectively, during an integration time of 3 min. Since both the off- and the on-source integrations deliver different velocity shifts, their effects were included in the systematic error budget. The total

integration time of 6 min delivered a spread of ~ 2.4 m s^{-1} in the telescope velocities due to the rotation of the Earth, which translates in a shift of, at most, ~ 1.2 kHz in the observed frequencies, which corresponds to a contribution to the systematic error budget of $\delta^{\Delta\mu/\mu}_{\text{rotation}} = 0.1 \times 10^{-8}$.

6.6.3. TOTAL SYSTEMATIC UNCERTAINTY

The total systematic uncertainty on the fiducial values was derived by adding in quadrature the contributions from the Doppler tracking and the underlying methanol hyperfine structure. This returned an error of $\sim 0.2 \times 10^{-8}$. Therefore, the final fiducial value of $\Delta\mu/\mu$ obtained from the comparison of the observed frequencies with rest frame frequencies by Xu *et al.* [181] is $\Delta\mu/\mu = (-3.3 \pm 1.9_{\text{stat}} \pm 0.2_{\text{syst}}) \times 10^{-8}$.

6.7. CONCLUSION

Methanol (CH_3OH) emission in the cold core L1498 was investigated in order to constrain the dependence of the proton-to-electron mass ratio on matter density, thereby testing the chameleon scenario for theories beyond the Standard Model of physics [24, 25]. The result presented in this study is derived through the methanol method, which involves observations of methanol transitions only, thereby avoiding assumptions of cospatiality among different molecules. This work strengthens the results previously obtained from radio astronomical searches [67–69] by adding robustness against systematics effects such as chemical segregation. The methanol method provides future prospects for improved constraints on varying constants in the chameleon framework, if additional low-frequency lines can be detected.

In addition to this fundamental physics quest, the astrophysical properties of the L1498 cloud and its methanol A and E column densities were studied with Large Velocity Gradient radiative transfer calculations. The two spatially resolved methanol emission peaks (SE and NW) reported by [71] were targeted for ~ 18 hrs using the IRAM 30m telescope. Six methanol transitions were detected in the brighter methanol emission peak, L1498-1, and five in the other position, L1498-2.

By comparing the accurate observed frequencies with the reference rest frame values reported by Xu *et al.* [181], a value of $\Delta\mu/\mu$ was derived for each methanol emission peak. The weighted average of these values returned $\Delta\mu/\mu = (-3.3 \pm 1.9_{\text{stat}} \pm 0.2_{\text{syst}}) \times 10^{-8}$, which is consistent with no variation at a level of 6×10^{-8} (3σ). This result is delivered by the analysis of emission lines belonging to a single molecular species, hence it is not depending on assumptions on the spatial distribution of the considered molecules. While *E* and *A* type methanol may be regarded as two different species, previous methanol observations in this system [71] did not find evidence of chemical segregation between the two methanol types and our radiative transfer calculations indicate that they trace gas with similar physical properties. The $\Delta\mu/\mu$ constraint is three times less stringent than that found by Lev-

shakov *et al.* [69], which represents the most stringent constraint at the present day, but our limit is based on data from a single molecule and is therefore not affected by potential caveats caused by astrochemical processes.

The RADEX non-LTE model was used to derive the physical characteristics of the cloud. RADEX was used to find the best solution by optimising the E- and A-type methanol column densities as functions of the kinetic temperature and the molecular hydrogen density. The best fit solutions for both L1498-1 and L1498-2 return molecular hydrogen densities of order $n(H_2) \sim 3 \times 10^5$ cm^{-3}, kinetic temperatures of $T_{\rm kin} \sim 6$ K and total methanol column densities of several 10^{12} cm^{-2}. E- and A-type methanol abundance ratios appear to be close to unity.

The $\Delta\mu/\mu$ value presented in this work can be improved by further observing methanol emission in cold cores. The $\Delta\mu/\mu$ value presented here relies predominantly on the $1_0 - 1_{-1}$ E transition at $\sim$ 157.270 GHz, which is the only one with a sensitivity coefficient $K_i \neq -1$ in the considered sample. Observing extra lines with different sensitivities in L1498 will improve the ΔK_i and thereby the accuracy on $\Delta\mu/\mu$. For example, observing the $2_0 \rightarrow 3_{-1}$ E transition at $\nu_{\rm rest} = 12.178$ GHz (sensitivity coefficient of $K_i = -32.5$) will enhance the ΔK_i used to derive the $\Delta\mu/\mu$ constraint, thereby improving it by one order of magnitude. This line has actually been observed in enhanced absorption again the cosmic microwave background radiation in the cold dark clouds TMC 1 and L 183 [187]. Further observations of low frequency methanol transitions with larger sensitivity coefficients are planned with the Effelsberg 100m telescope and will improve the current constraint. Future observations of methanol lines in different cores showing low degrees of turbulence [e.g. L1517B, 71, 166], will provide independent constraints on the dependence of μ from matter density.

ACKNOWLEDGMENTS

The authors MD, HLB, and WU thank the Netherlands Foundation for Fundamental Research of Matter (FOM) for financial support. WU acknowledges the European Research Council for an ERC-Advanced grant under the European Union's Horizon 2020 research and innovation programme (grant agreement No 670168). AL is supported by the Russian Science Foundation (project 17-12-01256). This work was partially carried out within the Collaborative Research Council 956, subproject A6, funded by the Deutsche Forschungsgemeinschaft (DFG). We thank L. H. Xu (University of New Brunswick) for useful discussions about the calculated methanol rest frame frequencies. We thank A. v.d Avoird (Radboud University Nijmegen) and B. Lankhaar (Chalmers University Göteborg) for elucidating discussions and for making available the data on calculations of splittings and relative intensities of the hyperfine components for the six lines listed in Table 6.2. We thank the staff of the IRAM 30m telescope for support during the observations.

BIBLIOGRAPHY

[1] P. A. M. Dirac, *The Cosmological Constants,* Nature **139**, 323 (1937).

[2] P. Jordan, *Die physikalischen Weltkonstanten,* Naturwissenschaften **25**, 513 (1937).

[3] J.-P. Uzan, *Varying Constants, Gravitation and Cosmology,* Living Rev. Relat. **14**, 2 (2011).

[4] M. Fierz, *On the physical interpretation of P. Jordanı s extended theory of gravitation,* Helv. Phys. Acta **29**, 128 (1956).

[5] M. J. Duff, L. B. Okun, and G. Veneziano, *Trialogue on the number of fundamental constants,* J. High Energy Phys. **3**, 023 (2002).

[6] M. J. Duff, *How fundamental are fundamental constants?* Contemporary Phys. **56**, 35 (2015).

[7] M. Born, *The mysterious number 137,* Proc. Indian Acad. Sci. **2**, 533 (1935).

[8] V. V. Flambaum, D. B. Leinweber, A. W. Thomas, and R. D. Young, *Limits on variations of the quark masses, QCD scale, and fine structure constant,* Phys. Rev. D **69**, 115006 (2004).

[9] S. Sturm, F. Kohler, J. Zatorski, A. Wagner, Z. Harman, G. Werth, W. Quint, C. H. Keitel, and K. Blaum, *High-precision measurement of the atomic mass of the electron,* Nature **506**, 467 (2014).

[10] X. Calmet and H. Fritzsch, *The cosmological evolution of the nucleon mass and the electroweak coupling constants,* Eur. Phys. J. C **24**, 639 (2002).

[11] P. Langacker, G. Segrè, and M. J. Strassler, *Implications of gauge unification for time variation of the fine structure constant,* Phys. Lett. B **528**, 121 (2002).

[12] T. Dent and M. Fairbairn, *Time-varying coupling strengths, nuclear forces and unification,* Nucl. Phys. B **653**, 256 (2003).

[13] T. Dent, *Fundamental constants and their variability in theories of high energy physics,* Eur. Phys. J. Spec. Top. **163**, 297 (2008).

[14] T. Kaluza, *Zum Unitätsproblem der Physik,* Sitzungsberichte der Königlich Preußischen Akademie der Wissenschaften (Berlin) , 966 (1921).

[15] O. Klein, *Quantentheorie und fünfdimensionale Relativitätstheorie,* Zeitschrift fur Physik **37**, 895 (1926).

[16] E. Bergshoeff, E. Sezgin, and P. K. Townsend, *Supermembranes and eleven-dimensional supergravity,* Phys. Lett. B **189**, 75 (1987).

[17] M. J. Duff, P. S. Howe, T. Inami, and K. S. Stelle, *Superstrings in D=10 from supermembranes in D=11,* Phys. Lett. B **191**, 70 (1987).

[18] E. Witten, *String theory dynamics in various dimensions,* Nucl. Phys. B **443**, 85 (1995).

[19] J. D. Bekenstein, *Fine-structure constant: Is it really a constant?* Phys. Rev. D **25**, 1527 (1982).

[20] J. D. Barrow, H. B. Sandvik, and J. Magueijo, *Anthropic reasons for nonzero flatness and* Λ, Phys. Rev. D **65**, 123501 (2002).

[21] H. B. Sandvik, J. D. Barrow, and J. Magueijo, *A Simple Cosmology with a Varying Fine Structure Constant,* Phys. Rev. Lett. **88**, 031302 (2002).

[22] R. R. Caldwell, R. Dave, and P. J. Steinhardt, *Cosmological Imprint of an Energy Component with General Equation of State,* Physical Review Letters **80**, 1582 (1998).

[23] P. J. Peebles and B. Ratra, *The cosmological constant and dark energy,* Rev. Mod. Phys. **75**, 559 (2003).

[24] J. Khoury and A. Weltman, *Chameleon Fields: Awaiting Surprises for Tests of Gravity in Space,* Phys. Rev. Lett. **93**, 171104 (2004).

[25] P. Brax, C. van de Bruck, A.-C. Davis, J. Khoury, and A. Weltman, *Detecting dark energy in orbit: The cosmological chameleon,* Phys. Rev. D **70**, 123518 (2004).

[26] D. F. Mota and D. J. Shaw, *Evading equivalence principle violations, cosmological, and other experimental constraints in scalar field theories with a strong coupling to matter,* Phys. Rev. D **75**, 063501 (2007).

[27] K. A. Olive and M. Pospelov, *Environmental dependence of masses and coupling constants,* Phys. Rev. D **77**, 043524 (2008).

[28] R. I. Thompson, *The determination of the electron to proton inertial mass ratio via molecular transitions,* A&A Lett. **16**, 3 (1975).

[29] D. A. Varshalovich and S. A. Levshakov, *On a time dependence of physical constants.* Sov. J. Exp. Theor. Phys. **58**, 237 (1993).

[30] M. Daprà, M. L. Niu, E. J. Salumbides, M. T. Murphy, and W. Ubachs, *Constraint on a Cosmological Variation in the Proton-to-electron Mass Ratio from Electronic CO Absorption,* Astrophys. J. **826**, 192 (2016).

[31] M. A. Zwaan and J. X. Prochaska, *Where Is the Molecular Hydrogen in Damped Ly α Absorbers?* Astrophys. J. **643**, 675 (2006).

[32] R. A. Jorgenson, M. T. Murphy, R. Thompson, and R. F. Carswell, *The Magellan uniform survey of damped Lyman α systems - II. Paucity of strong molecular hydrogen absorption,* Mont. Not. Roy. Astron. Soc. **443**, 2783 (2014).

[33] J. Philip, J. P. Sprengers, T. Pielage, C. A. de Lange, W. Ubachs, and E. Reinhold, *Highly accurate transition frequencies in the H_2 Lyman and Werner absorption bands,* Can. J. Chem. **82**, 713 (2004).

[34] W. Ubachs and E. Reinhold, *Highly Accurate H_2 Lyman and Werner Band Laboratory Measurements and an Improved Constraint on a Cosmological Variation of the Proton-to-Electron Mass Ratio,* Phys. Rev. Lett. **92**, 101302 (2004).

[35] E. Reinhold, R. Buning, U. Hollenstein, A. Ivanchik, P. Petitjean, and W. Ubachs, *Indication of a Cosmological Variation of the Proton-Electron Mass Ratio Based on Laboratory Measurement and Reanalysis of H_2 Spectra,* Phys. Rev. Lett. **96**, 151101 (2006).

[36] W. Ubachs, R. Buning, K. S. E. Eikema, and E. Reinhold, *On a possible variation of the proton-to-electron mass ratio: H_2 spectra in the line of sight of high-redshift quasars and in the laboratory,* J. Mol. Spectrosc. **241**, 155 (2007).

[37] E. J. Salumbides, D. Bailly, A. Khramov, A. L. Wolf, K. S. E. Eikema, M. Vervloet, and W. Ubachs, *Improved Laboratory Values of the H_2 Lyman and Werner Lines for Constraining Time Variation of the Proton-to-Electron Mass Ratio,* Phys. Rev. Lett. **101**, 223001 (2008).

[38] T. I. Ivanov, M. Roudjane, M. O. Vieitez, C. A. de Lange, W.-Ü. L. Tchang-Brillet, and W. Ubachs, *HD as a Probe for Detecting Mass Variation on a Cosmological Time Scale,* Phys. Rev. Lett. **100**, 093007 (2008).

[39] T. I. Ivanov, G. D. Dickenson, M. Roudjane, N. D. Oliveira, D. Joyeux, L. Nahon, W.-U. L. Tchang-Brillet, and W. Ubachs, *Fourier-transform spectroscopy of HD in the vacuum ultraviolet at λ = 87-112 nm,* Mol. Phys. **108**, 771 (2010).

[40] J. Bagdonaite, W. Ubachs, M. T. Murphy, and J. B. Whitmore, *Constraint on a Varying Proton-Electron Mass Ratio 1.5 Billion Years after the Big Bang,* Phys. Rev. Lett. **114**, 071301 (2015).

[41] A. L. Malec, R. Buning, M. T. Murphy, N. Milutinovic, S. L. Ellison, J. X. Prochaska, L. Kaper, J. Tumlinson, R. F. Carswell, and W. Ubachs, *Keck telescope constraint on cosmological variation of the proton-to-electron mass ratio,* Mont. Not. Roy. Astron. Soc. **403**, 1541 (2010).

[42] P. Noterdaeme, J.-K. Krogager, S. Balashev, J. Ge, N. Gupta, T. Krühler, C. Ledoux, M. T. Murphy, I. Pâris, P. Petitjean, H. Rahmani, R. Srianand, and W. Ubachs, *Discovery of a Perseus-like cloud in the early Universe: HI-to-H2 transition, carbon monoxide and small dust grains at zabs=2.53 towards the quasar J0000+0048,* A&A (2016).

[43] M. Daprà, P. Noterdaeme, M. Vonk, M. T. Murphy, and W. Ubachs, *Analysis of carbon monoxide absorption at $z_{abs}\simeq 2.5$ to constrain variation of the proton-to-electron mass ratio,* Mont. Not. Roy. Astron. Soc. **467**, 3848 (2017).

[44] P. Noterdaeme, P. Petitjean, R. Srianand, C. Ledoux, and S. López, *The evolution of the cosmic microwave background temperature. Measurements of T_{CMB} at high redshift from carbon monoxide excitation,* A&A **526**, L7 (2011).

[45] P. Noterdaeme, P. Petitjean, C. Ledoux, S. López, R. Srianand, and S. D. Vergani, *A translucent interstellar cloud at z = 2.69. CO, H_2, and HD in the line-of-sight to SDSS J123714.60+064759.5,* A&A **523**, A80 (2010).

[46] M. Daprà, J. Bagdonaite, M. T. Murphy, and W. Ubachs, *Constraint on a varying proton-to-electron mass ratio from molecular hydrogen absorption towards quasar SDSS J123714.60+064759.5,* Mont. Not. Roy. Astron. Soc. **454**, 489 (2015).

[47] P. Noterdaeme, C. Ledoux, P. Petitjean, and R. Srianand, *Molecular hydrogen in high-redshift damped Lyman-α systems: the VLT/UVES database,* A&A **481**, 327 (2008).

[48] R. Srianand, P. Noterdaeme, C. Ledoux, and P. Petitjean, *First detection of CO in a high-redshift damped Lyman-α system,* A&A **482**, L39 (2008).

[49] P. Noterdaeme, C. Ledoux, R. Srianand, P. Petitjean, and S. Lopez, *Diffuse molecular gas at high redshift. Detection of CO molecules and the 2175 Å dust feature at z = 1.64,* A&A **503**, 765 (2009).

[50] E. J. Salumbides, M. L. Niu, J. Bagdonaite, N. de Oliveira, D. Joyeux, L. Nahon, and W. Ubachs, *CO A-X system for constraining cosmological drift of the proton-electron mass ratio,* Phys. Rev. A **86**, 022510 (2012).

[51] C. Henkel, N. Jethava, A. Kraus, K. M. Menten, C. L. Carilli, M. Grasshoff, D. Lubowich, and M. J. Reid, *The kinetic temperature of a molecular cloud*

at redshift 0.7: ammonia in the gravitational lens B0218+357, A&A **440**, 893 (2005).

[52] C. Henkel, J. A. Braatz, K. M. Menten, and J. Ott, *The kinetic temperature of a molecular cloud at redshift 0.9: ammonia in the gravitational lens PKS 1830-211,* A&A **485**, 451 (2008).

[53] S. Muller, A. Beelen, M. Guélin, S. Aalto, J. H. Black, F. Combes, S. J. Curran, P. Theule, and S. N. Longmore, *Molecules at z = 0.89. A 4-mm-rest-frame absorption-line survey toward PKS 1830-211,* A&A **535**, A103 (2011).

[54] M. T. Murphy, V. V. Flambaum, S. Muller, and C. Henkel, *Strong Limit on a Variable Proton-to-Electron Mass Ratio from Molecules in the Distant Universe,* Science **320**, 1611 (2008).

[55] C. Henkel, K. M. Menten, M. T. Murphy, N. Jethava, V. V. Flambaum, J. A. Braatz, S. Muller, J. Ott, and R. Q. Mao, *The density, the cosmic microwave background, and the proton-to-electron mass ratio in a cloud at redshift 0.9,* A&A **500**, 725 (2009).

[56] N. Kanekar, *Constraining Changes in the Proton-Electron Mass Ratio with Inversion and Rotational Lines,* Astrophys. J. Lett. **728**, L12 (2011).

[57] P. Jansen, L.-H. Xu, I. Kleiner, W. Ubachs, and H. L. Bethlem, *Methanol as a Sensitive Probe for Spatial and Temporal Variations of the Proton-to-Electron Mass Ratio,* Phys. Rev. Lett. **106**, 100801 (2011).

[58] P. Jansen, I. Kleiner, L.-H. Xu, W. Ubachs, and H. L. Bethlem, *Sensitivity of transitions in internal rotor molecules to a possible variation of the proton-to-electron mass ratio,* Phys. Rev. A **84**, 062505 (2011).

[59] S. A. Levshakov, M. G. Kozlov, and D. Reimers, *Methanol as A Tracer of Fundamental Constants,* Astrophys. J. **738**, 26 (2011).

[60] T. Wiklind and F. Combes, *The redshift of the gravitational lens of PKS1830-211 determined from molecular absorption lines,* Nature **379**, 139 (1996).

[61] S. P. Ellingsen, M. A. Voronkov, S. L. Breen, and J. E. J. Lovell, *First Cosmological Constraints on the Proton-to-electron Mass Ratio from Observations of Rotational Transitions of Methanol,* Astrophys. J. Lett. **747**, L7 (2012).

[62] J. Bagdonaite, P. Jansen, C. Henkel, H. L. Bethlem, K. M. Menten, and W. Ubachs, *A Stringent Limit on a Drifting Proton-to-Electron Mass Ratio from Alcohol in the Early Universe,* Science **339**, 46 (2013).

[63] J. Bagdonaite, M. Daprà, P. Jansen, H. L. Bethlem, W. Ubachs, S. Muller, C. Henkel, and K. M. Menten, *Robust Constraint on a Drifting Proton-to-Electron Mass Ratio at z=0.89 from Methanol Observation at Three Radio Telescopes,* Phys. Rev. Lett. **111**, 231101 (2013).

[64] N. Kanekar, W. Ubachs, K. M. Menten, J. Bagdonaite, A. Brunthaler, C. Henkel, S. Muller, H. L. Bethlem, and M. Daprà, *Constraints on changes in the proton-electron mass ratio using methanol lines,* Mont. Not. Roy. Astron. Soc. **448**, L104 (2015).

[65] D. L. Jones, R. A. Preston, D. W. Murphy, D. L. Jauncey, J. E. Reynolds, A. K. Tzioumis, E. A. King, P. M. McCulloch, J. E. J. Lovell, M. E. Costa, and T. D. van Ommen, *Interstellar Broadening of Images in the Gravitational Lens PKS 1830-211,* Astrophys. J. Lett. **470**, L23 (1996).

[66] J. Bagdonaite, E. J. Salumbides, S. P. Preval, M. A. Barstow, J. D. Barrow, M. T. Murphy, and W. Ubachs, *Limits on a Gravitational Field Dependence of the Proton-Electron Mass Ratio from H_2 in White Dwarf Stars,* Phys. Rev. Lett. **113**, 123002 (2014).

[67] S. A. Levshakov, P. Molaro, A. V. Lapinov, D. Reimers, C. Henkel, and T. Sakai, *Searching for chameleon-like scalar fields with the ammonia method,* A&A **512**, A44 (2010).

[68] S. A. Levshakov, A. V. Lapinov, C. Henkel, P. Molaro, D. Reimers, M. G. Kozlov, and I. I. Agafonova, *Searching for chameleon-like scalar fields with the ammonia method. II. Mapping of cold molecular cores in NH_3 and HC_3N lines,* A&A **524**, A32 (2010).

[69] S. A. Levshakov, D. Reimers, C. Henkel, B. Winkel, A. Mignano, M. Centurión, and P. Molaro, *Limits on the spatial variations of the electron-to-proton mass ratio in the Galactic plane,* A&A **559**, A91 (2013).

[70] P. Friberg, A. Hjalmarson, S. C. Madden, and W. M. Irvine, *Methanol in dark clouds,* A&A **195**, 281 (1988).

[71] M. Tafalla, J. Santiago-García, P. C. Myers, P. Caselli, C. M. Walmsley, and A. Crapsi, *On the internal structure of starless cores. II. A molecular survey of L1498 and L1517B,* A&A **455**, 577 (2006).

[72] J. B. Whitmore and M. T. Murphy, *Impact of instrumental systematic errors on fine-structure constant measurements with quasar spectra,* Mont. Not. Roy. Astron. Soc. **447**, 446 (2015).

[73] W. Ubachs, J. Bagdonaite, E. J. Salumbides, M. T. Murphy, and L. Kaper, *Colloquium : Search for a drifting proton-electron mass ratio from* H_2, Rev. Mod. Phys. **88**, 021003 (2016).

[74] M. G. Kozlov and S. A. Levshakov, *Microwave and submillimeter molecular transitions and their dependence on fundamental constants,* Ann. Phys. **525**, 452 (2013).

[75] P. Jansen, H. L. Bethlem, and W. Ubachs, *Perspective: Tipping the scales: Search for drifting constants from molecular spectra,* J. Chem. Phys. **140**, 010901 (2014).

[76] J. Ge and J. Bechtold, *H_2 and C I in Damped LY alpha Quasar Absorbers at Intermediate and High Redshifts,* in *Highly Redshifted Radio Lines*, ASP Conf. Ser., Vol. 156, edited by C. L. Carilli, S. J. E. Radford, K. M. Menten, and G. I. Langston (1999) p. 121.

[77] R. Srianand, P. Petitjean, and C. Ledoux, *The cosmic microwave background radiation temperature at a redshift of 2.34,* Nature **408**, 931 (2000).

[78] A. V. Ivanchik, E. Rodriguez, P. Petitjean, and D. A. Varshalovich, *Do the Fundamental Constants Vary in the Course of Cosmological Evolution?* Astron. Lett. **28**, 423 (2002).

[79] D. C. Morton and H. L. Dinerstein, *Interstellar molecular hydrogen toward zeta Puppis,* Astrophys. J. **204**, 1 (1976).

[80] H. Abgrall, E. Roueff, F. Launay, J. Y. Roncin, and J. L. Subtil, *The Lyman and Werner Band Systems of Molecular Hydrogen,* J. Mol. Spectrosc. **157**, 512 (1993).

[81] A. V. Ivanchik, P. Petitjean, S. A. Balashev, R. Srianand, D. A. Varshalovich, C. Ledoux, and P. Noterdaeme, *HD molecules at high redshift: the absorption system at z = 2.3377 towards Q 1232+082,* Mont. Not. Roy. Astron. Soc. **404**, 1583 (2010).

[82] S. A. Balashev, P. Petitjean, A. V. Ivanchik, C. Ledoux, R. Srianand, P. Noterdaeme, and D. A. Varshalovich, *Partial coverage of the broad-line region of Q1232+082 by an intervening H_2-bearing cloud,* Mont. Not. Roy. Astron. Soc. **418**, 357 (2011).

[83] J. A. King, J. K. Webb, M. T. Murphy, and R. F. Carswell, *Stringent Null Constraint on Cosmological Evolution of the Proton-to-Electron Mass Ratio,* Phys. Rev. Lett. **101**, 251304 (2008).

[84] J. A. King, M. T. Murphy, W. Ubachs, and J. K. Webb, *New constraint on cosmological variation of the proton-to-electron mass ratio from Q0528-250,* Mont. Not. Roy. Astron. Soc. **417**, 3010 (2011).

[85] J. Bagdonaite, M. T. Murphy, L. Kaper, and W. Ubachs, *Constraint on a variation of the proton-to-electron mass ratio from H_2 absorption towards quasar Q2348-011,* Mont. Not. Roy. Astron. Soc. **421**, 419 (2012).

[86] J. Bagdonaite, W. Ubachs, M. T. Murphy, and J. B. Whitmore, *Analysis of Molecular Hydrogen Absorption toward QSO B0642-5038 for a Varying Proton-to-electron Mass Ratio,* Astrophys. J. **782**, 10 (2014).

[87] M. T. Murphy, *Uves_popler: Post-pipeline echelle reduction software,* (2016).

[88] R. F. Carswell and J. K. Webb, *VPFIT: Voigt profile fitting program,* Astrophysics Source Code Library (2014).

[89] U. Hollenstein, E. Reinhold, C. A. de Lange, and W. Ubachs, *High-resolution VUV-laser spectroscopic study of the $B^1\Sigma^+_{(u)}(v'=0-2) \leftarrow X^1\Sigma^+_{(g)}(v''=0)$ Lyman bands in H_2 and HD,* J. Phys. B **39**, L195 (2006).

[90] H. Abgrall, E. Roueff, F. Launay, and J.-Y. Roncin, *The $B'^1\Sigma_u{}^+ \rightarrow X^1\Sigma_g{}^+$ and $D^1\Pi_u{}^+ \rightarrow X^1\Sigma_g{}^+$ band systems of molecular hydrogen,* Can. J. Phys. **72**, 856 (1994).

[91] H. Abgrall, E. Roueff, and I. Drira, *Total transition probability and spontaneous radiative dissociation of B, C, B′ and D states of molecular hydrogen,* A&AS **141**, 297 (2000).

[92] H. Abgrall and E. Roueff, *Theoretical calculations of excited rovibrational levels of HD. Term values and transition probabilities of VUV electronic bands,* A&A **445**, 361 (2006).

[93] H. Akaike, *A New Look at the Statistical Model Identification,* IEEE Trans. Aut. Contr. **19**, 716 (1974).

[94] D. A. Varshalovich, A. V. Ivanchik, P. Petitjean, R. Srianand, and C. Ledoux, *HD Molecular Lines in an Absorption System at Redshift z=2.3377,* Astron. Lett. **27**, 683 (2001).

[95] P. Noterdaeme, P. Petitjean, R. Srianand, C. Ledoux, and F. Le Petit, *Physical conditions in the neutral interstellar medium at $z = 2.43$ toward Q 2348-011,* A&A **469**, 425 (2007).

[96] S. A. Balashev, D. A. Varshalovich, and A. V. Ivanchik, *Directional radiation and photodissociation regions in molecular hydrogen clouds,* Astron. Lett. **35**, 150 (2009).

[97] A. Ivanchik, P. Petitjean, D. Varshalovich, B. Aracil, R. Srianand, H. Chand, C. Ledoux, and P. Boissé, *A new constraint on the time dependence of the proton-to-electron mass ratio. Analysis of the Q 0347-383 and Q 0405-443 spectra,* A&A **440**, 45 (2005).

[98] H. Rahmani, M. Wendt, R. Srianand, P. Noterdaeme, P. Petitjean, P. Molaro, J. B. Whitmore, M. T. Murphy, M. Centurion, H. Fathivavsari, S. D'Odorico, T. M. Evans, S. A. Levshakov, S. Lopez, C. J. A. P. Martins, D. Reimers, and G. Vladilo, *The UVES large program for testing fundamental physics - II. Constraints on a change in μ towards quasar HE 0027-1836,* Mont. Not. Roy. Astron. Soc. **435**, 861 (2013).

[99] K. Chance and R. L. Kurucz, *An improved high-resolution solar reference spectrum for earth's atmosphere measurements in the ultraviolet, visible, and near infrared,* J. Quant. Spectrosc. Radiat. Transfer **111**, 1289 (2010).

[100] J. Meléndez, M. Asplund, B. Gustafsson, and D. Yong, *The Peculiar Solar Composition and Its Possible Relation to Planet Formation,* Astrophys. J. Lett. **704**, L66 (2009).

[101] J. Datson, C. Flynn, and L. Portinari, *Solar analogues and solar twins in the HARPS archive,* Mont. Not. Roy. Astron. Soc. **439**, 1028 (2014).

[102] K. Griest, J. B. Whitmore, A. M. Wolfe, J. X. Prochaska, J. C. Howk, and G. W. Marcy, *Wavelength Accuracy of the Keck HIRES Spectrograph and Measuring Changes in the Fine Structure Constant,* Astrophys. J. **708**, 158 (2010).

[103] J. B. Whitmore, M. T. Murphy, and K. Griest, *Wavelength Calibration of the VLT-UVES Spectrograph,* Astrophys. J. **723**, 89 (2010).

[104] F. van Weerdenburg, M. T. Murphy, A. L. Malec, L. Kaper, and W. Ubachs, *First Constraint on Cosmological Variation of the Proton-to-Electron Mass Ratio from Two Independent Telescopes,* Phys. Rev. Lett. **106**, 180802 (2011).

[105] D. Albornoz Vásquez, H. Rahmani, P. Noterdaeme, P. Petitjean, R. Srianand, and C. Ledoux, *Molecular hydrogen in the z_{abs} = 2.66 damped Lyman-α absorber towards Q J 0643-5041. Physical conditions and limits on the cosmological variation of the proton-to-electron mass ratio,* A&A **562**, A88 (2014).

[106] M. Wendt and P. Molaro, *QSO 0347-383 and the invariance of m_p/m_e in the course of cosmic time,* A&A **541**, A69 (2012).

[107] S. A. Balashev, P. Noterdaeme, V. V. Klimenko, P. Petitjean, R. Srianand, C. Ledoux, A. V. Ivanchik, and D. A. Varshalovich, *Neutral chlorine and molecular hydrogen at high redshift,* A&A **575**, L8 (2015).

[108] F. A. Pepe, S. Cristiani, R. Rebolo Lopez, N. C. Santos, A. Amorim, G. Avila, W. Benz, P. Bonifacio, A. Cabral, P. Carvas, R. Cirami, J. Coelho, M. Comari, I. Coretti, V. De Caprio, H. Dekker, B. Delabre, P. Di Marcantonio, V. D'Odorico, M. Fleury, R. García, J. M. Herreros Linares, I. Hughes, O. Iwert, J. Lima, J.-L. Lizon, G. Lo Curto, C. Lovis, A. Manescau, C. Martins, D. Mégevand, A. Moitinho, P. Molaro, M. Monteiro, M. Monteiro, L. Pasquini, C. Mordasini, D. Queloz, J. L. Rasilla, J. M. Rebordão, S. Santana Tschudi, P. Santin, D. Sosnowska, P. Spanò, F. Tenegi, S. Udry, E. Vanzella, M. Viel, M. R. Zapatero Osorio, and F. Zerbi, *ESPRESSO: the Echelle spectrograph for rocky exoplanets and stable spectroscopic observations,* in *Society of Photo-Optical Instrumentation Engineers (SPIE) Conference Series*, Society of Photo-Optical Instrumentation Engineers (SPIE) Conference Series, Vol. 7735 (2010) p. 9.

[109] J. K. Webb, V. V. Flambaum, C. W. Churchill, M. J. Drinkwater, and J. D. Barrow, *Search for Time Variation of the Fine Structure Constant,* Phys. Rev. Lett. **82**, 884 (1999).

[110] J. K. Webb, J. A. King, M. T. Murphy, V. V. Flambaum, R. F. Carswell, and M. B. Bainbridge, *Indications of a Spatial Variation of the Fine Structure Constant,* Phys. Rev. Lett. **107**, 191101 (2011).

[111] R. I. Thompson, J. Bechtold, J. H. Black, D. Eisenstein, X. Fan, R. C. Kennicutt, C. Martins, J. X. Prochaska, and Y. L. Shirley, *An Observational Determination of the Proton to Electron Mass Ratio in the Early Universe,* Astrophys. J. **703**, 1648 (2009).

[112] M. Wendt and P. Molaro, *Robust limit on a varying proton-to-electron mass ratio from a single H_2 system,* A&A **526**, A96 (2011).

[113] W. Ubachs, J. Bagdonaite, M. T. Murphy, R. Buning, and L. Kaper, *Search for Cosmological μ-Variation from High-Redshift H_2 Absorption; A Status Report,* in *From Varying Couplings to Fundamental Physics: Proceedings of Symposium 1 of JENAM 2010* (Springer Berlin Heidelberg, Berlin, Heidelberg, 2011) pp. 125–137.

[114] M. Wendt, *Constraints on variations of m_P/m_e based on UVES observations of H_2,* Astron. Nachr. **335**, 106 (2014).

[115] H. Dekker, S. D'Odorico, A. Kaufer, B. Delabre, and H. Kotzlowski, *Design, construction, and performance of UVES, the echelle spectrograph for the UT2 Kueyen Telescope at the ESO Paranal Observatory,* in *Optical and IR Telescope Instrumentation and Detectors*, Proc. SPIE, Vol. 4008, edited by M. Iye and A. F. Moorwood (2000) pp. 534–545.

[116] P. Petitjean, C. Ledoux, P. Noterdaeme, and R. Srianand, *Metallicity as a criterion to select H_2-bearing damped Lyman-α systems,* A&A **456**, L9 (2006).

[117] P. Molaro, S. A. Levshakov, S. Monai, M. Centurión, P. Bonifacio, S. D'Odorico, and L. Monaco, *UVES radial velocity accuracy from asteroid observations. I. Implications for fine structure constant variability,* A&A **481**, 559 (2008).

[118] M. T. Murphy, P. Tzanavaris, J. K. Webb, and C. Lovis, *Selection of ThAr lines for wavelength calibration of echelle spectra and implications for variations in the fine-structure constant,* Mont. Not. Roy. Astron. Soc. **378**, 221 (2007).

[119] M. P. Savedoff, *Physical Constants in Extra-Galactic Nebulæ,* Nature **178**, 688 (1956).

[120] V. A. Dzuba, V. V. Flambaum, and J. K. Webb, *Space-Time Variation of Physical Constants and Relativistic Corrections in Atoms,* Phys. Rev. Lett. **82**, 888 (1999).

[121] V. V. Flambaum and M. G. Kozlov, *Limit on the Cosmological Variation of m_p/m_e from the Inversion Spectrum of Ammonia,* Phys. Rev. Lett. **98**, 240801 (2007).

[122] P. Tzanavaris, J. K. Webb, M. T. Murphy, V. V. Flambaum, and S. J. Curran, *Limits on Variations in Fundamental Constants from 21-cm and Ultraviolet Quasar Absorption Lines,* Phys. Rev. Lett. **95**, 041301 (2005).

[123] N. Kanekar, G. I. Langston, J. T. Stocke, C. L. Carilli, and K. M. Menten, *Constraining Fundamental Constant Evolution with H I and OH Lines,* Astrophys. J. Lett. **746**, L16 (2012).

[124] D. C. Morton and L. Noreau, *A compilation of electronic transitions in the CO molecule and the interpretation of some puzzling interstellar absorption features,* Astrophys. J., Suppl. Ser. **95**, 301 (1994).

[125] M. L. Niu, E. J. Salumbides, D. Zhao, N. de Oliveira, D. Joyeux, L. Nahon, R. W. Field, and W. Ubachs, *High resolution spectroscopy and perturbation analysis of the CO $A^1\Pi$ - $X^1\Sigma^+$ (0,0) and (1,0) bands,* Mol. Phys. **111**, 2163 (2013).

[126] M. L. Niu, F. Ramirez, E. J. Salumbides, and W. Ubachs, *High-precision laser spectroscopy of the CO $A^1\Pi$ - $X^1\Sigma^+$ (2,0), (3,0), and (4,0) bands,* J. Chem. Phys. **142**, 044302 (2015).

[127] M. L. Niu, E. J. Salumbides, A. N. Heays, N. de Oliveira, R. W. Field, and W. Ubachs, *Spectroscopy and perturbation analysis of the CO $A^1\Pi$ - $X^1\Sigma^+$ (2,0), (3,0) and (4,0) bands,* Mol. Phys. **114**, 627 (2016).

[128] M. Larsson, *Conversion formulas between radiative lifetimes and other dynamical variables for spin-allowed electronic transitions in diatomic molecules,* A&A **128**, 291 (1983).

[129] R. W. Field, B. G. Wicke, S. J. D., and S. G. Tilford, *Analysis of perturbations in the $d^3\Pi$ and $A^1\Pi$ states of CO,* J. Mol. Spectrosc. **44**, 383 (1972).

[130] A. C. Le Floch, F. Launay, J. Rostas, R. W. Field, C. M. Brown, and K. Yoshino, *Reinvestigation of the CO $A^1\Pi$ state and its perturbations: The $v = 0$ level,* J. Mol. Spectrosc. **121**, 337 (1987).

[131] M. Eidelsberg, F. Rostas, J. Breton, and B. Thieblemont, *Vibrational band oscillator strengths and dipole transition moment of the $A^1\Pi$ - $X^1\Sigma^+$ system of CO,* J. Chem. Phys. **96**, 5585 (1992).

[132] W. Chan, G. Cooper, and C. Brion, *Absolute optical oscillator strengths for discrete and continuum photoabsorption of carbon monoxide (7-200 eV) and transition moments for the $X^1\Sigma^+ \leftarrow A^1\Pi$ system,* Chem. Phys. **170**, 123 (1993).

[133] Z. P. Zhong, S. L. Wu, Z. Xu, L. F. Zhu, X. J. Zhang, R. F. Feng, and K. Z. XU, *A study of optical oscillator strengths and differential cross sections in the discrete region of carbon monoxide,* Acta Phys. Sin. **47**, 419 (1998).

[134] R. W. Field, O. Benoist d'Azy, M. Lavollée, R. Lopez-Delgado, and A. Tramer, *Radiative decay rates from deperturbed v=0-7 vibrational levels of CO $A^1\Pi$ measured using synchrotron radiation,* J. Chem. Phys. **78**, 2838 (1983).

[135] R. L. DeLeon, *Erratum: CO (A-X) electric dipole transition moment [J. Chem. Phys. 89, 20 (1988)],* J. Chem. Phys. **91**, 5859 (1989).

[136] H. A. van Sprang, G. R. Möhlmann, and F. J. de Heer, *Radiative lifetimes of the CO $a'^3\Sigma^+$, $b^3\Sigma^+$, $c^3\Pi$, $d^3\Delta$ and $B^1\Sigma^+$ states. Absolute emission cross sections for t,* Chem. Phys. **24**, 429 (1977).

[137] M. Drabbels, W. L. Meerts, and J. J. ter Meulen, *Determination of electric dipole moments and transition probabilities of low-lying singlet states of CO,* J. Chem. Phys. **99**, 2352 (1993b).

[138] S. R. Federman, M. Fritts, S. Cheng, K. M. Menningen, D. C. Knauth, and K. Fulk, *Oscillator Strengths for B-X, C-X, and E-X Transitions in Carbon Monoxide,* Astrophys. J., Suppl. Ser. **134**, 133 (2001).

[139] G. Stark, A. N. Heays, J. R. Lyons, P. L. Smith, M. Eidelsberg, S. R. Federman, J. L. Lemaire, L. Gavilan, N. de Oliveira, D. Joyeux, and L. Nahon, *High-Resolution Oscillator Strength Measurements of the v' = 0,1 Bands of the B-X, C-X, and E-X Systems in Five Isotopologues of Carbon Monoxide,* Astrophys. J. **788**, 67 (2014).

[140] M. Drabbels, J. Heinze, J. J. ter Meulen, and W. L. Meerts, *High resolution double-resonance spectroscopy on Rydberg states of CO,* J. Chem. Phys. **99**, 5701 (1993a).

[141] E. Krishnakumar and S. K. Srivastava, *Radiative lifetimes of B and C 1Sigma(+) states of CO,* Astrophys. J. **307**, 795 (1986).

[142] P. Cacciani, F. Brandi, I. Velchev, C. Lyngå, C.-G. Wahlströ"m, and W. Ubachs, *Isotope dependent predissociation in the $C^1\Sigma^+$, $v = 0$ and $v = 1$ states of CO,* Eur. J. Phys. D **15**, 47 (2001).

[143] P. Cacciani and W. Ubachs, *High resolution study of Q-branches in the $E^1\Pi$ - $X^1\Sigma^+$ (0,0) band of $^{12}C^{16}O$, $^{13}C^{16}O$, and $^{13}C^{18}O$,* J. Mol. Spectrosc. **225**, 62 (2004).

[144] P. Cacciani, W. Hogervorst, and W. Ubachs, *Accidental predissociation phenomena in the $E^1\Pi$, $v = 0$ and $v = 1$ states of $^{12}C^{16}O$ and $^{13}C^{16}O$,* J. Chem. Phys. **102**, 8308 (1995).

[145] P. Cacciani, W. Ubachs, P. C. Hinnen, C. Lyngå, A. L'Huillier, and C.-G. Wahlström, *Lifetime Measurements of the $E\,^1\Pi$, v=0 and v=1 States of $^{12}C^{16}O$, $^{13}C^{16}O$, and $^{13}C^{18}O$,* Astrophys. J. Lett. **499**, L223 (1998).

[146] P. Petitjean, R. Srianand, and C. Ledoux, *Molecular hydrogen at z_{abs} =1.973 toward Q0013-004: dust depletion pattern in damped Lyman α systems,* Mont. Not. Roy. Astron. Soc. **332**, 383 (2002).

[147] M. Eidelsberg and F. Rostas, *Spectroscopic, absorption and photodissociation data for CO and isotopic species between 91 and 115 NM,* A&A **235**, 472 (1990).

[148] K. S. E. Eikema, W. Hogervorst, and W. Ubachs, *Predissociation rates in carbon monoxide: dependence on rotational state, parity and isotope,* Chem. Phys. **181**, 217 (1994).

[149] M. T. Murphy and J. C. Berengut, *Laboratory atomic transition data for precise optical quasar absorption spectroscopy,* Mont. Not. Roy. Astron. Soc. **438**, 388 (2014).

[150] D. C. Morton, *Atomic data for resonance absorption lines. I - Wavelengths longward of the Lyman limit,* Astrophys. J., Suppl. Ser. **77**, 119 (1991).

[151] J. X. Prochaska, Y. Sheffer, D. A. Perley, J. S. Bloom, L. A. Lopez, M. Dessauges-Zavadsky, H.-W. Chen, A. V. Filippenko, M. Ganeshalingam, W. Li, A. A. Miller, and D. Starr, *The First Positive Detection of Molecular Gas in a GRB Host Galaxy,* Astrophys. J. Lett. **691**, L27 (2009).

[152] J. Ma, P. Caucal, P. Noterdaeme, J. Ge, J. X. Prochaska, T. Ji, S. Zhang, H. Rahmani, P. Jiang, D. P. Schneider, B. Lundgren, and I. Pâris, *Cold gas and a Milky Way-type 2175-Å bump in a metal-rich and highly depleted absorption system,* Mont. Not. Roy. Astron. Soc. **454**, 1751 (2015).

[153] M. Daprà, M. van der Laan, M. T. Murphy, and W. Ubachs, *Constraint on a varying proton-to-electron mass ratio from H2 and HD absorption at $z_{abs} \simeq$ 2.34,* Monthly Notices of the Royal Astronomical Society **465**, 4057 (2017).

[154] S. A. Levshakov, *Differential Measurements of the Fine-Structure Constant from Quasar Spectra - a Test of Kaluza-Klein Cosmologies,* Mont. Not. Roy. Astron. Soc. **269**, 339 (1994).

[155] T. M. Evans, M. T. Murphy, J. B. Whitmore, T. Misawa, M. Centurion, S. D'Odorico, S. Lopez, C. J. A. P. Martins, P. Molaro, P. Petitjean, H. Rahmani, R. Srianand, and M. Wendt, *The UVES Large Program for testing fundamental physics - III. Constraints on the fine-structure constant from three telescopes,* Mont. Not. Roy. Astron. Soc. **445**, 128 (2014).

[156] P. Brax, *Environmental variation of constants in screened modified theories of gravity,* Phys. Rev. D **90**, 023505 (2014).

[157] J. C. Berengut, E. Epelbaum, V. V. Flambaum, C. Hanhart, U.-G. Meißner, J. Nebreda, and J. R. Peláez, *Varying the light quark mass: Impact on the nuclear force and big bang nucleosynthesis,* Phys. Rev. D **87**, 085018 (2013).

[158] H. Suzuki, S. Yamamoto, M. Ohishi, N. Kaifu, S.-I. Ishikawa, Y. Hirahara, and S. Takano, *A survey of CCS, HC_3N, HC_5N, and NH_3 toward dark cloud cores and their production chemistry,* Astrophys. J. **392**, 551 (1992).

[159] F. J. Lovas, *NIST Recommended Rest Frequencies for Observed Interstellar Molecular Microwave Transitions-2002 Revision,* J. Phys. Chem. Ref. Data **33**, 177 (2004).

[160] P. C. Myers, R. A. Linke, and P. J. Benson, *Dense cores in dark clouds. I - CO observations and column densities of high-extinction regions,* Astrophys. J. **264**, 517 (1983).

[161] C. A. Beichman, P. C. Myers, J. P. Emerson, S. Harris, R. Mathieu, P. J. Benson, and R. E. Jennings, *Candidate solar-type protostars in nearby molecular cloud cores,* Astrophys. J. **307**, 337 (1986).

[162] M. Tafalla, P. C. Myers, P. Caselli, C. M. Walmsley, and C. Comito, *Systematic Molecular Differentiation in Starless Cores,* Astrophys. J. **569**, 815 (2002).

[163] T. B. H. Kuiper, W. D. Langer, and T. Velusamy, *Evolutionary Status of the Pre-protostellar Core L1498,* Astrophys. J. **468**, 761 (1996).

[164] D. Wolkovitch, W. D. Langer, P. F. Goldsmith, and M. Heyer, *Physical Conditions in Quiescent Dark Cloud Cores Determined from Multitransition Observations of CCS,* Astrophys. J. **477**, 241 (1997).

[165] K. Willacy, W. D. Langer, and T. Velusamy, *Dust Emission and Molecular Depletion in L1498,* Astrophys. J. Lett. **507**, L171 (1998).

[166] M. Tafalla, P. C. Myers, P. Caselli, and C. M. Walmsley, *On the internal structure of starless cores. I. Physical conditions and the distribution of CO, CS, N_2H^+, and NH_3 in L1498 and L1517B,* A&A **416**, 191 (2004).

[167] M. Carter, B. Lazareff, D. Maier, J.-Y. Chenu, A.-L. Fontana, Y. Bortolotti, C. Boucher, A. Navarrini, S. Blanchet, A. Greve, D. John, C. Kramer, F. Morel, S. Navarro, J. Peñalver, K. F. Schuster, and C. Thum, *The EMIR multi-band mm-wave receiver for the IRAM 30-m telescope,* A&A **538**, A89 (2012).

[168] F. L. Schöier, F. F. S. van der Tak, E. F. van Dishoeck, and J. H. Black, *An atomic and molecular database for analysis of submillimetre line observations,* A&A **432**, 369 (2005).

[169] F. F. S. van der Tak, J. H. Black, F. L. Schöier, D. J. Jansen, and E. F. van Dishoeck, *A computer program for fast non-LTE analysis of interstellar line spectra. With diagnostic plots to interpret observed line intensity ratios,* A&A **468**, 627 (2007).

[170] D. Rabli and D. R. Flower, *The rotational excitation of methanol by molecular hydrogen,* Mont. Not. Roy. Astron. Soc. **406**, 95 (2010).

[171] P. F. Goldsmith and W. D. Langer, *Molecular cooling and thermal balance of dense interstellar clouds,* Astrophys. J. **222**, 881 (1978).

[172] P. F. Goldsmith, *Molecular Depletion and Thermal Balance in Dark Cloud Cores,* Astrophys. J. **557**, 736 (2001).

[173] R. M. Lees and J. G. Baker, *Torsion-Vibration-Rotation Interactions in Methanol. I. Millimeter Wave Spectrum,* J. Chem. Phys. **48**, 5299 (1968).

[174] R. M. Lees, *On the El-E2 Labeling of Energy Levels and the Anomalous Excitation of Interstellar Methanol,* Astrophys. J. **184**, 763 (1973).

[175] H. E. Radford, *Remeasurement of the Rest Frequency of the 36-CENTIMETER Radio Line of Methanol,* Astrophys. J. **174**, 207 (1972).

[176] J. E. M. Heuvel and A. Dymanus, *Hyperfine structure of CH_3OH,* J. Mol. Spectrosc. **45**, 282 (1973).

[177] L. Gaines, K. H. Casleton, and S. G. Kukolich, *Beam Maser Measurements of CH_3OH Rotational Transitions,* Astrophys. J. Lett. **191**, L99 (1974).

[178] S. C. Mehrotra, H. Dreizler, and H. Mäder, *J-Dependence of T_2-Parameters for Rotational Transitions of SO_2 and CH_3OH in K-Band,* Z. Naturforschung **40a**, 683 (1985).

[179] H. S. P. Müller, K. M. Menten, and H. Mäder, *Accurate rest frequencies of methanol maser and dark cloud lines,* A&A **428**, 1019 (2004).

[180] S. Tsunekawa, T. Ukai, A. Toyama, and K. Takagi, Department of Physics, Toyama University, Japan (1995).

[181] L.-H. Xu, J. Fisher, R. M. Lees, H. Y. Shi, J. T. Hougen, J. C. Pearson, B. J. Drouin, G. A. Blake, and R. Braakman, *Torsion-rotation global analysis of the first three torsional states (v_t = 0, 1, 2) and terahertz database for methanol,* J. Mol. Spectrosc. **251**, 305 (2008).

[182] J. T. Hougen, I. Kleiner, and M. Godefroid, *Selection Rules and Intensity Calculations for a C_s Asymmetric Top Molecule Containing a Methyl Group Internal Rotor,* J. Mol. Spectrosc. **163**, 559 (1994).

[183] L.-H. Xu and F. J. Lovas, *Microwave Spectra of Molecules of Astrophysical Interest. XXIV. Methanol (CH_3OH and $^{13}CH_3OH$),* J. Phys. Chem. Ref. Data **26**, 17 (1997).

[184] L. H. Coudert, C. Gutlé, T. R. Huet, J.-U. Grabow, and S. A. Levshakov, *Spin-torsion effects in the hyperfine structure of methanol,* J. Chem. Phys. **143**, 044304 (2015).

[185] S. P. Belov, G. Y. Golubiatnikov, A. V. Lapinov, V. V. Ilyushin, E. A. Alekseev, A. A. Mescheryakov, J. T. Hougen, and L.-H. Xu, *Torsionally mediated spin-rotation hyperfine splittings at moderate to high J values in methanol,* J. Chem. Phys. **145**, 024307 (2016).

[186] B. Lankhaar, G. C. Groenenboom, and A. van der Avoird, *Hyperfine interactions and internal rotation in methanol,* J. Chem. Phys. **145**, 244301 (2016).

[187] C. M. Walmsley, W. Batrla, H. E. Matthews, and K. M. Menten, *Anti-inversion of the 12.1 GHz methanol line towards dark clouds,* A&A **197**, 271 (1988).

LIST OF PUBLICATIONS

THE CHAPTERS IN THIS THESIS ARE BASED ON THE FOLLOWING PUBLICATIONS:

Chapter 2: *Constraint on a varying proton-electron mass ratio from H_2 and HD absorption in Q1232+082 at $z_{abs} \simeq 2.34$*
Daprà, M., van der Laan, M., Murphy, M. T., Ubachs, W.
Mont. Not. Roy. Astron. Soc. **465**, 4057 (2017)

Chapter 3: *Constraint on a varying proton-to-electron mass ratio from molecular hydrogen absorption toward quasar SDSS J123714.60+064759.5*
Daprà, M., Bagdonaite, J., Murphy, M. T., Ubachs, W.
Mont. Not. Roy. Astron. Soc. **454**, 489 (2015)

Chapter 4: *Constraint on a cosmological variation in the proton-to-electron mass ratio from electronic CO absorption*
Daprà, M., Niu, M. L., Salumbides, E. J., Murphy, M. T., Ubachs, W.
Astrophys. J. **826**, 192 (2016)

Chapter 5: *Analysis of carbon monoxide absorption at $z_{abs} \simeq 2.5$ to constrain variation of the proton-to-electron mass ratio*
Daprà, M., P. Noterdaeme, Vonk, M., Murphy, M. T., Ubachs, W.
Mont. Not. Roy. Astron. Soc. **467**, 3848 (2017)

Chapter 6: *Testing the variability of the proton-to-electron mass ratio from observations of methanol in the dark cloud core L1498*
Daprà, M., Henkel, C., Levshakov, S. A., Menten, K. M., Muller, S., Bethlem, H., Leurini, S., Lapinov, A. V., Ubachs, W.
Mont. Not. Roy. Astron. Soc. **472**, 4434 (2017)

THE AUTHOR ALSO CONTRIBUTED TO THE FOLLOWING PUBLICATIONS:

- *Enhanced C* I *in a lensed submillimiter galaxy at z* = 2.64*: evidence for a molecular outflow at high redshift*
  Roberts-Borsani, G. W., Jiménez-Donaire, M. J., Daprà, M., Alatalo, K., Aretxaga, I., Baker, A. J., Fujimoto, S., Gallardo, P. A., Gralla, M., Hughes, J. P., Laporte, N., Marriage, T. A., Nati, F., Rivera, J., Weiß, A., Wilson, G., Wollack, E., Yun, M. S.
  Astrophys. J. **844**, 110 (2017)

- *Constraints on changes in the proton-electron mass ratio using methanol lines*
  Kanekar, N., Ubachs, W., Menten, K. M., Bagdonaite, J., Brunthaler, A., Henkel, C., Muller, S., Bethlem, H. L., Daprà, M.
  Mont. Not. Roy. Astron. Soc. **448**, L104 (2015)

- *Robust Constraint on a Drifting Proton-to-Electron Mass Ratio at z=0.89 from Methanol Observation at Three Radio Telescopes*
  Bagdonaite, J., Daprà, M., Jansen, P., Bethlem, H. L., Ubachs, W., Muller, S., Henkel, C., Menten, K. M.
  Phys. Rev. Lett. **111**, 231101 (2013)

- *NPARSEC: NTT Parallaxes of Southern Extremely Cool objects. Goals, targets, procedures and first results*
  Smart, R. L., Tinney, C. G., Bucciarelli, B., Marocco, F., Abbas, U., Andrei, A., Bernardi, G., Burningham, B., Cardoso, C., Costa, E., Crosta, M. T., Daprà, M., Day-Jones, A., Goldman, B., Jones, H. R. A., Lattanzi, M. G., Leggett, S. K., Lucas, P., Mendez, R., Penna, J. L., Pinfield, D., Smith, L., Sozzetti, A., Vecchiato, A.
  Mont. Not. Roy. Astron. Soc. **433**, 2054 (2013)

- *Parallaxes of Southern Extremely Cool Objects. I. Targets, Proper Motions, and First Results*
  Andrei, A. H., Smart, R. L., Penna, J. L., d'Avila, V. A., Bucciarelli, B., Camargo, J. I. B., Crosta, M. T., Daprà, M., Goldman, B., Jones, H. R. A., Lattanzi, M. G., Nicastro, L., Pinfield, D. J., da Silva Neto, D. N., Teixeira, R.
  Astron. J **141**, 54 (2011)

ACKNOWLEDGMENTS

Writing this Ph. D. thesis required a constant work during the past five years. Nevertheless, I would have not made it without the help of a few people, I would like to thank here.

First and foremost I would like to thank my Ph. D. supervisor Wim Ubachs, who gave me his trust. Wim, you gave me a fantastic opportunity and I am deeply grateful for this. Under your supervision I believe I grew up not only as a scientist, but also as a person.

This thesis would have not been written without the inestimably help from Julija Bagdonaite, who taught me all the secrets of VPFIT. I would like to thank Michael Murphy who, despite being literally on the other side of the world, always gave me help and support. I am grateful to Christian Henkel, who taught me all about radio astronomy and the IRAM 30m. I want to thank my co-advisor Rick Bethlem for his help and the many discussions throughout the past years. A big thank also to Edcel Salumbides: I really appreciate the enthusiasm you put in your work every day. Thanks for all the energy you passed to during our interactions. I would like to thank all my present and past colleagues from the AML group, *primi inter pares* Aernout and Remy, for the science, the games and the fun we had together. Thanks.

It does not happen everyday to come back from a summer school with a paper, a successful observing proposal and so many wonderful colleagues. Luckily this was the case for the SMG group I am very proud to have joined in 2015. I want to thank M. J. Jimenez, Guido Roberts-Borsani and Katey Alatalo for all the good times we had while working on J2029. I wish all of you good luck with your future endeavours.

To move and settle into a new country is already tough, even without working on a Ph. D. I wish to thank here all the good friends who made this step way easier by sharing good moments, laughs, drinks and simply by having been there. Andrea, my 'Ph. D. brother' who now is on the other side of the Atlantic, thank you for all the good moments we had since the first day we moved to Amsterdam. I wish you and Carlotta all the best with your new American life. Thanks to Marco, for countless lunches, beers and philosophical discussions. Niki, I am incredibly lucky to have found part of the family here in Amsterdam. Thanks to Alberto, for the games, the comics, the dinners and for sharing updates on nearly sci-fi future developments. A big thank you to the rest of the Italian community: Luigi, Luca, Vincenzo, Giuseppe, Sabrina, Anna, Juri and Sara, Jacopo, Paio, Thomas and Daniele. To conclude, thanks to SVU family, Vittorio, Francesco, Michel, Werner, Sam, Marit and Niek for all the good moments and the tournaments.

Last but not least, thanks to Lenka for her enormous support and infinite patience.